1-1-2020

FATIGUE BEHAVIOR AND DEFECT-BASED LIFE PREDICTION OF ALUMINUM CASTINGS UNDER AXIAL, TORSION, AND MULTIAXIAL LOADINGS

Ahmad Nourian Avval

FATIGUE BEHAVIOR AND DEFECT-BASED LIFE PREDICTION OF ALUMINUM CASTINGS UNDER AXIAL, TORSION, AND MULTIAXIAL LOADINGS

by

Ahmad Nourian-Avval

A Dissertation

Submitted in Partial Fulfillment of the

Requirements for the Degree of

Doctor of Philosophy

Major: Mechanical Engineering

.

The University of Memphis

May 2020

To Mom, Dad, and Masi, my kind wife and friend

For your unconditional and never ending

love and support

Acknowledgments

I like to appreciate everyone who supported and helped me during my doctoral degree. First and foremost, I would like to thank and dedicate all my success to my lovely wife for her continuous encouragement and support over years.

I would like to express my deep gratitude to my advisor, Dr. Ali Fatemi, for his continuous support, encouragement, and patience during my graduate studies at the University of Memphis. His technical and editorial advice was essential to the completion of this dissertation. Dr. Gladius Lewis, Dr. Amir Hadadzadeh, Dr. Jason Carroll are also greatly acknowledged for serving on my Ph.D. committee. I would also like to thank Eaton Corporation for funding this research study.

Finally, I would like to thank my parents and family for their continuous support and encouragements throughout this long journey from primary school to doctoral degree.

.

Abstract

Defects in metallic components can be formed in many manufacturing techniques. These defects can significantly affect the mechanical properties, especially fatigue behavior of industrial components. In this study, the effect of defects on fatigue behavior and life prediction of a cast aluminum alloy, as an illustrative material containing defects, was investigated. Defect characterization was performed by using metallography, X-ray radiography and micro-computed tomography techniques. The variability of defects between the specimens of two sizes, different porosity levels, and based on location within the specimens were studied. The maximum defect size within the specimens was also estimated using extreme value statistics. In addition to fully-reversed fatigue tests, tension-tension as well as rotating bending tests were conducted to study the effects of mean stress and stress gradient. Fatigue tests were also performed under torsion, and under in-phase and out-of-phase combined axial-torsion loadings. Fatigue life predictions were performed using long and small crack growth models based on the observed defects size from fracture surfaces, as well as the maximum defect size estimated by extreme value statistics. Considering the effect of mean stress and overall plastic deformation, a small crack growth model is proposed which predicts fatigue lives in very good agreement with experimental results. Variable amplitude loading fatigue test results representative of service load histories were also predicted following both S-N and fracture mechanics approaches and the results are compared and discussed with reference to the experiments conducted.

Table of Contents

List of Tables

List of Figures

List of Nomenclature

$\sqrt{A}$	Murakami's defect parameter
A	materials constants
a	crack length
a_i, a_f	initial, final crack length
a_0	intrinsic crack length
b	fatigue strength exponent
b_0	shear fatigue strength exponent
c	fatigue ductility exponent
C, D	materials constants
E	elastic modulus
K	monotonic strength coefficient
K_0	shear monotonic strength coefficient
K'	cyclic strength coefficient
K_0'	shear cyclic strength coefficient
ΔK	stress intensity factor (SIF) range
K_{max}	SIF at maximum stress
ΔK_{thr}	crack growth threshold
m	materials constants
n	monotonic strain hardening exponent
n_0	shear monotonic strain hardening exponent
n'	cyclic strain hardening exponent
n_0'	shear cyclic strain hardening exponent
N_f	number of cycles to failure
r	specimen radius

r_p	cyclic plastic zone size at crack tip
s, t	materials constants
$T, \Delta T$	torque, range
Y	geometry factor
$\gamma, \Delta\gamma$	shear strain, range
$\varepsilon_{1,a}$	maximum principal strain amplitude
ε_f'	fatigue ductility coefficient
$\theta_{95,IP}$	range of planes experiencing 95% of fatigue damage for IP loading
$\theta_{95,OP}$	range of planes experiencing 95% of fatigue damage for OP loading
σ_a	axial stress amplitude
$\bar{\sigma}_{1,a}$	maximum principal stress amplitude
σ_f'	fatigue strength coefficient
$\sigma_{n,max}$	maximum normal stress
σ_{SWT}	Smith-Watson-topper equivalent stress
$\bar{\sigma}_{vM,a}$	von Mises stress amplitude
σ_u	ultimate tensile strength
σ_y	monotonic yield strength
σ_y'	cyclic yield strength
$\tau, \Delta\tau$	shear stress, range
τ_a	shear stress amplitude

Chapter 1

Introduction

1.1. Motivation for the Study and Objectives

Defects are inevitable in many industrial components, manufactured by processes like casting, powder metallurgy, and additive manufacturing. These defects weaken the mechanical performance of components in general, and fatigue behavior in particular [1,2]. Regarding the increasing use of these materials, a deeper understanding of the mechanisms controlling the fatigue properties and prediction of fatigue life are necessary to design durable components.

On the other hand, producing complex geometries economically and efficiently has made casting an attractive manufacturing method for producing a large number of industrial components, particularly in aerospace and automotive industries. Casting of aluminum alloys has made it possible to produce lighter structures with improved fuel efficiency [3].

Fatigue properties of cast components are inferior to those of wrought alloys [4–6]. The primary contribution to decreased fatigue resistance in cast alloys is the presence of defects formed during solidification [7]. In addition, not only at a given stress amplitude level defect containing materials exhibit shorter life in comparison to defect free materials, but the fatigue life is accompanied with larger scatter [4,8–10]. Therefore, in order to consider this inconsistency in

fatigue performance, it is required to consider a higher safety factor in designing of cast components, which often results in an overdesign.

The influence of defects on fatigue performance of these materials primarily depends on size of defects. It has been shown that there is a critical size for defects, below which the fatigue performance is not controlled by them [1]. Therefore, it would be ideal to reduce the defect size by applying some manufacturing techniques or post processing treatments to improve the fatigue performance. However, reducing defects size below the critical size is not always technically, nor economically possible in many manufacturing techniques or for all components. Therefore, a robust design methodology for these materials should consist of statistical evaluation of defects and prediction of fatigue life using an appropriate defect-based model, which is applicable for different loading conditions.

In spite of the fact that most components are subjected to multiaxial stresses, much of the research in the literature is on fatigue behavior of defect containing materials under uniaxial loading and there are only a few works published on fatigue behavior of these materials under torsion or combined loadings or variable amplitude loading condition. In addition, most of the models presented in the literature are not general enough to predict the fatigue life under different loadings. Therefore, the main objective of this work was to investigate the fatigue performance of cast aluminum alloy, as an illustrative material, under different loading conditions and develop a general defect-based model for fatigue life predictions.

Given these goals, the first specific objective of this work was to investigate the fatigue behavior of a cast aluminum alloy and study the effects of defects, section size, stress gradient, and mean stress. Therefore, the fatigue test results conducted on two specimen sizes and under various loading conditions including tension-compression, tension-tension, and rotating bending

were used. The scatter in fatigue life data was evaluated using statistical analysis. In addition, fatigue performance of this material under different testing conditions was predicted using the maximum size of crack-initiating defects measured on fracture surfaces.

The second specific objective was defect characterization and analysis of their variability. To achieve this goal, pore distributions in specimens with different sizes and porosity levels were compared, and the variability of defects based on location within the specimens was analyzed. The maximum defect size within the specimens was also estimated by extreme value statistics using the evaluated defect data from both metallography and μCT scan examinations. The advantage of extreme value statistics is that the maximum defect size in a component of the desired volume can be estimated. Therefore, the fatigue behavior can be predicted using the estimated maximum defect without a prior knowledge about the actual defects within the components.

The other specific objective of this work was to study the fatigue performance of cast aluminum alloy under axial, torsion and multiaxial loading conditions and evaluate the fatigue life using defect-based models. Given this goal, fatigue tests were performed under different loading conditions including axial, torsion, in-phase, and out-of-phase combined axial-torsion loadings. The fatigue crack growth mechanism was investigated. In order to study the crack face interaction during fatigue crack growth process, some tests were also conducted under cyclic torsion with static tension or compression.

Fatigue life prediction under different loading conditions was also another main objective of this study. Therefore, fatigue life data obtained under different loading conditions were analyzed using both long and small crack growth models. A general small crack growth model was also proposed, which can predict the fatigue life under different loading conditions. The fatigue life data under different loading conditions were evaluated using the size of fatal defects measured

from fracture surfaces. Fatigue life prediction was also performed using the proposed model assuming the maximum defect size estimated by extreme value statistics as an initial crack size.

Finally, the fatigue performance of cast aluminum alloy was studied under variable amplitude loading condition. Variable amplitude axial fatigue tests were conducted using a real industrial load spectrum. Mean stress effect was also studied by conducting variable amplitude fatigue tests with significant mean stress. The fatigue life of the specimens under different loading conditions was predicted using both *S-N* approach as well as fracture mechanics approach. The effect of considering the load sequence on fatigue life prediction was also studied.

1.2. Outline of Dissertation

This study is presented in eight chapters. Chapter 2 presents a brief literature survey on the effect of defects on fatigue performance of castings. In this chapter, different types of defects in castings and their effect on fatigue behavior are summarized. Fatigue damage mechanisms as well as fatigue life prediction approaches are reviewed. In addition, different approaches for defect characterization and estimating the maximum defect size within the specimens or components through extreme value statistics are also discussed.

Chapter 3 presents the analysis of defect characterization in high pressure die cast aluminum alloy. The results of defect evaluation using metallography and micro-computed tomography techniques, as well as statistical analysis of variability of defects between the specimens of two sizes and different porosity levels are presented. The analysis of defect distributions based on location within the specimens are also discussed. Moreover, the estimates of maximum defect size within the specimens obtained through extreme value statistics based on both 2D and 3D defect data are included. The accuracy of each approach is verified by comparing

the estimated maximum defect size within the specimens with the maximum observed defects on fracture surfaces of fatigue specimens.

Chapter 4 presents the effect of defects on fatigue behavior of cast A356-T6 aluminum alloy, as an illustrative material. This chapter consists of uniaxial fatigue tests results conducted at two different stress ratios as well as rotating bending tests on two specimen sizes. The effects of defects, specimen size, mean stress and stress gradient on fatigue performance are discussed. The scatter in fatigue life data are studied using statistical analysis. The discussions of correlating the fatigue life data under different stress ratios using a mean stress correction factor, as well as fatigue life predictions under different testing conditions based on the maximum defect size observed on fracture surfaces are also included.

Chapter 5 presents fatigue life analysis using both long and small crack growth models. A small crack growth model is also proposed which considers the effect of mean stress as well as overall plastic deformation. Fatigue life predictions based on the defects size measured from the fracture surfaces, as well as the maximum defect size estimated by extreme value statistics within the stressed volume are presented. Discussions of fatigue limit, mean stress, and the effect of defect parameters on fatigue life are also included.

Chapter 6 investigates the fatigue performance of A356-T6 under different loading conditions. In addition to monotonic and cyclic deformation behaviors, fatigue tests results performed under axial, torsion, in-phase and out-of-phase combined loadings are presented. In addition, the results of fatigue tests under cyclic torsion with static tension or compression are also included to study the fatigue crack propagation mechanism. Smith-Watson-Topper (SWT) damage parameter is used to correlate the fatigue data. Fatigue life predictions based on fatal defects size

on fracture surfaces as well as the maximum defect size estimated by extreme value statistics are also included.

Chapter 7 evaluates the fatigue performance of A356-T6 aluminum alloy under variable amplitude loading conditions. The results of fatigue tests under a real industrial load spectrum at high and low mean stress conditions are presented. The predicted fatigue lives based *S*-*N* approach as well as fracture mechanics approach using direct summation method and FASTRAN program assuming the defects as initial cracks are compared and discussed with reference to the experimental results. Finally, a summary of the dissertation is presented in Chapter 8. Some suggestions for future studies on fatigue life prediction of defect containing materials are also presented in this chapter.

Chapter 2

Literature Survey

2.1. Introduction

A large number of components used in many industries, including aerospace, automotive, electrical, and railroad are manufactured by casting, since complex geometries or large parts can be produced economically [3]. On the other hand, excellent castability, corrosion resistance, and especially high strength to weight ratio have made cast aluminum alloys attractive materials to produce lighter structures with improved fuel efficiency [3,11].

Aluminum castings can be produced by many casting processes, which can produce components with different engineering properties. High-Pressure die casting (HPDC) is the preferred production process for large production volumes. This process involves high-velocity injection of molten metal into metal dies and solidification under high pressure. The cycle time is relatively short, typically a few second for relatively small castings and less than a minute for large parts. Dimensional accuracy and surface finish of castings are good, so subsequent machining processes are minimized [11,12]. For smaller production volumes low-pressure die casting (LPDC), permanent mold casting, and sand casting can be used. Investment casting is also used in

production of small complex components with high dimensional accuracy and surface finish [11,12].

One of the major problems in castings is the presence of defects, which can limit the application of cast components by affecting their mechanical properties, particularly fatigue behavior [13,14]. These defects can be classified as oxide films, gas porosity and shrinkage porosity. Oxide films form due to reaction of melt with atmosphere. Oxides have a good bonding to melt. However, when the oxide film folds (bifilms) there is no bonding between the two dry surfaces. If these bifilms are transferred to the mold, they will act like a crack in cast component and weaken the mechanical properties.

Gas porosities can form during casting process either by entrapped gas due to turbulence of melt during mold filling or by releasing the dissolved gas from melt during solidification. In case of aluminum alloys, hydrogen can be formed by reaction of molten aluminum with humidity from the atmosphere and dissolved in melt. However, its solubility in melt is reduced significantly during solidification, leading to rejected hydrogen which results in forming gas porosity. Gas pores are normally more or less spherical because the growth is without restrictions in the melt to reduce the gas-melt interface energy [3,11,12].

Shrinkage porosities result from the natural contraction of melt during solidification, due to density difference between solid and liquid alloy phases. The solidification of pure aluminum is accompanied by 7% decrease in volume during phase change from liquid to solid. Common aluminum casting alloys exhibit volumetric shrinkages in the range of 5 to 6%. As solidification progresses, molten metal flows to compensate for the liquid-solid volume change. However, the ability to feed becomes more and more difficult due to the decreasing size of the channels along which feeding take place, i.e. the interdendritic network. Eventually the channels freeze

completely, isolating small areas from a supply of fresh molten metal, which results in shrinkage porosities due to lack of melt between dendrites during solidifications. Shrinkage porosities have irregular and branched shapes. When they are studied by metallographic examination, they appear on metallography cross section as complex forms or a group of smaller pores due to sectioning of the various dendrite arms during sample preparation. The size of individual microshrinkage pores may range in length from a few microns to a few millimeters [3,11,12]. Some SEM micrographs of fracture surfaces of specimens containing these defects are illustrated in Figure 2.1.

2.2. Fatigue Damage in Defect Containing Materials

A large number of cast components are subjected to cyclic stresses and strains during service and they are susceptible to fatigue failure. Fatigue failure is a consequence of accumulation and progression of microdamage in a material due to cyclic loading. This damage progression in metals can typically be divided into two stages including crack initiation and growth [1,15,16].

Crack initiation includes the initial stages of microstructural damage that lead to creation of microscopic cracks and the coalescence of these cracks to form a dominant crack. In this stage the growth of micro cracks is affected by microstructural barriers which may lead to retardation or arresting of microcracks. Once the cracks length become larger than microstructural features, they experience stable growth.

Stable crack growth includes stable growth of small cracks and long cracks. The growth behavior of small fatigue cracks is fundamentally different from that of long cracks because of crack closure effects. This is because as the crack grows, a wake of plastically deformed material develops around the crack and causes the faces of the crack come into contact during unloading before the point of zero load is reached (plasticity-induced crack closure). In addition, the contact

between the crack surfaces as a result of rough crack morphology (roughness-induced crack closure) can reduce the driving force for crack propagation. However, when the cracks are small, they do not experience the same level of crack closure which results in faster growth rate and having less crack growth threshold compared to long cracks [17,18].

There are several ways to define small cracks [17]. Cracks with a length comparable to the scale of microstructure, e.g. in the order of grain size, are called microstructurally small cracks, cracks with length comparable to the local plasticity are called mechanically small cracks, and cracks which are simply physically small, typically in the order of 0.1-2 mm, are called physically small cracks [17]. In the case of microstructurally small cracks and mechanically small cracks, there is a continuum mechanics limitation because the crack growth consists of accelerated crack growth along with retardation or arresting at the microstructural barriers. However, in physically small cracks the crack length is long in terms of continuum mechanics, while the cracks propagate more quickly in comparison to that of long cracks under the same nominal driving force due to less crack closure in small cracks in comparison to long cracks [17,18]. Therefore, the total fatigue life of a component is modeled as the sum of numbers of cycles spent in several consecutive stages, as follows [19]:

$$N_f = N_{nuc} + N_{MSC} + N_{PSC} + N_{LC} \tag{2.1}$$

where N_{nuc} is the number of cycles for crack nucleation, N_{MSC} is the number of cycles for growth of microstructurally small crack, N_{PSc} is the number of cycles spent on physically small crack growth, and N_{LC} is also the number of cycles spent on long crack growth.

The size of defects in cast aluminum alloys are such that cracks originated from them are in the range of physically small cracks [9,20–22]. Since the rate of crack growth increases with

increasing the crack size, it has been suggested that a significant portion of the entire crack growth life is spent in growing of small cracks [21,23].

2.2.1. Fatigue failure mechanism in castings under axial loading

Either of the two stages of fatigue failure, crack initiation or growth, can dominate fatigue life depending on the loading conditions, microstructure, and environment. In cast Al-Si alloys fatigue cracking involves competitive and often synergistic micro-mechanisms operating at different length scales as influenced by various structural features, including defects and second phase particles. Although these mechanisms may not necessarily operate individually, it is reported that cracks originate from the following regions:

1. Processing defects, such as porosity [4,10,24] or oxide films [25,26]
2. Microstructural features, including eutectic Si particles, primary Si particles and various types of intermetallic compounds [20,27,28]
3. Persistent slip bands at the surface when there is no critical defects or secondary microstructural phase [20,22]

The influence of defects on the fatigue performance depends on the defect size. It has been shown that there is a critical defect size, below which fatigue performance is not controlled by defects but by other microstructural features. Murakami and Endo [1,29] studied the effect of defect size on fatigue limit of different materials by introducing small artificial holes into the surface of the specimens and concluded that there is a critical defect size below which the fatigue limit will not change and at that stress cracks initiated from these defects will not grow during cyclic loading. However, as the defects become larger the fatigue limit may drop significantly. This phenomenon is illustrated in Figure 2.2.

Couper et al. [6] suggested that for cast aluminum alloys also there is a critical pore size, below which fatigue life is controlled by microstructural features. Shiozawa et al. [22] studied the fatigue properties of Al-Si alloys produced by squeeze casting, containing porosities of maximum size around 20 μm and observed that the crack initiated from Si particles or intermetallic silicon particles near the surface. Boileau and Allison [4] also studied the effect of age hardening heat treatment on fatigue behavior of W319 in as-cast and HIPed conditions and concluded that in the absence of porosity the fatigue resistance is enhances significantly by crack nucleation at microstructural features. Further, they observed that the fatigue resistance of HIPed specimens was enhanced by heat treatment, while heat treatment did not affect the fatigue properties of non-HIPed specimens significantly. Similar results were reported by Caton et al. [20,21] who also studied the effect of hot isostatic pressing (HIP) on fatigue behavior of cast W319 aluminum alloy. Wang et al. [10] investigated fatigue behavior of HIPed A356-T6 alloy and indicated that the critical pore sizes for this material is around 25 μm for castings with secondary dendrite arm spacing (SDAS) equal to 20-25 μm, while it may increase to ~50μm for castings with SDAS equal to 70-75 μm for the same alloy under stress amplitudes of 70-100 MPa and stress ratios of 0.1-0.2.

However, fractography examinations of fatigue specimens have shown that in cast aluminum alloys containing porosities, fatigue cracks initiate predominantly from pores. Boileau and Allison [4] found that fatigue failure of cast aluminum alloys containing porosity is independent of microstructure and almost always initiated from pores. Mayer et al. [30] found that 98.5% of fatigue failures of cast magnesium and cast aluminum alloys all produced by HPDC initiated from porosities. Ammar et al. [31] studied the fatigue performance of cast 319 and 356 aluminum alloys and observed that 92% of all tested specimens fractured because of surface porosity acting as a crack initiation site and concluded that surface porosity is the most important

casting defect affecting the fatigue life. Wang et al. [10] investigated fatigue behavior of cast A356-T6 alloy and found that in almost all non-HIPed specimens fatigue cracks initiated from defects, among which pores were more detrimental to fatigue life than oxides. Similar results were reported by Wang and Jones [26] who studied fatigue behavior of cast 319 type aluminum alloy and observed that fatigue cracks normally initiate from the largest pores in the stressed volume. The fact that porosity is more detrimental than oxides of comparable size to the fatigue performance has been confirmed by other reports as well, such as [5,8,25,32].

More eutectic silicon and intermetallic particles have been reported to be around pores as opposed to oxides and may explain why pores may be more detrimental [5], as shown in Figure 2.3(a). Finite element analysis performed by Gao et al. [32] has shown that the presence of these particles increases the local stress at the concave root of pores and therefore facilitate the initiation process by debonding, see Figure 2.3(b,c). Therefore, contrary to defect free materials, in which fatigue mechanism consists of crack initiation on microstructural features and crack growth [10,22,33], in presence of pores the crack initiation life is negligible and most of the fatigue life is spent on crack growth [9,10,34,35].

2.2.2. Fatigue failure mechanism under torsion and multiaxial loadings

In spite of much research in the literature on fatigue behavior of defect containing materials under uniaxial loading condition, there are only a few works published on fatigue behavior of these materials under torsion or combined loadings. Roy et al. [36] studied the fatigue limit (defined as fatigue strength at 10^6 cycles) of A356-T6 cast aluminum under tension, torsion and in-phase tension-torsion combined loadings and showed that the nucleation life was negligible for fatigue lives close to 10^6 cycles due to pre-existing defects. They also observed that under pure tension

and combined tension-torsion loadings crack growth occurred on the plane of maximum principal stress, while under pure torsion it was difficult to find a unique initiation site on fracture surfaces. They also estimated the fatigue limit using maximum principal stress and Crossland criteria and found that maximum principal stress criterion provided the closest estimation to experimental results, as shown in Figure 2.4.

Koutiri et al. [37] also studied the high cycle fatigue behavior of cast Al-Si alloy under plane bending, torsion, and equibiaxial bending. They observed that under torsion cracks initiated from Si-particles of the eutectic zones and grew on the plane of maximum shear stress, while under plane bending and equibiaxial bending initiation of the fatigue crack almost always occurred at a micro-shrinkage pore (see Figure 2.5). For plane bending, fatigue cracks were mainly oriented perpendicular to the loading direction, while under equibiaxial bending no preferred crack growth direction was observed and cracks were often branched. They then concluded that fatigue damage in this material is controlled by two different fatigue crack initiation mechanisms, one mechanism is associated with relatively large micro-shrinkage pores and the other is controlled by much smaller microstructural heterogeneities or the material matrix. They also studied the mean stress effect by conducting different stress ratios under plane bending and found that the fatigue life scatter drops significantly as the mean stress increases. In addition, they applied Dang Van criterion to the fatigue data and concluded that this model was not able to predict the multiaxial and the mean stress effects for this cast aluminum alloy.

Houria et al. [38] studied the influence of defects on fatigue limit of A356-T6 under multiaxial loading conditions including tension, torsion, and in-phase tension-torsion loading and reported that the fracture surfaces of specimens tested under combined tension–torsion loading were perpendicular to the direction of the maximum principal stress. They also reported a small

influence of mean stress on the fatigue limit under torsion loading, while under tension and combined tension–torsion loadings the effect of mean stress was much more pronounced in the presence of defects compared to defect free materials.

Le et al. [39], [40] studied high cycle fatigue behavior of three cast aluminum alloys with different microstructural characteristics under axial, torsion and proportional combined tension-torsion loading conditions and observed that casting porosity had a very detrimental influence on uniaxial and combined loadings, while a much lower influence was observed for torsional fatigue strength. They suggested that there are two crack initiation mechanisms. The first mechanism is related to crack propagation from casting pores located on the specimen surface and the second mechanism is controlled by microstructural features and slip bands. For porosity containing alloys these two mechanisms were observed on the same specimen, while for pore-free alloys the formation of persistent slip bands in the matrix was the major fatigue crack initiation mechanism, regardless of the loading mode, see Figure 2.6.

2.3. Effect of casting defects on fatigue behavior

The fatigue properties of cast components are significantly affected by defects formed during solidification. Defects introduce high stress concentrations within the specimens and components, serving as the main sites for crack nucleation [41-43].

It has also been reported by Avalle et al. [13] that increasing the porosity size leads to decreasing tensile strength, ductility, and fatigue limit of cast aluminum alloy. Boileau and Allison [4] also compared the fatigue properties of cast aluminum alloys in HIPed (almost pore free) and non-HIPed condition and showed that pores can significantly affect the fatigue properties of cast aluminum components by several orders of magnitude, as shown in Figure 2.7.

Wang et al. [10] classified the failed specimens in terms of the crack initiation sites and observed that the fatigue lives of specimens in which fatigue crack initiated from oxide films were ~4 to 5 times longer than those of the specimens that failed from porosity, while oxides were more detrimental than eutectic Si particles and slip bands, as shown in Figure 2.8.

Not only do defects weaken the fatigue performance of defect containing materials, but also they can result in significant scatter in fatigue life. Buffiere et al. [44] studied fatigue behavior of AlSi7Mg cast aluminum and found that the porosity level can significantly alter the average number of cycles to failure as well as increasing the lifetime scatter. They also found that the initiation of fatigue cracks occurs at the convex parts of pores which are located at or below the surface of the specimens. Wang and Jones [26] showed that in the specimens containing defects, the fatigue life has an inverse relation with the size of crack initiating defects. Davidson et al. [8] also studied the scatter in fatigue life of a cast aluminum alloy and confirmed that the scatter in fatigue life is associated with the size of crack initiating pores, as shown in Figure 2.9.

2.3.1. Effect of defect characteristics on fatigue performance

In spite of great effort dedicated to reducing porosity within cast components, complete elimination of defects is neither technically nor economically possible. This necessitates defect characterization. For defect characterization, size, location, shape, and orientation of defects can be considered.

2.3.1.1. Defect size

It has been suggested that the size of defects is the most important characteristic to be considered in evaluating the fatigue performance of defect containing materials since it has direct

influence on local stress and strain concentrations during cyclic loading. Experimental evaluations revealed that the most severe defects are the largest of those located at or near the surface of the specimen or component [9,10,26,45,46]. Larger defects are known to induce higher local stresses and strains [32,47] and are therefore more important for crack nucleating. Linder et al. [48] also reported that the specimens with larger pores show a lower fatigue strength in comparison to the specimens with smaller defects. Wang and Jones [26] studied the fatigue behavior of cast 319 type aluminum alloy and showed that fatigue failures in cast aluminum alloy are attributed to casting pores and the crack are normally initiated from the largest pores in the stressed volume.

Seniw et al. [45] examined the influence of pore size, morphology, and location on the fatigue properties of cast A356 aluminum and reported that cracks most likely initiate from pores that are larger and located closer to a free surface. Boileau and Allison [4] studied the fatigue behavior of cast W319 on the specimens taken from wedge-shape castings and from sections of cast components and observed that porosity size had a statistically significant effect on the fatigue life. Buffiere et al. [5] studied the fatigue properties of AlSi7Mg cast aluminum and found the defect size is more detrimental to fatigue life than the defect shape.

2.3.1.2. Defect location

The defects located at or near the free surface lead to higher stress and strain concentrations due to reduced constraint. It is therefore expected that the combined effect of size and location relative to the free surface will determine the severity of potential crack initiators. Larger near surface defects will therefore be more susceptible for crack nucleation and reduce the fatigue initiation period.

Seniw et al. [45] observed that the fatigue life of an A356 alloy containing pores of comparable size increased with their distance from the free surface and large pores far from the free surface had less detrimental effect on fatigue life compared to smaller pores located near the free surface. Several other authors have reported similar observations [49,50]. Gao et al. [32] used finite element analysis to study the effect of defect location on stress and strain concentrations around defects and demonstrated that surface porosities result in higher stress concentration than internal pores. It is therefore suggested that for the pores of same size, those located nearer the surface of castings have a higher probability of initiating fatigue cracks as opposed to those which are far from the surface.

2.3.1.3. Defect shape and orientation

Regarding the shape and orientation of defects, those with complex shapes containing arcs with sharp root radii are the preferred sites for fatigue crack initiation as opposed to those with a more spherical shape. Fan et al. [51] carried out FEA analysis using a realistic pore geometry in cast aluminum and observed that the maximum strain and stress concentrations were experienced in the vicinity of the arcs at the pore's major axis perpendicular to the loading direction, while the stress and strain concentration increased rapidly as the radius of curvature decreased. However, FEA analysis by Buffiere et al. [44] reported only a 10% difference between the stress intensity factor of a pore with a complex shape and that of elliptical one with the same projected defect size. Gao et al. [32] also showed that the maximum stress concentration around a pore with a complex shape was only 3% higher than that with a simpler shape but equivalent projected area and local curvature radii. Therefore, they suggested that a shape effect quite unlikely have significant effect on crack growth, see Figure 2.10.

Li et al. [43] also suggested that the stress and strain concentrations are significantly affected by the projected area on the transverse plane to the loading direction, rather than the local radius of curvature of defects. Therefore, shape and orientation effects may be insignificant if there is no change in the effective size of the pores and their local curvature radii, see Figure 2.11.

2.3.1.4. Clustering and spatial distribution of defects

Closely spaced multiple pores are expected to increase the local concentration of stresses and strains around the pores or particles. Skallerud et al. [9] showed that multiple small pores can initiate the fatigue failure as frequently as a larger single pore. When there are clusters or multiple small pores, the fatigue cracks initiate from these pores and grow in a manner that allows them to coalesce into one dominant crack that causes failure. It is suggested that crack initiation is easier in cases of multiple pores close to each other because of higher local plastic strains resulting from overlapping the slip bands from individual pores in the cluster.

2.4. Modeling and Prediction Approaches

2.4.1. Fatigue limit predictions

Considering the size of critical defects in cast aluminum alloys, which are typically between 100-1500 μm, the cracks initiating from these defects are in the range of physically small cracks. It has been shown that physically small fatigue cracks do not behave in accordance with conventionally acquired long crack growth data. When stress intensity factor, ΔK, is used for evaluation of crack growth rates, the small cracks grow at ΔK values less than long crack threshold, ΔK_{th}, and even grow faster than long cracks at equivalent ΔK levels. This is due to less crack closure experienced by small cracks compared to long cracks which results in faster growth rate.

El-Haddad et al. [52] proposed a method to compensate the difference between ΔK_{th} of small and long cracks by artificially increasing the physically small crack length, as follows:

$$\Delta K_{th}\sqrt{a_0 + a} = \Delta K_{th,l}\sqrt{a} \tag{2.2}$$

Consequently, the fatigue limit for crack containing material can be obtained by:

$$\Delta\sigma_{th} = \Delta K_{th,l}/\sqrt{\pi(a + a_0)} \tag{2.3}$$

where ΔK_{th} and $\Delta K_{th,l}$ are the crack growth threshold for small and long cracks, respectively, $\Delta\sigma_{th}$ is the fatigue limit range of a materials containing a crack of length a, and a_0 is the intrinsic crack length. Considering Equation (2.3), it is inferred that as the crack length increases, the fatigue limit of the materials decreases. This issue is well described by Kitagawa-Takahashi diagram in which the fatigue limit is also described as a function of small defects within the material, as shown in Figure 2.12.

Another approach to considering the effect of small cracks (defects) on the fatigue limit is the Murakami approach, in which the fatigue limit is related to both hardness and the maximum defect size within the material. Murakami [1] showed that for a material containing a crack or defect with an irregular shape, ΔK can be estimated by:

$$\Delta K = Y\Delta\sigma\sqrt{\pi\sqrt{A}} \tag{2.4}$$

where $\sqrt{A}$ is Murakami's defect parameter expressing the square root of area of defects on the plane perpendicular to the load direction used for representing the crack (defect) size, and Y is the geometry factor equal to 0.65 for surface cracks. Using $\Delta\sigma_{th}$ in Equation (2.4) will result in ΔK_{th}. Murakami and Endo [29] also showed that for small cracks the threshold is proportional to crack size, $\sqrt{A}$, as given by:

$$\Delta K_{th} \propto \left(\sqrt{A}\right)^{1/3} \tag{2.5}$$

Combining Equations (2.4) and (2.5) and considering the hardness of different materials, they suggested that the fatigue limit of the material containing surface defects can be estimated as:

$$\Delta\sigma_{th} = \frac{1.43(HV+120)}{(\sqrt{A})^{1/6}} \tag{2.6}$$

where *HV* is Vicker's hardness of the material. This model is commonly used due its simplicity and easy application in design. However, it has been reported that estimating the fatigue limit or long life strength using Equation (2.6) is non-conservative for non-ferrous metals, including aluminum alloys [53,54]. In order to address this problem, Noguchi et al. [55] proposed that the fatigue strength of non-ferrous alloys at 10^7 cycles can be estimated by modifying Murakami's model using the ratio of elastic modulus of non-ferrous alloy, i.e. aluminum alloy, E_{Al}, to that of steel, E_{St}, as given by:

$$\Delta\sigma_{th} = \frac{1.43(HV+120\times\frac{E_{Al}}{E_{St}})}{(\sqrt{A})^{1/6}} \tag{2.7}$$

Having studied the fatigue strength of cast aluminum specimens containing artificial drilled holes, Ueno et al. [56] also proposed the following relation for estimating the long life fatigue strength of aluminum alloys:

$$\Delta\sigma_{th} = \frac{1.43(HV+75)}{(\sqrt{A})^{1/6}} \tag{2.8}$$

Tajiri et al. [57] also used this model for fatigue limit prediction of cast aluminum alloys and reported reasonable predictions.

2.4.2. Fatigue life predictions

To predict the fatigue life in defect containing materials both long and short crack growth models have been used in the literature. Long crack growth models are characterized by linear elastic fracture mechanics (LEFM), in which the fatigue crack growth rate in region II of the

sigmoidal $\mathrm{d}a/\mathrm{d}N - \Delta K$ curve can be considered to model the crack growth. Paris and Erdogan proposed a power law relation between the crack growth rate and stress intensity range, given by:

$$\frac{\mathrm{d}a}{\mathrm{d}N} = C_1 \Delta K^{m_1} \tag{2.9}$$

where C_1 and m_1 are Paris's constant and exponent, respectively. This equation was later modified by Elber [58] to account for the effect of crack closure:

$$\frac{\mathrm{d}a}{\mathrm{d}N} = C_2 \left(\Delta K_{eff}\right)^{m_2} \tag{2.10}$$

in which ΔK_{eff} is the effective stress intensity factor range, $\Delta K_{eff} = K_{max} - K_{cl}$, where K_{max} and K_{cl} are the stress intensity factors associated to the maximum stress and the stress at which the crack closure occurs, respectively. However, in order to consider the entire $\mathrm{d}a/\mathrm{d}N - \Delta K$ curve, Newman [59] expanded Paris equation to a more complex equation form:

$$\frac{\mathrm{d}a}{\mathrm{d}N} = C_3 (\Delta K)^{m_3} \frac{1-\left(\Delta K_{th,eff}/\Delta K_{eff}\right)^2}{1-(K_{max}/K_{1c})^2} \tag{2.11}$$

where $\Delta K_{th,eff}$ and K_{1c} are the effective threshold intensity factor range and fracture toughness, respectively.

Following the LEFM concept for fatigue life of porosity containing cast aluminum alloys, Buffiere et al. [5] reported that prediction of fatigue life using a LEFM-based model was reasonable at high stresses, but very conservative at long lives. Couper at al. [6] predicted the fatigue life of cast CP601 cast aluminum alloys using expanded Paris equation (Equation 2.10) where the effective stress intensity factor was defined as $\Delta K_{eff} = U(a)Y(a)\Delta\sigma\sqrt{\pi a}$, in which $U(a)$ is the crack closure factor and $Y(a)$ is the geometry factor. They also reported reasonable predictions, but the predictions were slightly non-conservative, particularly at high stress levels.

Wang et al. [10] and Davidson et al. [8] demonstrated the fatigue life data in terms of modified *S-N* plots by considering the effect of initial defect size on *S-N* diagrams. Integrating

Paris equation and assuming that the final crack size is much larger than the initial defect size (a_i) results in Equation (2.12) which relates fatigue life (N_p) to initial defect size and stress level:

$$\sigma_a^{m_2} N_p a_i^{(m_2-2)/2} = B \tag{2.12}$$

where

$$B = \left[\left(m_2 - \frac{1}{2}\right) C_2 Y(a)^{m_2} U(a)^{m_2} \pi^{\frac{m}{2}}\right]^{-1} \tag{2.13}$$

However, they obtained the constants B and m_2 by fitting Equation (2.12) to the experimental data. They also used extreme-value statistics to estimate the maximum defect size and reported that this model gives reasonable fatigue life predictions for cast aluminum alloys.

Skallerud and coworkers [9] modified the Paris equation by considering the threshold stress intensity factor, as follows:

$$\frac{\mathrm{d}a}{\mathrm{d}N} = C_4(\Delta K_{eff}{}^{m_4} - \Delta K_{th}{}^{m_4}) \tag{2.14}$$

However, they reported that the fatigue life prediction for cast Al-7Si-0.4Mg aluminum alloy tends to be nonconservative. They further expanded this model by introducing an effective crack length into the definition of stress intensity factor, given by:

$$\Delta K_{eff} = Y\Delta\sigma\sqrt{\pi(a + a_0)} \tag{2.15}$$

where a_0 is the intrinsic crack length, defined by El-Haddad as:

$$a_0 = \frac{1}{\pi}\left(\frac{\Delta k_{th}}{Y\Delta\sigma_0}\right)^2 \tag{2.16}$$

in which Δk_{th} is the threshold SIF and $\Delta\sigma_0$ is the fatigue strength range of the material at 10^7 cycles. In fact, by artificially increasing the crack length in stress intensity factor relation, the higher crack growth rates in small cracks was considered. They observed the estimated fatigue life using this model to also be conservative.

It has been argued that the discrepancy between the estimated fatigue life using LEFM concept and experimental data is due to the small crack effect of the cracks originated from defects. Small crack growth rate as a function of crack length (a) and stress level (σ_a) was defined by Frost and Dugdale [60] and then by Nisitani et al. [61] as:

$$\frac{\mathrm{d}a}{\mathrm{d}N} = C_5 \sigma_a^{m_5} a \tag{2.17}$$

where C_5 and m_5 are material constants and σ_a is the stress amplitude. This model was further modified by Goto and Nisitani [62] to consider the influence of material properties, such as ultimate tensile strength or yield strength. They explained that the growth rate of small cracks can be modeled by considering crack tip opening displacement (CTOD) which is related to cyclic plastic zone size, r_p, at the tip of a crack:

$$r_p/a \propto \left(\sigma_a/\sigma_y\right)^{m_6} \tag{2.18}$$

The crack growth rate can then be approximated by:

$$\frac{\mathrm{d}a}{\mathrm{d}N} = C_6 \left(\frac{\sigma_a}{\sigma_b}\right)^{m_6} a \tag{2.19}$$

where σ_b can be either yield strength (σ_y) or ultimate strength (σ_u).

This model was used by Shiozawa et al. [22] for modeling of small crack growth in two squeeze cast aluminum alloys (AC8A-T6 and AC4C-T6). They found crack growth in the two cast aluminum alloys to obey Equation (2.19) well when the ultimate tensile strength is used for σ_b. Later, Caton et al. [20] argued that in Equation (2.19) the effect of crack tip plasticity is taken into accounts only by considering the relation between cyclic plastic zone size, applied stress amplitude, and crack size, while the contribution of global deformation applied to the specimen during loading cycle is not considered. Therefore, the following relation was proposed by taking global strain into consideration:

$$\frac{\mathrm{d}a}{\mathrm{d}N} = C_7 \left(\varepsilon_{max} \frac{\sigma_a}{\sigma_y}\right)^{m_7} a \tag{2.20}$$

where ε_{max} is the maximum total strain during the loading cycle. The constants C_7 and m_7 were then determined by fitting Equation (2.20) to the small crack growth rates for cast W319 aluminum alloy.

2.5. Defect Characterizing Tools and Extreme Value Statistics

The accuracy of the life prediction strongly depends on the defect characteristics and population within the material. The size of the largest defect has been recognized as the most important parameter in determining the fatigue properties of aluminum castings. Therefore, evaluating the defects for analyzing the fatigue data and predicting the fatigue life is of great importance. Characterization of the defects may be performed non-destructively by X-ray micro-computed tomography (μCT) [63-65] or destructively using metallography examination [5,66].

Metallography is an accessible and cost effective approach, which is commonly used to study the porosity of castings and compare the casting processes. Metallography examination provides two-dimensional information of defects on polished cross sections. It has been frequently reported that fatigue crack initiating pores are much larger than those obtained from 2D metallographic measurements [7,26]. Fatigue crack initiating pores measured from fracture surfaces can be as much as 10 times larger than the largest pores observed on metallographic surfaces, illustrated in Figure 2.13. One reason for this is that the evaluation of defects based on metallography examination highly depends on the location of the random cross section and secondly, the inadequate representation of porosity in 2D micrographs can be the reason for difference of the metallographic defect evaluation with those on fracture surfaces. A large irregularly shaped shrinkage pore with several arms spreading out in a 3D dimensional form will

most certainly appear as a cluster of smaller pores on a 2D micrograph. This kind of cluster of small pores results from random sectioning in metallographic examination is shown in Figure 2.14.

On the other hand, X-ray micro-computed tomography (μCT) is a powerful imaging technique, which is increasingly used in defect evaluation of castings. In this method, the specimen is exposed to high density X-ray beam from different directions and the internal structure of the specimen is reconstructed through synthesizing the stack of individual projections in different directions. Therefore, the defects can be evaluated in a large material volume in 3D scale without need for specimen preparation. This method has the capability of evaluating the pores in three-dimensional scale, but it is costly and not always accessible [5,63,64,67]. The application of X-CT allows the accurate non-destructive 3-D reconstruction of pores within a volume of aluminum alloy (i.e. distribution, size and morphology). A schematic representation of the process of 3D scan of the specimens using X-CT is shown in Figure 2.15.

As the fatigue cracks are most likely to originate from larger defects relative to smaller ones, determining the maximum defect is advantageous in prediction the lower bond for fatigue life. However, the maximum defect size is unlikely to be observed by metallography examination. Although μCT provides accurate defect size in the scanned section of the specimen, the maximum defect size may differ from one specimen to another. Therefore, in order to estimate the maximum defect size within the desired volume, extreme value statistics can be used.

Using metallography evaluation, Murakami et al. [1] proposed an experimental procedure based on block maxima (BM) approach to estimate the largest defect expected in a volume of material. According to this procedure, a statistically significant number of separate regions (control areas) each of the same area, S_0, within metallography cross sections are analyzed and the largest defect size in each control area is determined, see Figure 2.16. Having obtained the cumulative

probability distribution of the defects, the extreme value (EV) distribution function is fitted to determine the location and scale parameters, μ and σ. The EV distribution function is given by:

$$F(x) = exp\left[-exp\left(-\frac{x-\mu}{\sigma}\right)\right] \tag{2.21}$$

Then, the characteristic largest defect, which is the maximum defect expected to be exceeded once in the desired volume, is the defect size corresponding to the return period, given as:

$$T = \frac{V}{S_0 h} \tag{2.22}$$

in which V is the volume of the specimen or component, S_0 is the control area, and h is the average value of the maximum defects from different inspected areas. It is noteworthy that Equation (2.21) can be rearranged to a linear form, as follows:

$$-\ln\left(-ln\big(F(x)\big)\right) = \frac{x}{\sigma} - \frac{\mu}{\sigma} \tag{2.23}$$

Therefore, when the cumulative probability distribution of defects is plotted as $-\ln\big(-\ln\big(F(x)\big)\big)$ vs the equivalent defect size, the data points should be aligned on a straight line. However, it has been shown that in the case of cast aluminum alloys, the defect data points do not always align on a straight line [42,68-70].

It has been shown that Generalized Extreme Value (GEV) distribution function gives rise to a better fit to pore size distribution in cast aluminum alloys [71]. The GEV distribution function is given by:

$$F(x) = exp\left\{-\left[1 + \xi\left(\frac{x-\mu}{\sigma}\right)\right]^{-\frac{1}{\xi}}\right\} \tag{2.24}$$

where μ, σ and ξ are location, scale and shape parameters, respectively. In fact, EV distribution function is a special case of GEV function when the shape parameter approaches to zero. However, the advantage of using GEV is that the data themselves will determine the most appropriate value for shape parameter.

On the other hand, for estimating the maximum defect size based on defect size data obtained through X-ray μCT, peak-over-threshold (POT) approach can be used. In this approach, all the defects within the scanned volume above a given threshold are considered, therefore, no important information is lost. The Generalized Pareto distribution (GPD) function is then fitted to the cumulative probability distribution of defects, given by:

$$F(x) = 1 - \left(1 + \gamma \frac{x-u}{\sigma}\right)^{-1/\gamma} \tag{2.25}$$

where γ, σ, and u are shape, scale and location parameters, respectively. The maximum defect size is, then, the one attributed to the return period, T, which for the prospective material volume, V, containing a constant defect density, ρ_d, is given by:

$$T = \rho_d V \tag{2.26}$$

2.6. Summary of the Literature Survey

One of the major problems in castings is the presence of defects, which can limit the application of cast components by affecting their mechanical properties, particularly fatigue behavior. Defects introduce high stress concentrations within the specimens and components, which makes them the main sites for crack nucleation.

The influence of defects on fatigue performance depends on defect size. It has been shown that there is a critical defect size, below which fatigue performance is not controlled by defects but by other microstructural features including intermetallic particles or slip bands. Fatigue cracks initiate predominantly from pores larger than the critical size.

It has been reported that in cast aluminum alloys containing porosity subjected to uniaxial loading, fatigue cracks almost always initiate from porosity, while a few works have been published on fatigue performance of cast components under torsion or combined loadings. It has

been suggested that under cyclic torsion, fatigue damage is controlled by two different mechanisms, one mechanism is associated with crack initiation from relatively large shrinkage pores and the other is controlled by much smaller microstructural heterogeneities or the material matrix.

Not only do defects weaken the fatigue performance of defect containing materials, but also they can result in significant scatter in fatigue life. The scatter in fatigue life is associated with the defect size distribution within the specimens or components. At a given stress amplitude level fatigue life has an inverse relation with the size of crack initiating defects.

As defects become larger, fatigue limit also decreases. This issue is well described by Kitagawa-Takahashi diagram, in which the fatigue limit is a function of defects size within the material. Considering the size of defects and hardness of the material, Murakami proposed a semi empirical model to estimate the fatigue limit. Murakami model was later modified by Noguchi et al. [55] and Ueno et al. [56] and it has been reported that the modified models can better predict the fatigue strength of aluminum alloys.

To predict the fatigue life in defect containing materials both long and short crack growth models have been used in the literature. It has been shown that prediction of fatigue life using long crack growth model is not satisfactory. The discrepancy between the estimated fatigue life using long crack growth models and experimental data is thought to be due to the small crack effect of the cracks initiate from defects, which experience lower crack closure levels, higher growth rates, and growing even below the threshold stress intensity factor of long cracks.

Considering the growth rate of small cracks as a function of crack tip opening displacement (CTOD), Nisitini and Goto [61] proposed a small crack growth model, which has been used for several materials including aluminum alloys. This model was later modified by Caton et al. [21]

by considering the global strain. They showed that the modified model can predict the small crack growth rates under fully-reversed loading in W319 aluminum alloy.

The accuracy of life prediction strongly depends on defect characteristics and population within the material. For defect characterization, size, location, shape, and orientation of defects can be considered. It has been suggested that the size of defects is the most important characteristic to be considered in evaluating the fatigue performance. While, defects located at or near the free surface lead to higher stress and strain concentrations due to reduced constraint. It is therefore expected that the combined effect of size and location relative to the free surface will determine the severity of potential crack initiators.

FEA analysis has shown that stress and strain concentrations are significantly affected by the projected area on the transverse plane to the loading direction, rather than local radius of curvature of defects. Therefore, shape and orientation effects may be insignificant if there is no change in the effective size of pores and their local curvature radii.

Closely spaced multiple pores are also expected to increase the local concentration of stresses and strains around the pores or particles. Therefore, it is suggested that crack initiation is easier in cases of multiple pores close to each other because of higher local plastic strains resulting from overlapping the slip bands from individual pores in the cluster.

Characterization of the defects may be performed non-destructively by X-ray micro-computed tomography (μCT) or destructively using metallography examination. Metallography is an accessible and cost effective approach, which provides two-dimensional information of defects. While through μCT scan defects can be evaluated in three-dimensional scale, although it is costly and not always accessible.

As the fatigue cracks are most likely to originate from larger defects relative to smaller ones, determining the maximum defect is advantageous in prediction the lower bond for fatigue life. However, the maximum defect size is unlikely to be observed by metallography examination. Although μCT provides accurate defect size in the scanned section of the specimen, the maximum defect size may differ from one specimen to another. Therefore, in order to estimate the maximum defect size within the desired volume, extreme value statistics can be used.

Using metallography evaluation, Murakami et al. [1] proposed an experimental procedure based on block maxima (BM) approach to estimate the largest defect expected in a volume of material. According to this procedure, a statistically significant number of separate regions (control areas) each of the same area, S_0, within metallography cross sections are analyzed and the largest defect size in each control area is determined. Having obtained the cumulative probability distribution of defects, the extreme value (EV) distribution function is fitted to determine the location and scale parameters, μ and σ. Then, the characteristic largest defect, which is the maximum defect expected to be exceeded once in the desired volume, is the defect size corresponding to the return period, which is a function of the prospective volume and area of the controlled regions.

For estimating the maximum defect size based on defect size data obtained through X-ray μCT, peak-over-threshold (POT) approach can be used, in which all defects within the scanned volume above a given threshold are considered. The Generalized Pareto distribution (GPD) function is then fitted to the cumulative probability distribution of defects. The maximum defect size is, then, the one attributed to the return period, which is a function of the prospective material volume and defect density.

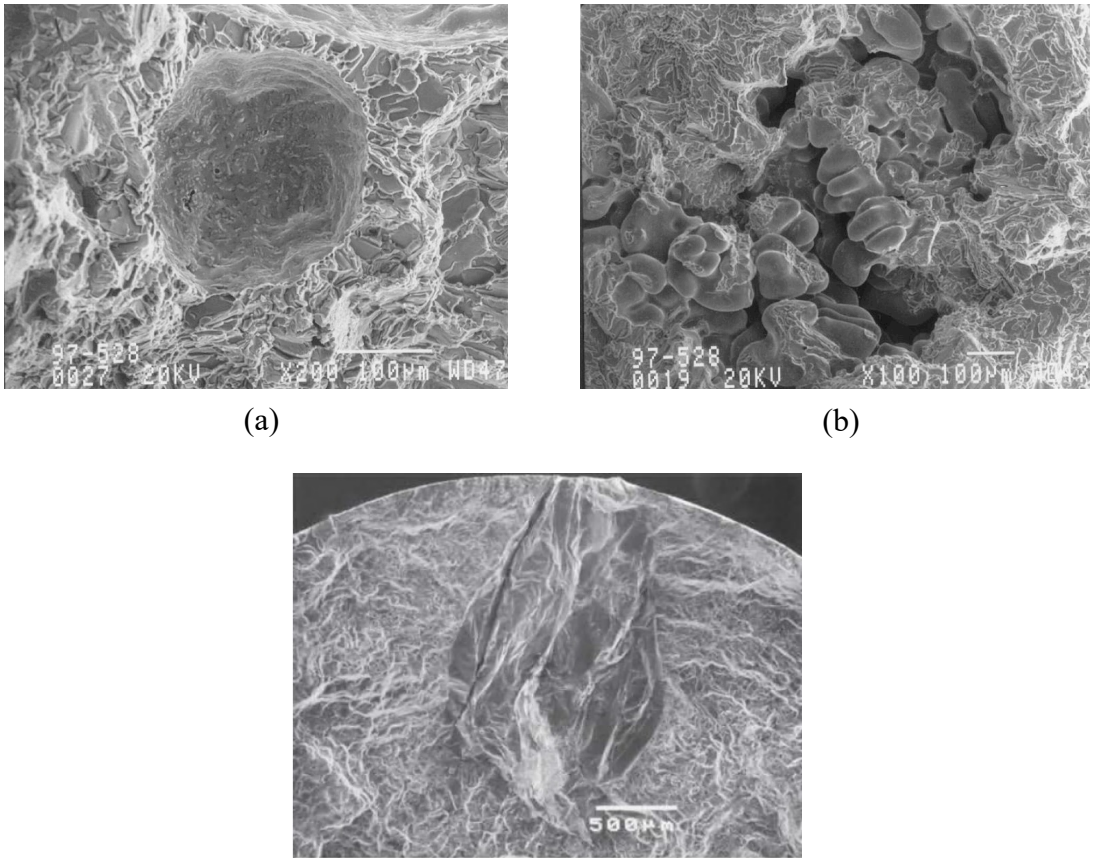

(a) (b)

(c)

Figure 2.1. SEM fractographs of A356 alloy including: a) gas porosity, b) shrinkage porosity, and (c) oxide films as the origin of fatigue crack [4,26].

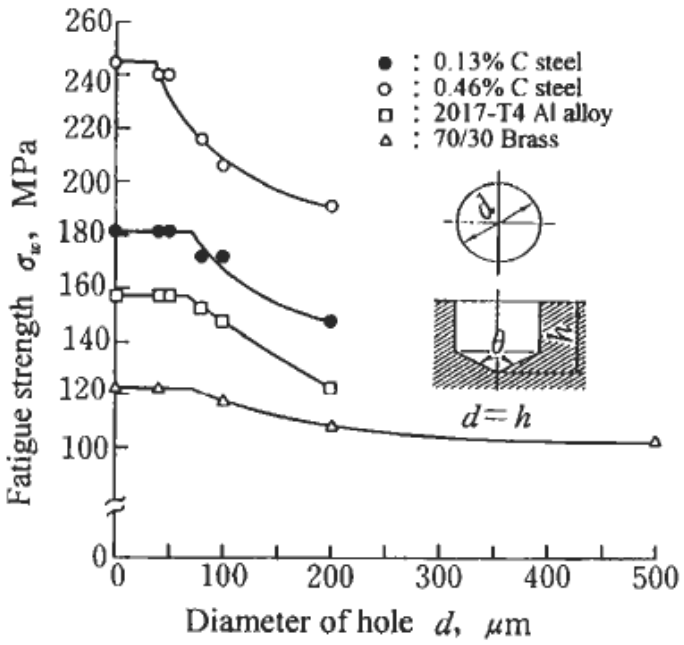

Figure 2.2. The influence of defect size on fatigue strength of different materials [1].

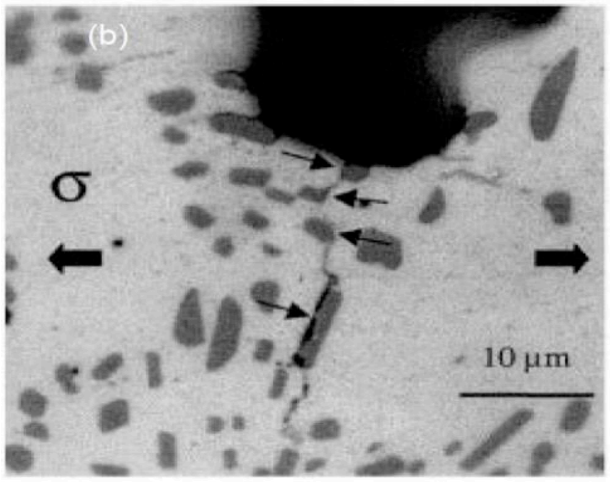

(a)

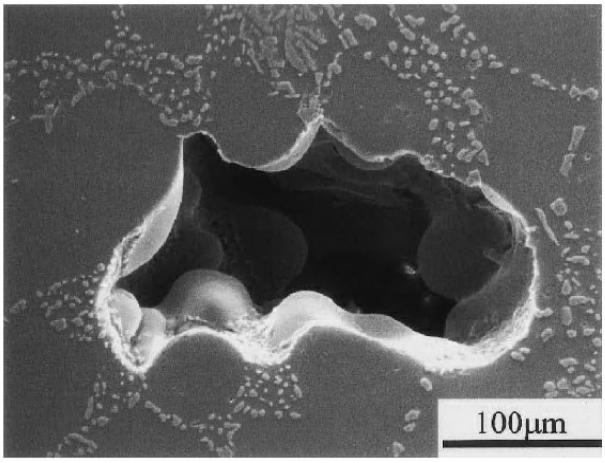

(b)

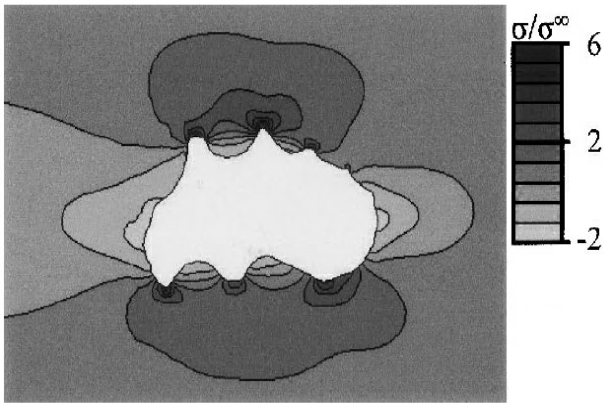

(c)

Figure 2.3. (a) Optical micrograph of the surface of A356 specimen showing the crack initiation from pore at the Si-Al interface [5], (b) SEM micrograph of a typical pore and (c) the normalized stress ratio, σ/σ^{∞} (σ and σ^{∞} are the local and far-field stress, respectively) [32].

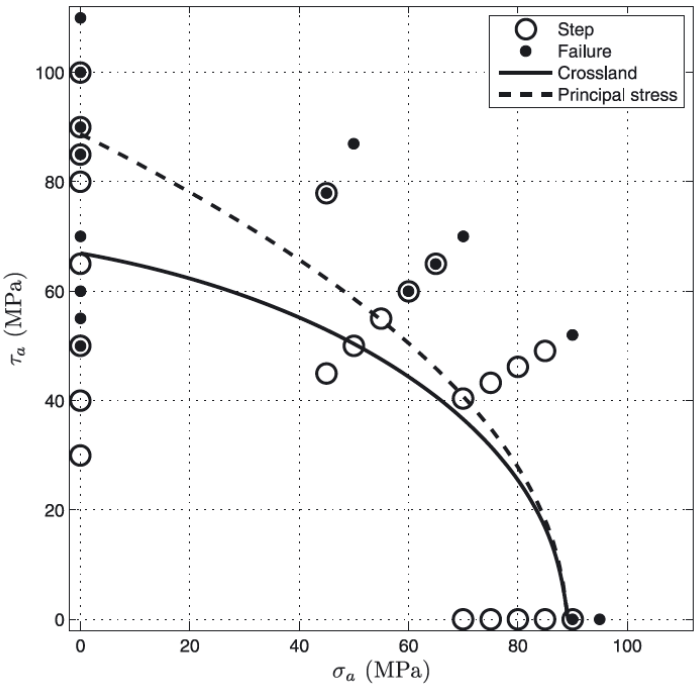

Figure 2.4. Correlation of fatigue limit under combined axial-Torsion loading using maximum principal stress and crossland criteria [36].

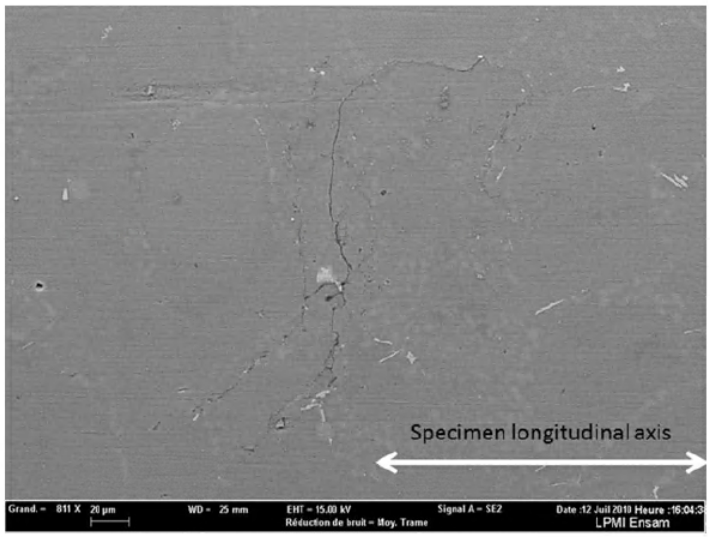

(a)

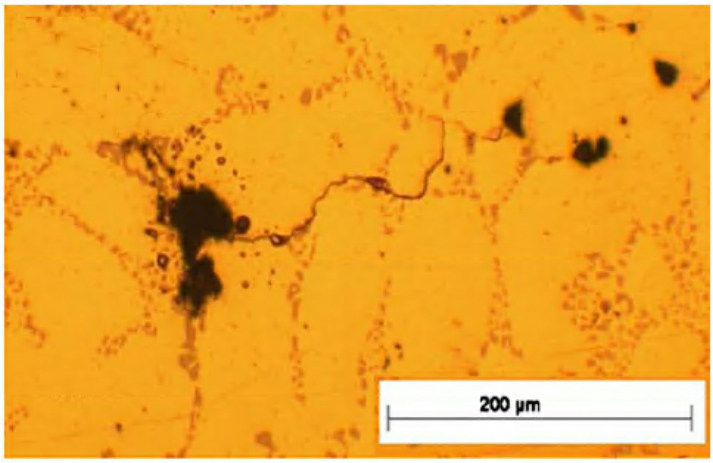

(b)

Figure 2.5. Crack initiation paths under (a) torsion from the eutectic zone, and (b) equibiaxial bending from pores [37].

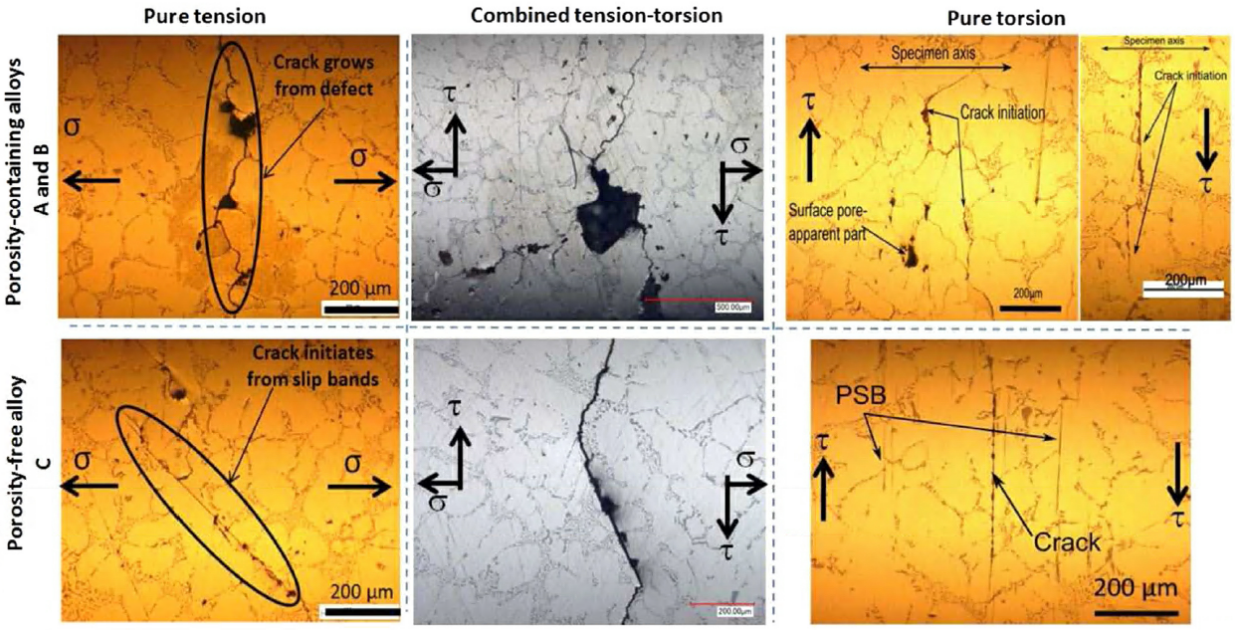

Figure 2.6. Fatigue damage mechanisms of porosity-containing and pore-free alloys for three loading modes (pure tension, combined tension-torsion and pure torsion), observed on the specimen surfaces [40].

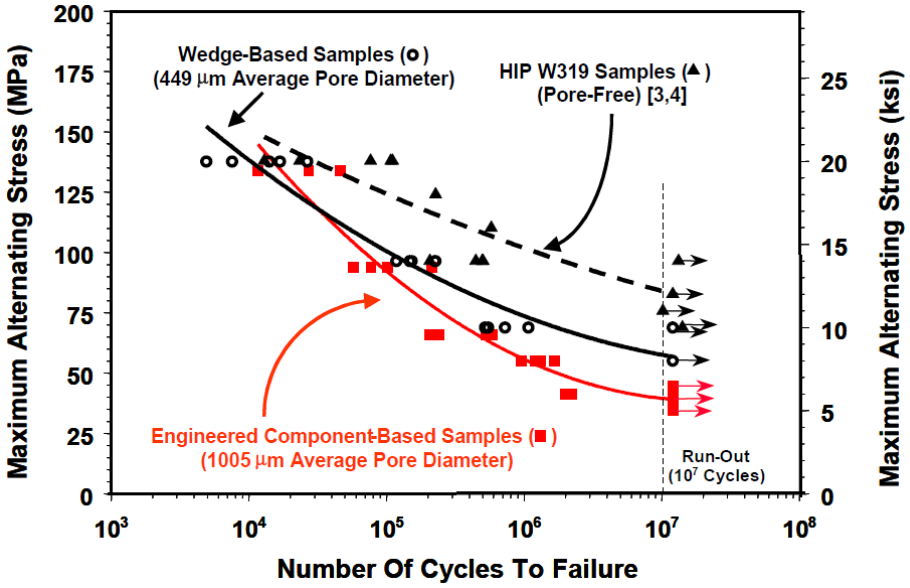

Figure 2.7. The Effect of porosity on fatigue properties of W319-T7 aluminum alloy in both pore-free (HIPed) and non-HIPed Conditions [4].

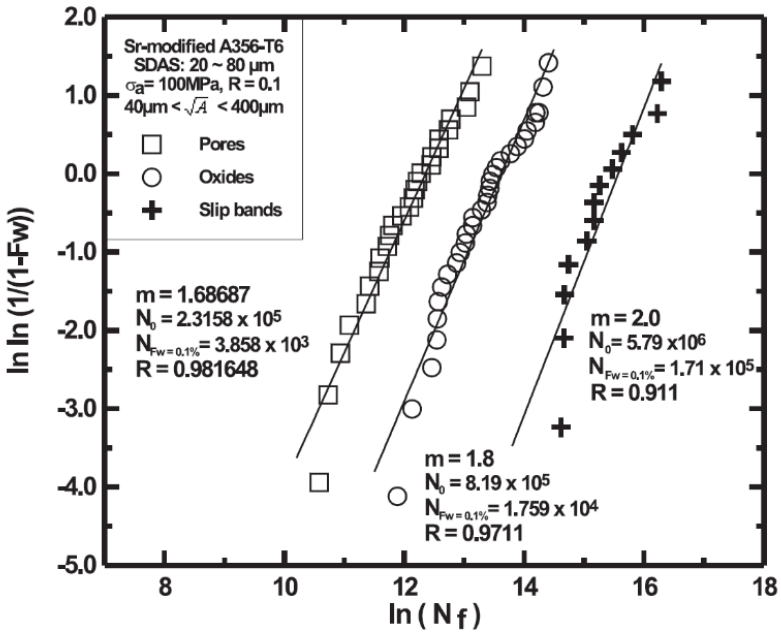

Figure 2.8. Two-parameter Weibull plots for fatigue lives of A356 casting alloy according to the fatigue crack initiation sites [10].

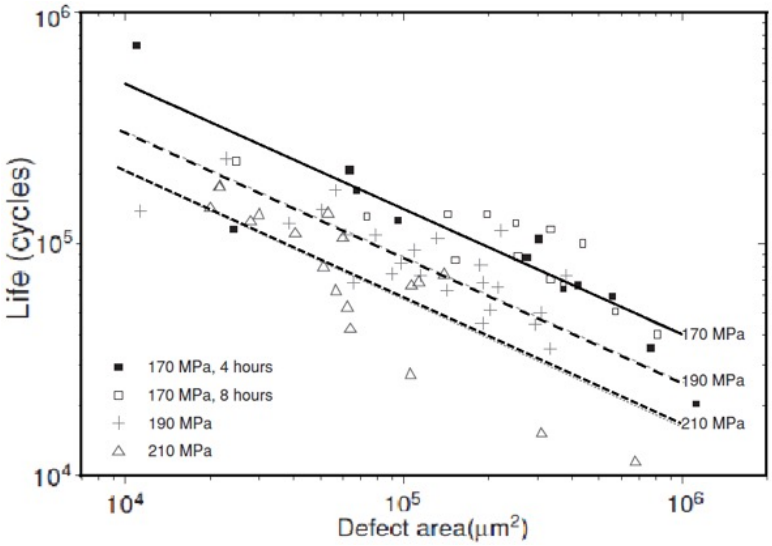

Figure 2.9. Distribution of fatigue life with defect size and stress amplitude in cast aluminum [8].

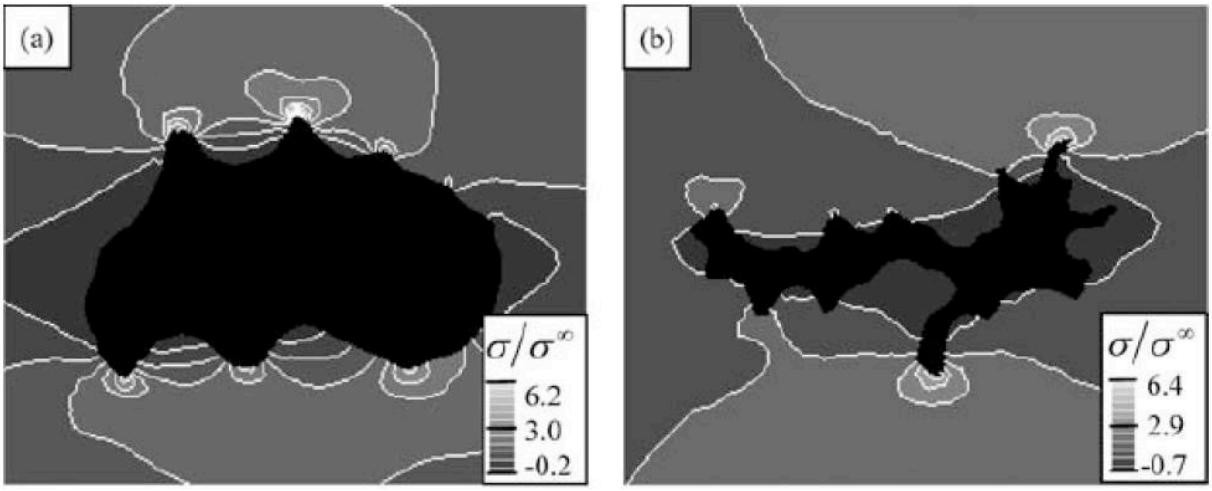

Figure 2.10. 2D FEA results for an A356 alloy showing the distribution of the maximum principal stress normalized with respect to the far field stress acting in a horizontal direction for two pores of different shapes but equivalent projected area [32].

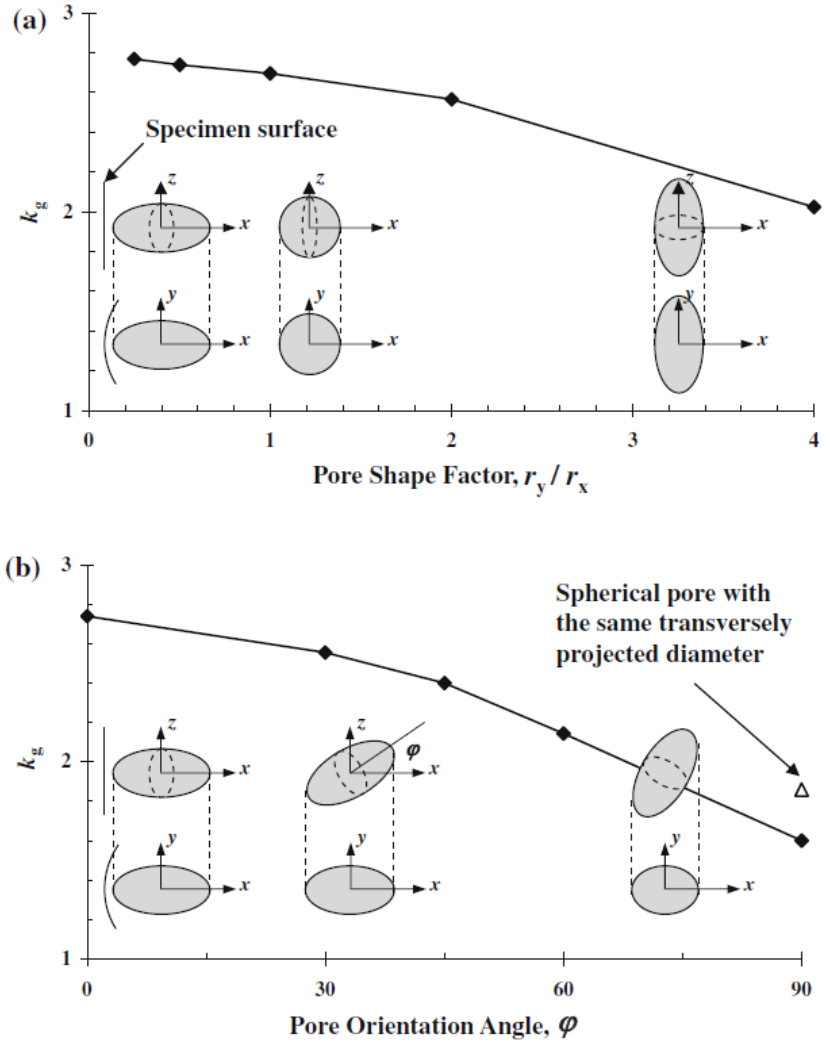

Figure 2.11. Stress–strain concentration factor (kg) as a function of (a) pore shape and (b) orientation [43].

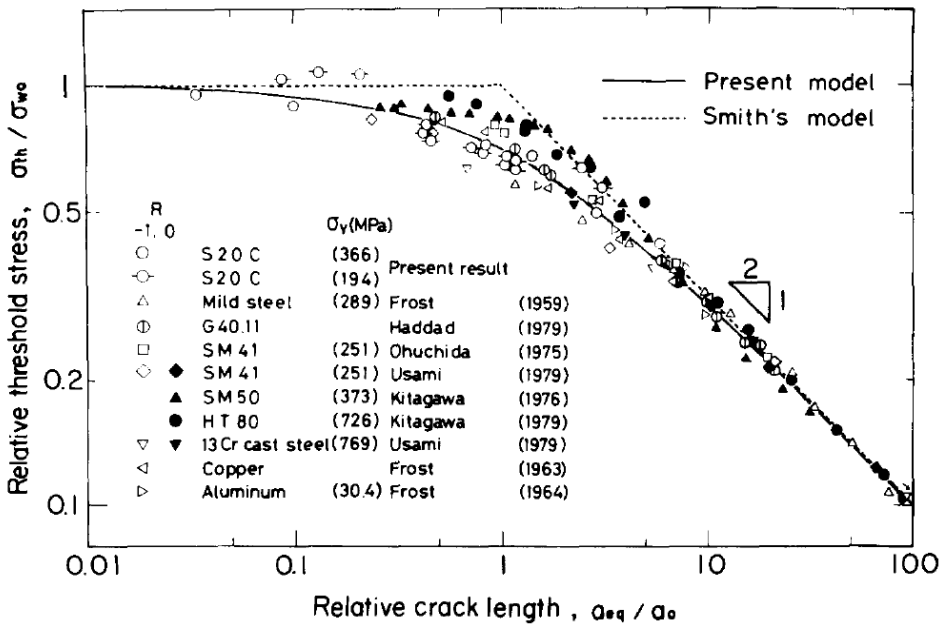

Figure 2.12. Normalized relation between threshold stress and crack length for various materials [72].

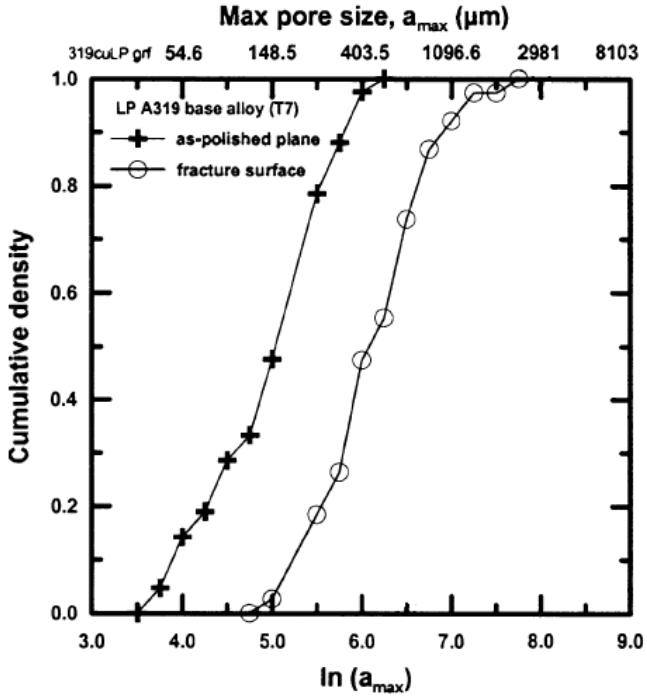

Figure 2.13. Comparison of the distribution of maximum pore sizes observed on as-polished planes and fracture surfaces [26].

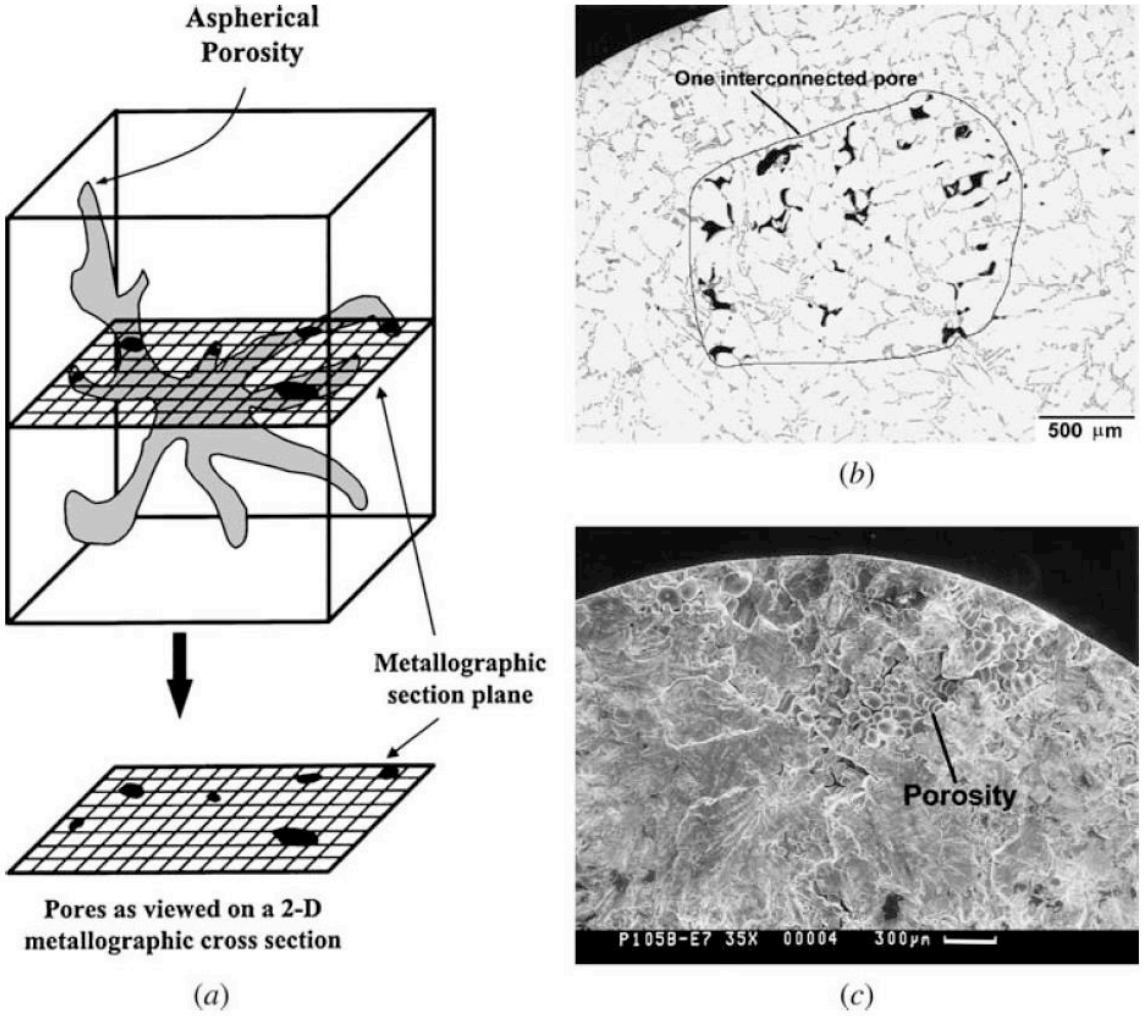

Figure 2.14. (a) Schematic illustration of a tortuous shrinkage porosity, (b) micrographs of the specimen containing shrinkage porosity by metallographically examination, and (c) Scanning Electron microscope of fracture surface containing a shrinkage porosity [26].

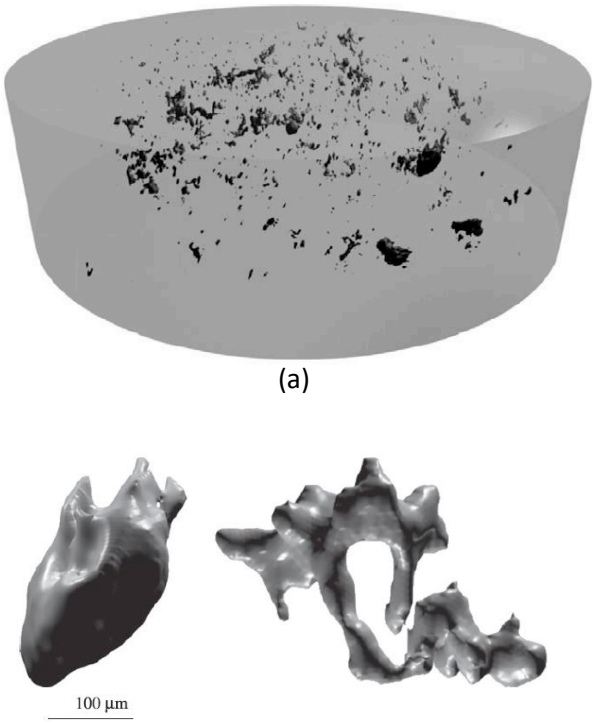

Figure 2.15. (a) 3D pore distribution in a volume of AlSi7Mg obtained by X-ray CT, and 3D representation of (b) a typical gas porosity and (c) and Shrinkage porosity[73].

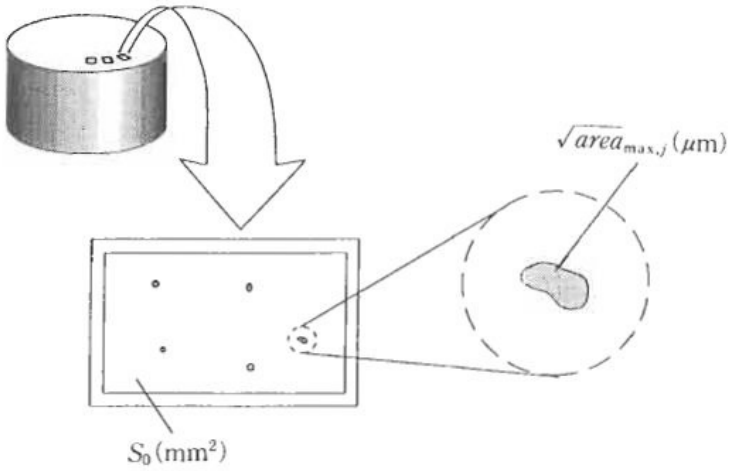

Figure 2.16. Illustration of defect inspection procedure [1].

Chapter 3

Characterization and Analysis of Porosities in High Pressure Die Cast Aluminum by Using Metallography, X-Ray Radiography, and Micro-Computed Tomography

3.1. Introduction

In this chapter defect characterization and analysis of their variability is investigated. Pore distributions in specimens with different sizes and porosity levels are compared, and the variability of defects based on location within the specimens is analyzed. Furthermore, the maximum defect size within the specimens is estimated by extreme value statistics using the evaluated defect data from both metallography and μCT scan. The accuracy of each approach is verified by comparing the estimated maximum defects with the maximum defect size observed on fracture surfaces of fatigue specimens. The estimated maximum defect size within the specimens will be the input to fatigue life prediction models to predict the fatigue life under different loading conditions, which are discussed in Chapters 4-7.

3.2. Materials and Methods

The material studied in this work was A356 aluminum alloy. Two specimen configurations with the nominal gauge section diameters of 5 mm and 10 mm were produced by high pressure die casting (HPDC) method. The geometries of the specimens are illustrated in Figure 3.1. Initial

evaluation of defects was carried out using X-ray radiography, through which the specimens were classified into four porosity levels with regards to the maximum detected defects size. Porosity level 1 contains the smallest porosities, while porosity level 4 has the largest detected porosities. The ranges of the maximum defects in different porosity levels are shown in Table 3.1. Defect evaluation and statistical analysis based on 2D and 3D defect data are compared by conducting metallography and X-ray micro-computed tomography (μCT) scan, respectively. The volume fraction of defects in small and large specimens measured from μCT scan results at different porosity levels is also compared in Table 3.1.

3.2.1. Defect evaluation using metallography examination

Metallography is an accessible and cost-effective approach, which is commonly used to study the porosity of castings and compare the casting processes. However, evaluating the defects using metallography examination highly depends on where the random section is made. Therefore, increasing the number of cross sections will increase the reliability of the measurements and the measured defect population will better reflect the defect population within the specimens or components. For this reason, eight equally-spaced surfaces throughout the gauge length of the specimens were prepared for each specimen size and at each porosity level. Then, each cross section was polished and examined by a VHX-6000 series digital microscope capable of automatically stitching up to 200 pictures taken from the surface in magnification of 500x. Therefore, high resolution micrographs of the whole cross sections were prepared. This procedure was followed for three small specimens at each porosity level and two large specimens at porosity levels 1 and 3. An example micrograph prepared from large specimen porosity level 3 is shown in Figure 3.2(a).

Having examined the polished surfaces using optical microscope, the defects information was extracted from the metallography micrographs using open source image analyzer software, ImageJ. Three different parameters were used to characterize the defects, the square root of actual area of defects, the square root of the ellipse fitted to each defect, and the maximum Feret diameter. These three defect parameters are demonstrated in Figure 3.2(b-d). The comparison of defect distribution using these three defect parameters is discussed in section 3.3.

3.2.2. Defect evaluation using X-ray micro-computed tomography

X-ray micro-computed tomography (μCT) is a powerful imaging technique, which is increasingly used in defect evaluation of castings. In this method, the specimen is exposed to high density X-ray beam from different directions and the internal structure of the specimen is reconstructed through synthesizing the stack of individual projections in different directions. Therefore, the defects can be evaluated in a large material volume in 3D scale without need for specimen preparation.

In this study, two specimens at each porosity level in small and large specimens were chosen randomly for μCT scan and 3D micrographs of the defects within a small part of the specimen gage section (10 mm from the uniform gauge length) were reconstructed. In order to study the repeatability of defects in different specimens, three additional specimens in porosity levels 1 and 3 were examined in small and large specimens, respectively. In order to have high resolution 3D images, the voxel size (volumetric pixel) of $(12\mu m)^3$ was selected, which is far below the critical defect size in this material (between 50 – 100 μm), below which fatigue performance is not controlled by the defects [6,10,22] . Examples of 3D reconstructed image obtained for small and large specimens are illustrated in Figure 3.3(a) and 3.3(b), respectively.

The 3D reconstructed images were analyzed using VG studio Max 3.3 (Volume Graphics GmbH). In analysis of defects, the maximum Feret diameter, volume, and the projected area of the defects on the plane perpendicular to the specimens axis were taken as defect parameters, characterizing the defects size. These defect parameters are shown in Figures 3.3(c) through 3.3(e).

3.3. Defect Characterization

Defects can be formed in castings in variety of complex ways. Gas porosities are normally more or less spherical, while the shrinkage porosities have irregular and branched shape. Therefore, in order to quantify and compare the characteristics of defects, i.e. size and shape, it is required to define a defect parameter.

In evaluating the defects using metallography, Murakami et al. [1] suggested that the square root of the projected area of defects on a plane perpendicular to the loading direction is a promising parameter to characterize the defects for evaluating the effect of both defect size and shape on fatigue strength. Furthermore, using finite element analysis, Gao et al. [32] showed that in a given projected area and local curvature, the maximum stress concentration factor of defects with different complexities are very close to each other. However, maximum Feret diameter, as the diameter of circumscribed circle (or sphere in 3D) on the defects is also widely used in literature for evaluating the effect of defects on fatigue behavior. In addition, the square root of the area of an ellipse fitted to the defects can also be a parameter to characterize the defects on polished surfaces. On the other hand, for evaluating the defects using X-ray μCT scan, three defect parameters can be used including the projected area of the defects on the transverse plane, the maximum Feret diameter, and cubic root of volume of the defects.

The comparison of different defect parameters and their deviation from an ideal circular or spherical defect for both 2D and 3D analysis is shown in Figure 3.4. It can be seen in this figure that the larger the pores, the more deviated they are from an ideal circular or spherical shape. This is due to the fact that larger pores are mostly shrinkage porosities with more complex and branched shape. The relation of size with sphericity (or circularity in 2D) of pores is shown in Figure 3.5. In this figure, sphericity is defined as the ratio of the surface area of a sphere with the same volume to the surface area of the actual defect. The same definition is also used for circularity using perimeter of the defects instead of surface area.

Sphericity (or circularity in 2D) of defects is a measure of irregularity of defect shape which ranges between zero and 1. As the sphericity decreases from 1 to zero, the irregularity of the defect increases from an ideal spherical defect to a highly irregular interconnected one. As can be seen in this figure, it is evident in both 2D and 3D evaluation that large defects are more tortuous with less sphericity (or circularity in 2D) than small ones. This fact is more evident in 3D results in comparison with the metallography data. This is because in 2D evaluation the tortuous defects may appear on metallography cross section as various complex shapes or a collection of small defects, due to sectioning of various dendritic arms during sample preparation.

Figure 3.6 shows how gas or shrinkage porosities may appear on random 2D surfaces, depending on the location of the cross section. As can be seen, the shape of shrinkage porosities on 2D surfaces depends on the location of the random cross section to a great extent. In the case of gas porosities which are more or less smooth, the dependency of defects shape on 2D surfaces is much less, in comparison to the shrinkage porosities. Furthermore, considering the comparison of different defect parameters in 2D scale (Figure 3.4a), it was observed that the average of $Feret_{max}/\sqrt{A_{Actual}}$ as well as $\sqrt{A_{Ellipse}/A_{Actual}}$ ratios for the defects larger than 100 μm are ~2

and ~1.3, respectively. This fact should be taken into account in evaluating and predicting the fatigue life of defect containing materials using different defect parameters.

The effect of volume of the defects on fatigue performance of the materials depends on the orientation of defects with respect to the loading direction. Li et al. [43] showed that the projected geometrical features of defects on the plane perpendicular to the loading direction are more important than the actual length or volume of the defects. Therefore, in evaluating the defects using μCT data in the next sections, only the square root of the projected area of defects is taken into account as the defect parameter.

3.4. Defect Variability

In this section the variability of defect distribution is evaluated statistically including the variability of the defects between different specimens, as well as the variability of defects between porosity levels, along with the variability of defects in height and radial direction within the specimens. This analysis was performed using both metallography and μCT results while square root of the projected area was considered as the defect parameter.

3.4.1. Variability of pore size distribution in specimens of the same size and porosity level

For a given porosity level or specimens size, defect evaluation was conducted between 2 to 5 specimens. The comparison of defect size distributions between the specimens in a given size and porosity level was performed by comparing the cumulative probability distribution vs defect size in different specimens. This comparison for small and large specimens at porosity levels 1 and 3 using the defect size data measured from both metallography and μCT micrographs are illustrated in Figure 3.7. As can be seen, the defect size distributions in different specimens are

very similar to each other in both metallography and μCT evaluations. Similar comparisons were performed for other porosity levels as well and similar results were observed.

To compare the defect size distributions statistically, the Kolmogorov-Smirnov (K-S) test was applied, which is one of the most useful nonparametric methods for comparing two data sets. In K-S test, the maximum value of the absolute difference between the two cumulative probability distributions (D) is calculated and compared to the critical value (D_α), which is a function of sample size of the two data sets and level of significance (α). The null hypothesis that the two data sets come from the same underlying distribution is rejected if D is larger than the critical value, D_α. Having applied this test, it was confirmed that in a given size and porosity level, the defect size distributions in different specimens pertain to one statistical population with significance level of 0.05. This result was expected considering similar casting condition for all specimens. Therefore, the defect data measured on different specimens can be combined for further statistical analysis.

3.4.2. Variability of defects size distribution between pre-defined porosity levels

The defect size distributions in different porosity levels can be compared for both small and large specimens, as shown in Figure 3.8. It can be seen that the defect size distribution plots obtained from μCT data for different porosity levels are very similar, while slight difference can be noticed between the distribution of defects in large specimens using 2D data. However, applying K-S test on defect distributions in small and large specimens revealed that the defect data at four porosity levels belong to one statistical population. This fact can also be confirmed by comparing the distribution of fatal defects observed on fracture surfaces of the failed specimens at different porosity levels under uniaxial fatigue tests, illustrated in Figure 3.9. This figure reveals

that the defect size distribution at different porosity levels are similar and no evident order can be seen in defect distributions. This suggests that using the common method of X-ray radiography often used in industrial application may not be reliable for defect evaluation. In X-ray radiography, the defects are evaluated based on their projections on two dimensional films, wherein the resolution is affected not only by the orientation of defects with respect to the source and the film, but also superposition of other defects.

In Table 3.2, the range of maximum pore sizes within the specimens at different porosity levels measured from metallography and μCT micrographs are compared with the fatal pore sizes observed on fracture surfaces of failed specimens under uniaxial fatigue tests. It should be mentioned that the maximum pore size observed on metallography cross sections is associated to 24 cross sections of small specimens and 16 cross section of large specimens at a given porosity level. In the case of μCT scan, the maximum defects pertain to the measured ones within 2 to 5 specimens at each porosity level. The ranges of maximum defect size observed on fracture surfaces is associated with between 20 to 25 specimens at a given porosity level. As can be seen in Table 3.2, the maximum defects observed on fracture surfaces are larger than those measured from metallography sections or μCT micrographs. Further, no significant difference can be seen between the maximum fatal pore on fracture surface of the specimens at different porosity levels.

The comparison between defect density as well as the volume (or area) fraction of defects at different porosity levels are shown in Figures 3.10(a) and 3.10(b). Considering these figures, no significant difference can be seen neither in defect density nor volume (or area) fraction of the defects within the specimens at different porosity levels. However, the volume (or area) fraction of defects as well as defect density of large specimens are significantly higher than those in small

specimens. This suggests that as the casting section size increases, both the defect size and the population of defects are increased.

The comparison of volume and area fraction of defects measured from μCT and metallography micrographs at different porosity levels is illustrated in Figure 3.10(c). As can be perceived in this figure, the area fraction of defects measured from metallography sections are smaller than volume fraction of defects measured from μCT micrographs which is due to smaller size of defects on 2D micrographs in comparison to 3D defect size in μCT micrographs. This issue can also be seen in Table 3.2 by comparing the maximum defect range from metallography and μCT evaluations.

3.4.3. Variability of defects between two specimen sizes

The comparison between defect distribution in small and large specimens using both metallography and μCT data is illustrated in Figure 3.11. As can be seen, the probability of having large defects in large specimens is significantly higher than that in small specimens based on both metallography and μCT data. This is in agreement with the observed fatal defects measured on fracture surfaces, shown in Figure 3.9. On the other hand, it can be clearly seen in Figure 3.11 that the defects observed on metallography cross sections are smaller than those measured from μCT micrographs, which is due to the dependency of defect analysis on location of metallographic cross sections in 2D evaluation of defects.

3.4.4. Variability of defect size in specimen height and radial directions

In order to study the variability of defects along the height of the specimens, the distribution of defect size within the gauge length of the specimens using the defect data obtained through μCT

is plotted vs height in Figure 3.12. As can be clearly seen, the defects are distributed randomly throughout the gauge length and there is no evident order in distribution of defects along the height of the specimens throughout the gauge length. Similar results were obtained using defect data from metallography examinations.

To study the variability of defect distribution in the radial direction, each micrograph in both metallography and μCT evaluation was divided into 4 and 8 subsections (coaxial rings) with equal volumes or areas in small and large specimens, respectively. Then, the radial distribution of the defects was studied by comparing the cumulative probability distribution of defects for different rings using 2D and 3D data as shown in Figures 3.13 and 3.14 for small and large specimens, respectively. As can be seen in Figure 3.13, the central ring in small specimens are likely to have larger defects in comparison to the outer ring. However, the number of large pores at the inner rings is not significant to make evident difference in the cumulative probability distribution of defects at different rings. Applying K-S test on these defect distributions also revealed that in small specimens the defect distribution at different rings are similar and the defects in all four rings can be considered as one statistical population. Therefore, it can be concluded that the defects in small specimens has been distributed randomly throughout the specimens.

In the case of large specimens, however, there is an order in defect distributions at different rings, where the outer ring (Ring 1) contains the smallest defects and the most inner ring (Ring 8) has the largest defects. The dissimilarity of the defect distribution at different rings can be confirmed by applying K-S test, using both 2D and 3D defect data (Tables 3.3 and 3.4). Using the K-S test results based on metallography data, it can be concluded that defects within Rings 1-5 belong to one statistical population, while the defect within Rings 6-8 can be considered as another

population. This classification is a little different when μCT data is used, where the outer region includes Rings 1-3 and the inner region contains Rings 4-8.

This difference between metallography and μCT data is associated with different appearance of the defects on metallography sections in comparison to the real defect size which can be measured from 3D micrographs. The difference between defect population in outer region of the large specimens from the inner part can be associated to different solidification rates in different regions of the specimens. The solidification rate in outer region of the specimens is higher which leads to less chance to have shrinkage porosity, while the cooling rate in inner region of the specimen is lower and the probability of having large shrinkage porosity is high. However, the lower thermal gradient from surface to center of small specimens results in a relatively uniform defect distribution in the entire cross section. Having combined the defect size data in similar rings in large specimens, the defect distribution of outer region and inner region can be obtained. Therefore, the defect data in Rings 1-3 and Ring 4-8 have been combined.

The distributions of the fatigue crack initiating defects measured on the fracture surface of the small and large specimens are demonstrated in Figure 3.15. Considering this figure, it can be inferred that the fatigue crack may originate from both outer and inner regions of the specimens. It is believed that the large defects at or near the specimen surface are more detrimental in fatigue. For defects of the same size, the stress concentration around a defect at the surface is higher than that of an internal one, while at a given distance from the surface, the stress concentration around large defects are higher than that of small defects [32]. Therefore, there is competition between the defects in terms of size and location.

3.5. Application of Extreme Value Statistics to Estimate the Maximum Defects

As the fatigue cracks are most likely to originate from larger defects relative to smaller ones, the fatigue properties of defect containing materials will be governed by the defects on the upper tail of the defect probability distribution. Therefore, in order to evaluate and predict the fatigue life of the specimens it will be advantageous to know the maximum defect size which may exist within the specimen or component. The maximum defect size is unlikely to be observed by metallography examination through random cross sections. On the other hand, using μCT scan on a specimen is costly but will provide accurate defect size in the scanned region of the specimen. However, even in a given cumulative probability distribution the maximum defect may differ from one specimen to another. Therefore, in order to estimate the maximum defect size within the desired volume, extreme value statistics (EVS) can be used which has shown to be very useful in predicting the maximum defect size based on metallography and μCT data. The estimated maximum defect can, then, be an input to fatigue life prediction models to estimate the fatigue life under the desired loading condition in fatigue design.

Regarding applying extreme value statistics on metallography data, block maxima (BM) is the most common approach in which several subsections with the same area, S_0, are inspected, and only the maximum defect within each inspected area is recorded. On the other hand, for estimating the maximum defect size using μCT data peak-over-threshold (POT) approach is often used which consists of considering all the defects within the scanned volume above a given threshold, u, therefore no important information is lost. In this study, the BM and POT approaches are followed to estimate the maximum defect within the specimens using metallography and μCT data, respectively. The accuracy of each method is, then, verified by comparing the estimated maximum defect with the maximum fatal defects observed on fracture surfaces.

3.5.1. Block maxima (BM) approach

To use BM approach to estimate the maximum defect size within the specimens several standard control areas are inspected on metallography micrographs and the maximum defects in each control area is determined. The controlled areas used for small and large specimens were 2.37 and 4.91 mm^2, respectively. In each control area, the maximum defect was determined and the maxima data points were plotted as cumulative probability distribution. Extreme value distribution functions were, then, fitted into the maxima data point. It should be mentioned that in predicting the maximum defect size within the specimens in addition to extreme value (Gumbel) distribution function, EV, which is very common to be used in estimating maximum defect size, Generalized Extreme Value (GEV) distribution function was also used. Therefore, both EV or GEV distribution functions are fitted to the defect size cumulative probability distributions using maximum likelihood (ML) method and the corresponding parameters including location, scale, and shape parameters were determined (see Equations 2.21 and 2.24).

The maximum defect size within the specimens is, then, the size of a defect associated with the return period, *T*, defined by Equation (2.22). Therefore, the maximum defect size within the specimens, associated to probability of $P = 1 - 1/T$, was estimated using Equations (3.1) and (3.2) based on EV and GEV distributions, respectively:

$$x_{EV} = \mu + \sigma\left[-\ln\left(-ln\left(1-\frac{1}{T}\right)\right)\right] \tag{3.1}$$

$$x_{GEV} = \mu - \frac{\sigma}{\xi}\left[1-\left(-ln\left(1-\frac{1}{T}\right)\right)^{-\xi}\right] \tag{3.2}$$

For estimating the maximum defect size using EV function, the data points are usually plotted as $-\ln\left(-ln(P)\right)$ vs defect size, which is expected to be linear according to Equation (2.23). However, it was observed that when the defect data are plotted based on EV distribution function

all the data points are not aligned on a straight line (see Figure 3.16). So, it can be inferred that EV distribution is not representative of the entire pore distribution. This nonlinearity of the data points can be attributed to presence of two kinds of porosity, i.e. small and large [89]. Therefore, a threshold for defect size was defined from EV distribution plots where the inflection occurs, which is in the range of 40-80 μm. Then, the defects with sizes above this threshold were considered in the evaluation. This approach was also followed in [69,68]. However, there are two challenges in this approach. Firstly, elimination of the defect with the sizes below the threshold may leave only few data points and prediction of the maximum defect size based on extrapolating the line fitted to few data points may not be reliable [70,90]. In addition, assuming a linear relation and extrapolating may cause a significant error in estimation of the maximum defect size.

The maximum defect size can also be estimated using the generalized extreme value by fitting the GEV function to the cumulative probability distribution of the defects, shown in Figure 3.17. In this way, the GEV parameters can be determined using maximum likelihood method and the maximum defect size is computed by Equation (3.2). The advantage of this method is that all data points can be considered in prediction, as opposed to the EV distribution function in which the line was fitted only to the defects larger than a threshold.

The maximum defect size predicted by EV and GEV functions is compared with the maximum size of fatal defects observed on fracture surfaces of 80 small specimens and 40 large specimens in Table 3.5. As can be seen in this table, the prediction of maximum defect within the specimens using GEV distribution function is in very good agreement with the maximum observed defects on fracture surfaces. The estimate of EV distribution function is lower than that of GEV function, which is due to the assumption of linear relation of the data and extrapolation. This can

also be attributed to a limited number of data points larger than the threshold, especially in the case of outer ring of large specimens, as shown in Figure 3.16(b).

It should be noted that in small specimens in which the defects are distributed randomly, the maximum defect in the entire cross section was computed. However, in large specimens where the defect distributions in outer and inner rings are different the maximum defects in each ring was calculated. For computing the maximum defect in the entire cross section of large specimens the concept of weakest link theory can be applied.

According to the weakest link theory, in a system consisting of i elements each with probability of survival P_i, the probability of survival of the whole system will be the product of survival probability of all the elements:

$$P = \prod_1^n P_i = P_1 . P_2 \dots P_n \tag{3.3}$$

In specimens or components containing defects, the probability of having defects smaller than a critical size corresponds to the cumulative probability distribution of defects:

$$P_X(x) = P(X \leq x) \tag{3.4}$$

where the critical defect size, x, can be defined as the size of a defect that the materials will not fail at a given cyclic stress level. Therefore, the cumulative probability distribution of defects can be considered as survival probability. As the defect distributions in different regions of large specimen are different and do not belong to the same statistical population, the probability distribution of the whole specimen can be obtained using the weakest link theory (Equation 3.3).

In nearly all the published works on evaluating defects in cast Al alloys it has been assumed that the defects are distributed randomly throughout the cross section. This assumption can be true when the size of the specimens is small, while in large specimens or components in which the solidification rates in different regions are different defects are distributed nonuniformly.

Therefore, the assumption of having uniform distribution may not be true and predicting the maximum defect based on this assumption may result in erroneous results. As a result, in order to study how the assumption of uniform defect distribution affects the estimate of the maximum defect size, the extreme value statistics was also applied to the whole cross section as one statistical population.

The estimated maximum defect when the whole cross section is considered as one statistical distribution and the one obtained by utilizing the weakest link theory for large specimens are reported in Table 3.5. As can be seen in this table, the assumption of uniform defect distribution results in overestimated prediction for maximum defect size using GEV approach, while prediction based on weakest link theory is in very good agreement with the maximum defects observed on fracture surfaces.

3.5.2.Peak-over-threshold approach

For estimating the maximum defect size using μCT data, peak-over-threshold (POT) approach is often used. In this approach all the defects within the scanned volume above a given threshold, u, are considered. The Generalized Pareto distribution (GPD) function is then fitted to the cumulative probability distribution of defects using maximum likelihood (ML) method to determine the shape, γ, and scale, σ, parameters (Equation 2.25).

The threshold value for defect size can be determined using mean excess plot, selecting the point over which the mean excess of the large data becomes linear. Using the μCT data, mean excess plots for small and large specimens was plotted, through which the threshold defect size of 40 μm and 100 μm was chosen for small and large specimens, respectively. As an example, mean excess plot for large specimens in inner ring is demonstrated in Figure 3.18.

Having determined the threshold defect size, the shape and scale parameter in GPD distribution function for small and large specimens, the maximum defect size within the specimens was computed using:

$$x_{GPD} = u - \frac{\sigma}{\gamma}(1 - T^{\gamma}) \tag{4.5}$$

where the return period, *T*, was calculated using Equation (2.26). The estimated maximum defects within small and large specimens are summarized and compared with the estimates of BM approach in Table 3.5. As can be seen, the prediction of maximum defects based on μCT data are in very good agreement with the maximum defects observed on fracture surfaces. Comparing the predictions of maximum defect based on metallography and μCT scan reveals that the predictions based on metallography data are underestimated relative to those of μCT data, while the discrepancy between the predictions is not significant. Lower estimation of maximum defect size based on metallography data is associated with the dependency of metallography on the location of the cross sections. This effect can be reduced by increasing the number of metallography sections, as was performed in this study.

3.6. Summary and Conclusions

As the mechanical properties of cast components can be significantly affected by existing defects, evaluation of defects within specimens or components is of great importance in design. This chapter investigated the defects characteristics in A356 aluminum specimens of two sizes, as an illustrative material containing defects. Initial evaluation of defects was carried out using X-ray radiography, through which the specimens were classified into four porosity levels with regards to the maximum detected defects size. The defects were then characterized using metallography as well as micro-computed tomography techniques. The variability of defects between the specimens

of two sizes as well as different porosity levels were studied statistically. The distributions of defects based on location within the specimens were also analyzed. Moreover, the maximum defect size within the specimens was estimated using extreme value statistics based on both 2D and 3D defects data. The following conclusions are drawn from these analyses:

1. Cumulative probability distributions of defects based on 2D and 3D evaluations as well as the measured defects size from the fracture surfaces of the specimens at different pre-defined porosity levels suggest that the common method of X-ray radiography often used in industrial application may not be reliable for defect evaluation.
2. Examining different defect characteristics in metallography examinations as well as μCT scan evaluations revealed that as the size of pores increases, they deviate more from ideal spherical (or circular in 2D) defect, indicating reduced sphericity (or circularity in 2D) of pores with increasing defect size.
3. Studying the variability of defects in radial distribution revealed that the pore distribution in the specimens produced by high pressure die cast may not be random throughout the cross section, especially in large section sizes. In addition, as the casting section size increases, both the defects size and density also increase.
4. Evaluating defects using μCT scan is very accurate but not always accessible, contrary to metallography approach which is accessible and cost effective while defects evaluation through metallography depends on the location of random cross section and the pores measured on metallography micrographs are smaller than those measured through μCT scan. However, increasing the number of metallography cross sections improves the accuracy of 2D measurements.

5. Applying Extreme value statistics to metallography data using GEV distribution function could estimate the maximum defects in reasonable agreement with the maximum observed defects on fracture surfaces. The estimate of maximum defect using POT approach to the μCT data was also in very good agreement with the maximum observed defect.
6. Although EV distribution function is commonly used for estimating the maximum defect size using metallography data, the estimated maximum defect using this approach was underestimated in comparison to the maximum observed defect on fracture surfaces.
7. To estimate the maximum defect size of the entire large specimen where the defects are not distributed randomly the weakest link theory was applied and the prediction of the weakest link theory was in better agreement with the maximum defect size on fracture surfaces, in comparison with the prediction using the assumption of random distribution throughout the cross section.

Table 3.1. Classification of specimens base on the maximum defects detected in X-ray radiography as well as the volume fraction of the defects in small and large specimens measured from μCT scan results.

Porosity Level	Max defect size (μm)	Volume fraction of defects (%)	
		Small Specimens	Large Specimens
1	0-62	0.013	0.251
2	63-124	0.010	0.193
3	125-184	0.021	0.317
4	185-250	0.018	0.215

Table 3.2. Comparison of observed maximum defect size in different porosity levels (the measurements are in μm).

	Small Specimens				Large Specimens	
	Porosity level 1	Porosity level 2	Porosity level 3	Porosity level 4	Porosity level 1	Porosity level 3
Metallography	51-173	59-104	88-207	112-208	153-234	589-866
μCT	175-288	155-167	243-283	391-522	461-520	662-1333
Fracture surface	84-463	67-337	93-578	47-571	252-1274	408-1141

Table 3.3. K-S test results for comparing defect distribution in large specimens at different "Rings" using metallography data.

	Ring 1	Ring 2	Ring 3	Ring 4	Ring 5	Ring 6	Ring 7	Ring 8
Ring 1	-	✔	✔	✔	✔	✘	✘	✘
Ring 2	✔	-	✔	✔	✔	✔	✘	✘
Ring 3	✔	✔	-	✔	✔	✔	✔	✘
Ring 4	✔	✔	✔	-	✔	✔	✔	✘
Ring 5	✔	✔	✔	✔	-	✔	✔	✔
Ring 6	✘	✔	✔	✔	✔	-	✔	✔
Ring 7	✘	✘	✔	✔	✔	✔	-	✔
Ring 8	✘	✘	✘	✘	✔	✔	✔	-

Table 3.4. K-S test results for comparing defect distribution in large specimens at different "Rings" using CT scan data.

	Ring 1	Ring 2	Ring 3	Ring 4	Ring 5	Ring 6	Ring 7	Ring 8
Ring 1	-	✔	✔	✘	✘	✘	✘	✘
Ring 2	✔	-	✔	✔	✔	✔	✘	✘
Ring 3	✔	✔	-	✔	✔	✔	✔	✔
Ring 4	✘	✔	✔	-	✔	✔	✔	✔
Ring 5	✘	✔	✔	✔	-	✔	✔	✔
Ring 6	✘	✔	✔	✔	✔	-	✔	✔
Ring 7	✘	✘	✔	✔	✔	✔	-	✔
Ring 8	✘	✘	✔	✔	✔	✔	✔	-

Table 3.5. Comparison of the maximum defect estimated by BM approach using metallography (2D) data as well as those estimated by POT approach using μCT (3D) data with the maximum fata defects observed on fracture surfaces (the unit of the estimates is in μm).

	Small specimens	Large Specimens			
		Outer Ring	Inner Ring	Whole Surface	Weakest Link
GEV (2D)	517	941	1232	1571	1362
EV (2D)	358	561	1022	1061	1113
GPD (3D)	602	1035	1303	1383	1426
Observed	578	963	1274	1274	1274

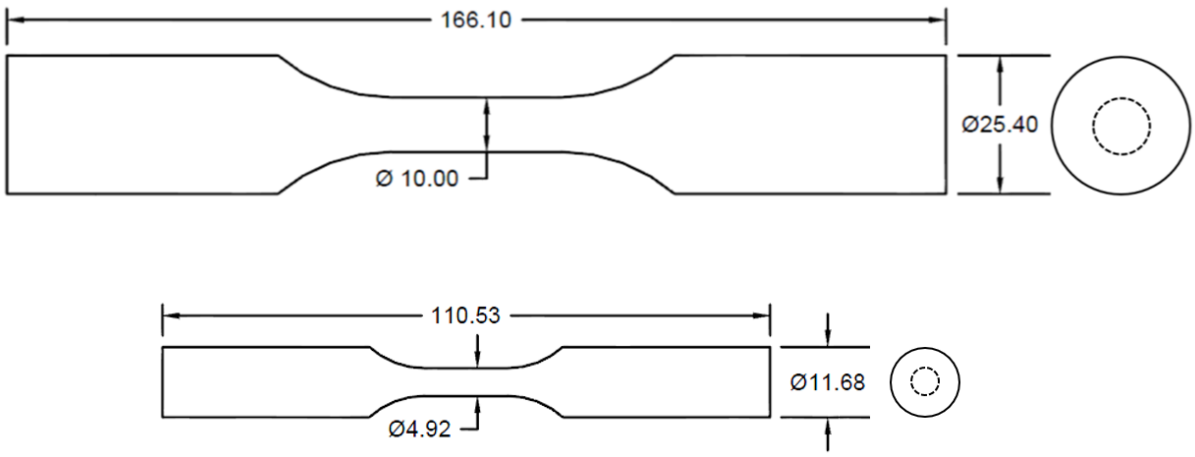

Figure 3.1 – Schematic illustration of the small and large specimens.

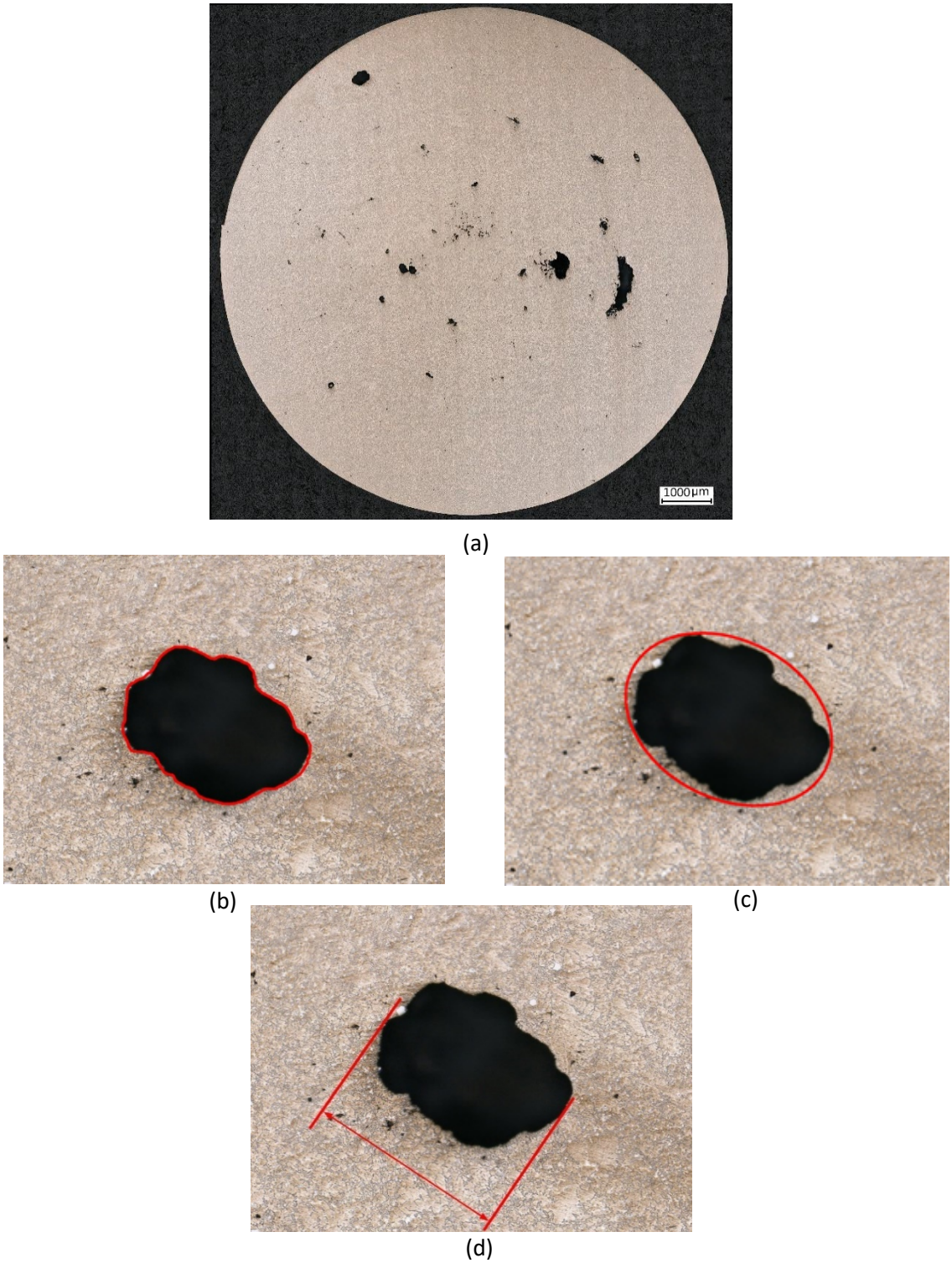

Figure 3.2. (a) An example of optical micrograph in a large specimen porosity level 3, Three different defect parameters to determine the size of the defects, (b) actual Area of the defect ($\sqrt{A_{actual}}$), (c) the Area of fitted ellipse ($\sqrt{A_{Ellipse}}$), (d) max ferret diameter ($Feret_{max}$).

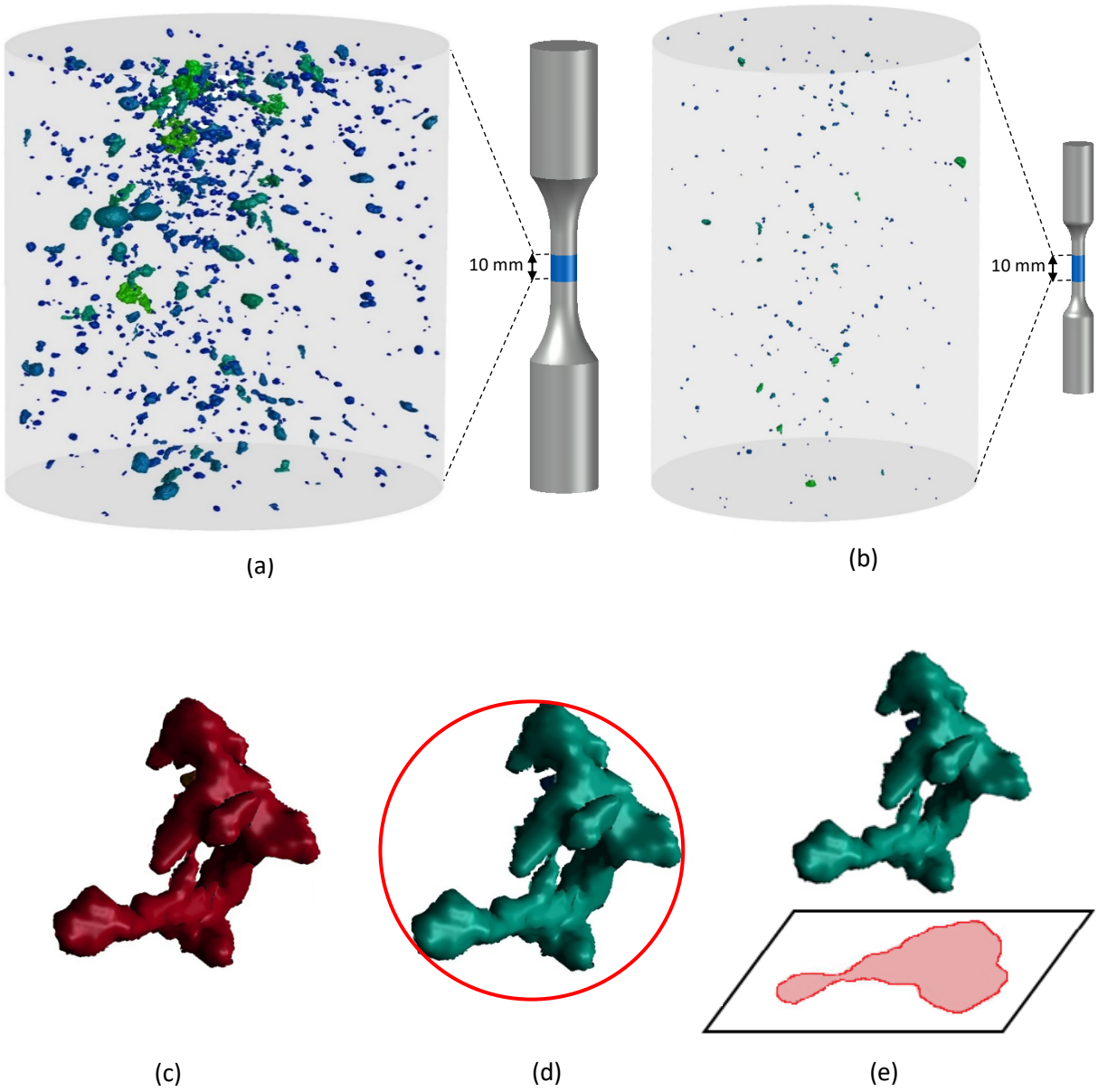

Figure 3.3. Examples of 3D images of defects in (a) Small Specimens, (b) large specimens, Three different defect parameters characterizing the defects size, (c) volume of the defect ($\sqrt[3]{Volume}$), (d) max Feret diameter ($Feret_{max}$), and (e) area of the projected area on the plane perpendicular to the specimen axis ($\sqrt{A_{projected}}$).

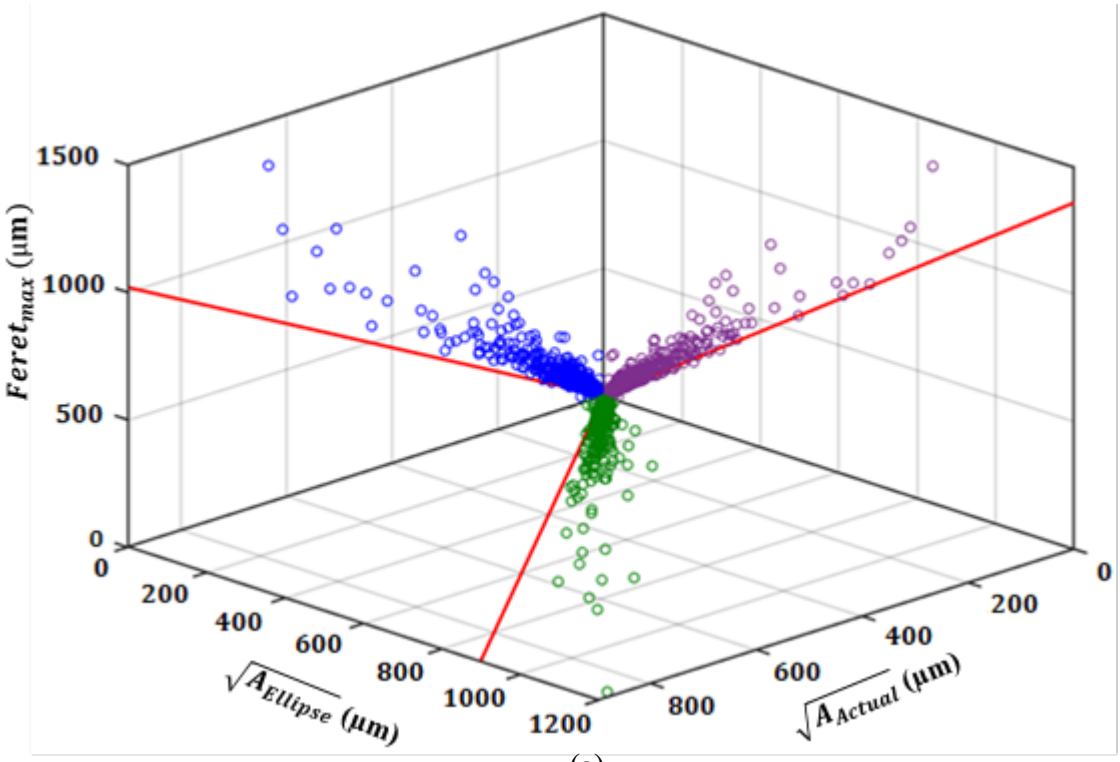

(a)

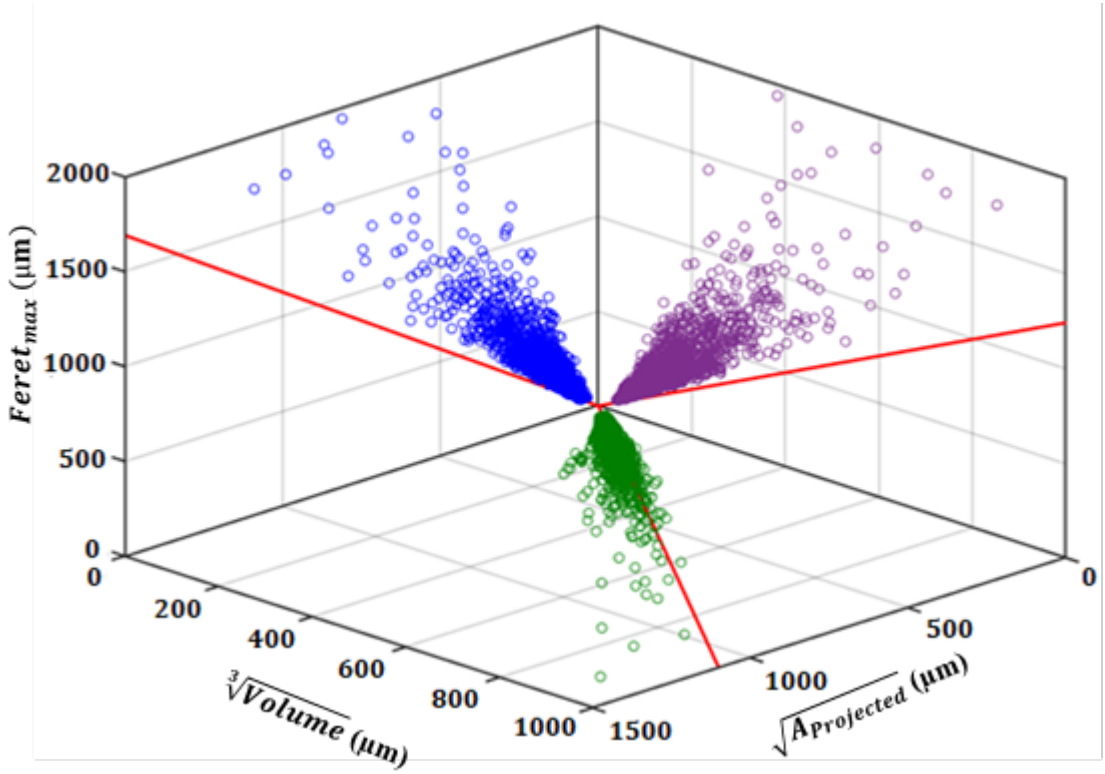

(b)

Figure 3.4. Comparison of different defect parameters; (a) metallography; (b) µCT scan evaluation, the solid diagonal lines pertain to the ideal spherical (circular) defect.

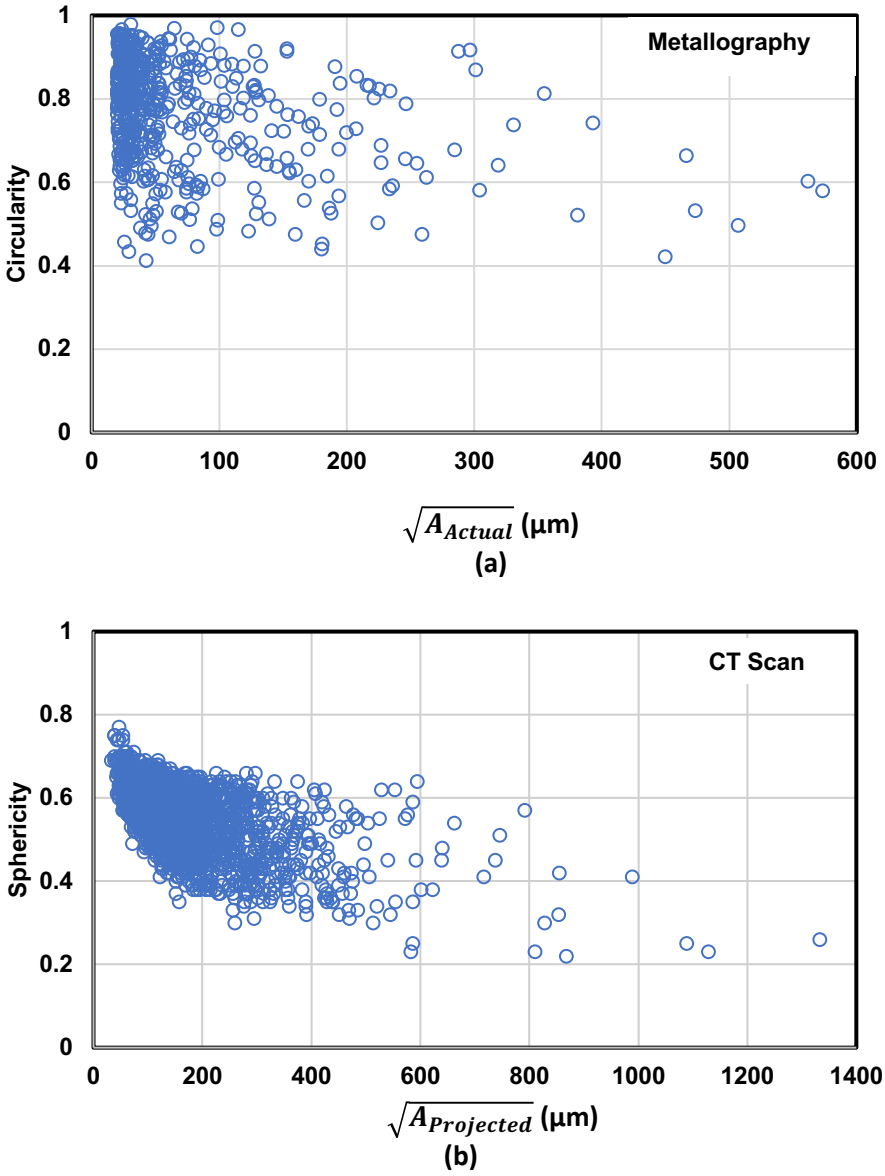

Figure 3.5. Comparison of the relation of defect size with sphericity or circularity of defect in (a) metallography, and (b) µCT evaluations.

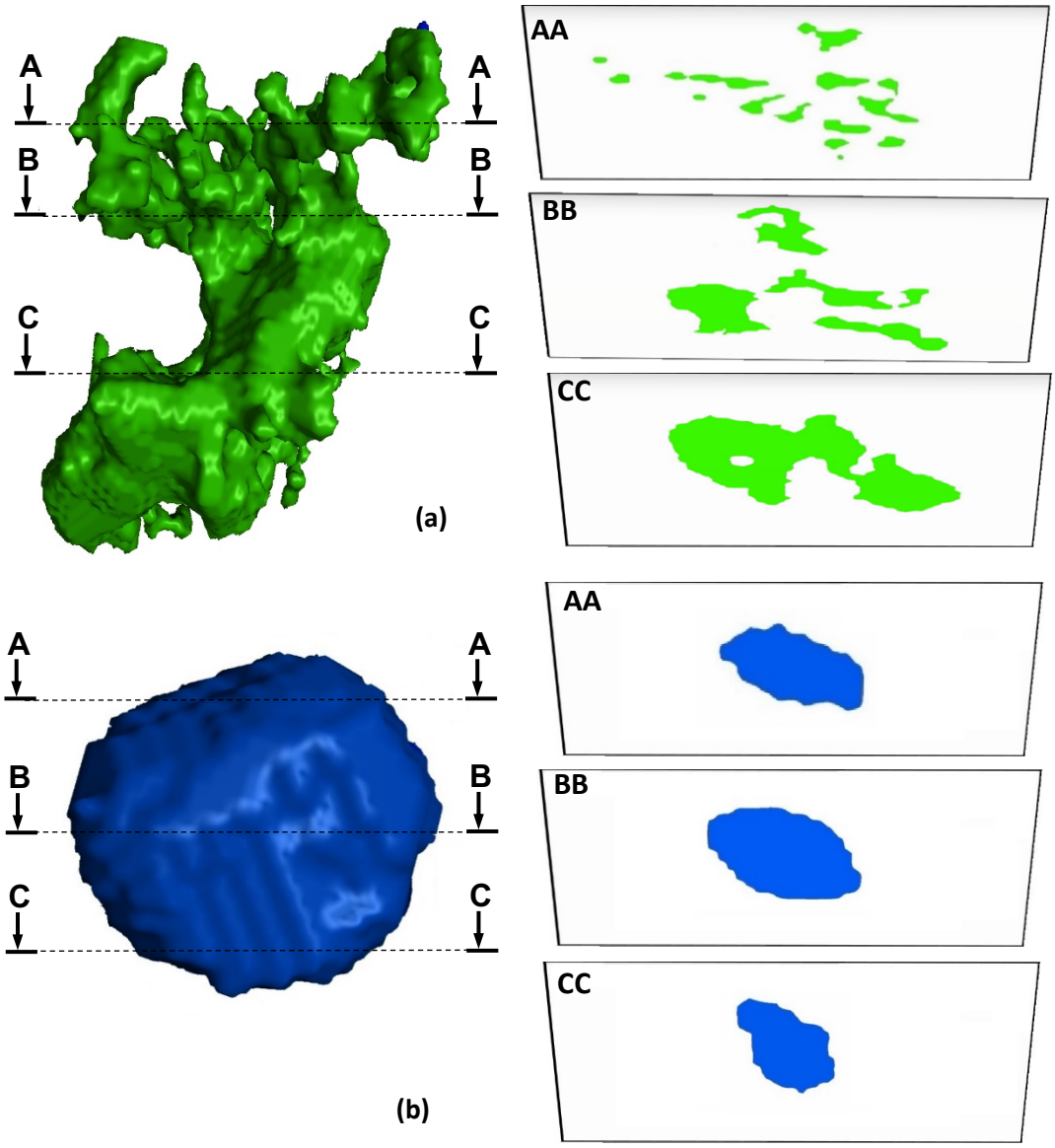

Figure 3.6. Illustration of (a) shrinkage and (b) gas porosity and their appearance on 2D surfaces.

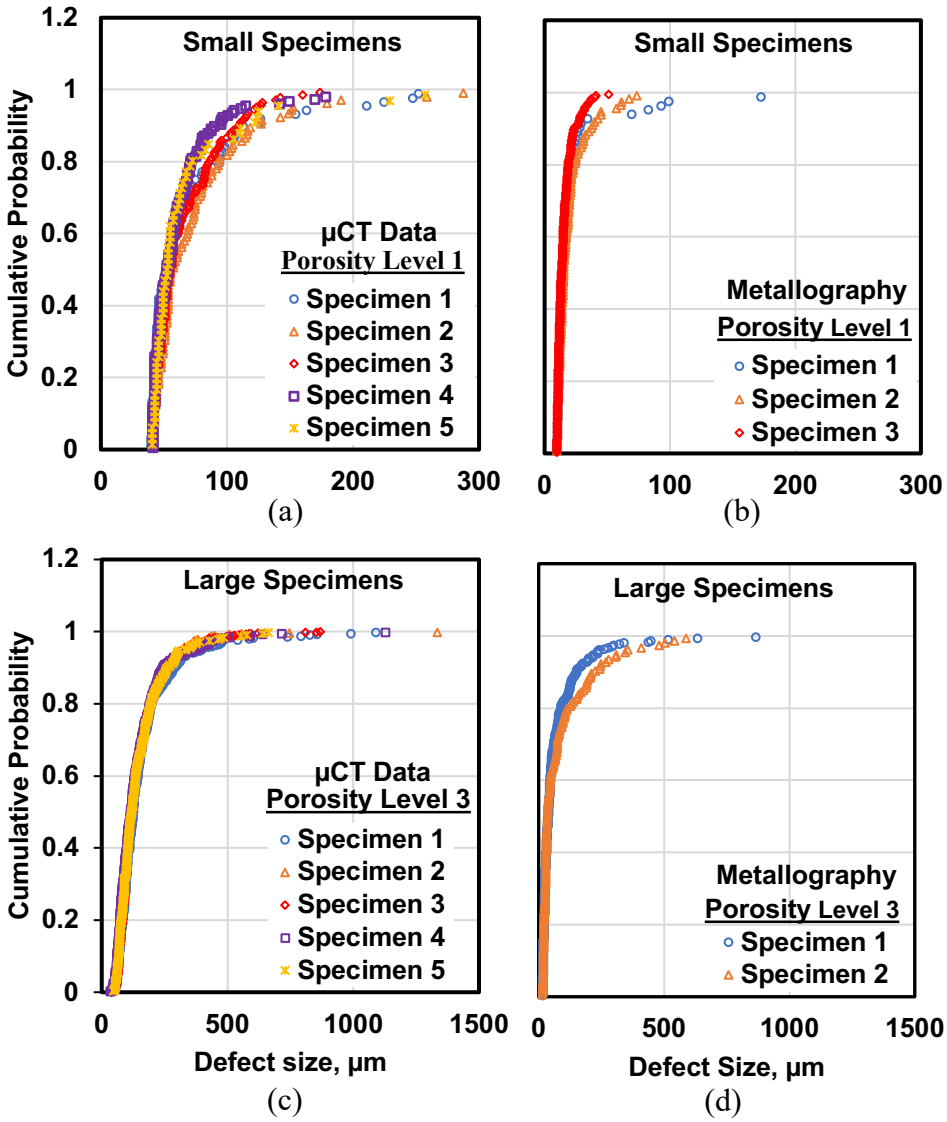

Figure 3.7. Examples of the defect distribution in different specimens of the size and porosity level using (a,c) μCT data and (b,d) Metallography data.

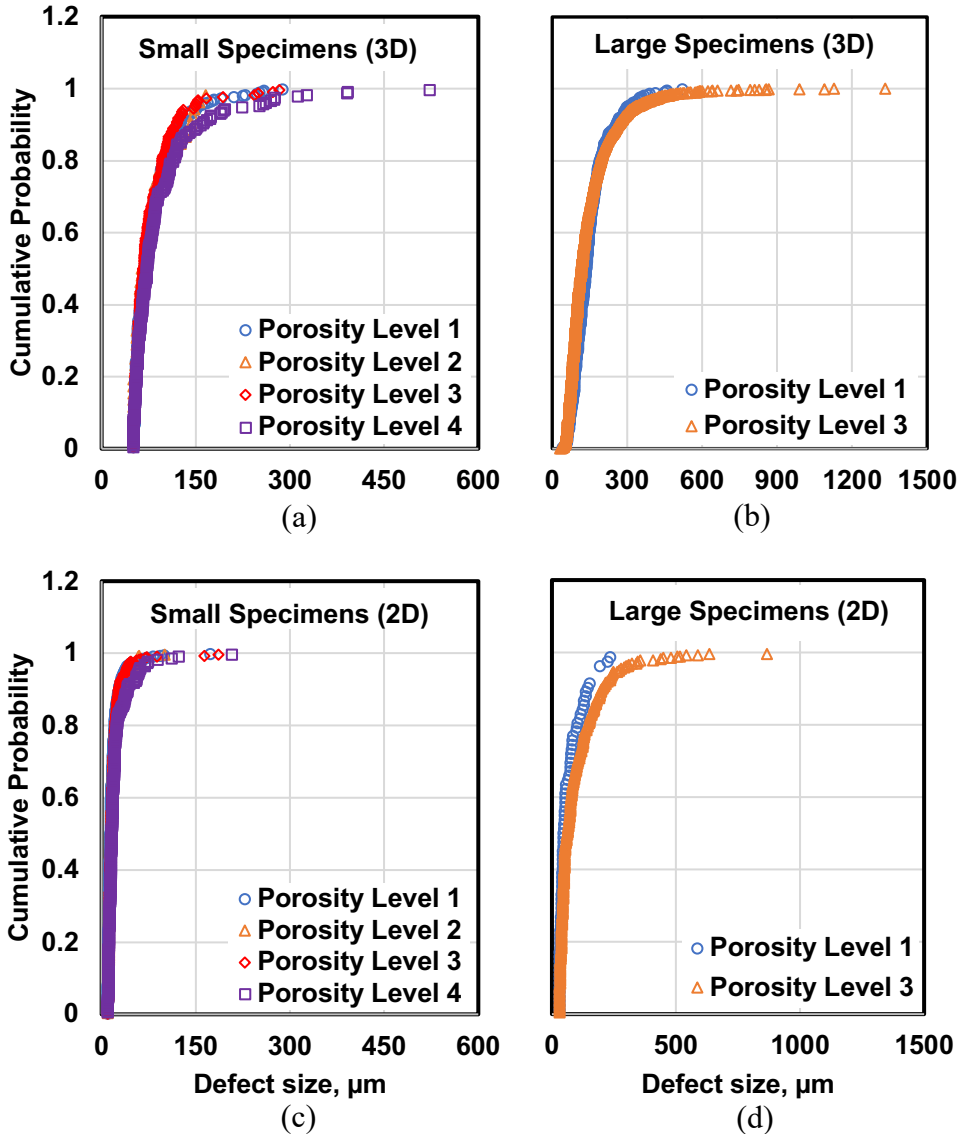

Figure 3.8. Comparison of defect distribution in different porosity levels measured by X-ray radiography in small and large specimens based on (a,b) µCT data, and (c,d) metallography data.

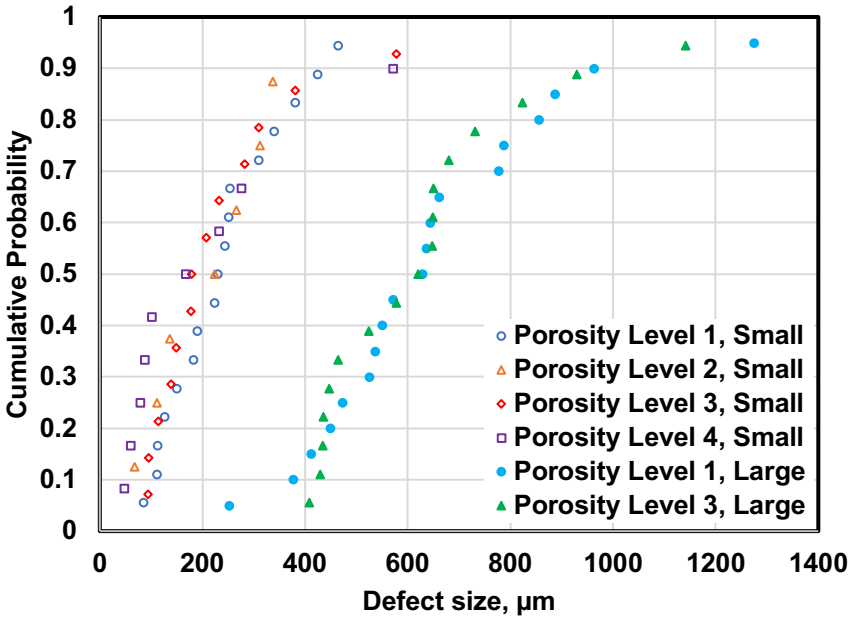

Figure 3.9. Comparison of defects distributions in different porosity levels based on observed defects on fracture surfaces.

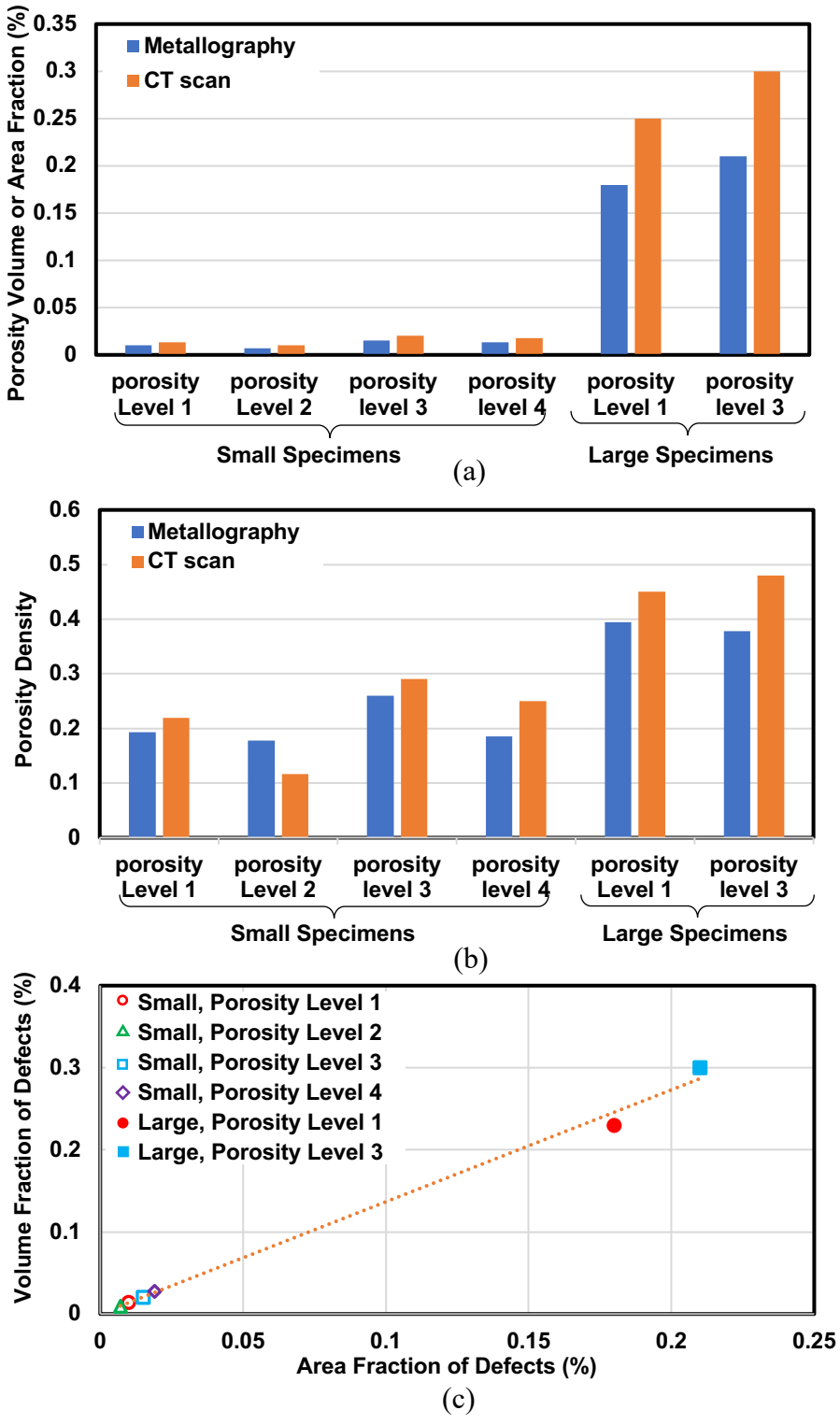

Figure 3.10. (a) volume or area fraction of defects, (b) porosity density per mm^3 for CT scan and per mm^2 for metallography data at each porosity level, (c) Volume fraction of defects from µCT scan vs area fraction of defects by metallography.

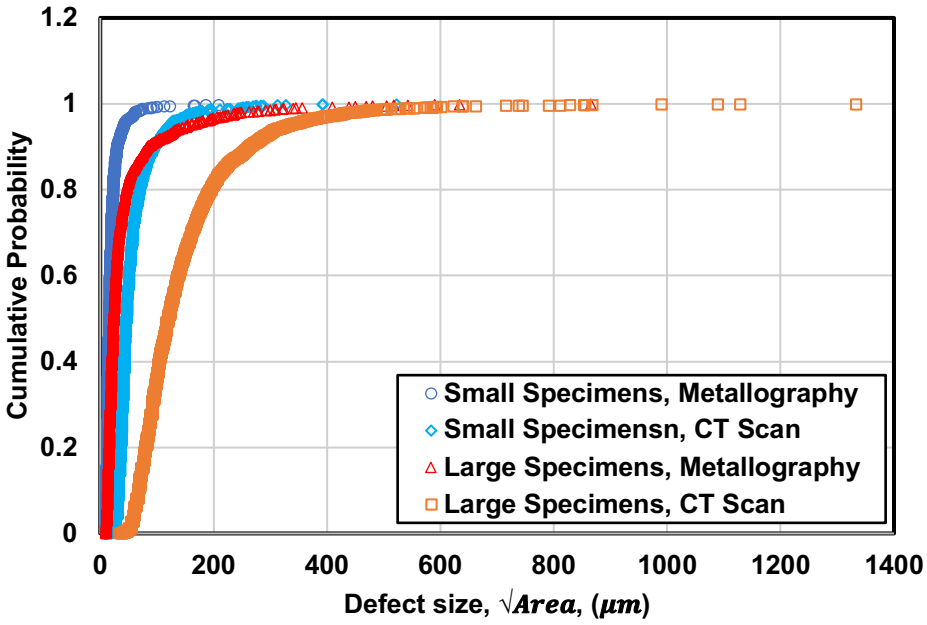

Figure 3.11. Comparison between defect distribution in small and large specimens using metallography and μCT data.

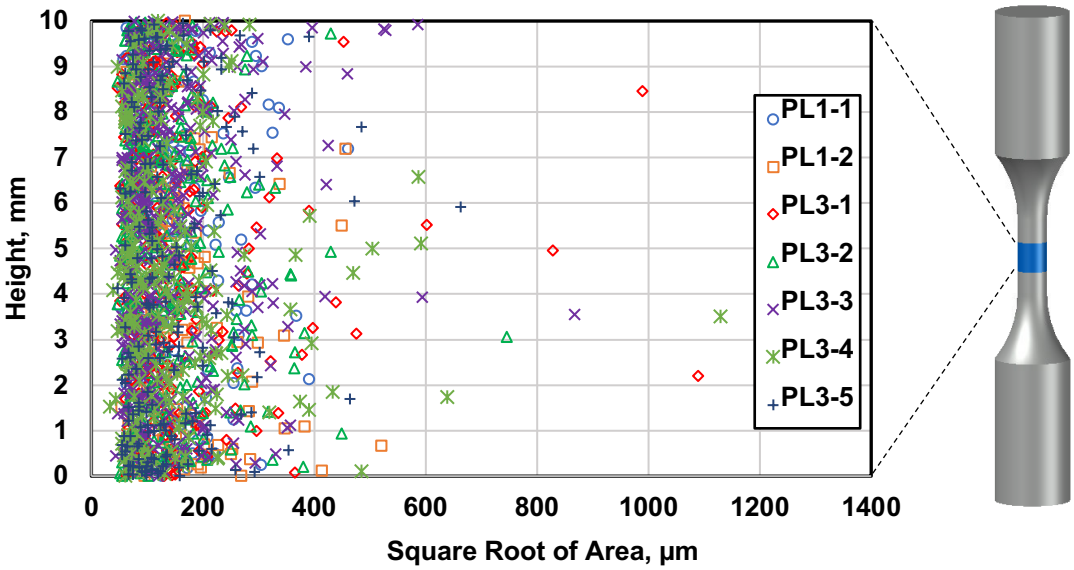

Figure 3.12. Distribution of defects along the height based on µCT data in large specimens. The symbols represent the defect data in different specimens at porosity levels 1 (PL1) and porosity level 3 (PL3).

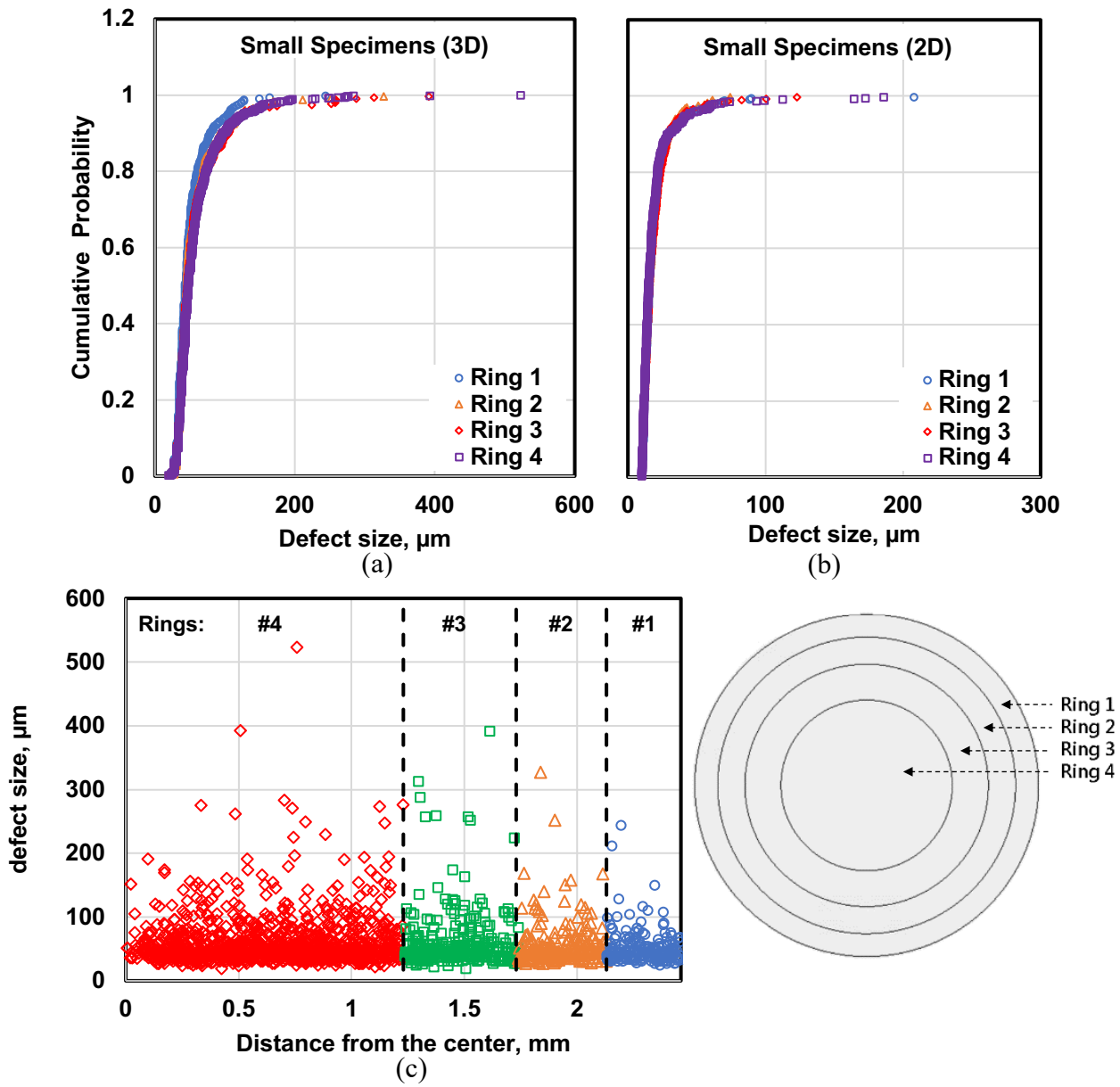

Figure 3.13. Comparison of the radial distribution of the defects within the cross section in small Specimens using (a) μCT data, (b) metallography data, (c) illustration of defect distribution in radial direction within small specimens.

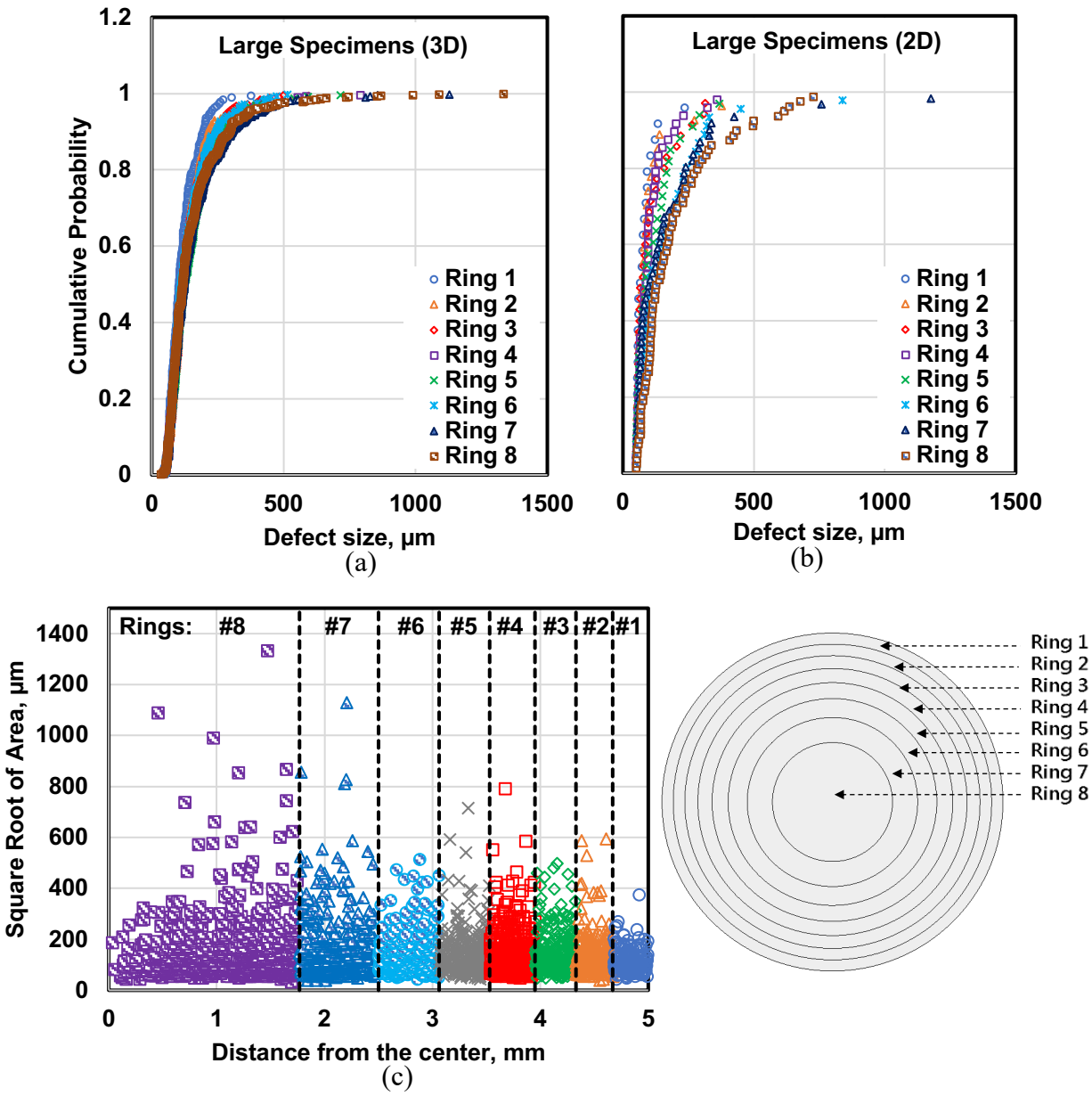

Figure 3.14. Comparison of the radial distribution of the defects within the cross section in large Specimens using (a) µCT data, (b) metallography data, (c) illustration of defect distribution in radial direction within large specimens.

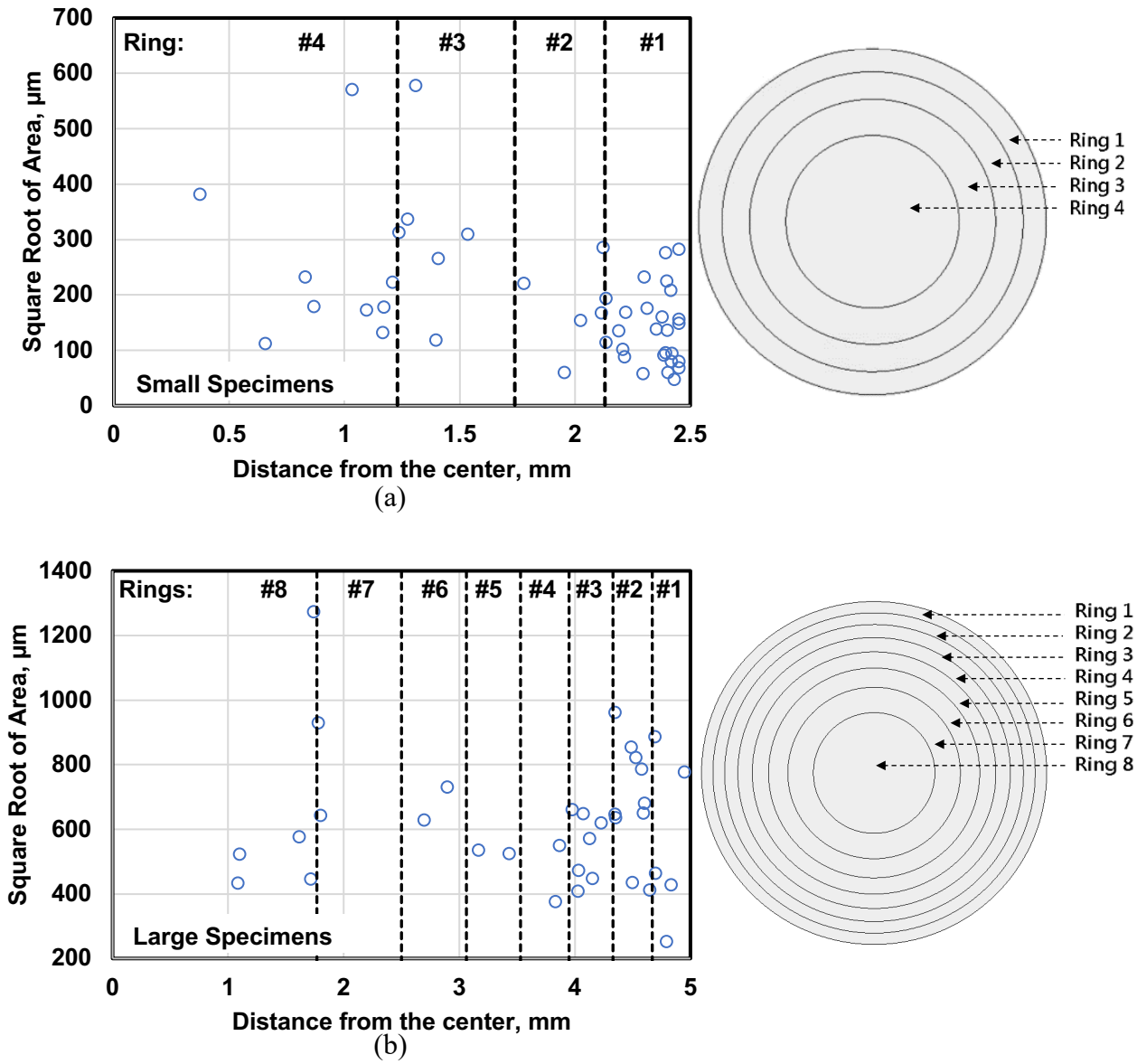

Figure 3.15. Comparison of the radial distribution of the fatal defects observed on fracture surfaces in terms of their distance from the center in (a) small, and (b) large specimens.

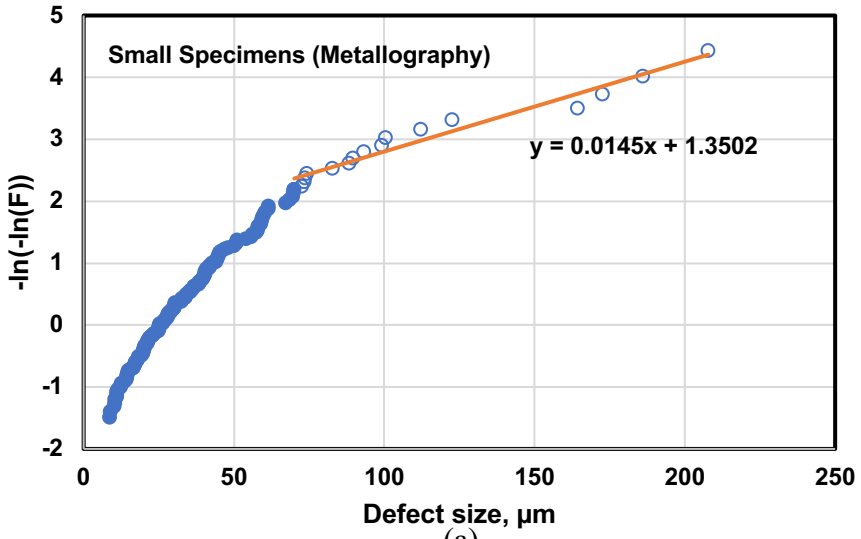

(a)

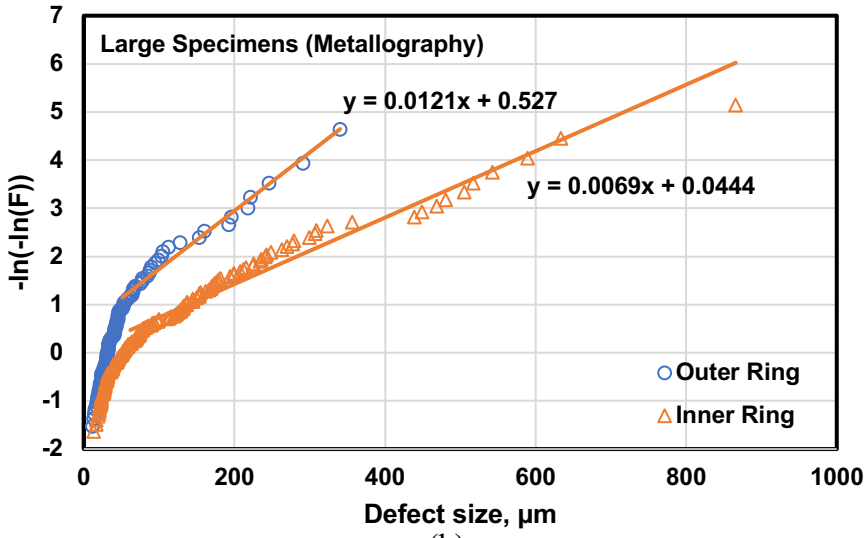

(b)

Figure 3.16. EV plot of defect data for (a) small, and (b) large specimens.

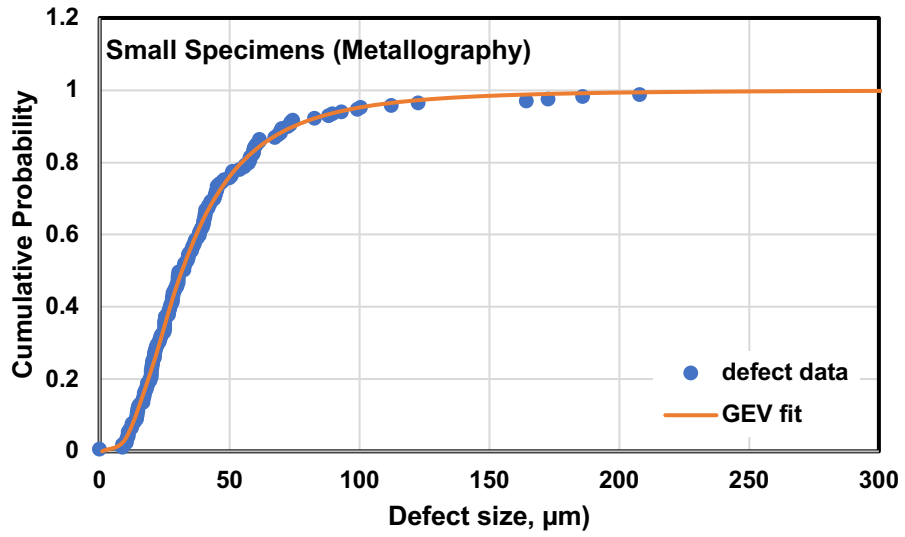

(a)

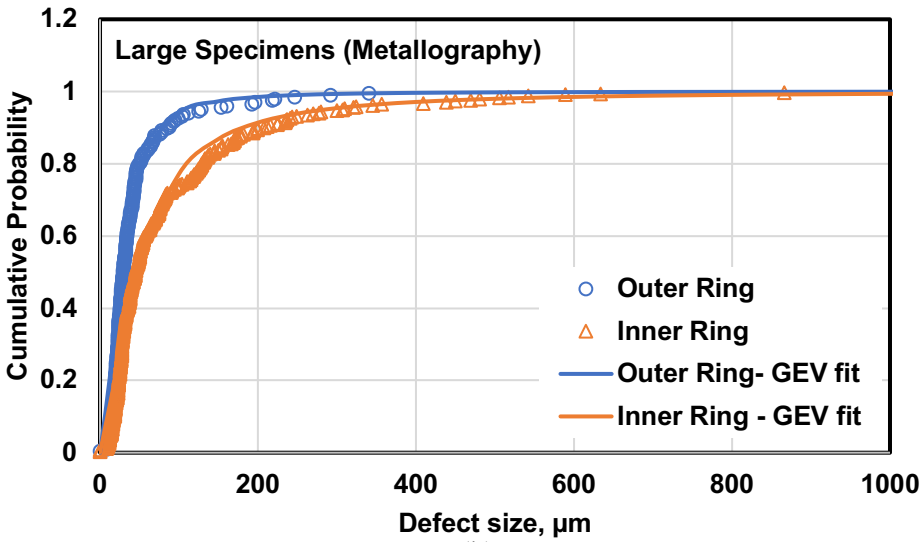

(b)

Figure 3.17. GEV plot of defect data for (a) small, and (b) large specimens.

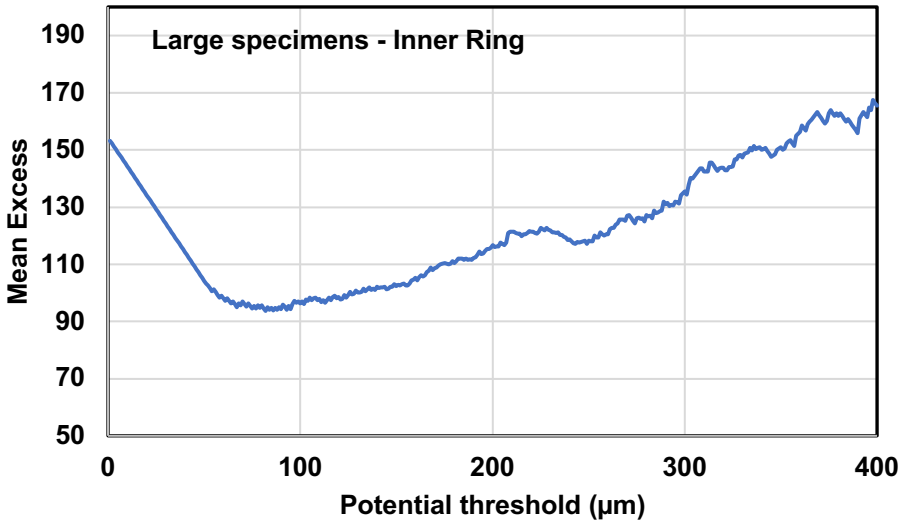

Figure 3.18. Mean excess plot using µCT data in large specimens in inner ring.

Chapter 4

Fatigue Behavior Under Uniaxial Stress State Including the Effects of Defects, Section Size, Stress Gradient, and Mean Stress

4.1. Introduction

In this chapter, the fatigue performance of a cast aluminum alloy, as an illustrative material containing defects, under different loading conditions and specimen sizes is studied. Uniaxial fatigue tests were conducted to study the fatigue behavior of this material with two specimen sizes and under various loading conditions including fully-reversed tension-compression to obtain basic fatigue properties of the material, tension-tension to study mean stress effect, and rotating bending to study stress gradient effect on materials containing defect. In addition, the fatigue performance of this material under different testing conditions was predicted using the maximum size of crack-initiating defects measured on fracture surfaces.

4.2. Experimental Program

The material used in this study was A356 aluminum alloy, which is a common cast aluminum alloy. In order to study the effect of specimen size on fatigue behavior of this material, two different specimen sizes, which, hereafter, will be called small (5 mm nominal diameter) and

large specimens (10 mm nominal diameter), were fabricated by high pressure die casting (HPDC) process, which is one of the most productive casting methods in producing a wide variety of aluminum components. This process involves high-velocity injection of molten metal into metal dies and solidification of the alloy under high pressure. Therefore, the dimensional accuracy and surface finish of castings produced by HPDC are good, so subsequent machining processes are minimized [12]. The specimen configuration and nominal dimensions are illustrated in Figure 3.1.

The specimens were heat treated as standard T6 procedure right after production. Since the majority of the aluminum cast components produced by HPDC process are used with no machining, the specimens were tested in as-cast surface condition. The only modification applied on the specimens was trimming of the flash remained from casting with 600 mesh abrasive paper [74].

An initial classification between specimens of each size was made by X-ray radiography examination with regards to porosity level. Therefore, four different porosity levels were defined based on the porosities detected through X-ray radiography examination, which are called porosity levels 1-4. Porosity level 1 contains the smallest porosities, while porosity level 4 has the largest ones. Moreover, to characterize the defects and study the variability of defects within the specimens, between 2 to 5 specimens at each porosity levels were also examined by X-ray micro-computed tomography (μCT) as well as metallography. The results of defect evaluation using metallography and μCT scan was discussed in Chapter 3, in which the defect distribution between deferent porosity levels and variability of defects with location within the specimens are investigated. The range of maximum defects from X-ray radiography, as well as volume fraction of the defects within the specimens at each porosity level obtained by micro-CT scan are summarized in Table 3.1.

Monotonic stress-strain behavior of the material was obtained by performing tension tests on two specimens at each porosity level using the test method specified by ASTM Standard E8-04 [75]. In addition, the cyclic deformation behavior was examined by conducting incremental cyclic step tests. At each stain level, sufficient number of cycles were applied so the material was stabilized before increasing the strain level. Fatigue tests were conducted in three different loading conditions including fully-reversed tension-compression (R = -1), tension-tension (R = 0), and rotating bending. Therefore, the effects of mean stress, stress gradient and specimen size on fatigue performance were investigated.

The stress levels for fatigue tests were chosen to obtain fatigue lives between 10^3 and 5×10^6cycles and the applied frequencies ranged from 0.5 to 25 Hz in axial tests and 10 - 16 Hz in rotating bending tests. Lower frequencies used at high stress amplitudes and high frequencies used at lower stress amplitudes. The specimens that survived 5×10^6cycles were considered as run out. All fatigue tests at each stress level were performed on three specimens for each porosity level. Fracture surfaces of all broken specimens were examined using digital optical microscope, Keyence VHX-6000 to identify the crack initiating pores and measure their size. The measured size of pores on the fracture surfaces were then used in predicting the fatigue life and evaluating the effect of defect size on fatigue performance.

4.3. Monotonic and Cyclic Deformation Behaviors

Monotonic tension tests were carried out on two specimens for each porosity level of small specimens and one porosity level of the large specimens. The obtained properties are summarized in Table 4.1. In this table, K and n are strength coefficient and strain hardening exponent, respectively. The monotonic stress-strain curves are also shown in Figure 4.1. As can be seen, both

yield strength and ultimate strength of the material in large specimens are lower than those in small specimens. Lower strength of the material in large specimens is attributed to more volume fraction of porosity, see Table 3.1, as well as larger pores in comparison to small specimens. As mentioned earlier, yield and ultimate strength as well as elongation decreased by increasing porosity level in [13].

Furthermore, the cyclic behavior of this material was evaluated by conducting cyclic step test on a large specimen at porosity level 3. This test was conducted under strain-controlled condition and the strain amplitude was sequentially increasing after the hardening process took place and the material was stabilized. The variation of stress vs elapsed cycle as well as stable stress-strain hysteresis loops in each strain amplitude level are illustrated in Figure 4.2. As can be seen in Figure 4.2(a), a cyclic hardening process leads to gradually increasing the required stress at each strain amplitude level, until it becomes approximately constant after a certain number of load cycles. Using the stable stress-strain hysteresis loops shown in Figure 4.2(b), the cyclic stress-strain curve was obtained, which is compared with monotonic stress-strain curve in Figure 4.2(c). As can be seen in this figure, a very significant hardening is experienced by this material due to cyclic load.

4.4. Fatigue Test Results

Fatigue tests were conducted under different loading conditions including axial fatigue tests at different stress ratios of R = -1 and R = 0, as well as rotating bending fatigue tests. Therefore, the effects of mean stress could be evaluated with R = 0 data and stress gradient effect could be studied by rotating bending data.

4.4.1. Fully-reversed (R = -1) axial loading condition

The results of fully-reversed uniaxial fatigue tests on different pre-defined porosity levels for small and large specimens are shown in Figure 4.3. The best fit curve is also plotted for each data set based on ASTM E739 [76] following least square approach taking the stress amplitude and fatigue life as independent and dependent variables, respectively. As can be seen in Figures 4.3(a)-4.3(b), there is no significant difference between fatigue performance of different porosity levels. The reason is that in spite of initial classification of specimens into four porosity levels through X-ray radiography examination, there is no significant difference between the specimens with the same size in terms of defect size. In X-ray radiography test, the defects are evaluated based on their projections on two dimensional films, wherein the resolution is affected not only by the orientation of defects with respect to the source and the film, but also superposition of other defects. Therefore, evaluation of defects based on X-ray radiography test is not reliable. This issue can be confirmed by comparison of the defects measured on fracture surfaces at different porosity levels, as shown in Figure 4.3(c). Therefore, all small or large specimens can be considered as having identical distribution of defects. The fatigue life of all small and large specimens as one porosity level are illustrated in Figure 4.4. Considerable scatter in fatigue life can be perceived in this figure for both small and large specimens, which is more than one order of magnitude. Such scatter is common in the materials containing defects and has also been reported in other works, such as [4,10,27,31]. It has been shown that the scatter in materials containing defects is attributed to the defect size distribution within the specimens, which is discussed later in section 4.6.

4.4.2. Tension-tension (R = 0) loading condition

In order to study mean stress effect, tension-tension fatigue tests ($R = 0$) were conducted

on small specimens at porosity levels 1 and 3. The results of these tests are demonstrated in Figure 4.5. As can be seen in Figure 4.5(a), there is no significant difference between the fatigue performance of the specimens from different porosity levels. Therefore, all the fatigue life data are considered as one population, similar to fatigue performance of the specimens under fully-reversed loading. The fatigue test results of small specimens as one porosity level is illustrated in Figure 4.5(b). Considering all fatigue data as one population, there is significant scatter in fatigue life at both high and low stress levels, more than one order of magnitude, which is associated with the defect variability within the specimens.

4.4.3. Rotating bending condition

Rotating bending fatigue tests results on small specimens at porosity levels 1 and 4 are shown in Figure 4.6(a). Similar to the axial loading condition, it can be inferred from Figure 4.6(a) that there is no significant difference between the fatigue behavior of specimens from porosity levels 1 and 4. Therefore, the fatigue life data for specimens from different porosity levels are combined and illustrated in Figure 4.6(b). In this case also significant scatter was observed due to existing casting defects. However, the scatter in fatigue lives under this loading condition is lower than that under axial loading condition. The reason is that contrary to axial loading in which the entire cross section is under uniform stress, under rotating bending only the surface of the specimens is under maximum stress. Therefore, the highly stressed volume under rotating bending is smaller than that under axial loading.

4.4.4. Fractography

Examining the fracture surfaces of the specimens failed under axial loading conditions

revealed that in the majority of small specimens (>80%), the failure happened due to fatigue cracks originating from porosity, while in large specimens the origin of all failures was from porosity. The information about the origin of fatigue failure is also shown in Figures 4.3, 4.5, and 4.6, in which solid, hollow and hatched marks represent failures due to cracks originated at internal pores, at surface with no visible pore, and at casting seam line, respectively.

The importance of defects as the main initiation site for fatigue cracks has also been mentioned for other cast aluminum alloys, such as in [4,6,7,13,30,31]. Higher number of specimens failed due to the cracks originating from pores in large specimens is attributed to larger defects as well as higher volume fraction of defect, as shown in Table 3.1. The probability of a defect existing larger than the critical defect size in large specimens is higher than that in small specimens. The defect size range measured on fracture surfaces of small and large specimens is summarized in Table 4.2. As can be seen in this table, the size of crack initiating defects in large specimens is considerably larger than that in small specimens.

It is also noteworthy that as appose to many reports in which the fatigue cracks originated from the pores at or near surface [2,9,27,32,49], it was observed that not only the fatigue cracks may originate from the porosity at or near surface, but also around 40% of specimens failed due to cracks originating from internal porosities. The reason is that in the majority of the other investigations on the effect of defects on fatigue performance of cast aluminum, the specimens were machined from a cast wedge, bar, or component, where the surface of the casting had been removed and the defect distribution in the specimens prepared from the center of castings were almost uniform. In this study, however, the specimens were tested in as-cast surface condition, which can simulate fatigue performance of components in real application because the majority of the components produced by high pressure die casting are used with minimized or no machining.

It was shown in Chapter 3 that the defects are not distributed randomly throughout the cross section, especially in the large specimens. The probability of having large defects at the specimen center is higher than that at the surface due to different cooling rate at surface and center of the specimen. Moreover, in uniaxial fatigue tests, the whole cross section experience approximately uniform stress. Therefore, the critical pore may not necessarily be at or near the surface. Figure 4.7(a-c) illustrates typical fracture surfaces of small and large specimens, in which fatigue failure happened from internal porosity under axial loading condition. In this figure, a fish eye failure corresponding to the internal crack growth originating from porosity towards the specimen surface can be clearly seen.

It is also noteworthy that in a couple of specimens the crack initiated from tiny cluster type pores in the center of the specimen, which had been formed because of shrinkage during solidification. It has already been shown that multiple small pores can initiate the fatigue failure as frequently as a larger single pore [9]. When there are clusters or multiple small pores, the fatigue cracks initiate from these pores and grow in a manner that allows them to coalesce into one dominant crack that causes failure. Crack initiation is expected to be easier in cases of multiple pores close to each other because of higher local plastic strains resulting from overlapping the slip bands from individual pores in the cluster.

Under rotating bending condition, the fatigue cracks originated either from the defects near surface or from surface imperfections, i.e. the casting seam line, while no specimen failed due to internal defects. This is expected as in rotating bending the maximum stress is experienced at the surface of the specimen and diminishes towards the center due to stress gradient. For this loading condition, crack initiation site depends on the probability of a critical defect existing at or near the surface. When there is no defect larger than the critical defect size in this region, the fatigue crack

may initiate from other imperfections at the surface. An example of the fracture surface under rotating bending test is shown in Figure 4.7(d), indicating the fatigue crack initiated from a defect near the surface of the specimen.

4.5. Evaluating the Effects of Specimen Size, Mean Stress, and Stress Gradient on Fatigue Behavior

4.5.1. Effect of specimen size

The comparison between small and large specimens has been illustrated in Figure 4.8(a), showing the best fit curve to the median fatigue life at a given stress level. The horizontal bars in this figure indicate the scatter in fatigue life at different stress levels. As can be clearly seen, the fatigue performance in large specimens is inferior to that in small specimens due to higher stressed volume in large specimens, which increases the probability of existing large defects. However, as it is observed in Tables 3.1 and 4.2, not only the volume fraction of defect in large specimens is higher than that in small specimens, but also the defect size in large specimens is larger than that in small specimens. The comparison of defect size distributions in small and large specimens using the defects observed on fracture surfaces is also demonstrated in Figure 4.8(b), which shows that large specimens contain larger pores in comparison to the small specimens.

4.5.2. Effect of mean stress

The comparison between fatigue test results under axial cyclic load with stress ratios of zero and -1 are shown in Figure 4.9. In this figure, the median fatigue life at each stress level and the associated best fit curves are compared, while the scatter of the fatigue life at each stress level is shown by horizontal lines. It can be clearly seen that at a given stress amplitude level the fatigue

life of the specimens under tension-tension cyclic condition is considerably shorter than that under fully-reversed condition. It is believed that the cracks grow only during the tensile part of the load cycle, therefore, under fully-reversed axial load the crack can grow only in half of the loading cycle, while under tension-tension condition the specimen is under tension in the entire loading cycle. The higher maximum stress in tension-tension loading by a factor of 2, in comparison to the fully-reversed condition for a given stress amplitude results in faster crack growth, which leads to shorter fatigue life.

4.5.3. Effect of stress gradient

The comparison of fatigue behavior of small specimens under fully-reversed axial loading and rotating bending using the median fatigue life at each stress level is shown in Figure 4.10. As can be seen in this figure, at a given stress amplitude, the fatigue life of the specimens under rotating bending fatigue test is higher than that under fully-reversed axial loading condition. The reason is that in axial loading condition, the whole cross section is under uniform stress and the probability of existing a critical defect in the uniformly stressed region is higher than that in rotating bending tests, where only the surface of the specimens is under maximum stress. This issue is confirmed by comparison of the defect size range measured on fracture surface of the small specimens under axial and rotating bending loading conditions, as illustrated in Table 4.2. It can be seen that the maximum size of crack initiating defects under axial loading is 578 μm, which is larger than that under rotating bending, equal to 252 μm.

4.6. Analysis of Scatter in Fatigue Life and the Effect of Defect Size

The variability of fatigue life was studied using Weibull and log-normal distributions for

each stress level, specimen size, and loading condition. The Weibull and log-normal cumulative probability functions are given by:

$$P(x) = \int_0^{N_f} \frac{1}{N_f \varphi \sqrt{2\pi}} exp\left(\frac{-\left(\ln(N_f)-\mu\right)^2}{2\varphi^2}\right) dN_f \quad (4.1)$$

$$P(x) = 1 - \exp\left(-\left(\frac{N_f}{N_0}\right)^{\alpha}\right) \quad (4.2)$$

In Equation (4.1), N_f is the number of cycles until fracture, and φ and μ are standard deviation and average of $\ln(N_f)$, respectively. In Equation (4.2), N_0 is the scale parameter and α is the shape parameter, alternatively referred to Weibull modulus. The statistical discrepancy between the experimental data and each probability distribution function was computed through Anderson-Darling test, which has been shown to be superior to other goodness-of-fit tests for a variety of distributions [77]. In this approach the goodness of fit can be quantified as:

$$A^2 = -n - \frac{1}{n}\sum_{i=1}^{n}[(2i-1)\ln\left(P(x_i) + (2n-1-2i)\ln\left(1-P(x_i)\right)\right] \quad (4.3)$$

where n is the sample size, and $P(x_i)$ is the cumulative probability for each data point calculated with the estimated distribution parameters. A higher confidence in fitting the hypothesized distribution will correspond to a lower value of A^2.

Using this approach, the fatigue life distribution of large and small specimens under different loading conditions were evaluated by both Weibull and lognormal distribution functions. For brevity, in Figure 4.11 the probability plots of fatigue life under only one stress level in each loading conditions is shown. Similar plots were obtained for other stress levels. As can be seen in this figure, both Weibull and lognormal distributions fit experimental fatigue data relatively well. However, applying Anderson-Darling tests revealed that lognormal distribution is a better representative of experimental fatigue life data in all loading conditions, in comparison to the Weibull distribution. The A^2 values for different fatigue data sets are compared in Table 4.3, which

shows less discrepancy between lognormal distribution function and fatigue experimental data in comparison to the Weibull distribution function.

As was mentioned in the previous sections, the defects affect the fatigue behavior by accelerating the crack initiation as well as causing scatter in fatigue life. In order to study the effect of defects on scatter of the fatigue life, the size of the fatal defects was measured on the fracture surfaces and the effect of pore size on fatigue life was considered at each stress level. The comparison of the effect of pore size on fatigue life at different stress levels in fully-reversed condition is illustrated in Figure 4.12. As can be seen in this figure, at a given stress level, increasing the pore size results in reducing the fatigue life. Larger defects are known to induce higher local stresses and strains, which facilitate crack nucleation under cyclic loading condition. Gao et al. [32] used finite element analysis to demonstrate that the maximum stress and strain concentrations around large pores are higher than that for small pores.

4.7. Fatigue Life Modeling and Predictions

Fatigue performance of materials is usually studied by conducting laboratory fatigue tests under axial or bending loading conditions on small specimens, while industrial components of different sizes, mean stresses, or stress gradients may result in different fatigue performance. Therefore, their effects should be modeled in design of such components.

4.7.1. Mean stress effect

Several correction methods have been proposed in literature to model mean stress effect, among which modified Goodman [78], Smith-Watson-Topper (SWT) [79] and Walker [80] are most widely used [15]. Dowling et al. [81,82] compared various approaches to consider mean

stress in a wide range of materials and noted that modified Goodman equation is not very accurate in considering mean stress effect, while SWT parameter is quite accurate, especially for aluminum alloys. In addition, Walker equation with an adjustable constant, γ, resulted in superior results. The SWT and walker equations for mean stress correction are given as:

$$\sigma_{SWT} = \sqrt{\sigma_{max}\sigma_a} \tag{4.4}$$

$$\sigma_{Walker} = {\sigma_{max}}^{1-\gamma}{\sigma_a}^{\gamma} \tag{4.5}$$

where γ is a material constant indicating the mean stress sensitivity that ranges from zero to 1. A γ value of 0.5 results in the SWT equation. In the case of A356-T6, which is the focus of this study, the exponent γ was found to be 0.563 [83], so the equivalent stress computed through SWT and Walker are close to each other. Therefore, in this study only SWT is used for predictions. It is worth mentioning that Equation (4.4) is the stress-based version of SWT relation, however, when plastic deformation is involved during cyclic loading, its strain-based version can be applied:

$$\sigma_{ar} = \sqrt{E\sigma_{max}\varepsilon_a} \tag{4.6}$$

The correlation of fatigue life data for fully-reversed axial tests and tension-tension loading condition using the SWT approach is demonstrated in Figure 4.13. It can be seen that this approach is quite accurate in predicting the fatigue life with applied mean stress.

4.7.2. Effect of defect size

Fatigue performance of defect containing materials can be significantly affected by type and distribution of defects, which, in turn, depends on the manufacturing method, production parameters, size of the component, etc. Avalle et al. [13] studied the fatigue performance of a die cast aluminum alloy including different porosity levels using non-optimized feeding channel during casting and found that the fatigue strength of the material decreases with increasing the

porosity level. Similar conclusion was made by Linder et al. [48], who studied the fatigue properties of sand and permanent mold cast aluminum alloys.

On the other hand, it is well known that the fatigue limit of materials containing defects can be defined by Kitagawa-Takahashi diagram [84]. According to this diagram, the fatigue strength depends on the size of defects, larger than a critical size. By means of an intrinsic crack size, a_0, defined by El-Haddad [52], the fatigue limit of a material containing defects can be estimated as:

$$\Delta\sigma_e = \Delta\sigma_0 \sqrt{\frac{a_0}{a+a_0}} \tag{4.7}$$

where $\Delta\sigma_0$ is the fatigue limit range of the material with no defect larger than the critical defect size, $\Delta\sigma_e$ is the fatigue strength of the material with maximum defect size equal to a, and a_0 is intrinsic defect size defined as:

$$a_0 = \frac{1}{\pi}\left(\frac{\Delta K_{th,l}}{Y\Delta\sigma_0}\right)^2 \tag{4.8}$$

in which $\Delta K_{th,l}$ is the threshold stress intensity factor range for long cracks and Y is the geometry factor. As the effective threshold stress intensity factor range, $\Delta K_{th,eff}$, gives a safe lower fatigue limit [85,86] , $\Delta K_{th,eff}$ can be used in Equation (4.8) instead of $\Delta K_{th,l}$ which determines the fatigue limit only in case of large defect. It is noteworthy that for A356-T6, which is the focus of this study, the effective threshold stress intensity factor is reported to be 1.3 MPa$\sqrt{\text{m}}$ [19] and fatigue limit amplitude of this materials under fully-reversed axial cyclic load is about 90 MPa [87,88]. Therefore, considering the geometry factor, Y = 0.65 which is defined by Murakami and Endo [29] for surface defects, the intrinsic defect size is computed as 157 μm.

Knowing the relation of fatigue strength with maximum defect size, Equation (4.7), the fatigue strength within the specimens containing different defect distributions can be estimated by the following relation:

$$\frac{\sigma_{e,2}}{\sigma_{e,1}} = \sqrt{\frac{a_1+a_0}{a_2+a_0}} \tag{4.9}$$

where a_1 and a_2 are the maximum defect size in specimens with different defect distributions. Using this approach, the fatigue properties of small specimens under fully-reversed loading condition is taken as the reference and the fatigue performance of the material with larger specimen size and under rotating bending condition are estimated in sections 4.7.3 and 4.7.4, respectively.

4.7.3. Effect of specimen size

The Basquin relation for small specimens under fully-reversed loading condition was obtained using least square method on the experimental fatigue life data, taking fatigue life and stress amplitude as dependent and independent parameters, respectively (Figure 4.4). Therefore, the Basquin equation for small specimens is taken as the reference fatigue performance of the material, given by:

$$S_a = 717\ {N_f}^{-0.130} \tag{4.10}$$

Using this equation, the fatigue strength of the material at fatigue life of 10^7 cycles can be computed as 89 MPa. The calculated fatigue strength is in agreement with the one reported in literature for this material under fully-reversed loading condition [87,88].

The maximum defect size on fracture surfaces of small and large specimens under axial loading condition was measured as 578 μm and 1274 μm, respectively, as shown in Table 4.2. Therefore, using Equation (4.9), the fatigue strength of large specimens under fully-reversed loading condition can be estimated as 60 MPa, upon which the Basquin exponent can be computed

by considering the stress amplitude as the fatigue limit at the fatigue life of 10^7 cycles. Therefore, the Basquin equation for large specimens is obtained as:

$$\sigma_a = 717 {N_f}^{-0.149} \quad (4.11)$$

Having applied this procedure, the fatigue performance of large specimens under fully-reversed condition was predicted, which is compared to the experimental data in Figure 4.14. As can be seen in this figure, the estimated S-N curve for large specimens is in very good agreement with the experimental data.

4.7.4. Stress gradient effect

The experimental fatigue life data under fully-reversed uniaxial loading condition can also be used to estimate the fatigue performance under rotating bending condition. It is known that in rotating bending condition, only the surface of the specimens is under high stress. Therefore, in smaller stressed volume, the probability of finding a defect larger than critical defect size is lower in comparison to the axial loading condition, in which all the cross section of the specimens experiences high stress. Therefore, the maximum defects measured on fracture surfaces of the specimens under rotating bending is smaller than that under axial loading condition, as illustrated in Table 4.2.

Using the maximum defect size measured on the fracture surfaces of the specimens under axial loading, 578 μm, and the one under rotating bending, 252 μm, in Equation (4.9) results in the fatigue limit for rotating bending condition as 118 MPa. Therefore, the Basquin exponent can be obtained for rotating bending by considering the stress amplitude as the fatigue limit at the fatigue life of 10^7 cycles. The Basquin equation for rotating bending is given by:

$$S_a = 717\ {N_f}^{-0.111} \quad (4.12)$$

The comparison between the estimated fatigue life under rotating bending with the experimental fatigue data in axial and rotating bending conditions is demonstrated in Figure 4.15. As can be seen, the estimate of the fatigue performance under rotating bending condition is in good agreement with the experimental data.

4.8. Summary and Conclusions

The main objective of this chapter was to better understand the fatigue behavior of materials containing defects. A cast aluminum alloy was used as an illustrative material containing defects. The specimens were manufactured by high pressure die casting (HPDC), which is widely used to produce a wide range of industrial components. In order to study the effect of specimen size on fatigue performance, the specimens were produced in two different sizes with 5 mm and 10 mm in gauge section diameter. Since majority of the components manufactured by HPDC are used with no machining, the specimens were tested in as-cast surface finish. To evaluate the effect of mean stress on fatigue performance, the fatigue tests were conducted under two stress ratios of zero and -1. Stress gradient effect was also studied by conducting rotating bending fatigue tests.

Fatigue performance of industrial components of different sizes, mean stresses, or stress gradients are different from the laboratory specimens under axial or rotating bending. In this work, the fatigue properties of small specimens under fully-reversed loading condition was taken as the reference and the fatigue performance of the material with larger specimen size and under different loading conditions was predicted. The maximum defect size observed on fracture surfaces was used to predict the fatigue strength and the S-N equations under different loading conditions and specimen sizes.

Comparing the experimental results and statistical analysis and fatigue life modeling, the following conclusions can be made:

1. Based on monotonic tensile tests of small and large specimens, the yield and ultimate tensile strengths as well as elongation of larger specimens, containing larger defects were lower than those of smaller specimens.
2. Cyclic step tests of the specimens showed that significant hardening takes place on cast A356-T6 aluminum alloy during cyclic loading.
3. Fracture surfaces of the specimens under axial fatigue tests indicated that in almost all specimens fatigue cracks originated from porosity. However, contrary to many reports in which the fatigue cracks originated from pores at or near the specimen surface, it was observed that the fatal pores were randomly distributed in the entire cross section.
4. Considering the fatigue life data, significant scatter was observed in fatigue life under axial and rotating bending tests, while classification of the specimens based on the maximum defects detected through X-ray radiography test was not reliable, as confirmed by comparison between the fatal defects size measured on fracture surfaces at different pre-defined porosity levels.
5. The fatigue life of the large specimens under fully-reversed condition was shorter than that of small specimens by one order of magnitude. This is attributed to larger defect size in large specimens in comparison to small specimens.
6. The fatigue life of the specimens under tension-tension fatigue test was shorter than that under fully-reversed fatigue tests with the same stress amplitude and Smith-Watson-Topper (SWT) approach was quite accurate in predicting the fatigue life with the applied mean stress.

7. The fatigue life of the specimens under rotating bending was longer by a factor of 5 than that under axial loading, which is attributed to stress gradient effect and smaller stressed volume under rotating bending.
8. Statistical analysis of fatigue life at different stress levels revealed that both lognormal and Weibull distribution can fit the experimental data, however, based on Anderson-Darling test lognormal distribution is a better representative of the experimental data.
9. Studying the fracture surfaces of the specimens revealed that at a given stress level, the larger defects lead to shorter life, which shows that the defects are the main cause of scatter in fatigue life.
10. Taking the fatigue performance of small specimens as the reference, the fatigue behavior of large specimens and under rotating bending condition could be predicted reasonably well by estimating the fatigue strength using the maximum defect size within the specimens and updating the Basquin exponent with regard to the estimated fatigue strength at the fatigue life of 10^7 cycles.

Table 4.1. Monotonic tension properties of cast aluminum alloy for small and large specimens.

Specimens	Porosity	E (GPa)	σ_y	σ_u	Elongation	K (MPa)	n
Small	1	75.5	206	346	4.2	685	0.195
Small	1	75.6	200	348	5.1	688	0.199
Small	2	74.8	205	355	3.7	769	0.214
Small	2	70.0	195	339	3.7	708	0.208
Small	3	72.2	182	355	5.9	718	0.224
Small	3	73.8	203	339	3.5	697	0.020
Small	4	72.1	198	330	3.2	724	0.212
Small	4	69.0	217	326	2.0	758	0.202
Large	3	74.6	157	295	2.9	817	0.272
Large	3	73.4	151	263	1.8	793	0.275

Table 4.2. Defect size range measured on fracture surfaces of small and large specimens at different porosity levels (the measurements are in μm).

Loading Condition	Small Specimens				Large Specimens	
	Porosity level 1	Porosity level 2	Porosity level 3	Porosity level 4	Porosity level 1	Porosity level 3
axial loading	84-463	67-337	93-578	47-571	252-1274	408-1141
Rotating Bending	67-233	-	-	80-252	-	-

Table 4.3. The results of Anderson-Darling test for log-normal and Weibull distributions.

σ_a(MPa)	A^2 (Log-normal)	A^2 (Weibull)
Small specimens, Axial, R = -1		
225	0.456	0.485
200	0.287	0.384
185	0.210	0.300
170	0.364	0.339
155	0.428	0.680
140	0.374	0.681
125	0.368	0.559
Large specimens, Axial, R = -1		
225	0.266	0.413
200	0.345	0.426
170	0.271	0.249
150	0.531	0.602
125	0.135	0.172
100	0.619	0.756
Small specimens, Axial, R = 0		
160	0.208	0.353
140	0.311	0.283
120	0.563	0.684
105	0.317	0.480
85	0.138	0.201
Small specimens, Rotating Bending		
225	0.382	0.611
200	0.629	0.613
175	0.3899	0.5642

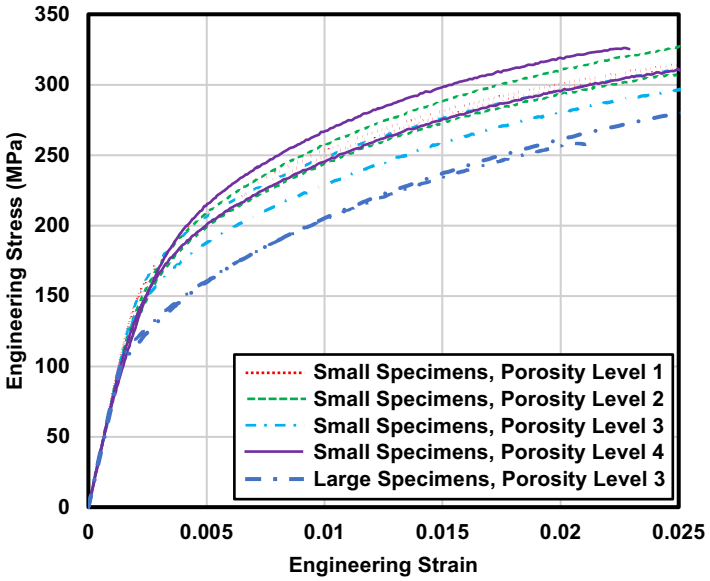

Figure 4.1. Comparison of monotonic stress-strain behavior of small and large specimens.

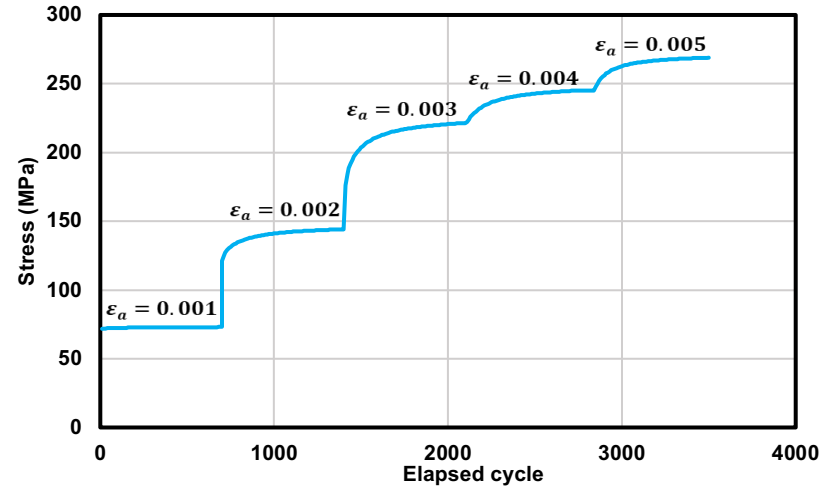

(a)

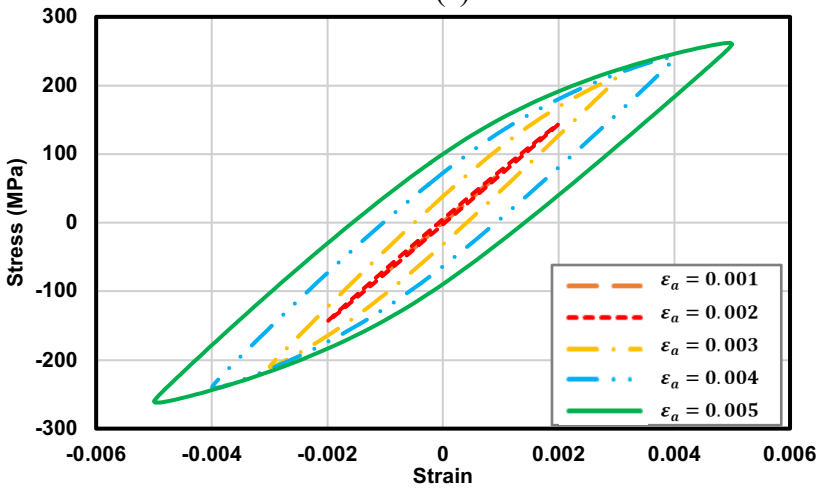

(b)

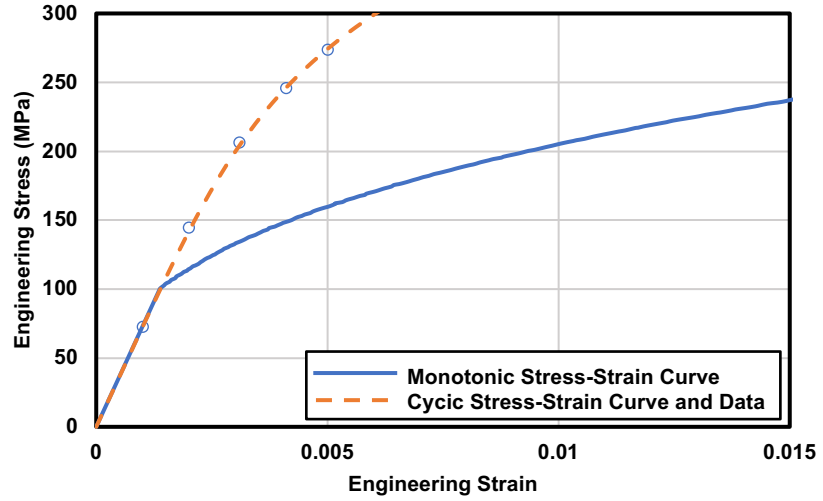

(c)

Figure 4.2. (a) Variation of stress vs elapsed cycle during cyclic step test; (b) Stable stress-strain hysteresis loops in different strain amplitude levels; (c) Comparison of monotonic and cyclic stress-strain curves.

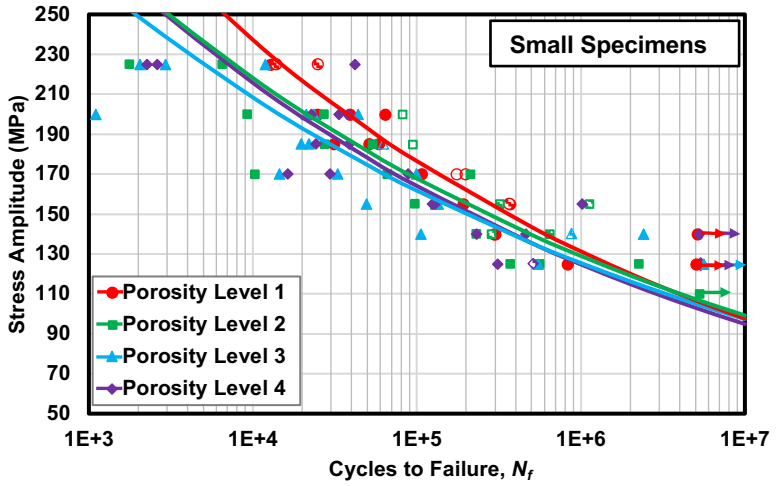

(a)

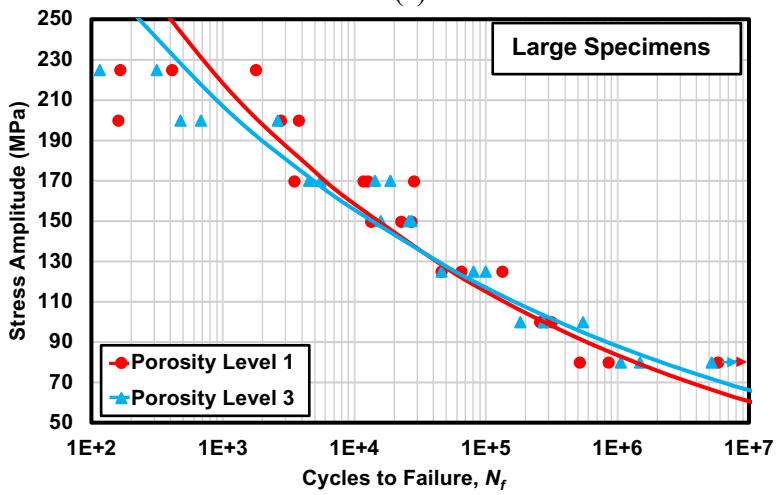

(b)

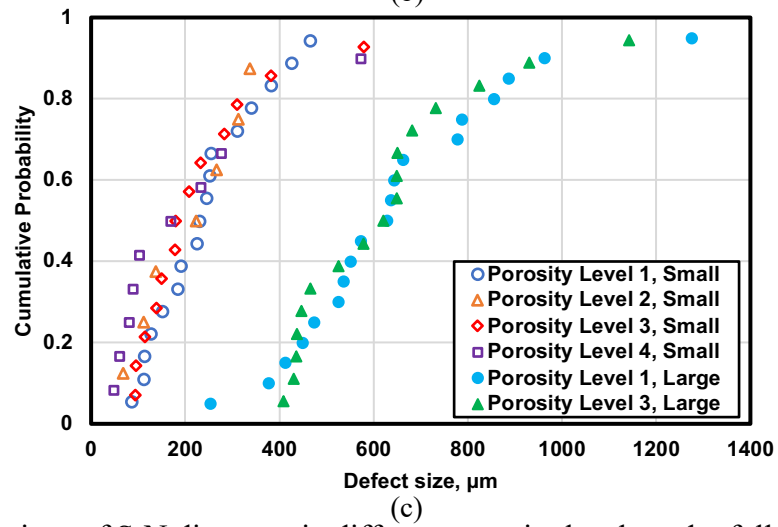

(c)

Figure 4.3. Comparison of S-N diagrams in different porosity levels under fully reversed axial loading, (a) small specimens, (b) large specimens (solid marks: failure at internal porosity; hatched mark: failure at seam location; hollow mark: failure at the surface), (c) The distribution of measured defect on the fracture surfaces at different porosity levels on small and large specimens.

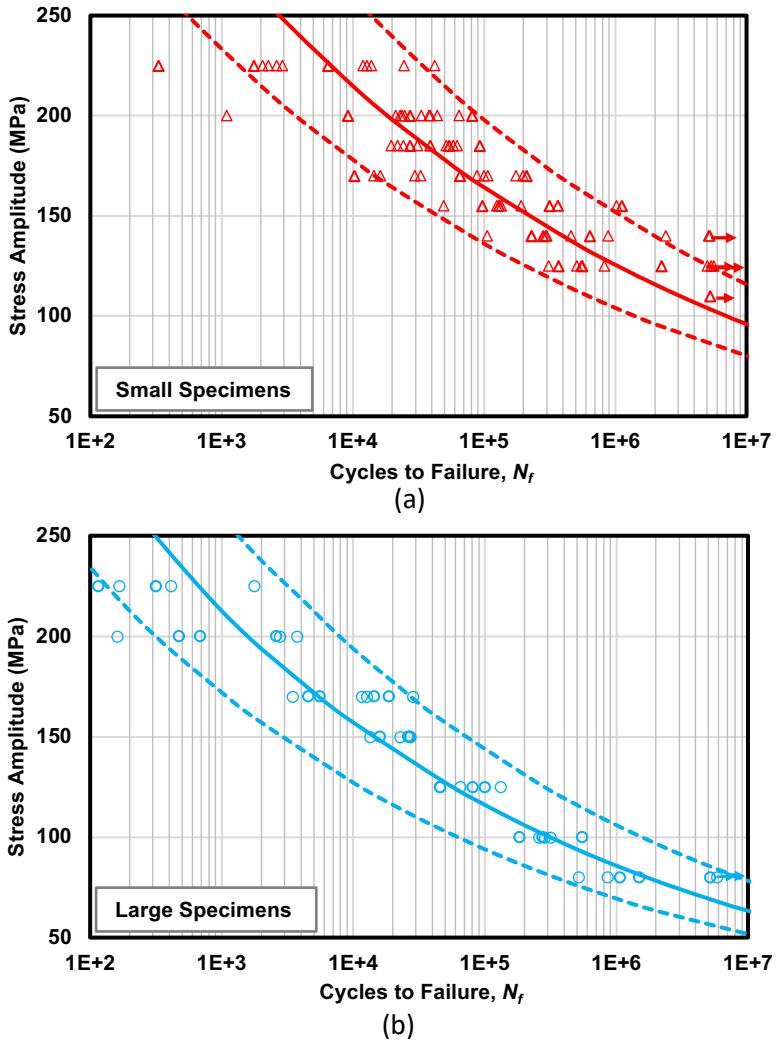

Figure 4.4. Fatigue performance of (a) small specimens, and (b) large specimens under fully-reversed axial loading condition (solid and dashed lines indicate the least square fit and the scatter bands of ±5).

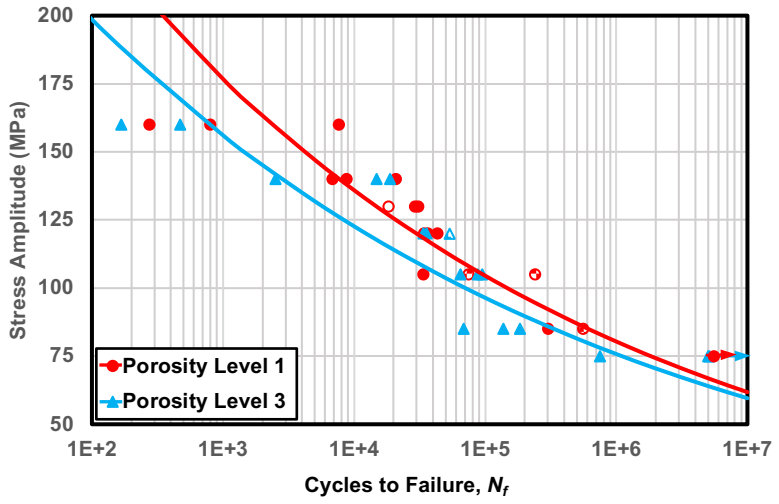

(a)

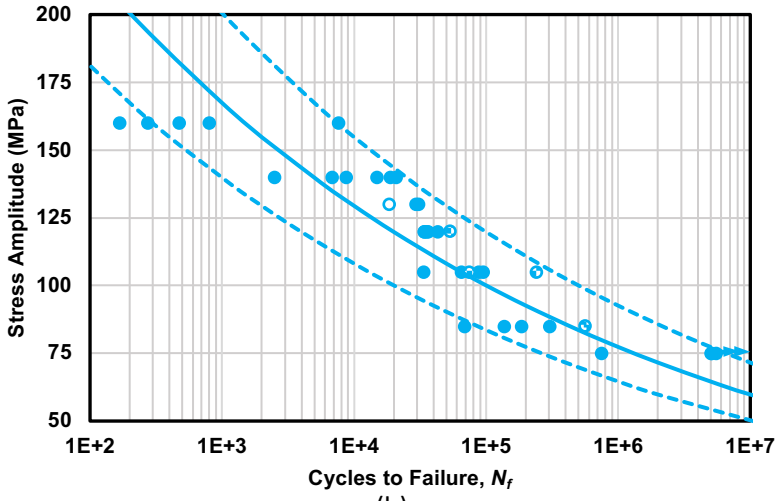

(b)

Figure 4.5. Fatigue test results under tension-tension ($R = 0$) loading condition, (a) considering different porosity levels; (b) considering all specimens as one porosity level. (solid marks: failure at internal porosity; hatched mark: failure at seam location; hollow mark: failure at the surface).

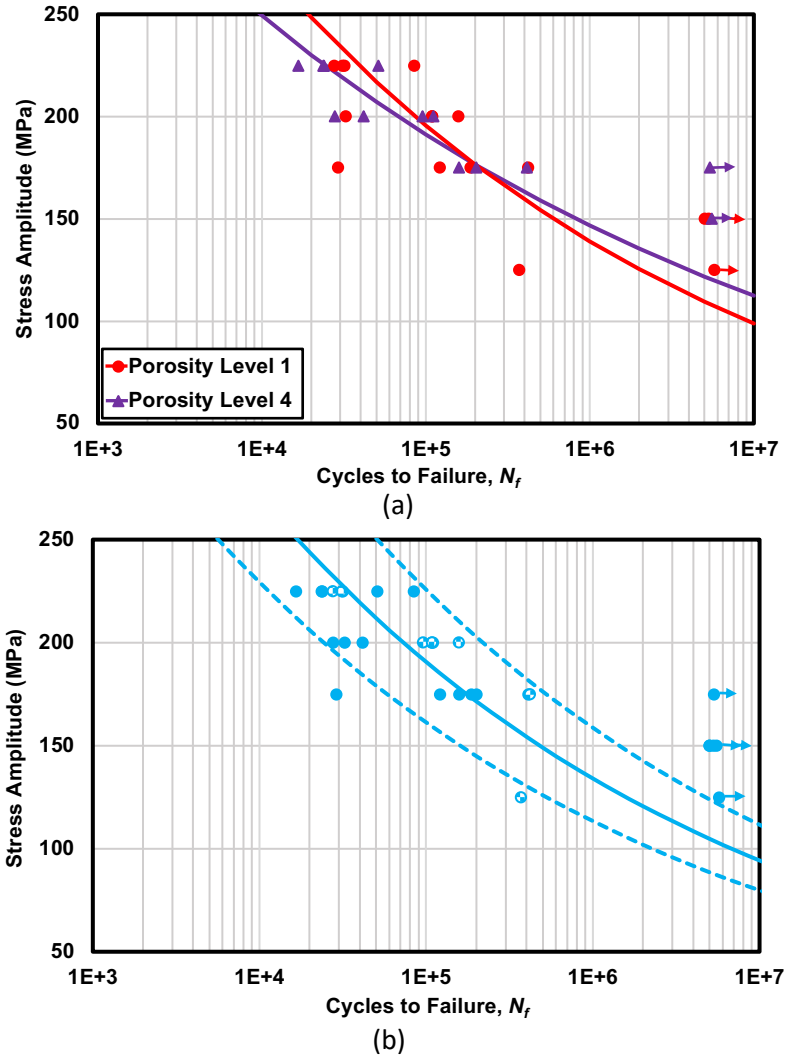

Figure 4.6. Fatigue behavior of small specimens under rotating bending loading condition, (a) considering different porosity levels; (b) considering all specimens as one porosity level (solid marks: failure at internal porosity; hatched mark: failure at seam location).

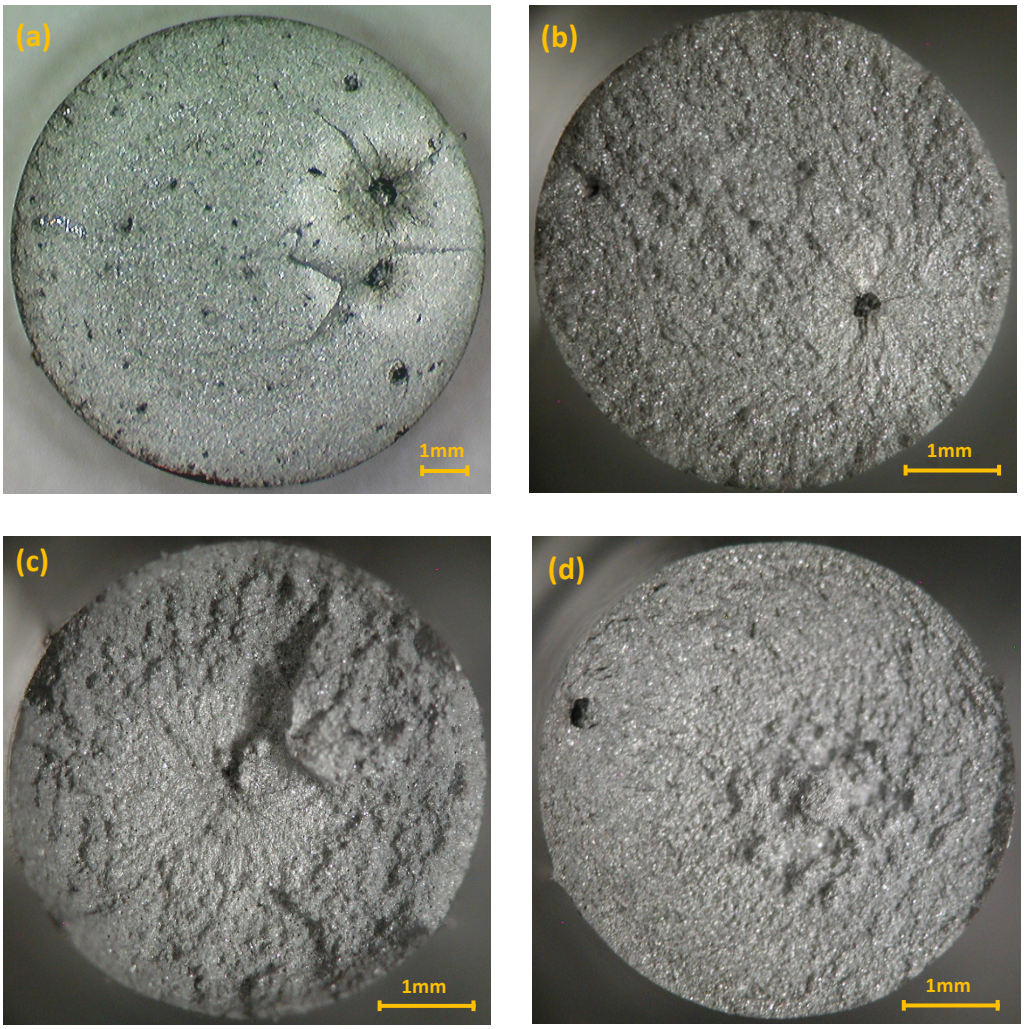

Figure 4.7. Typical fracture surfaces of the specimens failed under different loading conditions; (a) large and (b) small specimens under fully-reversed axial loading, (c) small specimen under axial loading (R = 0), and (d) small specimen under rotating bending condition.

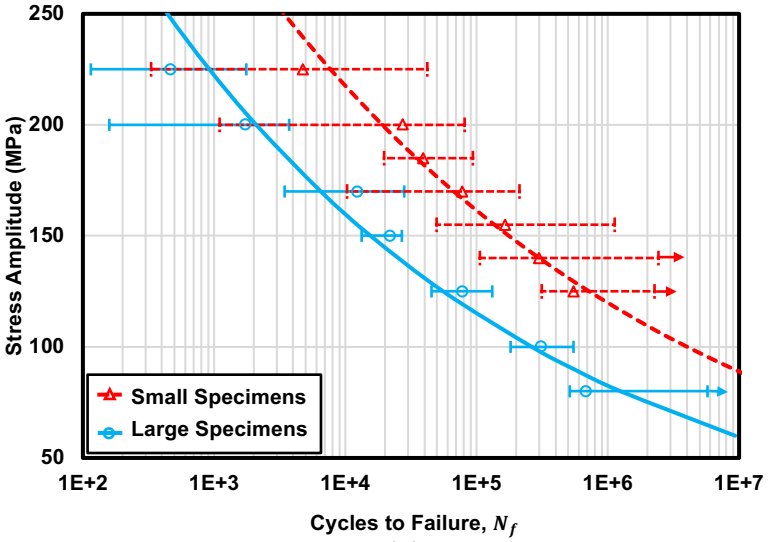

(a)

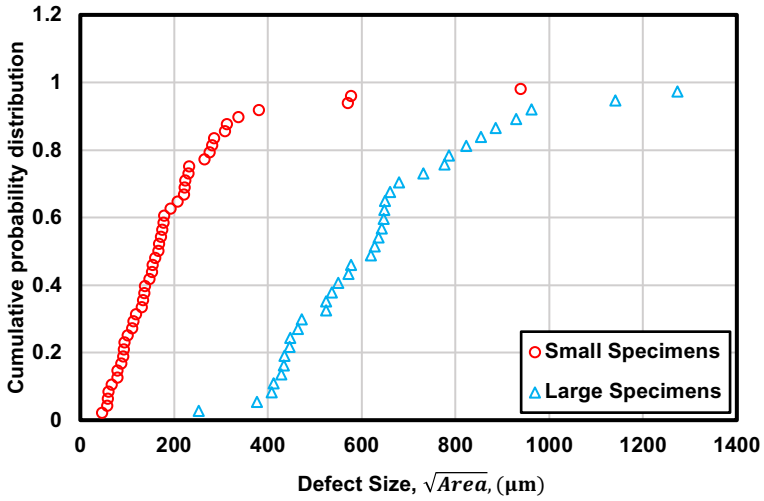

(b)

Figure 4.8. (a) Comparison of fatigue behavior of small and large specimens under fully-reversed axial fatigue tests (the horizontal bars indicate the scatter in fatigue life at different stress levels), (b) Comparison of defect size distributions in small and large specimens observed on fracture surfaces.

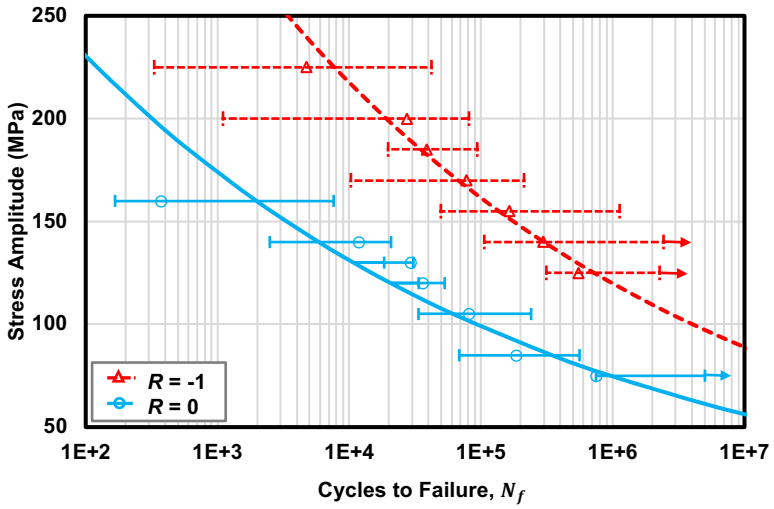

Figure 4.9. Comparison of fatigue behavior of small specimens under axial fatigue tests at $R = 0$ and $R = -1$. The horizontal bars indicate the scatter in fatigue life at different stress levels.

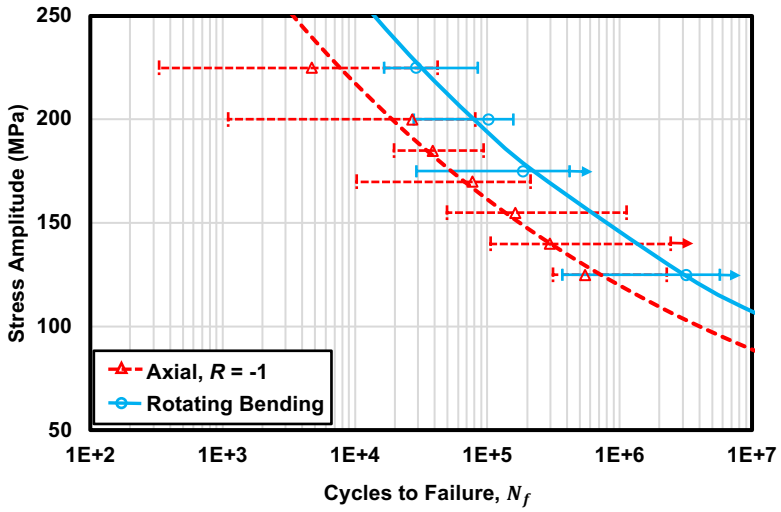

Figure 4.10. Comparison of fatigue behavior of small specimens under fully-reversed tension-compression and rotating bending conditions using the median fatigue life at each stress level. The horizontal bars indicate the scatter in fatigue life at different stress levels.

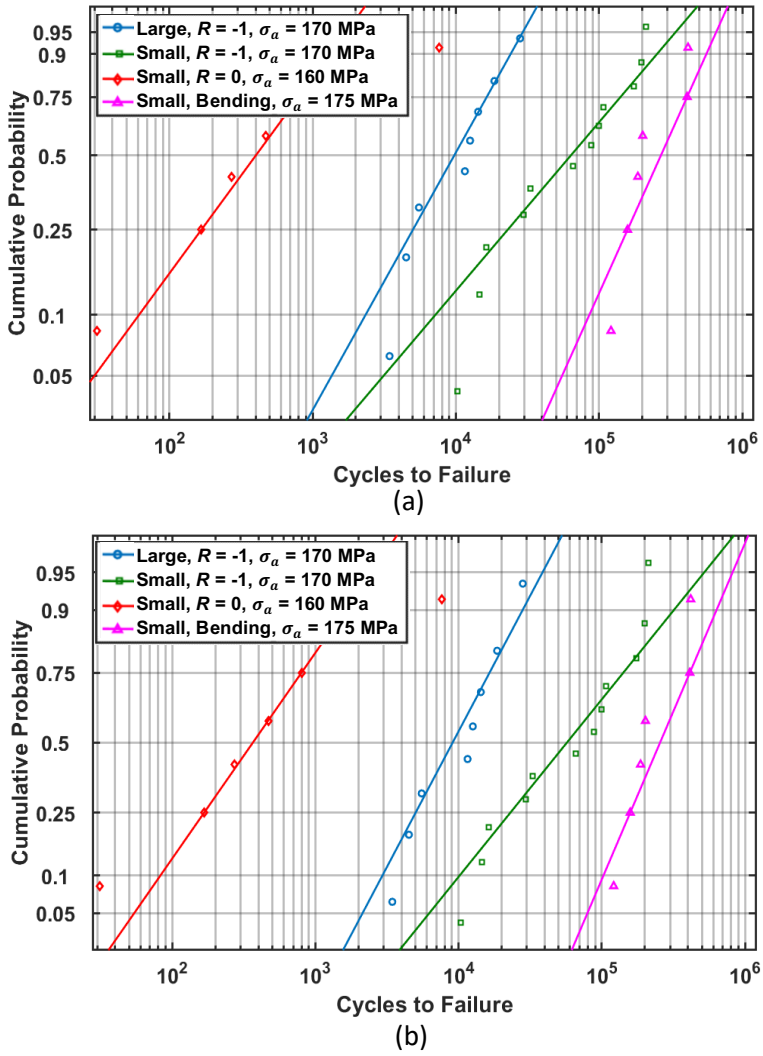

Figure 4.11. (a) Weibull, and (b) Log-normal distribution plots for large and small specimens under different loading conditions.

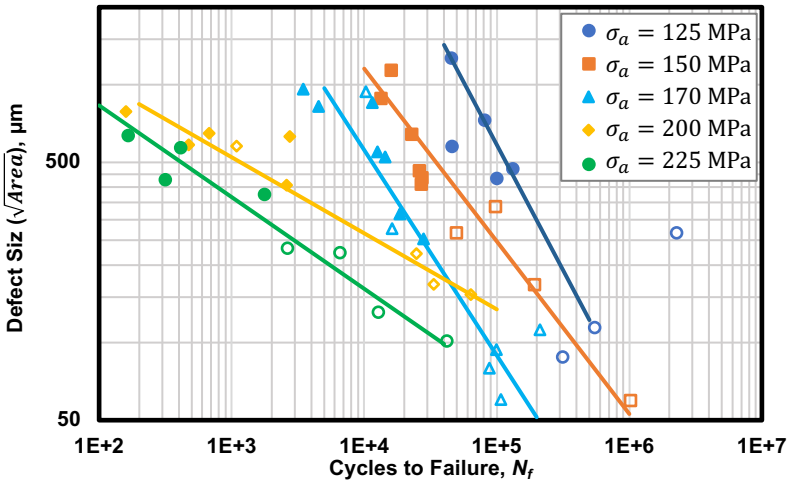

Figure 4.12. Comparison of the effect of measured pore size on fatigue life under fully reversed axial loading at different stress levels (solid/hollow marks represent defects in large/small specimens).

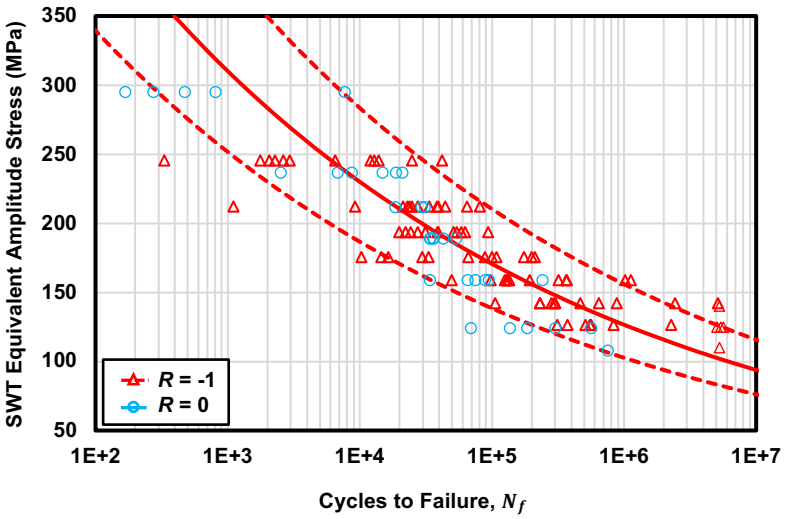

Figure 4.13. Correlation of fatigue data of small specimens under axial loading at $R = 0$ and $R = -1$ using SWT parameter for mean stress correction.

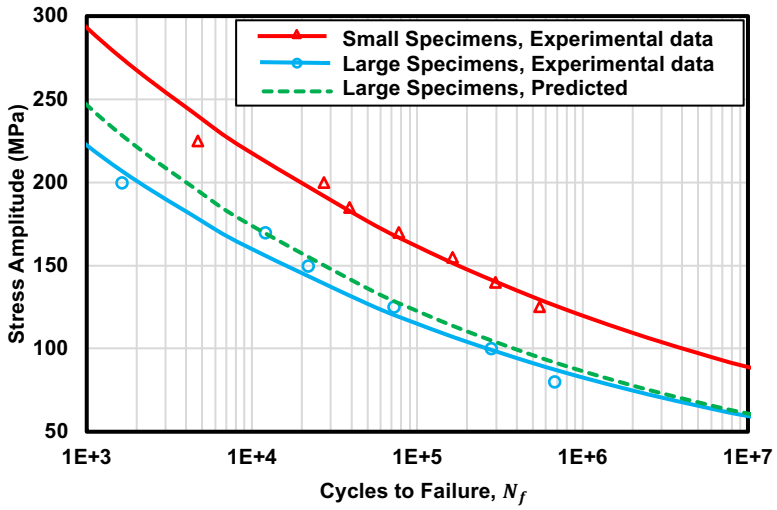

Figure 4.14. Comparison of predicted and experimental stress-life curves for large specimens under fully-reversed axial loading.

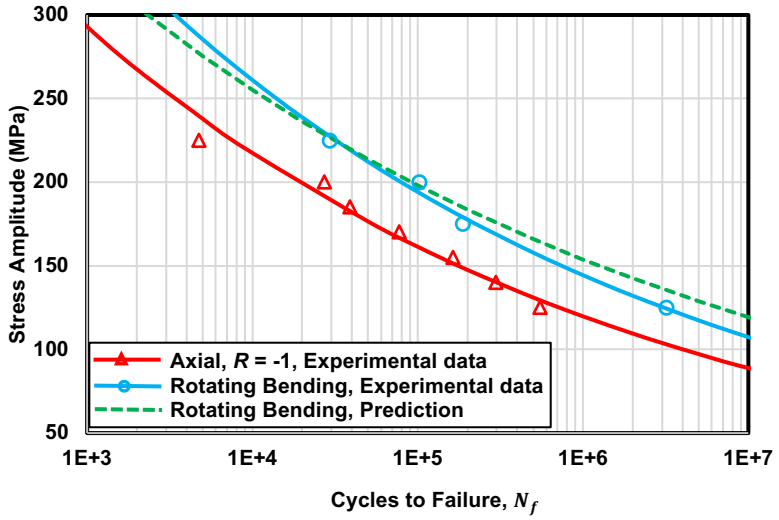

Figure 4.15. Comparison of predicted and experimental stress-life curves for small specimens under rotating bending loading condition.

Chapter 5

Fatigue Life Prediction under Uniaxial Stress State Based on Porosity Characteristics

5.1. Introduction

The objective of this chapter is to study the fatigue behavior of cast aluminum alloy, as an illustrative material containing defects, and to evaluate and model the fatigue lives using the fracture mechanics approach. Using the fatigue test data from Chapter 4, fatigue lives of the material were evaluated and modeled considering the effect of specimen size, stress gradient, and mean stress. Fatigue strengths under different loading conditions or specimen sizes were predicted using the maximum defects within the high stressed volume of the specimens. Furthermore, fatigue lives were predicted using both small and long crack growth models and the predictive capability of these models in evaluating the fatigue performance of defect containing materials was compared based on the size fatal defects measured from the fracture surfaces. As the fatal defects may vary from one specimen to the other, the maximum defect size within the specimens was estimated by extreme value statistics. Fatigue life of the specimens was also predicted using the estimated maximum defect size. This approach makes it possible to estimate the maximum defect size in a

component of the desire volume and predict the fatigue behavior without the knowledge of the actual fatal defect size.

5.2. Experimental Test Data

In Chapter 4 the effects of defects, section size, mean stress and stress gradient were investigated using the fatigue test results under uniaxial loading as well as rotating bending. In the results of these tests for small and large specimens, which are illustrated in Figures 4.4, 4.5(b) and 4.6(b), considerable scatter in fatigue life can be seen for all specimen size and loading conditions, such that the fatigue data in small and large specimens under different loading conditions are within the factors of 5 scatter bands from the mean life values. Studying the fracture surfaces of the fatigue specimens revealed that in almost all specimens failed under axial fatigue tests the fatigue crack initiated from internal porosities, while in rotating bending fatigue tests the fatal pores were located at or near the surface. This is because under axial loading all cross section of the specimen experiences approximately uniform high stress, while under rotating bending high stress is only exerted to the region near the surface.

The scatter in fatigue life in defect containing materials is attributed to scatter in fatal defects size within the specimens. The effect of defect size on fatigue life at different stress levels under fully-reversed axial loading condition was presented in Figure 4.12, using square root of actual area as defect parameter. As can be seen in this figure, at a given stress amplitude level larger defects lead to shorter fatigue lives. Gao et al. [32] used finite element analysis to study the effect of defect size on stress and strain concentration around defects and demonstrated that the maximum stress and strain concentrations around large pores are higher than those for small ones.

In this chapter, the fatigue life data under different loading conditions are used to evaluate and model the fatigue performance. To achieve this goal, the defects size on the fracture surfaces of fatigue specimens were measured using digital optical microscope. Similar to Chapter 3, three different defect parameters were defined for defect size including maximum Feret diameter, square root of the actual area of the defect, and square root of an ellipse fitted to the defect on fracture surface of the specimen. Using these defect parameters in evaluating the defects measured from both metallography (2D) and micro-CT micrographs (3D) revealed that the larger the defects, the more deviated the defect parameters from an ideal spherical or circular defect (Chapter 3), as shown in Figure 3.4. This is associated with the shrinkage porosities which are more tortuous as the size of pores become larger.

Using extreme value statistics (EVS), the maximum defects size within the specimens can be estimated. This issue has been discussed in Chapter 3, where the maximum defect size has been estimated using both metallography and μCT data and compared with the maximum defect size observed on fracture surface of the specimens failed under fatigue tests. The estimated maximum defect size within the specimens using metallography and μCT data are compared in Figure 5.1, which shows that the maximum defect size estimated by extreme value statistics using both μCT data (3D) and metallography data (2D) is in good agreement with the maximum observed defect on fracture surfaces. These estimates are used in current study for fatigue life prediction under different loading conditions.

5.3. Fatigue Crack Growth Behavior

Considering the size of critical defects in cast aluminum alloys, which are typically between 100-1500 μm, the cracks initiating from these defects are in the range of physically small

cracks. It has been shown that physically small fatigue cracks do not behave in accordance with conventionally acquired long crack growth data. When stress intensity factor, ΔK, is used for evaluation of crack growth rates, the small cracks propagate at ΔK values less than long crack threshold, ΔK_{th}, and even grow faster than long cracks at equivalent ΔK levels. This is because as the crack propagates, a wake of plastically deformed material develops around the crack and causes the faces of the crack come into contact during unloading before the point of zero load is reached (plasticity-induced crack closure). In addition, the contact between the crack surfaces as a result of rough crack morphology (roughness-induced crack closure) can reduce the driving force for crack propagation. However, when the cracks are small they do not experience the same level of crack closure which results in faster growth rate. Consequently, as the crack lengths become smaller, the values of ΔK_{th} decreases.

El-Haddad et al. [52] proposed a method to compensate the difference between ΔK_{th} of small and long cracks by artificially increasing the physically small crack length, as follows:

$$\Delta K_{th}\sqrt{a_0 + a} = \Delta K_{th,l}\sqrt{a} \tag{5.1}$$

Consequently, the fatigue limit for crack containing material can be obtained by:

$$\Delta\sigma_{th} = \Delta K_{th,l}/\sqrt{\pi(a + a_0)} \tag{5.2}$$

where ΔK_{th} and $\Delta K_{th,l}$ are the crack growth threshold for small and long cracks, respectively, $\Delta\sigma_{th}$ is the fatigue limit range of a materials containing a crack of length a, and a_0 is the intrinsic crack length. Considering Equation (5.2), it is inferred that as the crack length increases, the fatigue limit of the materials decreases. This issue is well described by Kitagawa-Takahashi diagram in which the fatigue limit is also described as a function of small defects within the material.

Another approach to considering the effect of small cracks (defects) on the fatigue limit is the Murakami approach, in which the fatigue limit is related to both the hardness and maximum

defect size within the material. Murakami [1,29] showed that for a material containing a crack or defect with an irregular shape, ΔK can be estimated by:

$$\Delta K = Y\Delta\sigma\sqrt{\pi\sqrt{A}} \tag{5.3}$$

where $\sqrt{A}$ is Murakami's defect parameter expressing the square root of area of defects on the plane perpendicular to the load direction used for representing the crack (defect) size, and Y is the geometry factor equal to 0.65 for surface cracks. Using $\Delta\sigma_{th}$ in Equation (5.3) will result in ΔK_{th}. Murakami and Endo [38] also showed that for small cracks the threshold is proportional to crack size, $\sqrt{A}$, as given by:

$$\Delta K_{th} \propto \left(\sqrt{A}\right)^{1/3} \tag{5.4}$$

Combining Equations (5.3) and (5.4), they suggested that for small cracks:

$$\Delta\sigma_{th} = \frac{C}{Y\left(\sqrt{A}\right)^{1/6}} \tag{5.5}$$

where C is the material constant depending on hardness and defect location.

5.4. Fatigue Limit Prediction

In infinite-life-design approach, industrial components are designed such that the maximum local stress level does not exceed the fatigue limit of the material determined for the high cycle regime, where the fatigue limit is defined as the threshold stress below which cracks will not propagate. However, for the case of cast aluminum alloys that do not exhibit a fatigue limit, fatigue strength is typically identified for a stress level associated to a lifetime of 10^7 cycle [1,56].

Following Murakami's approach explained in section 5.3, the fatigue limit of the material containing surface defects can be estimated as:

$$\Delta\sigma_{th} = \frac{1.43(HV+120)}{(\sqrt{A})^{1/6}} \tag{5.6}$$

where *HV* is Vicker's hardness of the material. This model is commonly used due its simplicity and easy application in design. However, it has been reported that estimating the fatigue limit or long life strength using Equation (5.6) is non-conservative for non-ferrous metals, including aluminum alloys [53,54]. In order to address this problem, Noguchi et al. [55] proposed that the fatigue strength of non-ferrous alloys at 10^7 cycles can be estimated by modifying Murakami's model using the ratio of elastic modulus of non-ferrous alloy, i.e. aluminum alloy, E_{Al}, to that of steel, E_{St}, as given by:

$$\Delta\sigma_{th} = \frac{1.43(HV+120\times\frac{E_{Al}}{E_{St}})}{(\sqrt{A})^{1/6}} \tag{5.7}$$

Having studied the fatigue strength of cast aluminum specimens containing artificial drilled holes, Ueno et al. [56] also proposed the following relation for estimating the long life fatigue strength of aluminum alloys:

$$\Delta\sigma_{th} = \frac{1.43(HV+75)}{(\sqrt{A})^{1/6}} \tag{5.8}$$

Tajiri et al. [57] also used this model for fatigue limit prediction of cast aluminum alloys and reported reasonable predictions. In addition, it was shown in Chapter 3 that for cast aluminum alloy, SWT parameter is an appropriate parameter for mean stress correction. Therefore, for the cases where mean stress is involved the fatigue limit can be estimated by:

$$\Delta\sigma_{th,R} = \Delta\sigma_{th,-1}\sqrt{\frac{1-R}{2}} \tag{5.9}$$

where *R* is the stress ratio, $\Delta\sigma_{th,R}$ is the fatigue strength when mean stress is involved, and $\Delta\sigma_{th,-1}$ is the fatigue strength under fully-reversed loading conditions calculated by Equations (5.6-5.8).

In Equations (5.6-5.8), $\sqrt{A}$ is the maximum defect size within the specimens. This parameter can be estimated using extreme value statistics for a prospective volume under high stress, i.e. typically the region experiencing at least 90% of the maximum stress. In Chapter 3 the maximum defect size within specimens were estimated as 602 and 1426 μm for small and large specimens under axial loading, respectively. Under rotating-bending conditions where there is a stress gradient, the maximum defects in the volume under more than 90% of maximum stress was estimated as 287 μm. Using these estimates for the maximum defects within the specimens, as well as the hardness of small and large specimens measured as 97 and 92 Vickers, respectively, the fatigue limit under different loading conditions can be predicted.

The experimental fatigue strength of the specimens associated with the fatigue life of 10^7 cycles under different loading conditions can also be computed using *S-N* data of the specimens, shown in Figures 4.4, 4.5(b) and 4.6(b). Comparisons of experimental fatigue limit with the predicted values using Murakami, Noguchi, and Ueno models under different loading conditions are illustrated in Figure 5.2. As can be seen in this figure, the fatigue limit predicted by Ueno model is in very good agreement with the experimental values, while the predictions using Murakami model are overestimated.

5.5. Fatigue Life Predictions and Modeling

Fatigue life prediction of components containing defects can be performed following damage tolerant approach using crack growth rate models and the initial crack (flaw) size. In this approach the defects can be considered as initial cracks within the specimens or components. Although a pore is not a crack at first, once a small crack is initiated at its edge, then the effective crack size will include that of the pore size.

The total fatigue life of a component subjected to cyclic loadings incorporates the number of cycles necessary for fatigue crack nucleation, microstructurally small crack growth, physically small crack growth, and long crack growth until failure. However, regarding the size of defects in castings, it is generally assumed that the entire fatigue life is spent on physically small crack growth and long crack growth. On the other hand, it is argued that most of the fatigue life in defect containing materials is spent on growing physically small cracks which may grow faster than long cracks. Therefore, prediction of fatigue life without considering small crack behavior may have a significant impact on the resulting life predictions. Nevertheless, for fatigue life prediction of defect-containing materials both long and small crack growth models have been used in the literature. In this study, the predictive capability of both long and small crack growth models for evaluating the fatigue life of the cast aluminum alloy investigated is compared.

5.5.1. Long crack growth model

In predicting the fatigue life using long crack growth models, it is assumed that the crack nucleation life is negligible and the fatigue life can be computed by integrating Paris equation from the initial flaw size, a_i, to critical size, a_f. The stress intensity factor of the defect containing materials was defined by Murakami and Endo [29] using the square root of projected area of the defect ($\sqrt{A}$) as the defect parameter (see Equation 5.3). Other defect parameters such as square root of the area of the fitted ellipse or maximum Feret diameter can also be used instead. However, in case of maximum Feret diameter, half crack length should be considered in SIF calculation considering defects as internal cracks.

In Equation (5.3), Y is the geometry factor that can be determined using the following relations for a semi-circular crack at the surface of a cylindrical specimen of diameter d for uniaxial and rotating bending conditions [19,91]:

$$Y_{axial} = 0.67 - 1.24\left(\frac{a_i}{d}\right) + 28.0\left(\frac{a_i}{d}\right)^2 - 162.4\left(\frac{a_i}{d}\right)^3 + 472.2\left(\frac{a_i}{d}\right)^4 - 629.6\left(\frac{a_i}{d}\right)^5 + 326.1\left(\frac{a_i}{d}\right)^6 \quad (5.10)$$

$$Y_{bending} = 0.677 - 2.982\left(\frac{a_i}{d}\right) + 19.93\left(\frac{a_i}{d}\right)^2 - 46.94\left(\frac{a_i}{d}\right)^3 + 40.37\left(\frac{a_i}{d}\right)^4 \quad (5.11)$$

The modified Paris equation for long crack growth behavior is written as [9]:

$$\frac{da}{dN} = C(\Delta K_{eff}{}^m - \Delta K_{eff,th}{}^m) \quad (5.12)$$

where the crack closure effect has been considered using the effective stress intensity factor range defined by:

$$\Delta K_{eff} = K_{max} - K_{op} \text{ if } K_{min} < K_{op} \quad (5.13)$$

$$\Delta K_{eff} = K_{max} - K_{min} \text{ if } K_{min} \geq K_{op} \quad (5.14)$$

where opening stress intensity factor is considered as [6]:

$$\begin{aligned} K_{op} &= 3.4 + 3.8R^2 && R > 0 \\ K_{op} &= 3.4(1 + R) && -1 \leq R \leq 0 \\ K_{op} &= 0 && R < -1 \end{aligned} \quad (5.15)$$

C and m are material constants which for A356-T6 have been reported as 1.5×10^{-11} m/cycle and 4.2, respectively. The threshold stress intensity factor, $\Delta K_{eff,th}$, is also given as 1.3 MPa$\sqrt{\text{m}}$ for this material [19]. Kujawski [92] proposed a new mechanical crack driving force parameter for ΔK_{eff} by considering only the positive part of the range of the applied SIF. This parameter is called K^* and can also consider the R-ratio effect:

$$K^* = (K_{max})^{\alpha}(\Delta K^+)^{1-\alpha} \quad (5.16)$$

where ΔK^+ is the positive part of the range of the applied SIF, K_{max} is the corresponding maximum value of the applied SIF, and $0 \leq \alpha \leq 1$ is a material parameter, which accounts for the relation between cyclic and monotonic plastic zone and may depend on cyclic hardening or softening behavior of the material [92]. It was shown that for the case of Al alloys tested in ambient environment α is close to 0.5. Therefore, the effective crack growth driving force is calculated as follows:

$$K^* = (K_{max}\Delta K^+)^{0.5} \tag{5.17}$$

Considering this parameter as ΔK_{eff} in Equation (5.12) and integrating from the initial pore size, $\sqrt{A}$, measured from the fracture surfaces of the broken specimens to the critical crack size, a_f, computed by $a_f = \frac{1}{\pi}\left(\frac{K_{1c}}{Y\sigma_{max}}\right)^2$ predicts the fatigue life under a given stress level, while the value of K_{1c} for this materials was considered to be 17.3 MPa$\sqrt{\text{m}}$ [19].

Comparisons of predicted life and experimental fatigue lives for different specimen sizes and loading conditions are shown in Figure 5.3(a). As can be seen in this figure, the fatigue lives predicted by the modified Paris equation are non-conservative, especially at higher stress levels. One reason for nonconservative prediction of fatigue life may be higher crack growth rates in small cracks in comparison to long cracks and this causes longer life to be predicted by the long crack growth model. Secondly, at high stress levels there is significant local plastic deformation which accelerates the crack growth rates, but it is not taken into account in LEFM-based models. Similar results were also reported by Couper et al. [6] and Skallerude et al. [9] who used the long crack growth model for prediction of fatigue life in cast aluminum alloys under uniaxial loading condition.

5.5.2. Short crack growth models

5.5.2.1. Modified Long crack growth models with El-Haddad parameter

As the defects size in cast aluminum alloys are in the range of 100-1500 μm, it is believed that the cracks initiating from defects are in the range of small cracks with less crack closure and higher growth rate than long cracks. One approach to consider the higher growth rate in small cracks is assuming a longer crack by extending the crack length artificially using the intrinsic crack length, initially defined by El-Haddad. Therefore, the stress intensity factor for small cracks can be considered as:

$$\Delta K = Y\Delta\sigma\sqrt{\pi(a + a_0)} \tag{5.18}$$

Using this relation in modified Paris equation will consider the behavior of the crack initiating from the pores as small cracks. Considering the fatigue strength amplitude of this material at 10^7 cycles around 90 MPa under fully-reversed uniaxial loading condition [87,88], the intrinsic crack length based on $\Delta K_{th} = 1.3\ \text{MPa}\sqrt{\text{m}}$ [19] is computed as 157 μm for this material.

Following the abovementioned approach, the fatigue life was predicted using modified Paris equation for different specimen sizes and loading conditions. In prediction of fatigue life the crack growth model was integrated from an initial crack length as the pore size, $\sqrt{A}$, measured on the fracture surfaces of the broken specimen to the finial crack length of the small crack typically around 2 mm.

Comparison of the experimental fatigue life data and those predicted by the modified Paris equation with El-Haddad parameters are demonstrated in Figure 5.3(b). As can be seen in this figure, modifying the long crack growth model to consider small crack growth behavior using the intrinsic crack length enhances the predictive capability of LEFM-based long crack model at low

stress levels. However, the fatigue lives predicted at high stress levels are still nonconservative. Again, this is due to the limitation of LEFM in considering plastic deformation at high stress levels.

5.5.2.2. Hartman-Schijve model

Hartman-Schijve model is a modification of Forman equation [93] by relating the crack growth rate to the amount of ΔK exceeding the fatigue threshold ΔK_{th} of the material, as given by:

$$\frac{\mathrm{d}a}{\mathrm{d}N} = \frac{C(\Delta K - \Delta K_{th})^m}{(1-R)K_C - \Delta K} \tag{5.19}$$

where K_C is the fracture toughness. Later, Jones et al. [94] used this concept and proposed a modification to this model and showed that the crack growth rates at different mean stress levels correlate well using the following model:

$$\frac{\mathrm{d}a}{\mathrm{d}N} = D\left(\frac{\Delta K - \Delta K_{thr}}{\sqrt{1-K_{max}/A}}\right)^m \tag{5.20}$$

in which ΔK_{thr} is the fatigue threshold and the subscript *r* has been used to show that it is a function of stress ratio as well as crack length. The exponent m is a constant corresponding to the slope of da/dN vs $\left[(\Delta K - \Delta K_{thr})/\sqrt{1 - K_{max}/A}\right]$, while A and ΔK_{thr} are chosen to best represent the experimental crack growth data. D is also the y-axis intercept at 1 MPa$\sqrt{\mathrm{m}}$ when the data are plotted in log-log scale [94,95]. Jones et al [94] applied this model to different crack growth data in different materials and found that the value of m is very close to 2 and the constant D can also be reasonably approximated by $D = 0.036/E\sigma_y$, where E and σ_y are in MPa.

They also showed that the small crack growth behavior can be predicted using the calculated constants D, A, and m for long cracks, but as the small cracks grow below the threshold of long cracks, different values of ΔK_{thr} are required for small cracks compared to the long cracks.

Therefore, in cases where small crack growth data are not available, they can be predicted using long crack growth data, but with different values for fatigue crack growth threshold.

In order to obtain the materials constants in Equation (5.20), the long crack growth data for A356-T6 with similar secondary dendrite arm spacing (SDAS) with the material studied in this work was used from [9]. Figure 5.4(a) illustrates Harman-Schijve representation of long crack growth data for this material under stress ratio of 0.1, indicating the value of D and m equal to 1.101×10^{-9} and 1.81, respectively, while A and ΔK_{thr} were determined as 20 MPa$\sqrt{\text{m}}$ and 5 MPa$\sqrt{\text{m}}$, respectively. The comparison of the experimental crack growth data with the Equation (5.20) using the determined constants are shown in Figure 5.4(b).

Having obtained the material constants, the small crack growth data was predicted. It has been reported that the fatigue threshold of this materials for small cracks under stress ratio of 0.1 is around 2.5 MPa$\sqrt{\text{m}}$ [96]. Therefore, the small crack growth behavior of this materials can be modeled by:

$$\frac{\mathrm{d}a}{\mathrm{d}N} = 1.101 \times 10^{-9} \left(\frac{\Delta K - 2.5}{\sqrt{1 - K_{max}/20}} \right)^{1.81} \tag{5.21}$$

Comparison of the experimental data for small crack growth of this material under R = 0.1 from [46] and Equation (5.21) predictions are demonstrated in Figure 5.4(c). As can be seen, the predicted small crack growth behavior is in a reasonable agreement with the experimental data. Assuming that the fatigue cracks do not propagate in the compressive part of the load cycle and the fatigue threshold at R = 0 is approximately equal to the one at R = 0.1, Equation (5.21) will be valid for R = -1 when only the positive part of ΔK is considered. Considering the fatal defect size on fracture surfaces, the fatigue life of the specimens can be computed by integrating Equation (5.21) from fatal defects size measured on fracture surfaces to a typical small crack length around 2 mm. The predicted fatigue life of the small and large specimens under different loading

conditions are shown in Figure 5.5. As can be seen in this figure, the predicted fatigue lives are in a reasonable agreement with the experimental lives at low stress levels. However, at high stress levels the predicted fatigue lives are underestimated. Again, this is due to limitation of LEFM in considering plastic deformation.

5.5.2.3. Modified Nisitani Model

It has been shown by Nisitani and coworkers [61,62] that in small cracks, the growth rate is a function of crack tip displacement (CTD) which is proportional to the cyclic plastic zone size at the crack tip, r_p. On the other hand, r_p is closely related to the far field stress as well as the crack length. Therefore, they proposed a small crack growth model, given by:

$$\frac{\mathrm{d}a}{\mathrm{d}N} = C\left(\frac{\sigma_a}{\sigma_y}\right)^s a \tag{5.22}$$

in which σ_y is the yield strength.

Caton et al. [21] studied the small crack growth behavior of W319 cast aluminum alloy and found a distinct effect of applied stress amplitudes on the small crack growth curves, where higher stress amplitude resulted in faster growth rates at a given ΔK level. This fact is associated with different degrees of plastic deformation at the crack tip which leads to violation of the small scale yielding assumption [61]. The same trend was also reported in literature for A356-T6 for different stress amplitude levels [97], as shown in Figure 5.6(a). Therefore, crack tip displacement, CTD, can be considered as the driving force for small crack growth which is also affected by the global deformation applied to the specimen during the loading cycle. Higher stresses cause greater deformation at the crack tip, which results in higher CTD. Therefore, Caton et al. [20,21] proposed a model considering the contribution of maximum tensile strain, ε_{max}, as well as stress amplitude σ_a and crack length, as follows:

$$\frac{\mathrm{d}a}{\mathrm{d}N} = A\left[\left(\varepsilon_{max}\frac{\sigma_a}{\sigma_y}\right)^s a\right]^t \tag{5.23}$$

They showed that this model worked well in correlating the small crack growth rate data for both coarse and fine microstructures of cast 319 aluminum alloy.

It should be mentioned that Equation (5.23) is not general enough to consider all loading conditions including different stress/strain ratios. The conducted fatigue tests by Caton et al. were in fully-reversed condition. On the other hand, Shiozawa et al. [22] studied small crack growth in cast A356-T6 aluminum alloy produced by squeeze casting and showed that the small crack growth rates obey Nisitani model (Equation 5.22) when yield strength is substituted with the ultimate strength. It was also shown in Chapter 4 that SWT equivalent stress is an effective parameter for mean stress correction of the material in this study. Therefore, in order to predict the fatigue life in the defect containing materials under different loading condition, Equation (5.22) is modified using strain-based version of SWT, as follows:

$$\frac{\mathrm{d}a}{\mathrm{d}N} = A\left[\left(E\frac{\sigma_{max}\cdot\varepsilon_a}{{\sigma_u}^2}\right)^s a\right]^t \tag{5.24}$$

where σ_u is ultimate strength.

In order to obtain the materials constants A, s, and t, the small crack growth rate data for this material were extracted for cast A356-T6 of medium SDAS (~25 μm) from [97]. Figure 5.6(b) shows the correlation of small crack growth rates for this material using Equation (5.24) under two stress amplitude levels at stress ratio of -1, assuming elastic behavior at these stress levels. Therefore, the parameters A, s, and t were determined as 7.86×10^{-3}, 2.4, and 1.24, respectively. It is noteworthy that in this study all the fatigue tests were conducted in load control condition and the strain amplitude in each stress level was calculated using the cyclic Ramberg-Osgood relation

obtained by applying the incremental step test on the specimens. The details of incremental step test to obtain the cyclic deformation behavior of this material is explained in Chapter 3.

The fatigue life of the specimens under different loading conditions was predicted by integrating the Equation (5.24) from the initial defect size, $\sqrt{A_{Actual}}$, measured on fracture surfaces to the typical size of small cracks around 2 mm. Comparisons of predicted fatigue lives with experimental lives under different loading conditions are illustrated in Figure 5.7(a). As can be seen in this figure, the fatigue lives predicted using Equation (5.24) are in a very good agreement with the experimental results. In addition, the capability of the model in predicting the fatigue life at high stress levels is better than the models used in previous sections. The discrepancy between the experimental and predicted fatigue lives at high stress levels may have resulted from the difference between the actual strain amplitude and the calculated one using the cyclic stress–strain relation. This relation was associated with the strain amplitude in stabilized condition after the hardening process was mostly completed within the material. However, in specimens failed under high stress levels the hardening process continued and stress-strain relation did not completely stabilize even when failure happened.

5.5.3. Comparing the predicted fatigue life using different defect parameters

As mentioned earlier, different defect parameters could be defined for evaluating the defects including maximum Feret diameter ($Feret_{max}$), square root of the actual area of the defect ($\sqrt{A_{Actual}}$), and square root of an ellipse fitted to the defect ($\sqrt{A_{Ellipse}}$). Using these defect parameters in evaluating the defects revealed that the larger the defects, the more deviated the defect parameters from an ideal spherical or circular defect (see Figure 3.4). However, the value of these parameters may not be the same for a given defect. Having determined these parameters

for the defects on metallography cross sections, it was observed that the average ratios of $Feret_{max}/\sqrt{A_{Actual}}$ as well as $\sqrt{A_{Actual}}/\sqrt{A_{Ellipse}}$ for the defects larger than 100 μm are ~2 and ~1.3, respectively.

To study the effect of different defect parameters on fatigue life prediction, the defect size on fracture surfaces of the broken specimens were characterized using these three defect parameters and the fatigue lives predicted using these different parameters as the initial crack size. The predicted fatigue lives shown in Figures 5.3, 5.5, 5.7(a) were based on the square root of the actual area of the defects measured from fracture surfaces. In this section, the effect of other defect parameters on fatigue life predicted by Equation (5.24) is studied.

Comparisons of the fatigue life predictions with the experimental data based of maximum Feret diameter and area of the ellipse fitted to the defects are shown in Figure 5.7(b,c). Comparing Figures 5.7(a) to 5.7(c), it can be seen that there is no significant difference in fatigue lives predicted using these three defect parameters. This issue has also been discussed by Fintova et al. [98] wherein two defect parameters including the maximum Feret diameter and square root of the area of defects on fracture surfaces were used for fatigue life predictions. They concluded that the predicted fatigue lives based on square root of the defects are longer than those predicted based on the maximum Feret diameter. However, when Feret diameter is used in fracture mechanics model, half crack (defect) length should be used. Considering this fact, it can be concluded that there is no significant difference in using these three defect parameters in fatigue life prediction.

5.5.4. Using extreme value statistics in prediction of fatigue performance

In the previous section, the fatigue life data were used to examine the capability of small and long crack growth models in predicting the fatigue lives under different loading conditions. It

was observed that the new modification to Nisitani model, Equation (5.24), could predict the fatigue lives under different stress levels satisfactorily. However, those predictions were based on the size of fatal defects measured from fracture surfaces. Fatigue life can also be predicted using the maximum defect size within the specimens estimated by extreme value statistics (EVS). In this case, fatigue life can be predicted without the knowledge of the actual fatal defect size.

In Chapter 3, the defects within the specimens were evaluated using both metallography examination and X-ray μCT scan and the maximum defect size within the specimens was also estimated using extreme value statistics. Under uniaxial loadings, where the entire cross section is subjected to approximately uniform stress, the maximum defect size was estimated for the whole cross section of the specimens. Using the square root of the actual area of the defect as the defect parameter, the maximum defect size within the specimens were determined as 602 μm and 1426 μm for small and large specimens, respectively. While under rotating bending loading condition where only the region near the surface of the specimens was subjected to high stresses, the maximum defect size is determined for a region experiencing a stress above 90% of the maximum stress. The maximum defect in this region was estimated as 278 μm in small specimens.

Using these estimates as the initial crack size in Equation (5.24), the *S*-*N* curves under different loading conditions were predicted which are compared with the experimental fatigue data in Figures 5.8(a) to 5.8(d). In addition, fatigue lives were also predicted using the estimated maximum defect sizes which are compared with the experimental data for different specimen sizes and loading conditions in Figure 5.8(e). As can be seen in these figures, the predicted *S*-*N* curves are in very good agreement with the experimental *S*-*N* data and the predicted fatigue lives using the estimated maximum defect are in a reasonable agreement with the experimental fatigue lives under different loading conditions.

5.6. Summary and Conclusions

The objective of this chapter was to evaluate and predict the fatigue life of a cast aluminum alloy, as an illustrative material containing defects, under different loading condition considering the effects of defects, section size, mean stress, and stress gradient. To achieve this goal, experimental fatigue tests results under different loading conditions were used. The fatigue strength of the material under different loading condition was predicted. Moreover, the predictive capability of long and short crack growth models was evaluated using the fatal defects measured from fracture surfaces as the initial cracks.

The modified Paris equation was used as long crack growth model, while Hartman-Schijve model as well as a proposed modified version of Nisitani model were used as small cracks growth models. In addition, the effect of defect characteristics for considering the defect size was studied by defining three defect parameters including square root of area of the defects on fracture surfaces, square root of the area of ellipse fitted to the defects, and maximum Feret diameter. Finally, fatigue life predictions were performed using the maximum defect size estimated by extreme value statistics.

The following conclusions are made from these analyses:

1. Predicting the long life fatigue strength of this aluminum alloy using Murakami model was non-conservative, while the predicted fatigue strength using Ueno model was in a very good agreement with the experimental data.
2. Fatigue lives predicted by the modified Paris equation, as a LEFM-based long crack growth model, were non-conservative while considering the effect of small cracks using the intrinsic crack length defined by El-Haddad in stress intensity factor relation enhanced the predictive capability of this model at low stress levels. At high stress levels, however, predicting the

fatigue lives were non-conservative in both models thought to be due to the limitation of LEFM in considering the plastic deformation at high stress levels.

3. Using long crack growth data, the modified Hartman-Schijve model could predict the small crack growth behavior in a reasonable agreement with the experimental data. Fatigue lives predicted by the modified Hartman-Schijve model were in a good agreement with experimental data at low stress levels. While at high stress levels the predicted fatigue lives were non-conservative due to limitation of LEFM in considering the plastic deformation at high stress levels.
4. The new proposed small crack growth model predicted the fatigue lives at both low and high stress levels reasonably well and the predictability of the model is better than that of the other discussed models. In addition, no significant difference was observed in predicted fatigue lives using different defect parameters.
5. Fatigue life prediction using maximum defect size estimated by extreme value statistic was satisfactory for predicting the fatigue performance of the defect containing materials under different loading conditions.

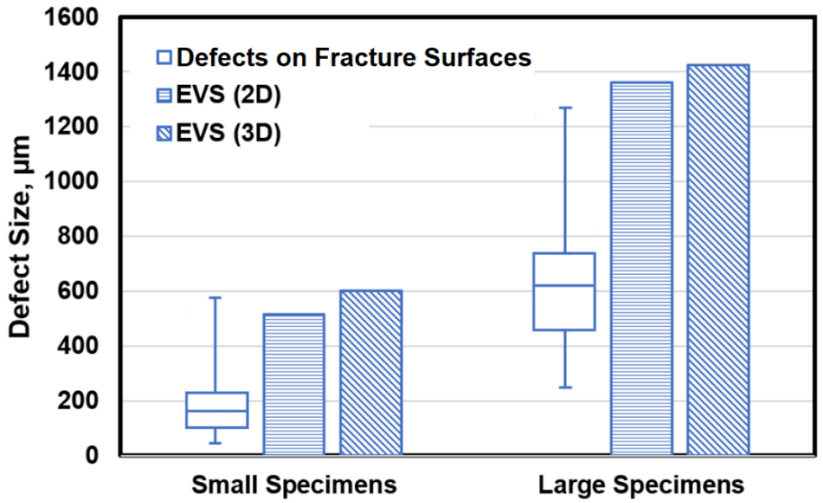

Figure 5.1. Comparison of the maximum defect estimated by extreme value statistics (EVS) using 2D and 3D data with the observed defects size measured from fracture surfaces of fatigue specimens. The upper tail, upper box, lower box, and lower tail for the observed defects each represent quartiles of defect population.

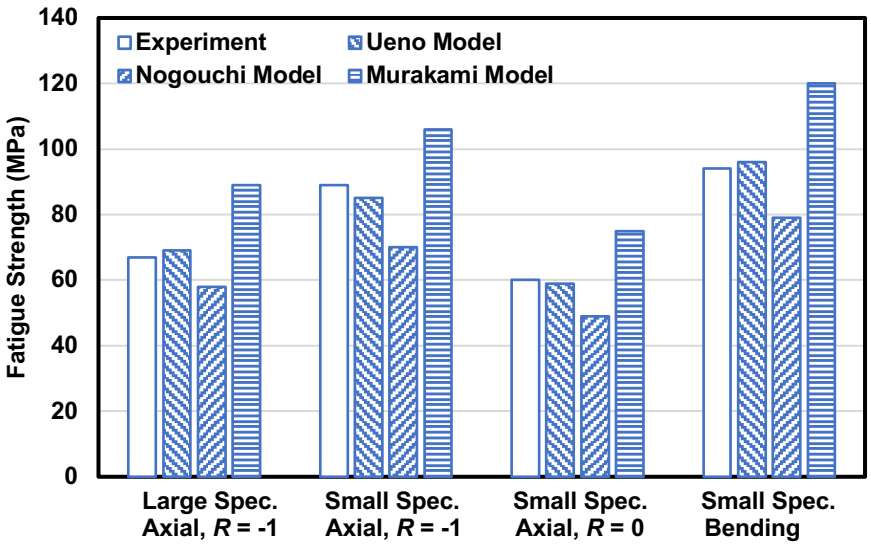

Figure 5.2. Comparison of the experimental fatigue strength of small and large specimens under different loading conditions with those predicted using different approaches.

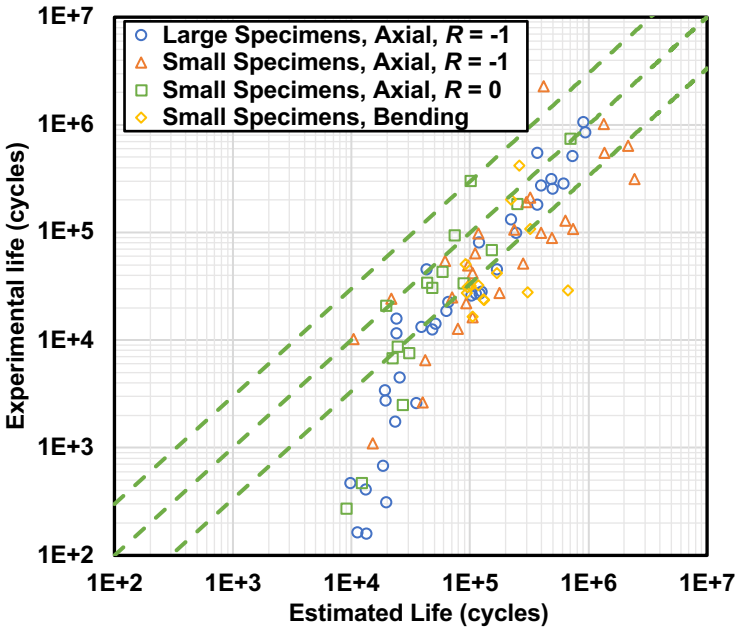

(a)

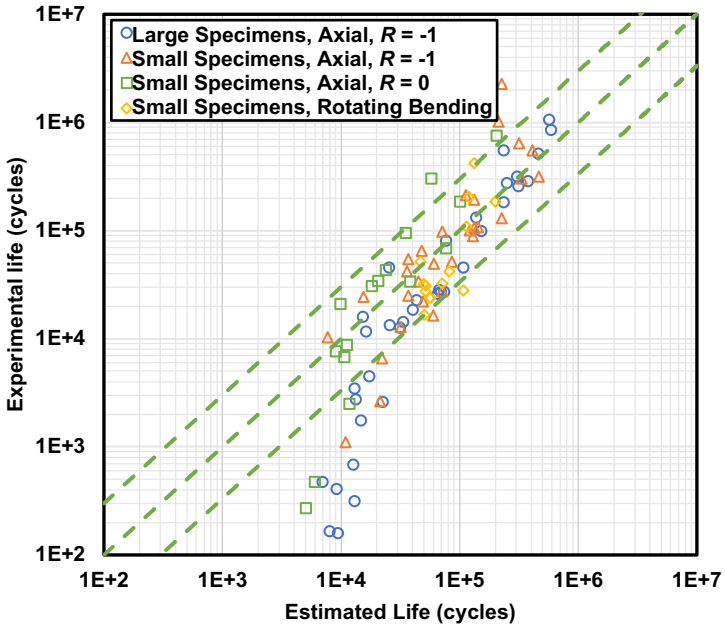

(b)

Figure 5.3. Comparison of the experimental and predicted fatigue lives based on fatal defect size on fracture surfaces using (a) modified Paris equation, (b) modified Paris equation with El-Haddad parameter.

.

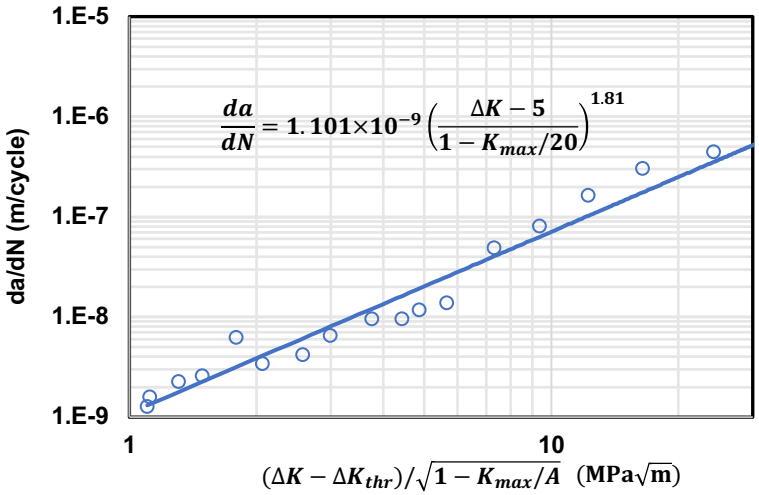

(a)

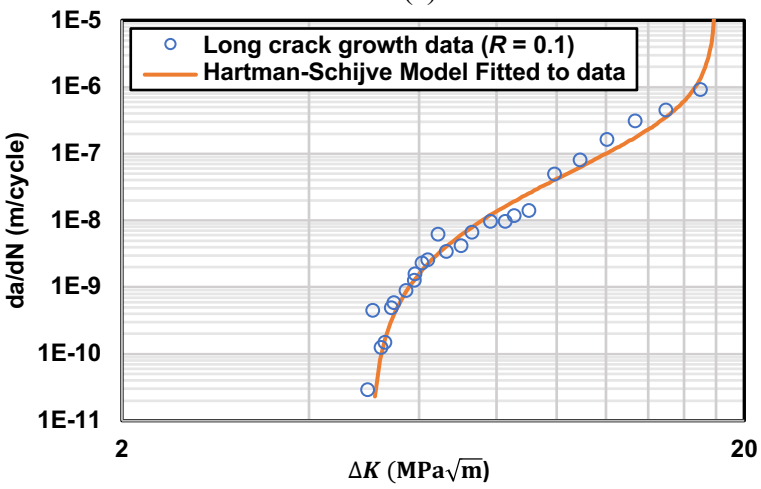

(b)

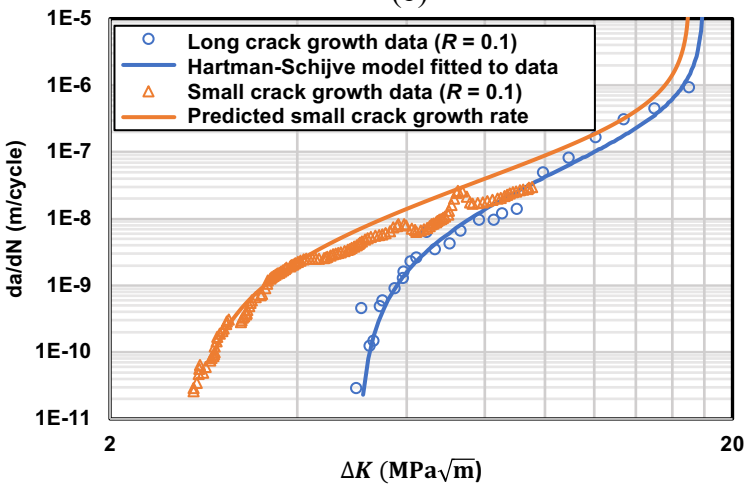

(c)

Figure 5.4. a) Hartman-Schijve representation of the long crack growth data from [9], b) Comparison of experimental long crack growth data with the Hartman-Schijve model, c) Comparison of the small crack growth data from [99] with the prediction.

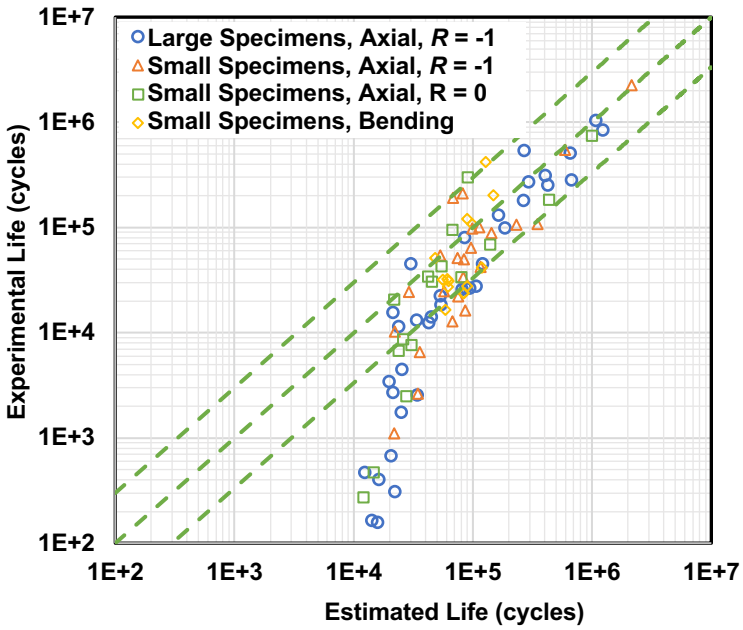

Figure 5.5. Comparison of the experimental and predicted fatigue lives based on fatal defect size on fracture surfaces using Hartman-Schijve model.

.

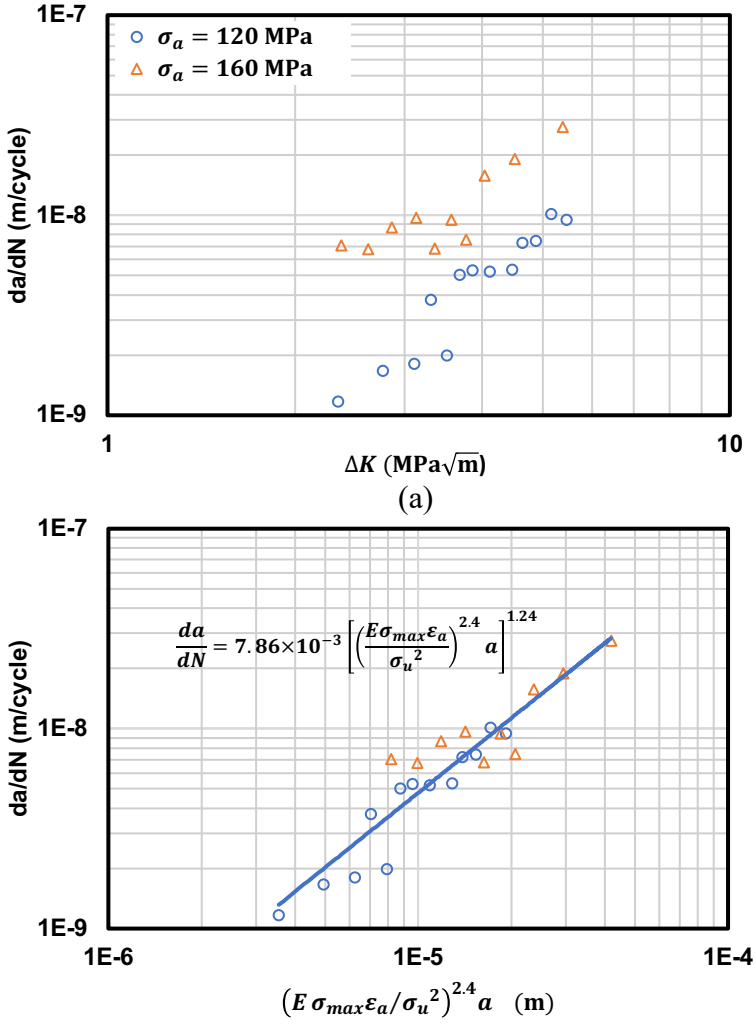

Figure 5.6. (a) Small crack growth curves for A356-T6 versus ΔK data under two different stress amplitude levels from [97], (b) the correlation of small crack growth rates under different stress levels using Equation (5.24).

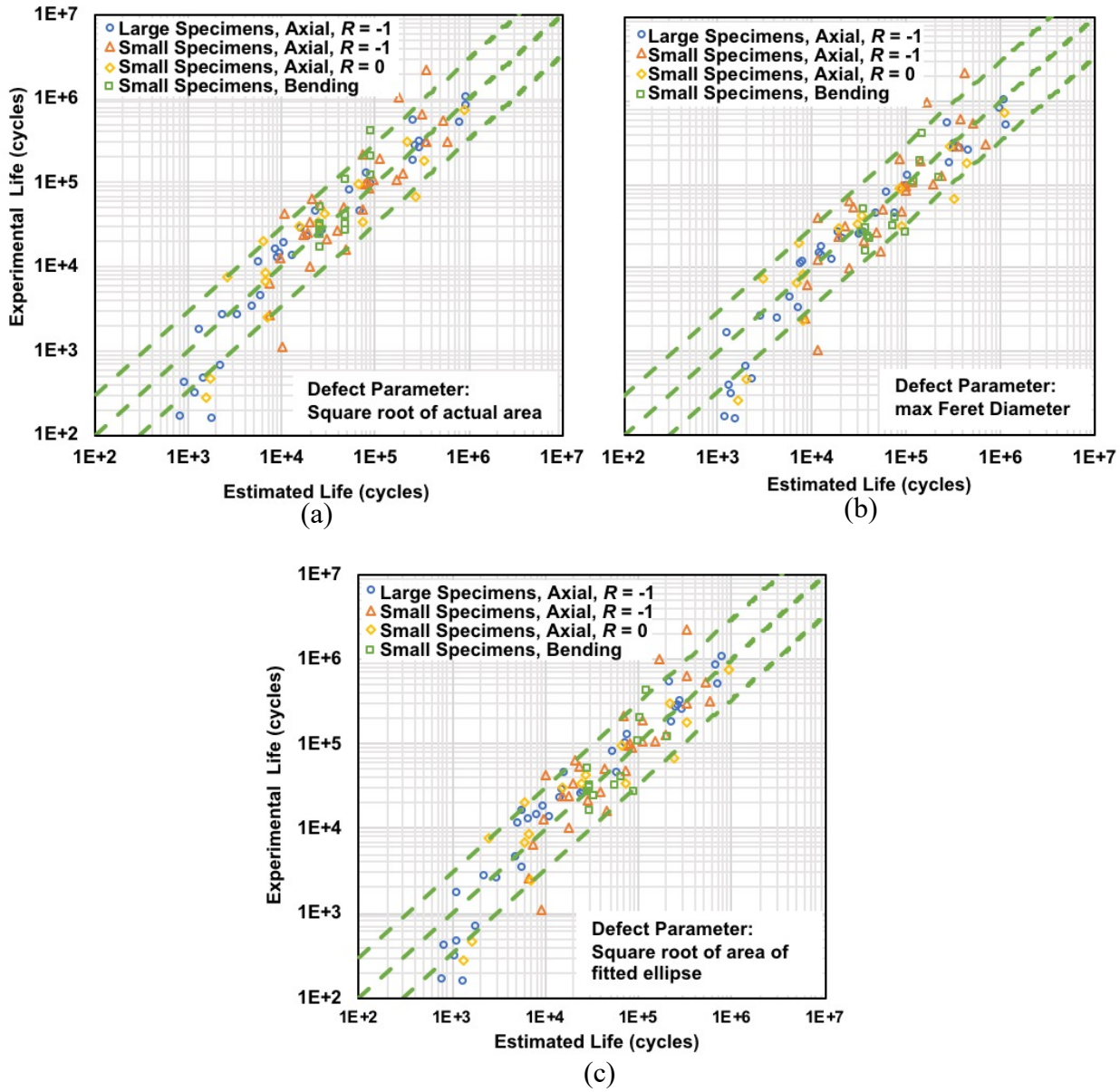

Figure 5.7. Comparison of the experimental and predicted fatigue lives using modified Nisitani model based on different characteristics of fatal defects measured on fracture surfaces, (a) Square root of actual area, (b) Max Feret Diameter, and (c) square root of area of fitted ellipse.

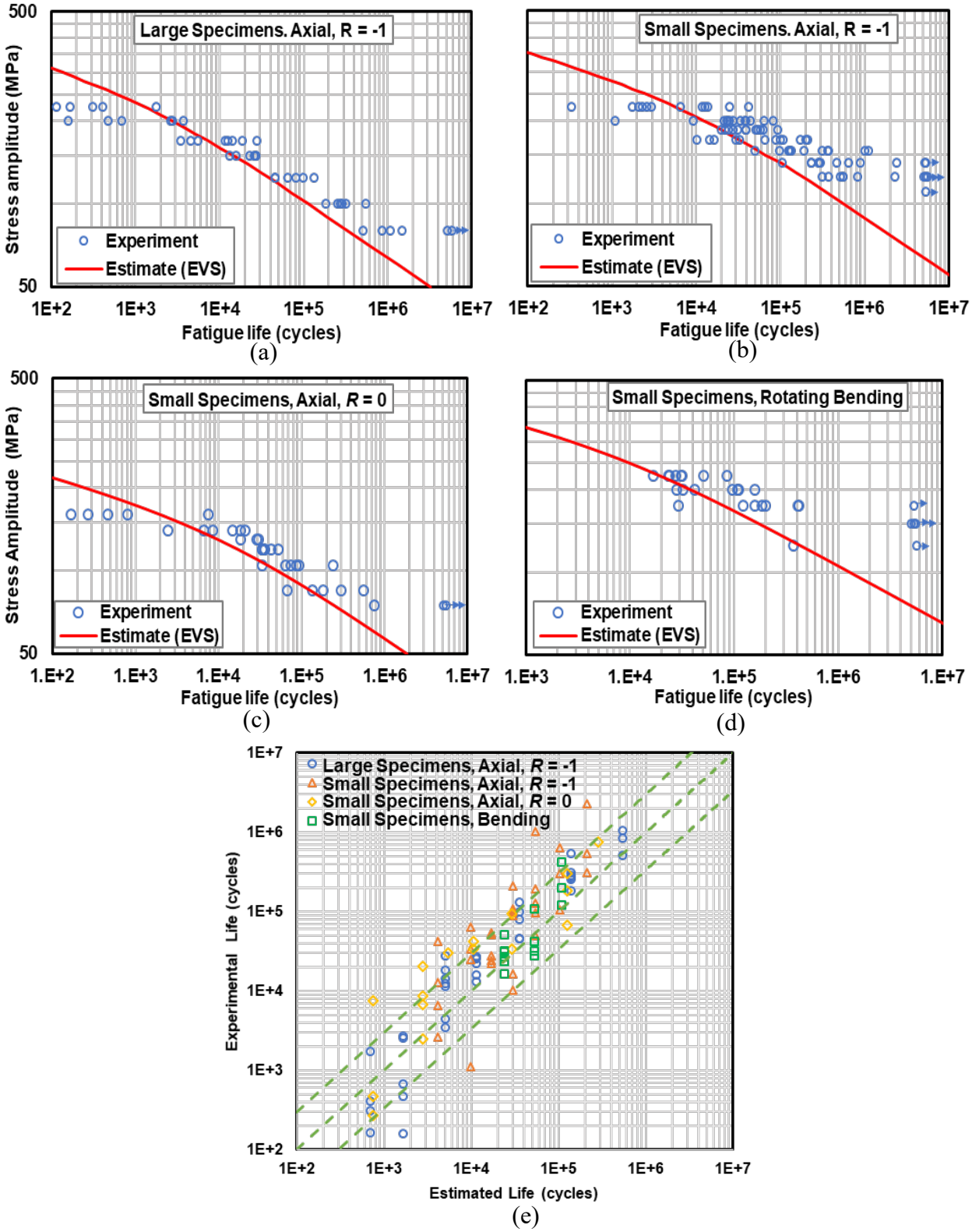

Figure 5.8. (a-d) Comparison of the *S-N* data and predicted *S-N* curves, and (e) comparison of experimental and predicted lives using the maximum defect size estimated by extreme value statistics.

Chapter 6

Fatigue Performance and Life Prediction under Axial, Torsion and Multiaxial Loadings

6.1. Introduction

In this Chapter, the fatigue performance of a cast aluminum alloy under axial, torsion and multiaxial loading conditions is studied and the fatigue life is evaluated using defect-based models. To achieve this goal, fatigue tests were performed under different loading conditions including axial, torsion, in-phase, and out-of-phase combined axial-torsion loadings. To study the fatigue crack growth mechanism as well as the effect of static axial mean stress, some tests were also conducted under cyclic torsion with static tension and compression. As evaluated in Chapter 5, small crack growth models could predict the uniaxial fatigue life of defect containing materials very well. Therefore, in this chapter small crack growth models are also used to evaluate the fatigue life under torsion and multiaxial loading conditions based on the defect size measured from fracture surfaces. Moreover, the fatigue life predictions are also performed using the maximum defect size estimated by extreme value statistics associated with the highly stressed volume under different loading conditions.

6.2. Experimental Program

The material used in this chapter was cast A356 aluminum alloy. The solid specimens (large specimens in Figure 3.1) were tested in as-cast surface finish condition. The only modification applied on the specimens was trimming of the flash remained from casting using 600 mesh sand paper.

Monotonic and cyclic stress-strain behaviors of this material under tension and torsion were obtained under strain-controlled condition. Cyclic stress-strain curves were generated by performing incremental cyclic step tests under axial and torsion loadings. The incremental step tests were performed under fully-reversed loading condition at several strain levels. At each strain level sufficient number of cycles was applied until the cyclic behavior of the material was nearly stabilized.

The fatigue tests were performed under different loading conditions including axial and torsion, as well as in-phase and out-of-phase combined axial-torsion loadings with $\tau_a/\sigma_a = 1$. This stress ratio implies the same fatigue damage contribution in combined axial-torsion tests according to the max principal stress criterion. All specimens were tested under fully-reversed (R = -1) loading at ambient temperature. In order to explore the fatigue mechanism as well as the role of static mean stress on crack face interaction during fatigue crack growth, a small number of specimens were tested under cyclic torsion with static tension or compression. Schematic illustration of the different loading paths is shown in Figure 6.1. The fatigue test conditions and test results are summarized in Table 6.1.

Fracture surfaces of failed specimens were examined using a digital optical microscope to identify the crack initiating defects and measure their size. The size of the fatal pores was measured as the square root of the area of the defects, $\sqrt{A}$. Murakami et al. [1] suggested that this parameter

is promising for considering the effect of both defect size and shape on fatigue life. The measured defect sizes were then used in fatigue life evaluation. Fatigue lives were also predicted using the maximum defect size estimated by extreme value statistics with regards to the highly stressed volume under different loading conditions. The analysis of variability of defects and estimating the maximum defect were discussed in Chapter 3.

6.3. Monotonic and Cyclic Deformation Behaviors

In order to calculate the shear stress at the surface of solid specimens in torsion tests, Miller and Chandler [100] approach was followed, given by:

$$\tau = \frac{1}{2\pi r^3}\left[3T + \gamma \frac{\mathrm{d}T}{\mathrm{d}\gamma}\right] \tag{6.1}$$

where r is the specimen radius, T is the applied torque, γ is the shear strain level, and $\mathrm{d}T/\mathrm{d}\gamma$ is the slope of torque vs shear strain curve.

The correlations of monotonic stress-strain curves under torsion and tension using von-Mises and Tresca criteria are illustrated in Figure 6.2(a). The following relations exist according to the von-Mises and Tresca criteria:

von-Mises: $K_0 = \frac{K}{\sqrt{3}}\left(\frac{1}{\sqrt{3}}\right)^n$ and $n_0 = n$ (6.2)

Tresca: $K_0 = \frac{K}{2}\left(\frac{2}{3}\right)^n$ and $n_0 = n$ (6.3)

where K or K_0 and n or n_0 are strength coefficient and strain hardening exponent under axial or shear loading, respectively. As can be seen in Figure 6.2(a), the correlation of stress-strain curves using von Mises criterion is better than that using Tresca criterion.

The variations of the applied torque as well as the shear strain vs elapsed cycles during torsion step test are illustrated in Figure 6.2(b). As can be seen, a cyclic hardening process leads

to gradually increasing the required torque at each shear strain amplitude level. Moreover, the gradual hardening continues even after considerable number of cycles at a given shear strain level. This is partly due to a stress gradient which cause different regions of the specimen experience different levels of hardening. Once the hardening process occurs in the region near the surface, higher required torque causes the plastic deformation and consequent hardening to gradually continue towards the center of the specimen by increasing the number of shear cycles.

Cyclic shear stress-strain curve was also obtained by using Equation (6.1) where T and γ are substituted by ΔT and $\Delta\gamma$, respectively. In this case, $\mathrm{d}\Delta T/\mathrm{d}\Delta\gamma$ is the average of the slops of torque vs shear strain hysteresis loop at the end of loading and unloading portions [100]. Comparison of monotonic and cyclic deformation behaviors of this material under torsion and axial loadings using von-Mises criterion is shown in Figure 6.2(c). As can be seen in this figure, under both axial and torsion cyclic loadings the material experiences significant hardening. In addition, the cyclic stress-strain curves under axial and torsion loadings correlate well using von Mises criterion. The obtained monotonic and cyclic properties under torsion and axial loadings are summarized in Table 6.2.

6.4. Fatigue Test Results

The correlation of all fatigue data under different loading conditions is illustrated in Figure 6.3. In this figure, von Mises and maximum principal stress criteria have been used to compute equivalent stress, given by:

$$\bar{\sigma}_{vM,a} = \sqrt{\sigma_a^2 + 3\tau_a^2} \tag{6.4}$$

$$\bar{\sigma}_{1,a} = \frac{\sigma_a}{2} + \sqrt{\left(\frac{\sigma_a}{2}\right)^2 + \tau_a^2} \tag{6.5}$$

These equations are used for torsion and in-phase loadings, while for out-of-phase combined loading tests a time dependent analysis is needed to evaluate the maximum value of equivalent stress during a cycle.

It can be seen from Figure 6.3(a) that the fatigue life data under different loading conditions correlate well when maximum principal stress is considered as the equivalent stress. It will be discussed in section 6.4.1, fatigue cracking under different loading conditions occurred on the plane of maximum principal stress. Therefore, the mechanism of fatigue damage in this material is tensile mode or mode I in fracture mechanic sense, which is typical of brittle behaving materials. This is due to the stress concentration effect of casting defects in the material.

Based on critical plane approach for brittle behaving materials, the Smith-Watson-Topper (SWT) parameter [79] is an appropriate approach to evaluate fatigue damage. In Chapter 4, this parameter was used for mean stress correction factor and reported that this approach is quite accurate in predicting the fatigue life with the applied mean stress. The stress version of the SWT damage parameter is given by:

$$\sigma_{SWT} = \sqrt{\sigma_{1,a}\sigma_{n,max}} \tag{6.6}$$

When the plastic deformation is also involved during cyclic loading, the strain-based version of SWT results in better predictions. The strain-based version of SWT for multiaxial loading conditions which is the product of maximum principal strain amplitude, $\varepsilon_{1,a}$, and maximum normal stress on the same plan, $\sigma_{n,max}$, can be written as:

$$\sigma_{SWT} = \sqrt{E\varepsilon_{1,a}\sigma_{n,max}} \tag{6.7}$$

The advantage of the strain-based version is that the deformation history of the material such as cyclic softening or hardening as well as the behavior of the materials under complex loading conditions (i.e. load path materials response dependence) can be taken into account.

The correlation of the fatigue data using stress and strain versions of SWT parameter are demonstrated in Figure 6.4. It can be seen that the correlation of the fatigue data based both SWT formulations are similar. However, the stress-based version, which for fully-reversed loading condition is identical to maximum principal stress, results in a better correlation of all fatigue life data under different stress states. The reason for the difference between the stress and the strain versions of SWT parameter is the multiaxial nature of the stress on the plane of maximum damage which causes normal strain to be higher than that under uniaxial loading.

6.4.1. Comparisons of axial with torsion loadings

Examining fracture surface of the specimens, it was observed that in all specimens failed under different loading conditions the fatigue cracks initiated from defects. However, under axial loading the crack initiating defects were located randomly in the entire cross section, while under torsion and combined axial-torsion loading conditions the location of crack initiating defects was near the surface. This is due to the difference in the volume under high stress in different loading conditions. Under axial loading the entire cross section is under high stress, while under torsion or combined loading stress states there is stress gradient and only the outer region of the specimens is under high stress.

The fatigue crack growth mechanism was also explored by considering the orientation of fatigue crack growth at the surface of the specimens before fracture. It was observed that under axial loading in all specimens crack growth and failure occurred on the plane perpendicular to the loading direction, which is the plane of maximum principal stress. Under torsion loading, in most specimens fatigue cracks initiated and grow on the plane of 45°, which is the plane of maximum principal stress, as shown in Figure 6.5a. However, in the case of two torsion specimens failed

under shear stress amplitudes of 145 MPa and 130 MPa the orientation of fatigue cracks at the surface of the specimens was somewhat different, as shown in Figure 6.5b. Considering the crack growth path of these specimens, a horizontal crack is observed. This suggests that the fatigue crack might have initiated on the plane of maximum shear stress and then grown on the plane of maximum principal stress. However, careful examination of the fracture surface revealed that the horizontal part was in the vicinity of a defect, see Figure 6.5b. In addition, the presence of another crack on the surface on the plane of 45° confirmed that both crack initiation and growth were on the plane of maximum principal stress.

6.4.2. Comparison of in-phase and out-of-phase loadings

Comparison of the fatigue life data under axial and torsion as well as combined axial-torsion loadings in Figure 6.4 shows that at a given equivalent fatigue damage the fatigue life under axial loading is shorter than that under torsion or combined loadings. This is due to the volume effect. Under axial loading the entire cross section is under high stress and the probability of large defects existing in highly stressed volume is higher than that under torsion or combined loading conditions. This is attributed to the stress gradient effect where only the outer region of the specimens experience high stress.

Crack growth path of specimens failed under in-phase and out-of-phase loadings are shown in Figure 6.6. It can be seen that under both loading conditions the fatigue crack grew along the plane of maximum principal stress. In addition, crack growth path under out-of-phase combined loading is more tortuous in comparison to the that under in-phase loading. This is due to variation of plane of maximum principal stress during the out-of-phase load cycling.

Comparison of the fatigue test results under in-phase and out-of-phase combined loadings is illustrated in Figure 6.7(a). As can be seen, at a given equivalent damage value fatigue life under out-of-phase loading is shorter than that under in-phase loading. The reason is thought to be due to the difference between the range of plane orientations experiencing high stress under in-phase and out-of-phase loadings. Variations of maximum principal stress vs plane orientation under in-phase and out-of-phase loadings as well as time within a cycle are shown in Figures 6.7(b) and 6.8(c), respectively. As can be seen, under out-of-phase loading a wider range of plane orientations within the specimens experience at least 95% of the maximum damage.

This phenomenon has also been reported for other materials. Shamsaei and Fatemi [101] observed that the small crack growth rate in 1050 steel and Inconel 718 under out-of-phase loading was higher than that under in-phase loading and suggested that this is due to a wider range of plane orientations experiencing more than 95% of the maximum damage under out-of-phase loading. This observation was also taken into account for fatigue life prediction and modeling under out-of-phase loading condition, as discussed in section 6.5.

6.4.3. Effect of static tension or compression axial load on cyclic torsion fatigue tests

In order to study the role of crack face interaction during fatigue crack growth process, some tests were conducted under cyclic torsion with static tension or compression. It was observed that the crack growth path orientation on the surface of the specimens failed under both loading conditions was on the plane of maximum principal stress, similar to Figure 6.5(a). This confirms that the tensile mode failure is the dominant mechanism of fatigue damage in this material.

This is contrary to the observations in [37] which reported that under uniaxial and biaxial loading conditions initiation of fatigue crack occurred at micro-shrinkage pores, while under

torsion cracks initiated at Si-particles of the eutectic zones on the plane of maximum shear stress. In fact, there is a competition between these two mechanisms which depends on the defect size distribution within the specimens. There is a critical defect size below which the fatigue performance is not affected by the defects. This issue has been investigated in [7,20,22] under uniaxial loading conditions. It was concluded that when the defect size is below the critical size, crack initiation and growth occurred at the secondary phase precipitates and large intermetallic compounds, while cracks grow from defects larger than critical size.

Comparison of the fatigue lives under pure cyclic torsion, cyclic torsion with a static tension, and cyclic torsion with a static compression is demonstrated in Figure 6.8(a). As can be seen in this figure, applying a static tensile stress along with cyclic torsion decreases the fatigue life. This is due to reduction in crack face friction and roughness induced crack closure effects. However, the fatigue life of the specimens under cyclic torsion with static compression was considerably increased. This may be related to increasing the roughness induced crack closure resulting from the compressive stress which reduces the driving force for crack growth.

Correlation of the fatigue life data under cyclic torsion with static tension or compression loadings with those under axial, torsion and axial-torsion combined loadings is given in Figure 6.4. As can be seen in this figure, using SWT parameter for fatigue damage evaluation is effective in taking the effect of static tension or compression into account.

Crack growth rate vs stress intensity factor of this material under uniaxial loading for both long [9] and small cracks [99] is illustrated in Figure 6.8(b). The initial and final stress intensity factors at several axial stress levels are also shown. The initial stress intensity factor was computed using the fatal defect size on the fracture surfaces and the final stress intensity factor was computed for the crack size of 2 mm length, which is typically the final crack length for small cracks. As can

be seen, the initial stress intensity factors are mostly below the long crack growth threshold where long cracks cannot grow. This suggests that cracks initiating from defects in this material are in the range of small crack growth. Moreover, at low stress levels the initial stress intensity factor is close to the threshold value. When a static compression is applied, the effective stress intensity factor is reduced due to crack closure effect which results in longer life. If the size of defects in highly stressed volume is small, the effective stress intensity factor may be shifted even below the small crack growth threshold where cracks do not grow, while in specimens containing large defects fatigue cracks can grow and cause to fracture. This phenomenon results in a larger scatter in fatigue life when static compression is applied, see Figure 6.8(a).

6.5. Fracture Mechanics-Based Fatigue Life Modeling and Predictions

In defect containing materials wherein defects can be considered as initial flaws (cracks), the fatigue life can be predicted following damage tolerant design philosophy. As the defects in these materials are considered to act as initial cracks, the fatigue crack initiation life is neglected and the total fatigue life is approximated as the life spent on crack growth. Although the defects are not cracks at first, due to their high stress and strain concentrations fatigue cracks can initiate in the first few cycles at their edges and then the defect size will be included in the effective crack size. The size of defects in cast aluminum alloys are such that that cracks originated from them are in the range physically small cracks, typically on the order of 0.1 mm - 2 mm. A significant portion of the fatigue life is spent on small crack growth stage [21,23]. Such cracks are characterized by experiencing lower crack closure levels, higher growth rates, and growing even below the threshold stress intensity factor of long cracks.

In Chapter 5, uniaxial fatigue life prediction using both long and small crack growth models were compared and it was concluded that using small crack growth model fatigue life yields satisfactorily life predictions. In this study, fatigue lives under different loading conditions are modeled using small crack growth models wherein the size of crack initiating defects measured from the fracture surfaces are assumed as the initial crack size. The fatigue lives are also predicted using the maximum defect size estimated by extreme value statistics. The analysis of variability of defects within the specimens and estimating the maximum defect size by extreme value statistics are discussed in Chapter 3.

6.5.1. Modified Hartman-Schijve model

This model which is in fact the modified version of Forman equation, is based on linear elastic fracture mechanics (LEFM). Jones et al. [94] proposed a modification to Hartman-Schijve model and showed that the modified version has the capability of including both small and long crack growth behaviors as well as mean stress or *R*-ratio effects. The modified Hartman-Schijve model is given by:

$$\frac{\mathrm{d}a}{\mathrm{d}N} = D\left(\frac{\Delta K-\Delta K_{thr}}{\sqrt{1-K_{max}/A}}\right)^{m} \tag{6.8}$$

where A, D, and m are material constants and ΔK_{thr} is the threshold stress intensity factor which is a function of stress ratio as well as crack length.

Applying this model to large number of materials, Jones et al. [94] showed that the value of m is around 2 and the constant D can be reasonably approximated by $D = 0.036/E\sigma_y$, where E and σ_y are in MPa. These constants can also be determined from the crack growth data by plotting $\mathrm{d}a/\mathrm{d}N$ vs $\left[(\Delta K - \Delta K_{thr})/\sqrt{1 - K_{max}/A}\right]$, wherein A and ΔK_{thr} are chosen to best represent the experimental crack growth data.

Numerous studies have reported that the small cracks do not behave in accordance with conventionally acquired long crack growth data. Jones et al. [94] showed that using Equation (6.8) small crack growth behavior can be predicted using the calculated constants D, A, and m for long cracks, but different values of ΔK_{thr} for small cracks. Using the long crack growth data from [9] for the same material as in this study, the constants A, D, and m were determined as 20 MPa$\sqrt{\text{m}}$, 1.10×10^{-9} m/cycle and 1.81, respectively. Using these material constants in Chapter 5, it was shown that this model can reasonably predicted the small crack growth behavior under uniaxial loading when the small crack growth threshold is 2.5 MPa$\sqrt{\text{m}}$.

In this study, this model is used to predict the fatigue lives under multiaxial loading conditions. However, as the fatigue failure mechanism in this material is crack growth on the plane of maximum principal stress, as discussed in section 6.4, the multiaxial stress state can be simplified by using the maximum principal stress as the equivalent stress. The fatal defect size measured on the fracture surface of the specimens is also assumed as the initial crack size, and the final crack size is taken to be 2 mm, which was the typical final length for small cracks. It should be emphasized that for measuring the defect size from the fracture surface of the specimens, the objective lens of the microscope was tilted perpendicular to the plane of crack growth and the square root of the area of defects on this plane was used as equivalent for the defect size, i.e. Murakami's approach [1]. The size of fatal defects measured from fracture surfaces are summarized in Table 6.1.

Under in-phase loading condition where the maximum axial and torsion loads are applied at the same time, the fatigue life can be predicted using Equation (6.8). However, the fatigue life predicted under out-of-phase loading using this model is non-conservative, due to wider range of plane orientations experiencing a high percentage of maximum principal stress under this loading,

relative to torsion and in-phase combined loadings as mentioned in section 6.4.2. Studying the small crack growth behavior under in-phase and out-of-phase loading conditions, Shamsaei and Fatemi [101] suggested that faster crack growth rate under out-of-phase compared to in-phase loading could be modeled by considering a factor of $\sqrt{\theta_{95,OP}/\theta_{95,IP}}$ along with the crack growth driving force, where $\theta_{95,OP}$ and $\theta_{95,IP}$ are the range of plane orientations experiencing more than 95% of the maximum damage under out-of-phase and in-phase loading, respectively. They used this factor along with the Fatemi-Socie Parameter as the driving force for crack growth rates when the plane of maximum shear stress is the maximum damage plane. Considering this factor to model the fatigue life under out-of-phase loading in this study where the maximum principal stress is the plane of maximum damage, the stress intensity factor can be modified as:

$$\Delta K = Y\Delta\sigma_{a,1}\sqrt{\frac{\theta_{95,OP}}{\theta_{95,IP}}\pi a} \tag{6.9}$$

Therefore, fatigue lives under axial, torsion, and in-phase loadings were predicted using Equation (6.8), while for predicting fatigue lives under out-of-phase loading the modified stress intensity factor, Equation (6.9), was considered. The ranges of plane orientations experiencing more than 95% of the maximum damage under in-phase and out-of-phase loadings were 22º and 54º, respectively, see Figure 6.7(b).

Comparisons of experimental and predicted fatigue lives under different loading conditions are shown in Figure 6.9(a). As can be seen, at low stress levels the predicted fatigue lives are in reasonable agreement with the experimental data, while at high stress levels the predictions are non-conservative. This may be due to the limitation of LEFM in predicting the fatigue life at high stress levels where the small scale yielding assumption is violated.

6.5.2. Modified Nisitani model

It has been reported that LEFM concept cannot model small crack growth behavior effectively. This is because at a given stress intensity factor with different applied stress amplitude levels the small crack growth rates are different due to different degrees of plastic deformation at the crack tip which can result in violation of the small scale yielding assumption. This fact has been reported for aluminum alloys in [21,97].

Studying small crack growth in steels, Nisitini and Goto [61] proposed the following model for small crack growth rate considering crack tip displacement (CTD) as the crack growth driving force:

$$\frac{\mathrm{d}a}{\mathrm{d}N} = C\left(\frac{\sigma_a}{\sigma_y}\right)^s a \tag{6.10}$$

where σ_y is the yield strength. The accuracy of this model has been confirmed for cast aluminum alloys by Shiozawa et al. [22], substituting the yield strength with the ultimate strength of the material. Based on Nisitani model given in Equation (6.10) and using SWT damage parameter to consider the fatigue damage under different loading conditions, a more general model is proposed here to evaluate the crack growth rates under different stress states when the damage mechanism is growth of cracks on plane of maximum principal stress, given by:

$$\frac{\mathrm{d}a}{\mathrm{d}N} = A\left[\left(E\,\frac{\varepsilon_{1,a}\,\sigma_{n,max}}{{\sigma_u}^2}\right)^s a\right]^t \tag{6.11}$$

where $\sigma_{n,max}$ and $\varepsilon_{1,a}$ are the maximum normal stress and the amplitude of maximum principal strain on the plan of maximum principal stress, respectively, σ_u is ultimate tensile strength, and A, n, and t are material constants which can be determined using small crack growth rate data. Using small crack growth rates from [97], the values for A, s, and t were determined as 7.86×10^{-3} m/cycle, 2.4, and 1.24, respectively. This model was used in Chapter 5 for predicting the fatigue

lives under axial loading conditions including mean stress and stress gradient effect and reported that the predicted fatigue lives were in very good agreement with the experimental data.

Using Equation (6.11) the fatigue lives under different stress states were predicted based on the defect size measured from fracture surfaces. However, as discussed in section 6.5.1 for predicting the fatigue lives under out-of-phase loading the faster crack growth rates due to wider range of plane orientations experiencing high damage could also be considered. Therefore, for out-of-phase loading the expression in bracket in Equation (6.11) is modified by multiplying by the $\theta_{95,OP}/\theta_{95,IP}$ ratio.

Following this approach, fatigue lives under different loading conditions were predicted using the size of crack initiating defects measured from fracture surfaces as the size of initial cracks. As the conducted fatigue tests in this study were in load control condition, cyclic deformation behaviors under axial and torsion loads were used to calculate the maximum principal strain (see Table 6.2 and Figure 6.2c) under different loading conditions.

Comparison of predicted and experimental fatigue lives under different loading conditions is illustrated in Figure 6.9(b). As can be seen, the predicted fatigue lives using this model are in very good agreement with the experimental data in a wide range of stress levels. The discrepancy between the experimental and predicted fatigue lives in few data points at high stress levels (short lives) may have resulted from the difference between the actual strain amplitude and the calculated one using the cyclic stress–strain relation. This relation was associated with the strain amplitude in stabilized condition after the hardening process was mostly completed within the material. However, in specimens failed under high stress levels the hardening process continued and stress-strain relation did not completely stabilize even when failure happened.

6.5.3. Fatigue life predictions using the maximum defect size estimated by extreme value statistics

Fatigue lives under different loading conditions in sections 6.5.1 and 6.5.2 were predicted using the size of crack initiating defects observed on fracture surfaces. However, in practical situations such information is not available as a priori. In such cases, the fatigue lives can be predicted using the maximum defect size estimated by extreme value statistics. In Chapter 3, the analysis of variability of defects was discussed and the maximum defect within the specimens was estimated based on both metallography or micro-computed tomography (μCT) evaluations. In this section, the estimated maximum defect sizes were used for fatigue life predictions.

Under axial loadings where the entire cross section experiences high stress, the maximum defect size was estimated for the whole cross section of the specimens. Using the square root of the actual area of defect as the defect parameter, the maximum defect size within the specimens was determined as 1426 μm. However, under torsion and combined axial-torsion loadings there is a gradient stress. Therefore, the maximum defect should be estimated only for the region near the surface of the specimens experiencing high stress. It has been empirically observed that the critical section of the specimens is the region where at least 90% of the nominal stress is experienced [1]. Therefore, considering this region under torsion, the maximum defect size was estimated as 578 μm, which is also very close to the maximum fatal defect size observed on the specimens under torsion as 534 μm. As less stress gradient is experienced by the specimens under in-phase and out-of-phase loadings, highly stressed volume under these loading conditions is larger than that under torsion, which results in larger defects.

Using the estimated maximum defects as the initial crack size in Equation (6.11), fatigue lives were predicted and are compared with the experimental lives in Figure 6.10. As can be seen in this figure, the predicted fatigue lives using the estimated maximum defect size for the whole

cross section are in very good agreements with the experimental fatigue lives under axial loading. The fatigue lives predicted using the estimated defect in high stressed volume under torsion are also in good agreement with the experimental fatigue lives under torsion. For in-phase and out-of-phase loadings, the prediction curves in Figure 6.10 will be between those under axial and torsion loadings.

6.6. Summary and Conclusions

This chapter reported on the fatigue performance of cast A356-T6 aluminum alloy under different stress states. The monotonic and cyclic deformation behaviors of this material were studied. The fatigue tests were conducted under axial, torsion, torsion with static tension or compression, as well as in-phase and out-of-phase combined axial-torsion loadings. The fatigue mechanism was explored by considering the crack growth path under different loading conditions. The fatigue life data were used to evaluate and model the fatigue performance based on crack initiating defect size measured from fracture surfaces using small crack growth models. Fatigue lives were also predicted using the maximum defect size estimated by extreme value statistics. From these analyses the following conclusions are made:

1. Correlation of monotonic and cyclic deformation behaviors of this material using von Mises criterion was better than that using Treca criterion. It was also found that under both axial and torsion loadings the material experienced significant hardening during cyclic loading.
2. Fatigue data under different loading conditions correlated well when maximum principal stress (for fully-reversed loading) and SWT (for fully-reversed loading and when an axial mean stress was present) are used as the equivalent stress. Crack growth path on the surface of the

specimens failed under different stress states revealed that the failure mode was tensile, which is typical of brittle behaving materials.

3. Fatigue lives under torsion and in-phase combined loadings at the same maximum principal stress were longer than those under axial loading. This is due to stress gradient under torsion and in-phase combined loading conditions. Under axial loading the whole cross section experience high stress which increases the probability of large defects existing in the stressed volume.
4. Fatigue lives under out-of-phase loading were shorter than those under in-phase loading at the same maximum principal stress, while the crack growth path was more tortuous under out-of-phase loading compared to in-phase loading. This is thought to be due to wider plane orientations experiencing high stress under out-of-phase loading.
5. Under cyclic torsion with static tension, fatigue lives were shorter compared to those under pure cyclic torsion. This is due to reduction in crack face friction and roughness induced crack closure effects. Under cyclic torsion with static compression fatigue lives were significantly longer than pure torsion, accompanied with larger scatter due to the increased roughness induced crack closure and reduction in the effective stress intensity factor.
6. Fatigue life predictions using the modified Hartman-Schijve model for small cracks were in reasonable agreement with the experimental data at low stress levels, while at high stress levels the predictions were non-conservative. This is thought to be due to the limitation of LEFM in considering the plastic deformation at high stress levels.
7. Using SWT damage parameter in Nisitani small crack growth model, a general model was proposed to evaluate the crack growth rates under different loading conditions when failure

mode is tensile. It was shown that fatigue life predictions using the proposed model were in very good agreement with the experimental data.

8. Predicted fatigue lives based on maximum defect size estimated by extreme value statistic for the whole surface were in very good agreement with the experimental fatigue lives under axial loading. Using maximum defect size estimated for highly stressed volume under torsion also resulted in reasonable predictions under torsion and combined axial-torsion loadings.

Table 6.1. Summary of the fatigue test conditions and results under different loading conditions.

Test Type[1]	σ_a (MPa)	σ_m (MPa)	τ_a (MPa)	Freq. (Hz)	$\sigma_{1,max}$ (MPa)	σ_{vM} (MPa)	σ_{SWT} (MPa)	Defect size[2], $\sqrt{A}$ (μm)	Cycles to failure, N_f
A	225	--	--	0.5	225	225	225	-, 492, -	115; 313; 5
A	200	--	--	0.5	200	200	200	649, 930, 408	678; 471; 2593
A	170	--	--	1	170	170	170	446, 792, 524, 823	18581; 5523; 14304; 4499
A	150	--	--	2	150	150	150	436, 1141, 465	26938; 15823; 25848
A	125	--	--	5	125	125	125	578, 435, 731	45622; 99277; 80546
A	100	--	--	20	100	100	100	651, 647, 620	181482; 547365; 272571
A	80	--	--	25	80	80	80	-, 682, 503	>5152421; 1057259; 1471740
T	--	--	220	0.5	220	381	220	512	466
T	--	--	190	1	190	329	190	534	6588
T	--	--	165	2	165	286	165	496	41753
T	--	--	145	4	145	251	145	351, 378	79880; 53605
T	--	--	130	6	130	225	130	348, 373	179946; 133031
T	--	--	110	8	110	190	110	192, 248	462364; 510620
T	--	--	90	10	90	156	90	528	1433477
TC	--	-50	130	5	107	231	117	529, 288, -	163353; 742568; $>10^6$
TT	--	50	130	5	157	231	142	410, 270	74280; 104127
IP	105	--	105	2	170	210	170	363, 416	20080; 17416
IP	90	--	90	4	145	180	145	508	30937
IP	77	--	77	4	125	154	125	439, 431	223593; 187774
IP	70	--	70	6	113	140	113	442	354031
IP	60		60	10	97	120	97	-	>2500000
OP	150	--	150	1	173	260	173	719, 342	4934; 5706
OP	110	--	110	3	127	191	127	185, 264	90757; 75534
OP	80	--	80	10	92	139	92	-	$>2.5\times10^6$

[1] A, Axial; T, Torsion; IP, Combined axial-torsion in-phase; OP, Combined axial-torsion 90° out-of-phase.
[2] size of fatal defect was measured on fracture surfaces and is reported in the same order as fatigue life listed for each test type.

Table 6.2. Summary of monotonic and cyclic mechanical properties under tension and torsion.

	Axial		Shear	
Monotonic properties				
Modulus, GPa	E	74.0	G	28.9
Yield strength, MPa	σ_y	154	τ_y	77.8
Ultimate strength, MPa	σ_u	279	τ_u	215
Strength Coefficient, MPa	K	805	K_0	443
Strain hardening exponent	n	0.274	n_0	0.280
Cyclic properties				
Yield strength, MPa	σ_y'	291	τ_y'	213
Strength Coefficient, MPa	K'	1096	K_0'	733
Strain hardening exponent	n'	0.213	n_0'	0.199
Fatigue strength coefficient	σ_f'	421	τ_f'	517
Fatigue Strength Exponent	b	-0.111	b_0	-0.116

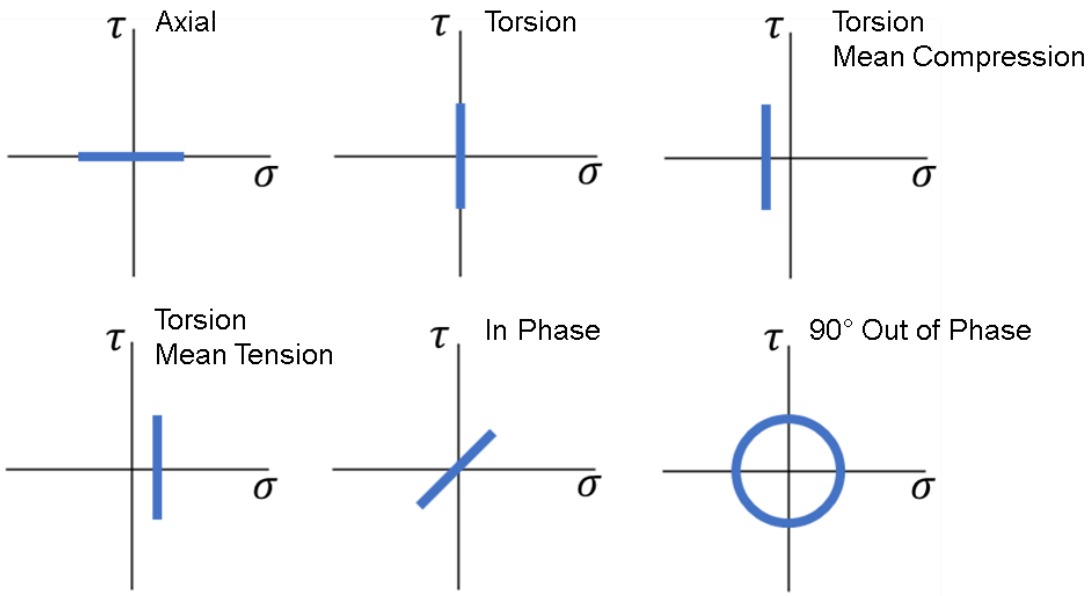

Figure 6.1. Schematic illustration of different loading paths.

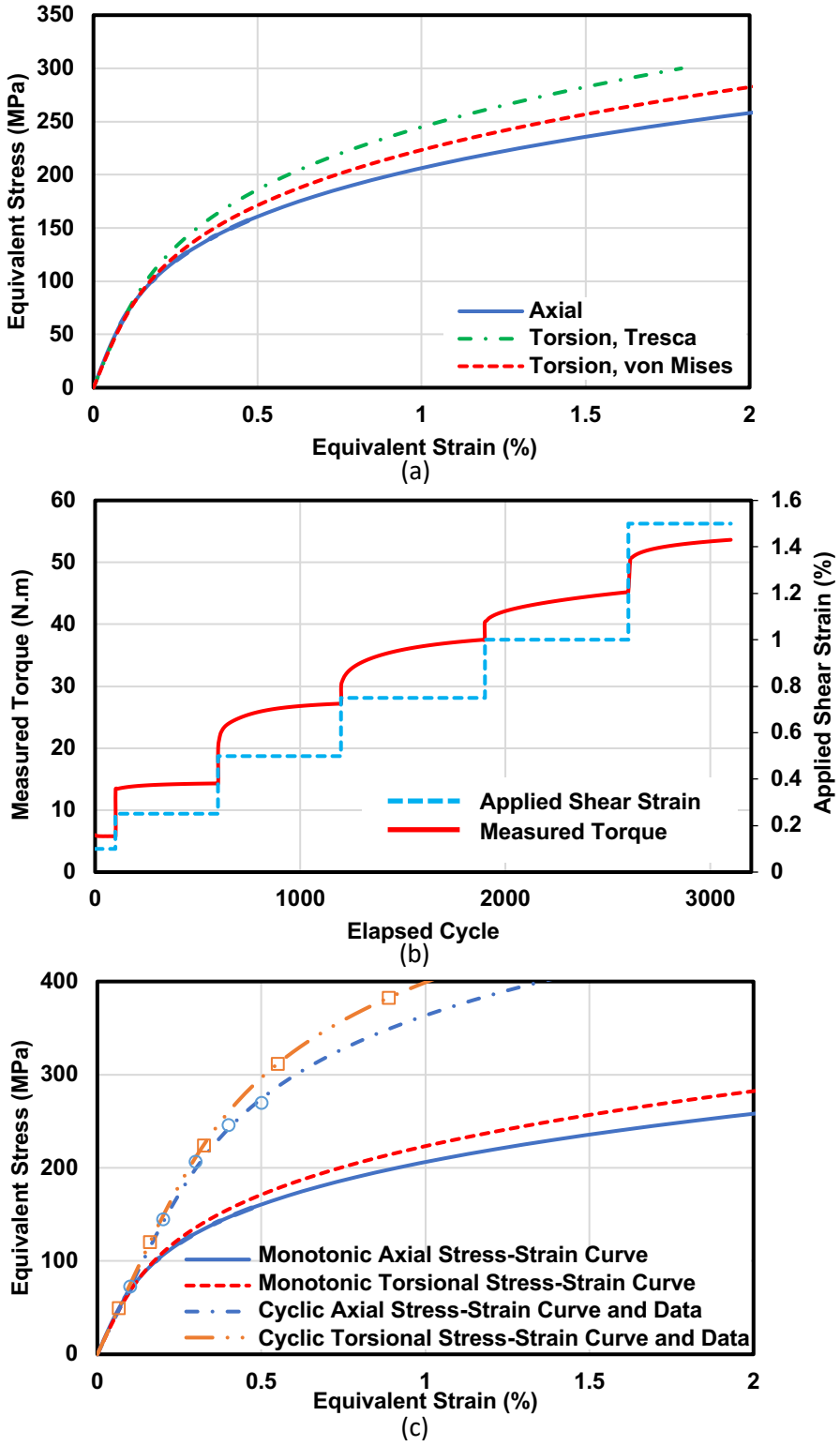

Figure 6.2. (a) Correlation of monotonic stress-strain curves under axial and torsion using Tresca and von Mises criteria, (b) variation of applied shear strain and torque vs elapsed cycle during torsion cyclic step test, and (c) superimposed cyclic and monotonic von-Mises equivalent stress-strain curves under axial and torsional loading conditions.

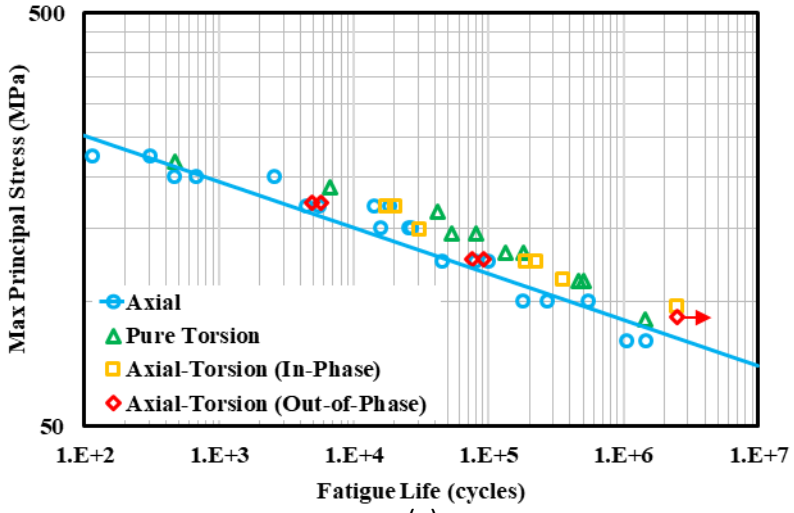

(a)

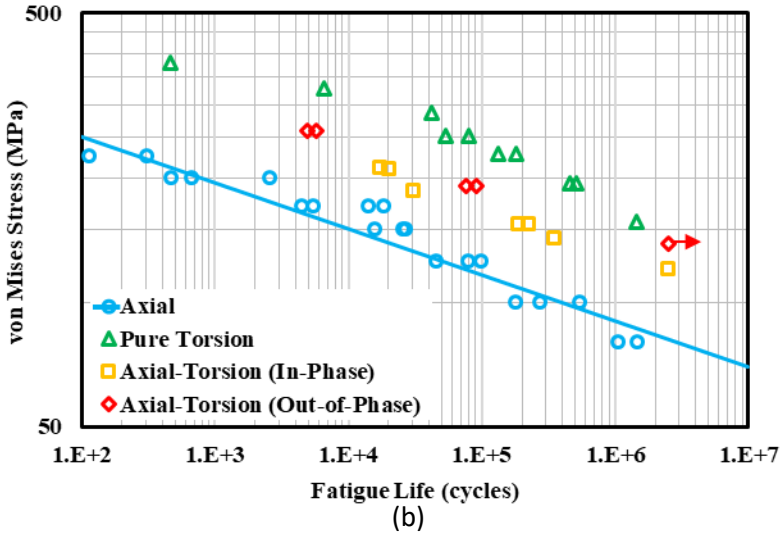

(b)

Figure 6.3. Correlation of fatigue life data under different loading conditions using (a) maximum principal stress, (b) von-Mises equivalent stress.

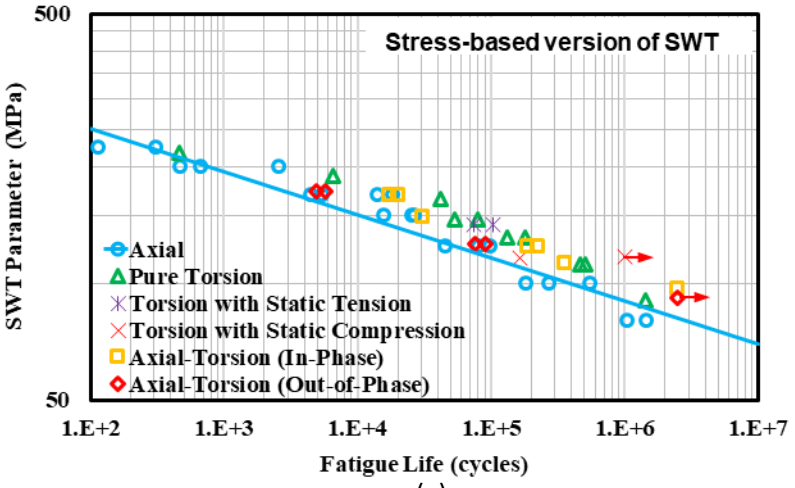

(a)

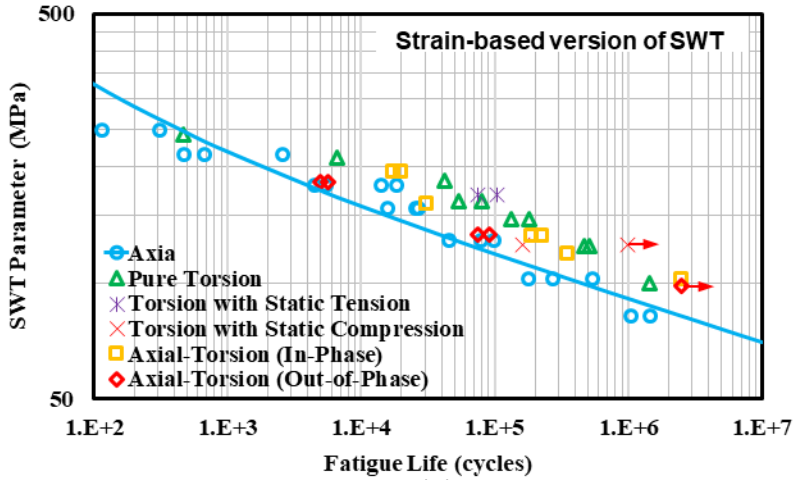

(b)

Figure 6.4. Fatigue life correlations in terms of (a) stress-based version of SWT damage parameter, and (b) strain-based version of SWT damage parameter.

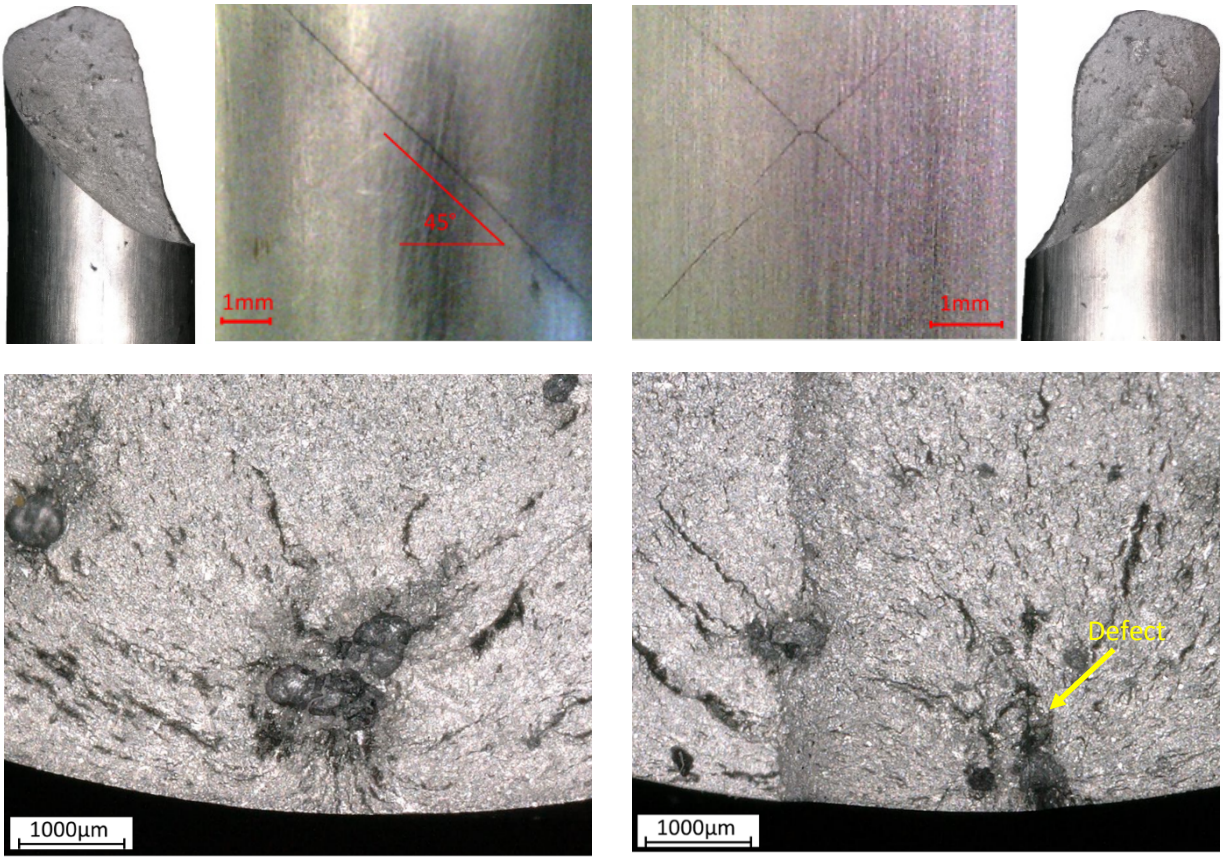

(a) (b)

Figure 6.5. Fracture surface and crack growth paths under pure torsion, (a) crack growth path on the plane of 45°, (b) crack growth paths on the specimen showing a horizontal region.

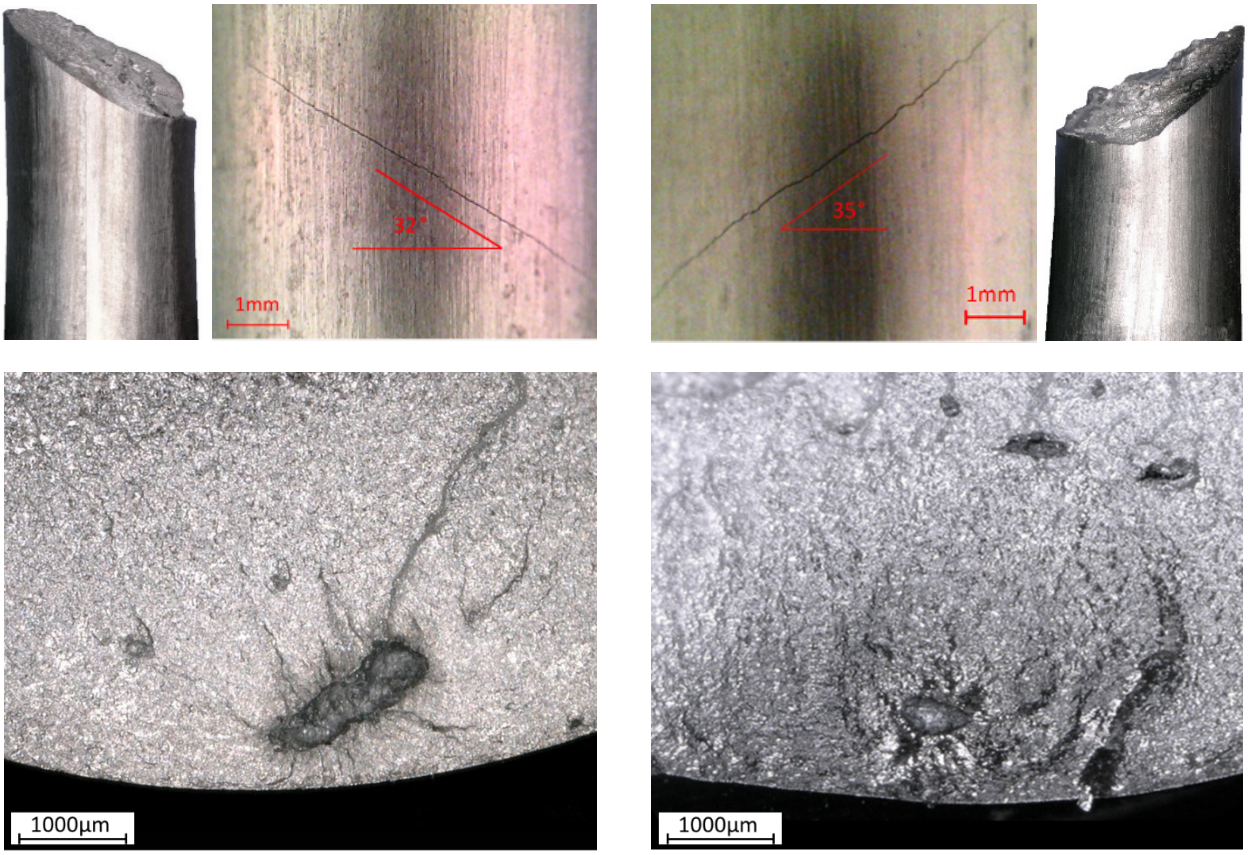

Figure 6.6. Fracture surface and crack growth path under (a) in-phase and (b) out-of-phase combined loadings.

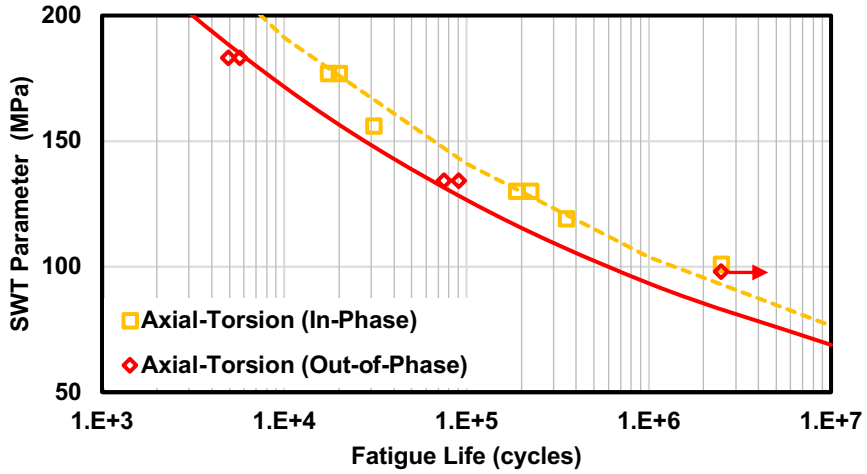

(a)

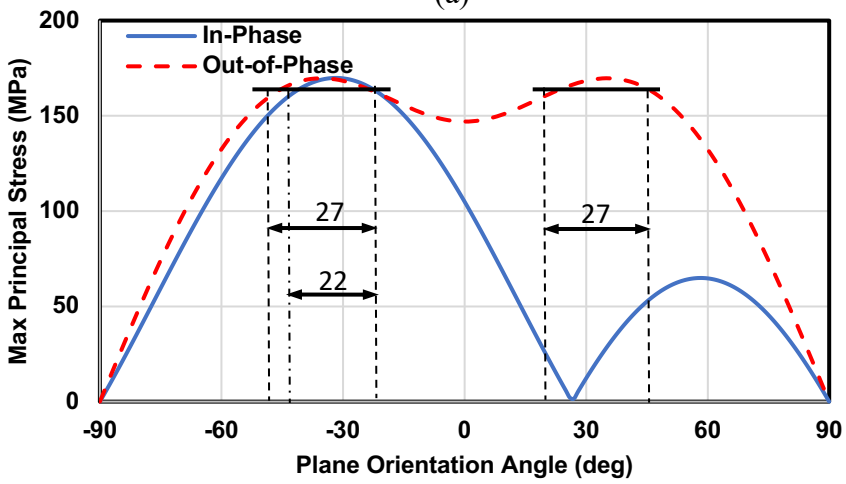

(b)

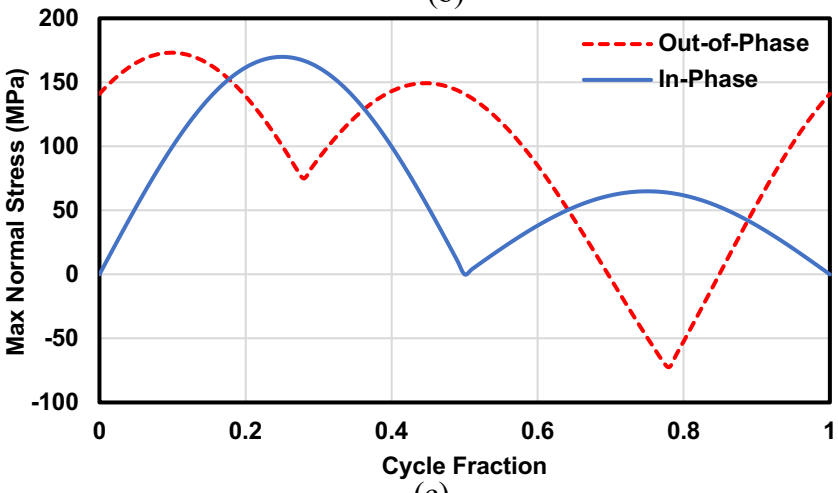

(c)

Figure 6.7. (a) Comparison of fatigue performance of the material under in-phase and out-of-phase loading conditions, (b) Comparison of maximum principal stress vs plane orientation under in-phase and out-of-phase loadings, and (c) Comparison of maximum normal stress on the plane of maximum damage under in-phase and out-of-phase loadings vs cycle fraction.

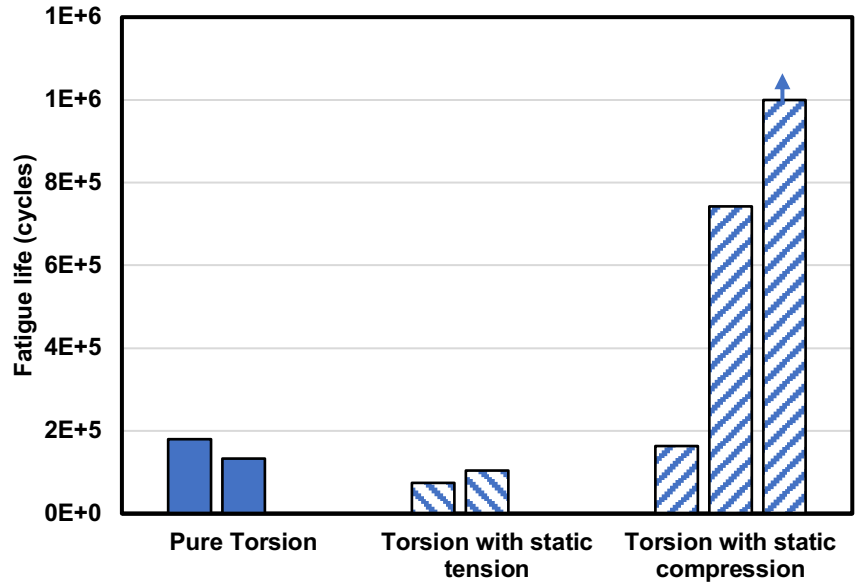

(a)

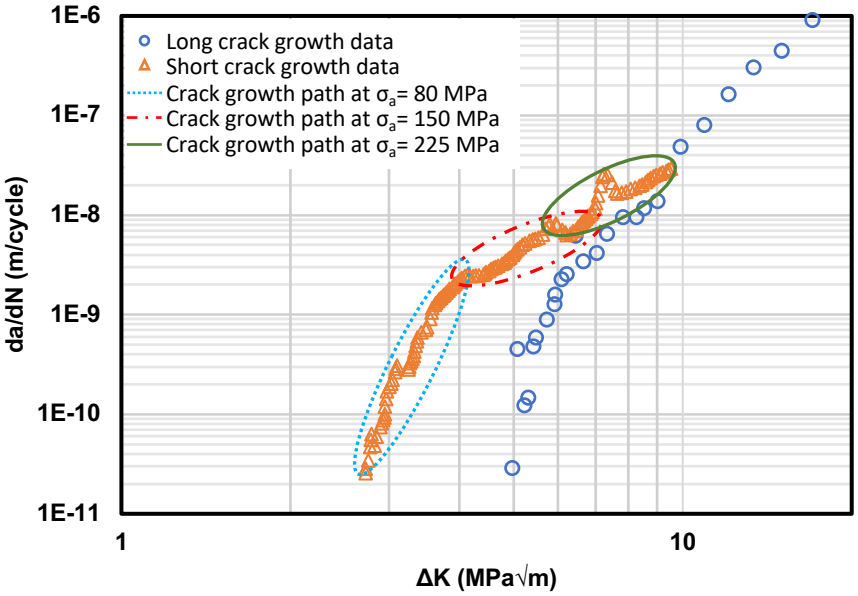

(b)

Figure 6.8. (a) Comparison of the fatigue life under pure torsion, torsion with static tension, and torsion with static compression, (b) illustration of the start and final short crack growth using the data under axial loading condition.

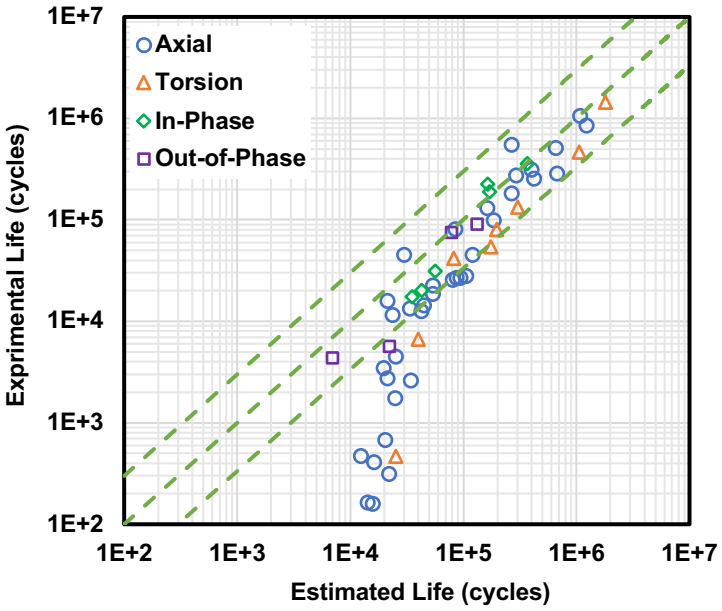

(a)

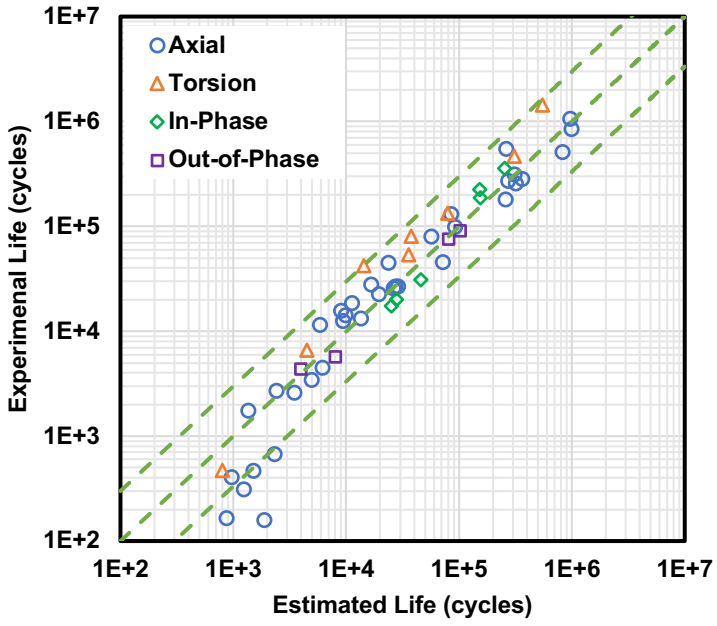

(b)

Figure 6.9. Comparison of experimental and predicted fatigue lives using (a) modified Hartman-Schijve model, and (b) modified Nisitani model.

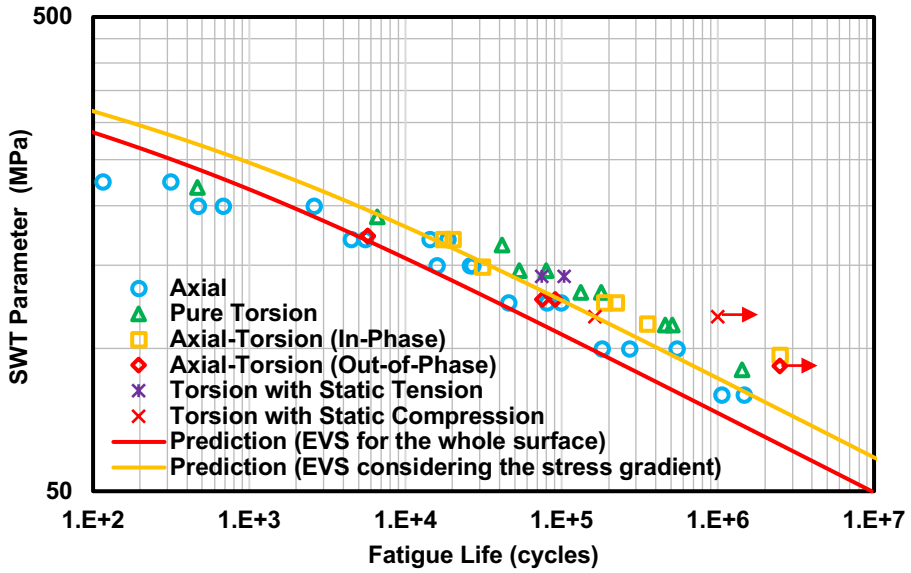

Figure 6.10. Comparison of the experimental and predicted fatigue lives using modified Nisitani model based on the maximum defect size estimated by extreme value statistics.

Chapter 7

Fatigue Performance and Modeling Under Variable Amplitude Loading

7.1. Introduction

In this chapter, the fatigue performance of cast aluminum alloy is studied under variable amplitude loading conditions. To achieve this goal, variable amplitude axial fatigue tests using a real industrial load spectrum were performed. Mean stress effect was also studied by conducting variable amplitude fatigue tests with significant mean stress. The fatigue life of the specimens under different loading conditions was estimated using both *S*-*N* approach as well as fracture mechanics approach.

For *S*-*N* approach, cycle counting was performed using rainflow counting method to separate the cycles with their ranges and mean stresses. The damage was then computed using stress-life (*S*-*N*) data from uniaxial fatigue tests under constant amplitude loading.

Fracture mechanics approach was also used to consider the effect defects as well as studying the effect of load sequence in estimating the fatigue life. Fatigue lives were estimated by neglecting the effect of load sequence using a small crack growth model through direct summation

approach, while the FASTRAN program was also used to consider the load sequence effect on estimated fatigue lives.

In fracture mechanics approach, the fatigue life was estimated from the observed defects on fracture surfaces of failed specimens, as well as the maximum defect size within the specimens estimated by extreme value statistics using metallography and micro-computed tomography evaluations. The advantage of extreme value statistics is that the maximum defect size in a component of the desired volume can be estimated. Therefore, a lower bond for fatigue behaviour can be estimated using the estimated maximum defect without a prior knowledge about the actual defects within the components.

7.2. Experimental Program

The material used in this study was A356 aluminium alloy. Solid dog-bone shape specimens with a nominal gauge section diameter of 5 mm, uniform gauge length of 30 mm, and grip diameter of 25 mm were manufactured by high pressure die cast (HPDC) process and heat treated as standard T6 procedure. As the majority of the components manufactured by HPDC products are used with no machining. the specimens were tested in as-cast surface finish condition. The only modification applied on the specimens was trimming of the flash remained from casting using 600 mesh sand paper. In Chapter 3 the maximum defect size within the specimens were estimated using extreme value statistics, which is used in this Chapter for fatigue life estimation.

Uniaxial fatigue tests were performed using a simulated variable amplitude service load history under load control condition. In order to study the effect of mean stress, some fatigue tests were also performed under high mean stress condition. The plots showing a representative portion

of the history of 58000 reversals under high and low mean stresses are shown in Figure 7.1. For each mean stress condition, tests were conducted at different stress levels until fracture occurred.

The fracture surface of each specimen was also studied by digital optical microscopy to identify the crack initiating pore. Typical fracture surface of the specimens failed under high mean stress condition are illustrated in Figure 7.2. As can be seen in this figure, the fatigue cracks initiated from defects and the beach marks corresponding to internal crack growth can be clearly seen, while the crack growth region under low stress level is longer than that under high stress level. Similar fracture surfaces were observed for the other specimens failed under high or low mean stress levels. The size of the fatal pores was measured by image analyzer software as the square root of the area of the defects. Murakami et al. [1] suggested that this parameter is promising for considering the effect of both defect size and shape on fatigue life. The measured defect sizes were then used in estimating the fatigue life. The summary of the loading conditions, the results of fatigue tests, and the size of fatal defects measured from the fracture surface of the specimens are presented in Table 7.1.

7.3. Fatigue Life Estimations Based on *S-N* Approach

S-N approach, in which the load sequence effect is neglected, is based on evaluating the damage defined as the sum of the fraction of life of a series of load cycles. Among a variety of approaches available to evaluate the damage under variable amplitude loading, Palmgren-Miner linear damage rule (LDR) is the most widely used [102]. The fatigue life evaluation based on this approach consists of cycle counting to compare the effect of variable amplitude load histories to fatigue data under constant amplitude loading. The cycle counting method followed in this study was rainflow cycle counting approach, which is the most commonly used method and detailed in

ASTM Standard E1049 [103]. The rainflow histograms of the two load histories including high and low mean stress level are illustrated in Figure 7.3.

The damage at each stress level is determined using the *S-N* curve from constant amplitude fatigue tests as the primary input. The experimental stress-life (*S-N*) curve of this material was obtained and discussed in Chapter 4 (see Figure 4.4b). However, as the mean stress is involved in variable amplitude loading, the effect of mean stress should be accounted. It has been shown in Chapter 3 that Smith-Watson-Topper (SWT) parameter is quite accurate in considering the mean stress effect. The stress-based version of SWT equivalent stress is given by [79]:

$$\sigma_{SWT} = \sqrt{\sigma_a \sigma_m} \tag{7.1}$$

As aluminum alloys, like many other metals, do not exhibit a fatigue limit under variable amplitude loadings, the *S-N* curve in a log-log plot, which is usually represented by Basquin equation, can be extrapolated to below the fatigue limit. The Basquin equation for this material was calculated using fatigue life data obtained under fully-reversed uniaxial loading condition by taking the fatigue life and stress amplitude as dependent and independent variables, respectively, as given by:

$$\sigma_a = 421 N_f^{-0.111} \tag{7.2}$$

Using Equation (7.1) for mean stress correction, the expected fatigue lives, $N_{f,i}$, at different stress levels were calculated by Equation (7.2). The damage was then computed considering the expected fatigue life and number of cycles at each stress level as $n_i/N_{f,i}$. Having summed the damages at different stress levels, the total damage of a block under variable amplitude loading can be calculated following the linear damage summation rule (LDR), as follows:

$$\sum \frac{n_i}{N_{f,i}} = \frac{n_1}{N_{f,1}} + \frac{n_2}{N_{f,2}} + \cdots = D_{cr} \tag{7.3}$$

The conventional value of the sum of damage ratios for failure, D_{cr}, in Equation (7.3), is 1. However, it has been shown in several studies, such as in [104–107], that when there is significant tensile mean stress, assuming fatigue failure at a damage sum equal to unity consistently results in non-conservative life estimation, particularly for aluminum alloys. This issue can be due to load sequence effect and interaction of high stress amplitude cycles which cause significant plastic deformation on the subsequent smaller cycles in a variable amplitude load history. Therefore, a value of 0.3 has been suggested for D_{cr}, in variable amplitude load histories containing significant tensile mean stress fluctuations. It is noteworthy that although the damage sum of 0.3 is empirically derived, its applicability has been supported by a large amount of experimental data [104–107]. Therefore, in this study the value of D_{cr} was assumed to be 0.3 when the mean stress was high, while it was accounted as unity when the mean stress was low.

The results of fatigue life estimation using *S-N* approach are summarized in Table 7.2. As can be seen in this table, considering the sum of damages equal to 1 and 0.3 for low and high mean stress conditions results in a reasonable estimation for fatigue life.

7.4. Fatigue Life Estimations Based on Fracture Mechanics Approach

7.4.1. Crack growth with neglecting the load sequence effect

In defect containing materials, due to high stress and strain concentrations around defects, cracks nucleate in the first few cycles and the fatigue life is dominated by crack growth. Therefore, for estimating the fatigue life the damage tolerant approach can be followed. According to this approach, the fatigue life of a component containing cracks (or flaws) is associated with crack growth from its initial length (or size) to some intermediate length (or size) or to the final length (or size) at fracture. It is worth mentioning that in defect containing materials, the defects are not

cracks at first, however, once cracks are initiated at either of their edges, then the effective crack size will include that of the defects. A significant advantage of this approach is that the defects and their contribution can be explicitly considered in life estimation.

One approach for estimating fatigue life based on crack growth under variable amplitude loading is summation of damage caused by each cycle through direct summation method [15]. In this method, the crack length after *N* cycles of load application is computed as:

$$a_N = a_0 + \sum_{i=1}^{N} \Delta a_i = a_0 + \sum_{i=1}^{N} f(a_i, \sigma_i) \tag{7.4}$$

where a_0 is the initial crack (flaw) size. The crack growth increment, Δa_i, associated with each cycle of variable amplitude loading can be estimated from a fatigue crack growth model. The increment of crack growth for each block can be estimated for different mean and stress amplitude levels obtained though rainflow counting method and summation of damage continues cycle by cycle until fracture occurs or predetermined crack length is reached.

For determining the crack growth increment at each cycle both long or small crack growth models can be used. However, as the size of defects in castings are typically in the range of physically small cracks, using small crack growth model will be appropriate. In Chapter 5, it was shown that using small crack growth models can predict the fatigue life in reasonable agreement with the experimental results. Using SWT damage parameter to consider mean stress correction, a small crack growth model was also proposed which is capable of predicting the fatigue life under different loading conditions. The proposed model is given by:

$$\frac{da}{dN} = A\left[\left(E\frac{\varepsilon_a \sigma_{max}}{{\sigma_u}^2}\right)^s a\right]^t \tag{7.5}$$

where E is elastic modulus, ε_{max} is maximum tensile strain, σ_a is stress amplitude, σ_u is ultimate tensile strength, a is crack length, and A, s and t are materials constants, which can be determined using small crack growth rate data.

In Chapter 5, the values of A, s, and t were determined as 7.86×10^{-3} m/cycle, 2.4, and 1.24, respectively, while the amount of maximum tensile strain was computed by Ramberg-Osgood equation obtained through incremental cyclic step test, as discussed in Chapter 3. This model was used in Chapters 5 and 6 for predicting the fatigue lives under constant amplitude axial loading including mean stress and stress gradient, as well as torsion and multiaxial loading conditions and reported that the predicted fatigue lives were in very good agreement with the experimental data.

Fatigue lives under variable amplitude loadings can also be predicted using this model through direct summation method, given in Equation (7.5). The advantage of this approach over S-N approach is that the contribution of defects is considered in life estimation explicitly.

Assuming the initial crack size as the defects size measured from fracture surfaces and a final crack length of 2 mm which is approximately the final crack length at fracture in the used specimens geometry and also the typical final length for small cracks, fatigue lives under different variable amplitude loading conditions were estimated. The results are summarized in Table 2 and compared with the experimental fatigue lives in Figure 7.5(a). As can be seen, the predicted fatigue lives using the defect size measured from fracture surfaces are in reasonable agreement with the experimental fatigue lives under both high and low mean stress levels. Although the direct summation method accounts for every cycle in the load history, it assumes that the crack growth increment related to each cycle or block is not influenced by the prior cycles. However, neglecting the load sequence effect for the applied load history in this study resulted in reasonable estimations, which may be due to the repeated number of the overloads within this load spectrum.

7.4.2. Crack growth with considering the load sequence effect

Under constant amplitude loading with uniform stress amplitude, the fatigue life can be simply estimated by integration of an appropriate crack growth model from the initial to the final crack length. However, the crack growth rate depends not only on the stress amplitude level and stress ratio, but also on previous load history which may have left tensile or compressive residual stress at the crack tip, leading to acceleration or retardation of crack growth, respectively. Therefore, estimation of fatigue life under variable loading requires extensive computation considering the effect of load history and changes in plasticity induced closure levels. Considering the complexity of such an analysis, FASTRAN crack growth program (version 5.42) was used. This program considers the load sequence effect along with the plasticity induced crack closure. The distribution of residual deformation in the crack wake is used to compute the contact stresses and far field opening stress level for a given crack configuration.

The FASTRAN program requires the input of several basic material properties, such as Young's modulus, yield strength, and ultimate strength. In addition, the characterization of crack growth rate as a function of applied effective stress intensity factor range, ΔK_{eff}, is also required. For obtaining the crack growth rate data as a function of effective stress intensity factor, the fatigue crack growth rate test data at different stress ratios are needed. The analytical crack closure model is then used to collapse crack growth data at different stress ratios onto a single curve. The crack growth rate data, then, can be defined either as universal crack growth rate equations (i.e. FASTRAN equation), or a table of closure corrected effective SIF range, ΔK_{eff}, versus crack growth rate. The effective stress intensity factor defied as:

$$\Delta K_{eff} = (1 - S_0/S_{max})/(1 - R)\Delta K \tag{7.6}$$

where S_0 is the crack opening stress which is a function of stress ratio, R, and stress level, S_{max}, as follows:

$$S_0/S_{max} = A_0 + A_1R + A_2R^2 + A_3R^3 \qquad \text{for } R \geq 0 \tag{7.7}$$

$$S_0/S_{max} = A_0 + A_1R \qquad \text{for } -1 \leq R \leq 0 \tag{7.8}$$

$$A_0 = (0.825 - 0.34\alpha + 0.05\alpha^2)[\cos(\pi S_{max}/2\sigma_0)]^{1/\alpha} \tag{7.9}$$

$$A_1 = (0.415 - 0.071\alpha)[S_{max}/\sigma_0] \tag{7.10}$$

$$A_2 = 1 - A_0 - A_1 - A_3 \tag{7.11}$$

$$A_3 = 2A_0 + A_1 - 1 \tag{7.12}$$

In Equations (7.9) and (7.10), σ_0 is the flow stress which is taken as the average between the uniaxial yield stress and ultimate strength of the material, and α is the constrain factor used to elevate the flow stress σ_0 at the crack tip to account for the influence of stress state ($\alpha\sigma_0$) on plastic zone sizes and crack-surface displacements. However, constraint factor is also important in the context of the FASTRAN analytical crack closure model to obtain the baseline fatigue crack growth rate data from the crack growth data typically collected using standard test specimen configurations such as Middle Tension, M(T), and Compact Tension, C(T), specimens.

Using the crack growth data from literature for cast A356-T6 aluminum [9,108], the value of 2 was computed for α, which is in agreement with the reported value for this parameter for aluminium alloys. Therefore, the crack growth data in terms of effective stress intensity factor can be obtained using the long crack growth data.

As mentioned earlier, the fatigue cracks from defect in cast aluminum alloys are in the range of small cracks, which can grow below the threshold of long cracks and faster than long

cracks. It has also been suggested that no fatigue limit can be considered for engineered materials under variable amplitude loadings. Therefore, in predicting fatigue life of metallic materials containing small defects (flaws), it can be assumed that fatigue-crack-growth thresholds, ΔK_{th}, may not exist and the crack growth rate plot can be extrapolated below the crack growth threshold obtained under constant amplitude levels [109]. Thus, crack growth data which were used as input to the FASTRAN program included a table of crack growth rates and stress intensity factors for long and small cracks. For long cracks in which crack closure is considerable the effective stress intensity factor was used, while for small cracks it was assumed that crack closure is negligible and the stress intensity factor data were extrapolated below the crack growth threshold. The long crack growth data from [9] and small crack growth data from [99] as well as the data points used for predicting the fatigue life using FASTRAN program are illustrated in Figure 7.5.

Another important issue in FASTRAN is the crack configuration. As mentioned earlier, in defect containing materials it can be assumed that the crack nucleation life can be neglected and most of the fatigue life is spent on small crack growth. Defects can be assumed as semi-circular surface cracks [13]. Therefore, fatigue life can be estimated using either the size of fatal defects measured from the fracture surface of failed specimens or the maximum defects estimated by extreme value statistics (EVS).

Having imported the materials properties and crack configuration, fatigue life can be estimated by FASTRAN program by considering the load sequence effect and variation in plasticity induced closure levels in the load history cycle by cycle. As both small and crack growth data were imported to the program the crack growth was simulated until fracture occurred. The results of fatigue life estimated by FASTRAN is compared with experimental fatigue lives in Figure 7.5(a). As can be seen in this figure, the fatigue lives estimated by considering the crack

growth cycle by cycle using FASTRAN are in very good agreement with the experimental lives when the actual defect size measured from fracture surfaces are considered as the initial cracks. Comparison of fatigue lives estimated by FASTRAN with those estimated by direct summation approach also reveals that both approaches could estimate the fatigue lives satisfactorily, which means that the load sequence effect for the load history used in this study did not have significant effect. This is thought to be due to the repeated number of the overloads in the load spectrum used in this study.

7.4.3. Fatigue life estimation using the maximum defect size estimated by extreme value statistics

In previous sections, the capability of different approaches in fatigue life estimation under variable amplitude loadings was evaluated based on the fatal defect size measured on fracture surfaces. In practical situations, the maximum defect size of a component of desire volume can be estimated using extreme value statistics. Fatigue life estimation can then be performed using the maximum defect size estimated by extreme value statistics.

Based on extreme value statistics, the maximum defect size within a component is estimated using the cumulative distribution of defects obtained from metallography examination or micro-computed tomography evaluation. The maximum defect size expected to be exceeded once in the desired volume is the defect size corresponding to the return period, which is a function of defect density and the prospective material volume. The maximum defect size in the specimens of this study was estimated as 1426 μm, discussed in Chapter 3. Therefore, using the fatigue performance of the laboratory specimens, the lower bond of fatigue behavior of an industrial component can be predicted.

Fatigue lives under both high and low mean stress levels were estimated by direct summation approach as well as FASTRAN program based the estimated maximum defect size, which are compared with experimental fatigue lives in Figure 7.5(b). As can be seen, using the maximum defect size results in conservative fatigue life estimations in comparison to the experimental data. It should be mentioned that in this study only two specimens in each loading condition were examined with variations in fatigue life between duplicate tests being a factor of 2. However, based on the fatigue test results under constant amplitude loading (Figure 4.4), it is expected that a more significant scatter on the fatigue life under variable amplitude loading will be observed with additional tests. In this case, the estimation of fatigue life using the maximum defect size obtained through extreme value statistics may be more appropriate.

7.5. Summary and Conclusions

This chapter investigated the fatigue performance of high pressure die cast A356-T6 aluminum alloy containing porosity under variable amplitude loading at different mean stress levels. Experimental fatigue tests were conducted using realistic service load history when the mean stress was relatively low or high. The fatigue lives were estimated using both *S*-*N* approach and fracture mechanics approach. For *S*-*N* approach, rainflow cycle counting method was used to obtain the number of cycles for each mean and amplitude stress level. The damage at each mean and amplitude stress level was evaluated using experimental *S*-*N* data, obtained under constant amplitude axial fatigue tests. The Smith-Watson-Topper (SWT) parameter was used to account for the mean stress effect. In fracture mechanics approach the fatigue lives were estimated using both direct summation method by neglecting the load sequence effect, as well as FASTRAN program in which the load sequence effect was considered.

Based on the results of this study, the following conclusions are made:

1. Following the *S*-*N* approach for fatigue life estimation, using the sum of the damage equal to unity resulted in a reasonable estimation for fatigue life when the mean stress level was low. When the tensile mean stress was high, assuming the sum of damage equal to 0.3 resulted in acceptable estimated lives within the scatter bands of ±3.
2. Fatigue life estimations by applying direct sumation method using a small crack growth model were in good agreement with the experimental fatigu lives, although the effect of load sequence was neglecting in this method. This may be due to the repeated number the overloads within the applied load spectrum.
3. Considering the load sequence and crack closure effects using FASTRAN program could estimate the fatigue lives in a very good agreement with the experimental results, when the actual defect size measured from fracture surface of failed specimens were used as initial cracks.
4. When the maximum defect size estimated by extreme value statistics was used as the initial defect size, the estimated fatigue lives were conservative. However, regarding the expected scatter on the fatigue life, the estimation of fatigue life using the maximum defect size obtained through extreme value statistics may be more appropriate.

Table 7.1. Summary of fatigue test results under different loading conditions.

Specimen ID	Mean stress	Max Stress (MPa)	Min Stress (MPa)	Frequency (Hz)	Fatigue life (Blocks)	Defect size[1] (μm)
VA380-1	Low	240	-240	5	6.3	827
VA380-2	Low	240	-240	5	11.2	656
VA320-1	Low	200	-200	10	55.4	861
VA320-2	Low	200	-200	10	38.5	1088
VA250-1	High	250	-64	5	0.92	1189
VA240-1	High	240	-61	5	3.42	1191
VA240-2	High	240	-61	5	4.41	1065
VA200-1	High	200	-51	10	36.74	615
VA200-2	High	200	-51	10	21.93	1071

[1]The defects size measured from fracture surfaces

Table 7.2. Summary of fatigue life estimation using both S-N and fracture mechanics approaches.

ID	Mean Stress	Experimental life (block to failure)	S-N Approach		Fracture Mechanic Approach			
					Direct Summation		FASTRAN	
			D_{cr}	Estimated life (block to failure)	Estimated life (block to failure) (based on observed defect)	Estimated life (block to failure) (based on EVS)	Estimated life (block to failure) (based on observed defect)	Estimated life (block to failure) (based on EVS)
VA250-1	High	0.92	0.3	2.1	3.4	2.3	3.6	2.7
VA240-1	High	3.42	0.3	3	4.6	2.7	5.1	3.6
VA240-2	High	4.42	0.3	3	5.6	2.7	6.1	3.6
VA200-1	High	36.74	0.3	15.6	35.7	9.3	34.7	13.7
VA200-2	High	21.93	0.3	15.6	17.7	9.3	20.6	13.7
VA380-1	Low	6.29	1	6.82	12.4	4.3	8.6	3.1
VA380-2	Low	11.22	1	6.82	16.3	4.3	11.4	3.1
VA320-1	Low	55.38	1	32	36.4	13.4	42.1	19.3
VA320-2	Low	38.49	1	32	25.6	13.4	30.2	19.3

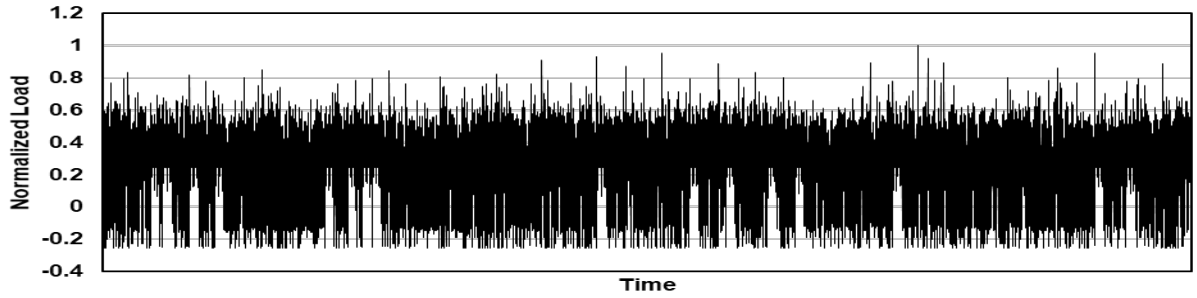

(a)

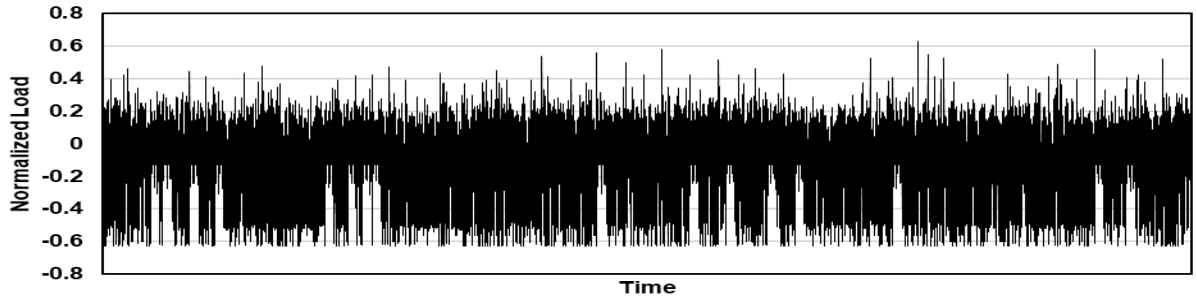

(b)

Figure 7.1. Representative portions of the load histories containing 15000 reversals used for (a) high mean stress, and (b) low mean stress conditions.

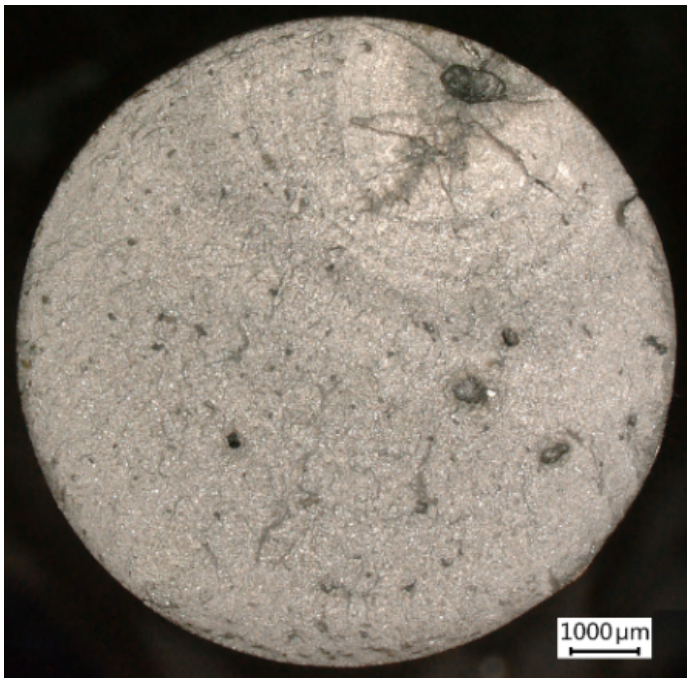

(a)

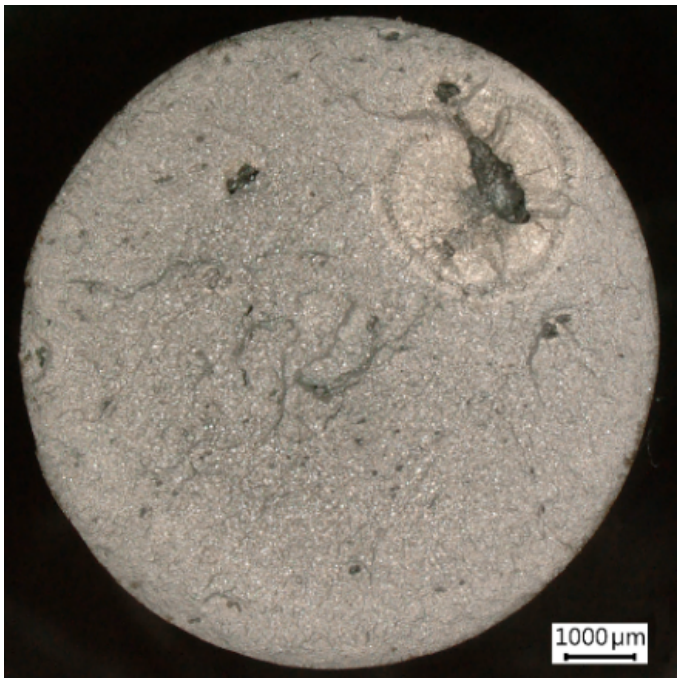

(b)

Figure 7.2. Fracture surface of the specimens failed under high mean stress condition when the maximum stress was (a) 200 MPa, and (b) 240 MPa.

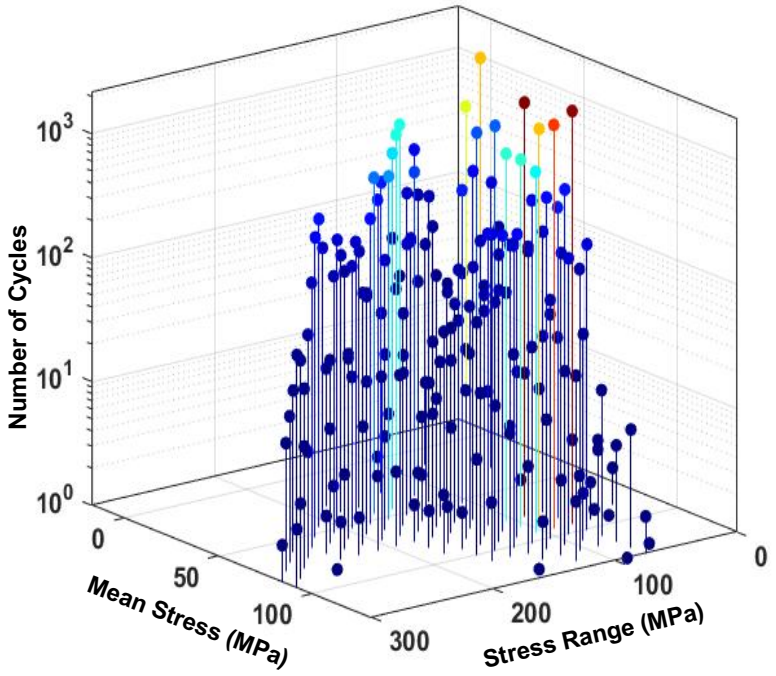

(a)

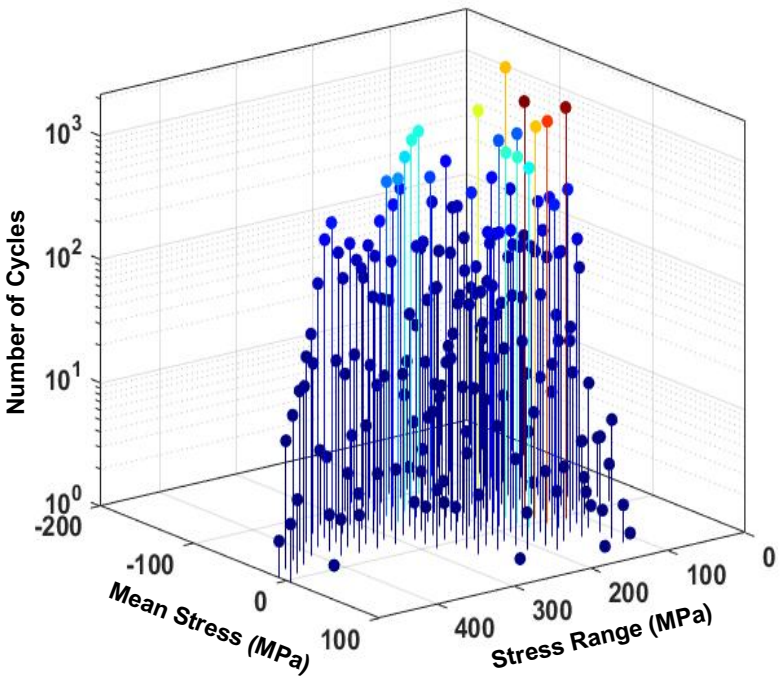

(b)

Figure 7.3. Rainflow histograms of load spectrums with (a) high mean stress, (b) low mean stress.

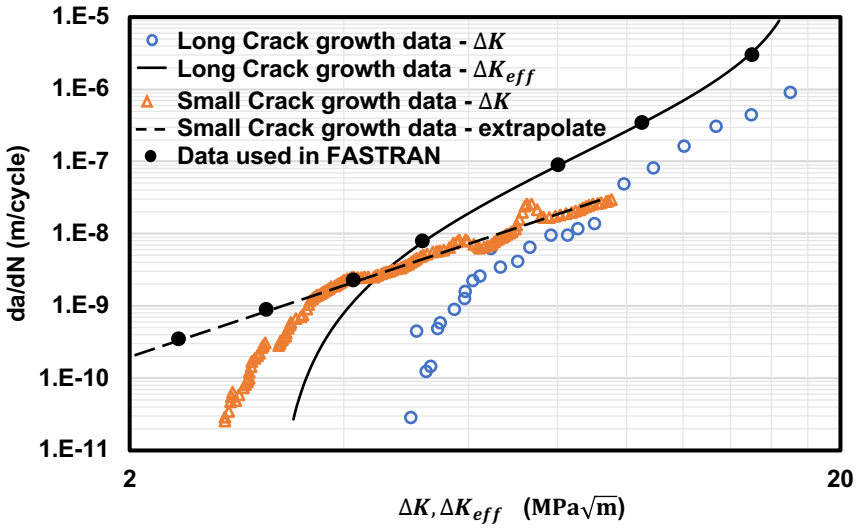

Figure 7.4. Illustration of long crack growth data from [9] and small crack growth data from [99] as well as the data points used for predicting the fatigue life using FASTRAN program.

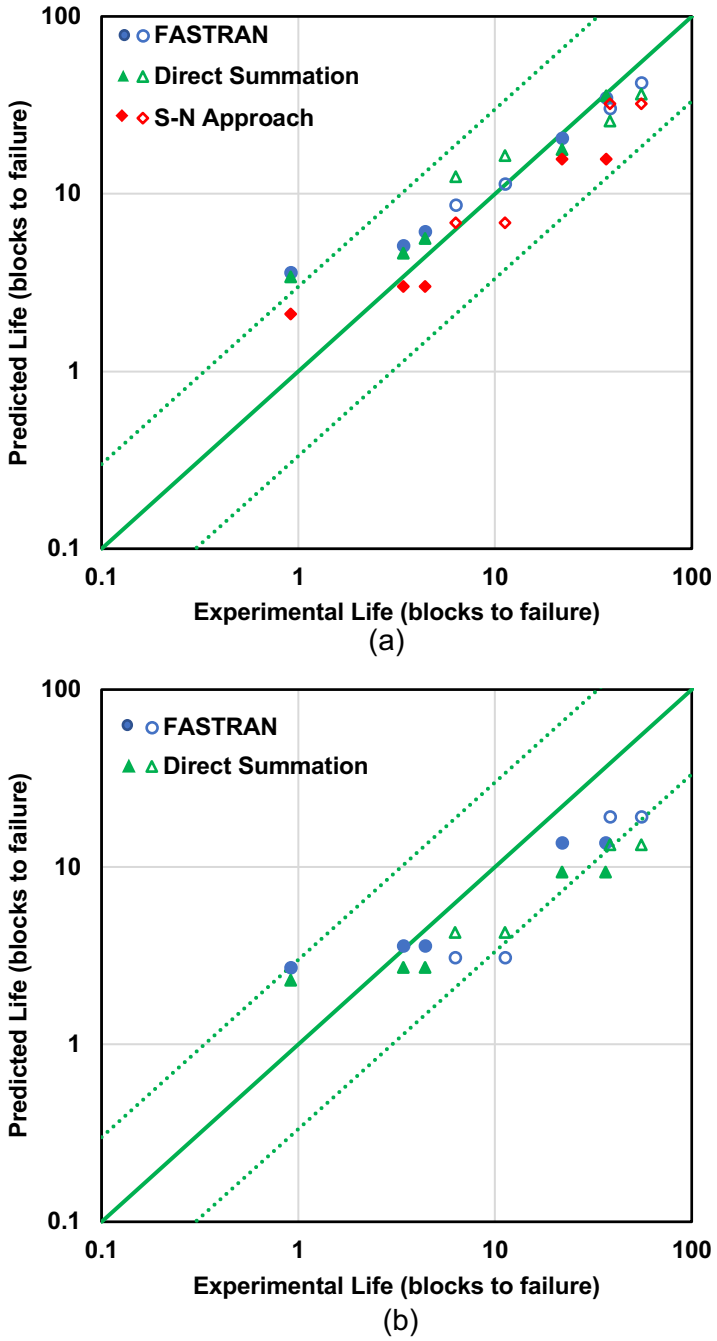

Figure 7.5. Comparison of experimental and estimated fatigue lives using different approaches (a) based on the size of fatal defects on fracture surfaces, (b) based on the maximum defect size estimated by extreme value statistics. Hollow symbols represent the data under low mean stress level and solid symbols are associated with the high mean stress condition.

Chapter 8

Summary and Suggestions for Future Research

8.1. Summary

Defects can affect the mechanical properties of industrial components significantly. Not only can defects weaken tensile strength, reduce ductility and lower fatigue performance, but also they result in inconsistency in mechanical performance, specifically by increasing the scatter in fatigue life. On the other hand, for many manufacturing techniques such as casting, additive manufacturing, or powder metallurgy, reducing the defect size below the critical size is not technically nor economically feasible. Therefore, deeper understandings of the mechanisms controlling the fatigue properties and prediction of fatigue life are necessary to design durable components.

The main Objective of this study was to study the fatigue performance of defect containing materials under different loading conditions and evaluate or develop models for fatigue life predictions. To achieve this goal, five specific objectives were followed including defect characterization and statistical analysis of defects, fatigue performance under uniaxial stress state, fatigue life prediction under uniaxial stress state, fatigue performance and life prediction under torsion and axial-torsion combined loadings, and fatigue performance and modeling under variable amplitude loading conditions. Therefore, a comprehensive experimental program was designed to

address all these objectives. The experimental tests were conducted on A356 cast aluminum specimens produced by high pressure die casting process, which is widely used to produce a wide range of industrial components. This material was used in this study as an illustrative material containing defects, while the methods used in this study may also be applicable for other defect containing materials.

As the mechanical properties of cast components can be significantly affected by existing defects, it is necessary to evaluate these defects. Therefore, the first specific objective of this study was defect evaluation and statistical analysis of defects by using metallography, X-ray radiography, and micro-computed tomography (μCT) techniques. It was observed that X-ray radiography which is often used in industrial applications may not be reliable for defect evaluation, while statistical analysis of defects using both metallography and μCT evaluations was reliable. In addition, increasing the number of metallography cross sections improves the accuracy of 2D measurements.

It was also observed in both 2D and 3D defect data that as the size of pores increases, they deviate more from ideal spherical (or circular in 2D) defect, indicating reduced sphericity (or circularity in 2D) of pores with increasing defect size. Moreover, statistical analysis of defects showed that the pore distribution in the specimens produced by high pressure die cast may not be random throughout the cross section, especially in large section sizes. In addition, as the casting section size increases, both defects size and density also increase.

The maximum defect size was estimated by extreme value statistics using both 2D and 3D data. It was observed that the estimated defect size using GEV distribution function (for 2D defect data) and GPD distribution function (for 3D defect data) were in very good agreement with the maximum observed defect size on fracture surfaces. The commonly used EV distribution function

for 2D defect data underestimated the maximum defect size in comparison to the maximum observed defect size on fracture surfaces. To estimate the maximum defect size of the entire large specimen where the defects are not distributed randomly the weakest link theory was applied. The prediction of the weakest link theory was in better agreement with the maximum defect size on fracture surfaces, in comparison with the prediction using the assumption of random distribution throughout the cross section.

The second objective of this work was to study the fatigue performance under uniaxial stress state. Fatigue behavior of this material was investigated under uniaxial stress state to study the effects of defects, section size, stress gradient, and mean stress. Fatigue tests were performed on two specimen sizes and under various loading conditions including tension-compression, tension-tension, and rotating bending were used. Studying the fracture surfaces of the specimens failed under different loading conditions indicated that in almost all specimens fatigue cracks originated from porosity. It was observed that under axial loadings the fatal pores were randomly distributed in the entire cross section, while under rotating bending the crack initiating defects were located near the surface of the specimens.

Considering the fatigue life data, significant scatter was observed in fatigue life under axial and rotating bending tests. Studying the fracture surfaces of the specimens revealed that at a given stress level, the larger defects lead to shorter life, which shows that the defects are the main cause of scatter in fatigue life. Further, at a given stress amplitude level, fatigue life of large specimens under fully-reversed condition was shorter than that of small specimens by one order of magnitude. This is attributed to larger defect size in large specimens in comparison to small specimens. In addition, fatigue life of the specimens under tension-tension fatigue test was shorter than that under fully-reversed fatigue tests with the same stress amplitude. Smith-Watson-Topper parameter was

used for mean stress correction and it was shown that this parameter was quite accurate in predicting the fatigue life with the applied mean stress. It was also shown that fatigue lives under rotating bending were longer by a factor of 5 than that under axial loading, which is attributed to stress gradient effect and smaller highly stressed volume under rotating bending. Statistical analysis of fatigue life at different stress levels revealed that both lognormal and Weibull distributions can fit the experimental data, however, based on Anderson-Darling test lognormal distribution was a better representative of the experimental data.

The third specific objective of this study was fatigue life modeling and predictions. To achieve this goal, the fatigue life data under uniaxial loading were used to study the predictive capability of different approaches. Fatigue strength was predicted using semi empirical approaches, i.e. Murakami, Noguchi, and Ueno models, using Vickers hardness and maximum defect size estimated by extreme value statistics. It was found that predicting the long life fatigue strength of this aluminum alloy using Murakami model was non-conservative, while the predicted fatigue strength using Ueno model was in a very good agreement with the experimental data.

Fatigue lives were predicted under different loading conditions. In one approach the fatigue performance of small specimens was taken as the reference to predict the fatigue behavior of large specimens and under rotating bending conditions. Predictions were performed by estimating the fatigue strength using the maximum defect size within the specimens and updating the Basquin exponent with regard to the estimated fatigue strength at the fatigue life of 10^7 cycles. Fatigue life prediction was also performed using fracture mechanics approach. The predictive capability of long and small crack growth models was evaluated using the fatal defects measured from fracture surfaces as the initial cracks. The modified Paris equation was used as long crack growth model, while the modified Paris equation with El-Haddad parameter and the modified Hartman-Schijve

model were used as small crack growth models. Furthermore, the fatigue lives were also predicted using a new small crack growth model proposed in this study using SWT damage parameter in Nisitani model.

It was concluded that fatigue lives predicted by the modified Paris Equation, as a LEFM-based long crack growth model, were non-conservative. Considering the effect of small cracks using the intrinsic crack length defined by El-Haddad in stress intensity factor relation enhanced the predictive capability of this model at low stress levels. At high stress levels, however, the predicted fatigue lives were non-conservative in both models, which is thought to be due to the limitation of LEFM in considering the plastic deformation at high stress levels. Moreover, using long crack growth data, the modified Hartman-Schijve model could predict the small crack growth behavior in a reasonable agreement with the experimental data. Fatigue lives predicted by the modified Hartman-Schijve model were also in a good agreement with experimental data at low stress levels. At high stress levels the predicted fatigue lives were non-conservative due to limitation of LEFM in considering the plastic deformation at high stress levels. Considering the nominal plastic deformation as well as mean stress effect, a modified version of Nisitani model was proposed. It was shown that this model predicted the fatigue lives at both low and high stress levels under different loading conditions reasonably well. The predictability of the model was better than those of the other discussed models.

The effect of defect parameter on fatigue life prediction was also evaluated by characterizing fatal defects on fracture surfaces as square root of actual area of defect, square root of the area of fitted ellipse to defect, and maximum Feret diameter of defect on fracture surfaces. No significant difference was observed in predicted fatigue lives using different defect parameters. Fatigue lives under different loading conditions were also predicted based on maximum defect size

estimated by extreme value statistic. It was shown that using the estimated maximum defect as the initial crack results in very good predictions for the lower bond of fatigue lives under different loading conditions.

The fourth specific objective of this work was to study the fatigue performance under torsion and multiaxial stress state. To achieve this goal, in addition to obtaining the monotonic and cyclic deformation behavior under axial and torsion, experimental fatigue tests under torsion as well as under in-phase and out-of-phase loading conditions were conducted. In order to study the crack face interaction, a few tests were also conducted under cyclic torsion with static tension or compression. Fatigue mechanism was explored by considering the crack growth path under different loading conditions on failed specimens.

Studying the fracture surfaces of the specimens failed under different loading conditions indicated that in almost all specimens fatigue cracks originated from porosity. It was observed that contrary to axial loadings in which the fatal pores were randomly distributed in the entire cross section, under torsion and combined axial-torsion loadings the crack initiating defects were located near the surface of the specimens. Considering the orientation of fatigue crack growth at the surface of the specimens before fracture also revealed that under all loading conditions crack growth and failure occurred on the plane of maximum principal stress. This indicates a tensile mode failure, which is typical of brittle behaving materials. The brittle behavior is partly due to the stress concentration effect of casting defects.

Smith-Watson-Topper parameter was used to evaluate fatigue damage under different loading conditions. It was shown that fatigue data under different loading conditions correlated well using maximum principal stress (under fully-reversed loading conditions) and SWT damage parameters (under fully-reversed loading and also when a mean stress is present). Fatigue lives

under torsion loading were longer than those under axial loading, due to stress gradient effect under torsion. In addition, fatigue lives under in-phase loading were longer than those under out-of-phase loading due to wider range of plane orientations experiencing at least 95% of the maximum damage under out-of-phase loading. Crack growth path was more tortuous under out-of-phase loading compared to in-phase loading, thought to be due to wider range of plane orientations experiencing high stress under out-of-phase loading.

The effect of crack face interaction was studied by conducting tests under cyclic torsion with static tension or compression. It was observed that under cyclic torsion with static tension fatigue lives were shorter compared to those under pure cyclic torsion. This is due to reduction in crack face friction and roughness induced crack closure effects. Under cyclic torsion with static compression the fatigue life was significantly longer accompanied with larger scatter, due to increasing the roughness induced crack and reducing the effective stress intensity factor.

Fatigue lives for multiaxial tests were also predicted using the modified Hartman-Schijve model as well as the proposed modified version of Nisitani model based on the defect size measured from fracture surfaces of failed specimens. It was observed that the modified Hartman-Schive model could predict the fatigue lives under axial, torsion, and in-phase combined loadings reasonably well at low stress level, but at high stress levels the predictions were non-conservative. For out-of-phase loading condition, the stress intensity factor was modified by considering the ratio of plane orientations experiencing at least 95% of the maximum damage under out-of-phase and in-phase loading conditions. Considering the nominal plastic deformation as well as mean stress effect, a general model was proposed for multiaxial stress states, and it was shown that based on the defect size measured from fracture surfaces the proposed model could predict the fatigue lives under different loading conditions when the failure mode was tensile. It was also shown that

the predictability of the model is better than that of the other discussed models. Fatigue life predictions were also performed using the maximum defects estimated by extreme value statistics. It was shown that when the maximum defect size was estimated based on the whole surface, the predictions were in very good agreement with the experimental fatigue lives under axial loading. Using maximum defect size estimated for highly stressed volume under torsion also resulted in reasonable predictions under torsion and in-phase loadings.

The fifth specific objective of this work was to study the fatigue performance of defect containing materials under variable amplitude loadings. To achieve this goal, fatigue tests were conducted using an actual service load history at high and low mean stress levels. Fatigue lives were also predicted using the fatal defect size measure from fracture surfaces of the specimens as well as the maximum defect size estimated by extreme value statistics. Fatigue lives under variable amplitude loading were predicted using both *S*-*N* approach and fracture mechanics approach. For *S*-*N* approach, rainflow cycle counting method was used to obtain the number of cycles for each mean stress and stress amplitude level. The damage was then computed using experimental *S*-*N* data obtained under constant amplitude axial fatigue tests. The Smith-Watson-Topper (SWT) parameter was used to account for the mean stress effect. Following this approach, fatigue lives were predicted based on linear damage rule using the sum of the damage equal to unity when the mean stress level was low, and equal to 0.3 when the tensile mean stress was high. In addition, fatigue lives were also predicted following fracture mechanics approach using both direct summation method by neglecting the load sequence effect, as well as FASTRAN program in which the load sequence effect was considered. Fatigue life estimations based on either of these methods were in good agreement with the experimental fatigu lives, although the effect of load sequence

was neglected in direct summation method. This may be due to the repeated number the overloads within the applied load spectrum

8.2. Study Limitations

The findings of this study have to be seen in the light of some limitations. In this work one aluminum casting was used as an illustrative example and additional casting aluminum alloys are needed to validate the generality of the developed model. Furthermore, the environmental effects including testing temperature and corrosive environments which can affect the fatigue performance of defect containing materials were not considered. All experimental tests in this study were conducted at ambient temperature and with no corrosive environment. Additional work in both testing and modeling would be needed to incorporate such effects.

8.3. Suggestions for Future Research

A robust model for evaluating the crack growth and predicting the fatigue life should be applicable to a wide variety of materials and manufacturing techniques. In this study a new version of Nisitani model was proposed and it was shown that it can predict the fatigue lives of a cast aluminum alloy under different loading conditions very well. One suggestion for the future research is to investigate the predictive capability of this model for other materials or manufacturing techniques.

The proposed model is appropriate for materials in which the failure mode is tensile, while the failure mechanism in other materials can be shear or mixed mode. For materials with shear mode failure, the proposed model may be expanded by using the Fatemi-Socie parameter, while in some other materials the failure mode depends on the stress amplitude level as well as defect

distribution. Therefore, another suggestion is to develop a general model which can predict the failure mode as well fatigue lives at different stress levels.

The variable amplitude test conducted in this study were performed under axial loading. It was observed that fatigue life predictions were in reasonable agreement with experimental fatigue lives. It is suggested to conduct variable amplitude fatigue tests under multiaxial loadings and evaluate the predictive capability of different approaches under multiaxial variable loadings.

In this study extreme value statistics was used to estimate the maximum defect within the specimens, and it was shown that this approach was effective. It was also shown that the predicted fatigue lives based on the estimated maximum defect size can generate a lower bond for fatigue performance of specimens. It is suggested to conduct fatigue tests on an actual industrial component and compare the experimental fatigue lives with predictions based on the maximum defect size estimated by extreme value statistics.

It was shown in this study that the fatigue lives in defect containing materials are accompanied with a significant scatter. However, the amount of scatter in fatigue life depends on both the loading condition and defect distribution in specimens or components. Another suggestion for future research is to consider the loading conditions as well as defect distribution to develop a statistical model to account for the scatter under different loading conditions.

References

[1] Y. Murakami, Metal fatigue: effects of small defects and nonmetallic inclusions. 2002.

[2] J. Z. Yi, Y. X. Gao, P. D. Lee, H. M. Flower, and T. C. Lindley, “Scatter in fatigue life due to effects of porosity in cast A356-T6 aluminum-silicon alloys,” Metall. Mater. Trans. A, 34, 9, 1879–1890, 2003.

[3] J. Campbell, Complete casting handbook : metal casting processes, metallurgy, techniques and design, Butterworth-Heinemann, 2015.

[4] J. Boileau and J. Allison, “The effect of porosity size on the fatigue properties in a cast 319 aluminum alloy,” SAE Trans, 648-659, 2001.

[5] J. Y. Buffière, S. Savelli, P. H. Jouneau, E. Maire, and R. Fougères, “Experimental study of porosity and its relation to fatigue mechanisms of model Al-Si7-MgO.3 cast Al alloys,” Mater. Sci. Eng. A, 316, 1–2, 115–126, 2001.

[6] M. J. Couper, A. E. Neeson, and J. R. Griffiths, “Casting defects and the fatigue behavior of an aluminum casting alloy,” Fatigue Fract. Eng. Mater. Struct., 13, 3, 213–227, 1990.

[7] J. M. Boileau and J. E. Allison, “The effect of solidification time and heat treatment on the fatigue properties of a cast 319 aluminum alloy,” Metall. Mater. Trans. A, 34, 9, 1807–1820, 2003.

[8] C. J. Davidson, J. R. Griffiths, and A. S. Machin, “The effect of solution heat-treatment time on the fatigue properties of an Al-Si-Mg casting alloy,” Fatigue Fract. Eng. Mater. Struct., 25, 2, 223–230, 2002.

[9] B. Skallerud, T. Iveland, and G. Härkegård, “Fatigue life assessment of aluminum alloys with casting defects,” Eng. Fract. Mech., 44, 6, 857–874, 1993.

[10] Q. Wang, D. Apelian, and D. . Lados, “Fatigue behavior of A356-T6 aluminum cast alloys. Part I. Effect of casting defects,” J. Light Met., 1, 1, 73–84, 2001.

[11] J. Davis, "Aluminum and aluminum alloys", ASM International, 1993.

[12] R. N. Lumley, "Fundamentals of aluminium metallurgy : production, processing and applications", Woodhead Pub, 2011.

[13] M. Avalle, G. Belingardi, M. P. Cavatorta, and R. Doglione, "Casting defects and fatigue strength of a die cast aluminium alloy: a comparison between standard specimens and production components", Int. J. Fatigue, 24, 1, 1-9, 2002.

[14] C. Nayhumwa, N. R. Green, and J. Campbell, “Influence of casting technique and hot isostatic pressing on the fatigue of an Al-7Si-Mg alloy,” Metall. Mater. Trans. A, 32, 2, 349–358, 2001.

[15] R. I. Stephens, A. Fatemi, A., R. R. Stephens, and H. O. Fuchs, "Metal fatigue in engineering", John Wiley & Sons, 2000.

[16] S. Suresh, "Fatigue of materials", Cambridge university press, 1998.

[17] S. Suresh and R. O. Ritchie, “Propagation of short fatigue cracks,” Int. Met. Rev., 29, 1, 445–475, 1984.

[18] R. Ritchi and P. JO, "Small fatigue cracks: mechanics, mechanisms and engineering applications." Mater. Trans., 42, 1, 58-67, 2001.

[19] D. McDowell, K. Gall, M. Horstemeyer, and J. Fan, "Microstructure-based fatigue modeling of cast A356-T6 alloy", Eng. Fract. Mech., 70, 1, 49-80, 2003.

[20] M. J. Caton, J. W. Jones, J. M. Boileau, and J. E. Allison, “The effect of solidification rate on the growth of small fatigue cracks in a cast 319-type aluminum alloy,” Metall. Mater. Trans. A, 30, 12, 3055–3068, 1999.

[21] M. Caton, J. Jones, and J. Allison, "Use of small fatigue crack growth analysis in predicting the SN response of cast aluminum alloys. In Fatigue Crack Growth Thresholds", ASTM International, 2000.

[22] K. Shiozawa, Y. Tohda, and S. M. Sun, “Crack initiation and small fatigue crack growth behavior of squeeze cast Al-Si aluminum alloys,” Fatigue Fract. Eng. Mater. Struct., 20, 2, 237–247, 1997.

[23] J. Schijve, "Significance of fatigue cracks in micro-range and macro-range." Fatigue crack propagation. ASTM International, 1967.

[24] Y. Jang, Y. Jeong, C. Yoon, and S. Kim, “Fatigue Life Prediction for Porosity-Containing Cast 319-T7 Aluminum Alloy,” Metall. Mater. Trans. A, 40, 5, 1090–1099, 2009.

[25] Q. G. Wang, P. N. Crepeau, C. J. Davidson, and J. R. Griffiths, “Oxide films, pores and the fatigue lives of cast aluminum alloys,” Metall. Mater. Trans. B, 37, 6, 887–895, 2006.

[26] Q. G. Wang and P. E. Jones, “Prediction of Fatigue Performance in Aluminum Shape Castings Containing Defects,” Metall. Mater. Trans. B, 38, 4, 615–621, 2007.

[27] J. Yi, Y. Gao, P. Lee, and T. C. Lindley, "Effect of Fe-content on fatigue crack initiation and propagation in a cast aluminum–silicon alloy (A356–T6)". Mater. Sci. Eng. A, 386, 1-2, 396-407, 2004.

[28] J. B. Jordon, M. F. Horstemeyer, N. Yang, N., J. F. Major, K. Gall, J. Fan, and D. L. McDowell, "Microstructural inclusion influence on fatigue of a cast A356 aluminum alloy", Metal. Mater. Trans. A, 41, 2, 356–363, 2010.

[29] Y. Murakami and M. Endo, “Effects of defects, inclusions and inhomogeneities on fatigue strength,” Int. J. Fatigue, 16, 3, 163–182, 1994.

[30] H. Mayer, M. Papakyriacou, B. Zettl, and S. E. Stanzl-Tschegg, “Influence of porosity on the fatigue limit of die cast magnesium and aluminium alloys,” Int. J. Fatigue, 25, 3, 245–256, 2003.

[31] H. R. Ammar, A. M. Samuel, and F. H. Samuel, “Effect of casting imperfections on the fatigue life of 319-F and A356-T6 Al-Si casting alloys,” Mater. Sci. Eng. A, 473, 1–2, 65–75, 2008.

[32] Y. X. Gao, J. Z. Yi, P. D. Lee, and T. C. Lindley, “The effect of porosity on the fatigue life of cast aluminium-silicon alloys”, Fatigue Fract. Eng. Mater. Struct., 27, 7, 559–570, 2004.

[33] B. Zhang, D. R. Poirier, and W. Chen, “Microstructural effects on high-cycle fatigue-crack initiation in A356.2 casting alloy,” Metall. Mater. Trans. A, 30, 10, 2659–2666, 1999.

[34] J. M. Boileau and J. E. Allison, “The Effect of Solidification Time on The Mechanical Properties of a Cast 319 Aluminum Alloy,” SEA Int, 2001.

[35] L. Lattanzi, A. Fabrizi, A. Fortini, M. Merlin, and G. Timelli, “Effects of microstructure and casting defects on the fatigue behavior of the high-pressure die-cast AlSi9Cu3(Fe) alloy,” Procedia Struct. Integr., 7, 505–512, 2017.

[36] M. Roy, Y. Nadot, D. M. Maijer, and G. Benoit, “Multiaxial fatigue behaviour of A356-T6,” Fatigue Fract. Eng. Mater. Struct., 35, 12, 1148–1159, 2012.

[37] I. Koutiri, D. Bellett, F. Morel, … L. A.-I. J. of, and undefined 2013, “High cycle fatigue damage mechanisms in cast aluminium subject to complex loads,” Elsevier.

[38] M. Houria, Y. Nadot, R. Fathallah, M. Roy, and D. M. Maijer, "Influence of casting defect and SDAS on the multiaxial fatigue behaviour of A356-T6 alloy including mean stress effect", Int. J. Fatigue, 80, 90-102, 2015.

[39] V. Le, F. Morel, D. Bellett, N. Saintier, and P. Osmond, "Simulation of the Kitagawa-Takahashi diagram using a probabilistic approach for cast Al-Si alloys under different multiaxial loads", Int. J. Fatigue, 93, 109-121, 2016.

[40] V. Le, F. Morel, D. Bellett, N. Saintier, N., and P. Osmond, "Multiaxial high cycle fatigue damage mechanisms associated with the different microstructural heterogeneities of cast aluminium alloys", Mater. Sci. Eng. A, 649, 426-440, 2016.

[41] J. Eady and D. M. Smith, "The effect of porosity on the tensile properties of aluminium castings", Materials forum, 9, 4, 217-223, 1986.

[42] L. Kuchariková, E. Tillová, M. Uhríčik, and J. Belan, “Porosity formation of AlSiCu cast alloy fatigue properties,” MATEC, 07003, 1–9, 2018.

[43] P. Li, P. D. Lee, D. M. Maijer, and T. C. Lindley, “Quantification of the interaction within defect populations on fatigue behavior in an aluminum alloy,” Acta Mater., 57, 12, 3539–3548, 2009.

[44] J. Buffiere, S. Savelli, P. Jouneau, E. Maire, and R. Fougeres, "Experimental study of porosity and its relation to fatigue mechanisms of model Al–Si7–Mg0. 3 cast Al alloys", Mater. Sci. Eng. A, 316, 1-2, 115-126, 2001.

[45] M. Seniw, M. Fine, E. Chen, M. Meshii, and J. Gray, “Relation of defect size and location to fatigue failure in Al alloy A356 cast specimens,” TMS, 1997.

[46] J. C. Ting and F. V. Lawrence, “Modeling the long life faigue behavior of a cast aluminum alloy,” Fatigue Fract. Eng. Mater. Struct., 16, 6, 631–647, 1993.

[47] K. Gall, M. Horstemeyer, B. W. Degner, D. L. McDowell, and J. Fan, "On the driving force for fatigue crack formation from inclusions and voids in a cast A356 aluminum alloy", Int. J. Fracture, 108, 3, 207-233, 2001.

[48] J. Linder, , A. Arvidson, and J. Kron, “The influence of porosity on the fatigue strength of high-pressure die cast aluminium,” Fatigue Fract. Eng. Mater. Struct., 29, 5, 357–363, 2006.

[49] J. M. Boileau and J. E. Allison, “The effect of solidification time and heat treatment on the fatigue properties of a cast 319 aluminum alloy,” Metall. Mater. Trans. A, 34, 9, 1807–1820, 2003.

[50] X. Zhu, J. Z. Yi, J. W. Jones, and J. E. Allison, “A Probabilistic Model of Fatigue Strength Controlled by Porosity Population in a 319-Type Cast Aluminum Alloy: Part I. Model Development,” Metall. Mater. Trans. A, 38, 5, 1111–1122, 2007.

[51] J. Fan, D. McDowell, M. Horstemeyer, and K. Gall, "Cyclic plasticity at pores and inclusions in cast Al–Si alloys", Eng. Fract. Mech., 70, 10, 1281-1302, 2003.

[52] M. H. El Haddad, K. N. Smith, and T. H. Topper, “Fatigue Crack Propagation of Short Cracks,” J. Eng. Mater. Technol., 101, 1, 42, 1979.

[53] M. Tebaldini, C. Petrogalli, G. Donzella, M. Gelfi, and G. M. La Vecchia, “A356-T6 wheels: Influence of casting defects on fatigue design,” Fatigue Fract. Eng. Mater. Struct., 41, 8, 1784–1793, 2018.

[54] M. Kobayashi and T. Matsui, "Prediction of fatigue strength of aluminum casting alloys by the√ area parameter model", Trans. JSME A, 62, 594, 341-346, 1996.

[55] H. Noguchi, K. Morishige, T. Fujii, T. Kawazoe, S. Hamada, “Proposal of method for estimation of threshold stress intensity factor range on small crack for light metals”, Jpn Soc. Mech. Sci., 56, 137-138, 2007.

[56] A. Ueno, S. Miyakawa, K. Yamada, and T. Sugiyama, “Fatigue behavior of die casting aluminum alloys in air and vacuum,” Procedia Engineering, 2, 1, 1937–1943, 2010.

[57] A. Tajiri, T. Nozaki, Y. Uematsu, T. Kakiuchi, M. Nakajima, Y. Nakamura, and H. Tanaka, "Fatigue limit prediction of large scale cast aluminum alloy A356", Procedia materials science, 3, 924-929, 2014.

[58] W. Elber, “Fatigue crack closure under cyclic tension,” Eng. Fract. Mech., 2, 1, 37–45, 1970.

[59] J. C. Newman, “A crack opening stress equation for fatigue crack growth,” Int. J. Fract., 24, 4, R131–R135, 1984.

[60] N. E. Frost, “A relation between the critical alternating propagation stress and crack length for mild steel,” Proc. Inst. Mech. Eng., 173, 1, 811–836, 1959.

[61] H. Nisitani, M. Goto, "A small crack growth law and its application to the evaluation of fatigue life, the behaviour of short fatigue cracks", Mech. Eng. Pub, 461, 1986.

[62] M. Goto and H. Nisitani, “Fatigue life prediction of heat treated carbon steels and low alloy steels based on a small crack growth law,” Fatigue Fract. Eng. Mater. Struct., 17, 2, 171–185, 1994.

[63] G. Nicoletto, G. Anzelotti, and R. Konečná, “X-ray computed tomography vs. metallography for pore sizing and fatigue of cast Al-alloys,” Procedia Engineering, 2, 1, 547–554, 2010.

[64] E. Ferrie, J. Buffiere, W. Ludwig, “3D characterisation of the nucleation of a short fatigue crack at a pore in a cast Al alloy using high resolution synchrotron microtomography,” Int J. Fatigue, 27, 10-12, 1215-1220, 2005.

[65] C. Garb, M. Leitner, M. Tauscher, M. Weidt, and R. Brunner, “Statistical analysis of micropore size distributions in Al-Si castings evaluated by X-ray computed tomography,” Zeitschrift fuer Met. Res. Adv. Tech., 109, 10, 889–899, 2018.

[66] M. Leitner, C. Garb, H. Remes, and M. Stoschka, “Microporosity and statistical size effect on the fatigue strength of cast aluminium alloys EN AC-45500 and 46200,” Mater. Sci. Eng. A, 707, 567–575, 2017.

[67] G. Nicoletto, R. Konečná, P. Baicchi, and V. Majerová, “Casting Porosity and Long-Life Fatigue Strength of a Cast Al-Alloy,” Mater. Sci. Forum, 567–568, 393–396, 2008.

[68] S. Fintova, V. Konstantová, R. Konečná, and G. Nicoletto, “Experimental Study of Porosity and Fatigue Behavior af Cast Al – Si Alloys,” Metal, 13, 15, 1–8, 2008.

[69] R. Konecna, G. Nicolletto, and V. Majerova, "Largest extreme value determination of defect size with application to cast Al-Si alloys porosity", Metal, 16, 94, 2007.

[70] Z. Li et al., “Study of 3D Pores and Its Relationship with Crack Initiation Factors of Aluminum Alloy Die Castings,” Metal. Materi. Trans. B 50, 3, 1204-1212, 2019.

[71] Y. Zhang, J. Xu, and T. Zhai, “Distributions of pore size and fatigue weak link strength in an A713 sand cast aluminum alloy,” Mater. Sci. Eng. A, 527, 16–17, 3639–3644, 2010.

[72] K. Tanaka, Y. Nakai, and M. Yamashita, “Fatigue growth threshold of small cracks,” Int. J.

Fract., 17, 5, 519–533, 1981.

[73] G. Nicoletto, G. Anzelotti, and R. Konečná, "X-ray computed tomography vs. metallography for pore sizing and fatigue of cast Al-alloys", Procedia Engineering, 2, 1, 547-554, 2010.

[74] B. Zhang, “The influence of porosity and its modeling on fatigue behavior of high pressure die cast aluminum including the effects of mean stress, stress gradient and specimen size”, University of Toledo, Toledo, OH, 2019..

[75] “ASTM E8 - 04 Standard Test Methods for Tension Testing of Metallic Materials”.

[76] “ASTM E739 - 10(2015) Standard Practice for Statistical Analysis of Linear or Linearized Stress-Life (S-N) and Strain-Life (ε-N) Fatigue Data”.

[77] M. Tiryakioğlu, "On the relationship between statistical distributions of defect size and fatigue life in 7050-T7451 thick plate and A356-T6 castings", Mater. Sci. Eng. A, 520, 1-2, 114-120, 2009.

[78] J. Goodman, Mechanics applied to engineering, Longman, Green, 1918..

[79] K. Smith, P. Watson, and T. H. Topper, “A stress-strain function for the fatigue of metals”, J. Mat., 5, 767-778, 1970

[80] K. Walker, "The effect of stress ratio during crack propagation and fatigue for 2024-T3 and 7075-T6 aluminum." ASTM International, 1970.

[81] N. E. Dowling, “Mean stress effects in strain-life fatigue,” Fatigue Fract. Eng. Mater. Struct., 32, 12, 1004–1019, 2009.

[82] N. E. Dowling, C. A. Calhoun, and A. Arcari, “Mean stress effects in stress-life fatigue and the Walker equation,” Fatigue Fract. Eng. Mater. Struct., 32, 3, 163–179, 2009.

[83] H. Özdeş, and M. Tiryakioğlu, "Walker Parameter for Mean Stress Correction in Fatigue Testing of Al-7% Si-Mg Alloy Castings", Materials, 10, 12, 1401, 2017.

[84] H. Kitagawa, and S. Takahashi, "Fracture mechanical approach to very small fatigue cracks and to the threshold", Trans J. Soc Mech Eng, 45, 1289-1303, 1979.

[85] B. Atzori, P. Lazzarin, and G. Meneghetti, “A unified treatment of the mode i fatigue limit of components containing notches or defects,” Int. J. Fract., 133, 1, 61–87, 2005.

[86] B. Tabernig, P. Powell, and R. Pippan, "Resistance curves for the threshold of fatigue crack propagation in particle reinforced aluminium alloys", ASTM International, 2000.

[87] M. Roy, Y. Nadot, D. M. Maijer, and G. Benoit, "Multiaxial fatigue behaviour of A356-T6" Fatigue Fract. Eng. Mater. Struct., 35, 12, 1148-1159, 2012.

[88] ASM Handbook, ASM International, Vol. 19, 1990.

[89] R. Konecna, G. Nicolletto and V. Majerova, "Largest extreme value determination of defect size with application to cast Al-Si alloys porosity", Metal, 16, 94, 2007.

[90] S. Fintová, V. Konstantová, R. Konečná, and G. Nicoletto, “Experimental study of porosty and fatigue behavior of cast Al-Si alloys,” METAL, 2008.

[91] O. E. Daoud and D. J. Cartwright, "Strain energy release rate for a circular-arc edge crack in a bar under tension or bending", J Strain Analysis Eng Des., 20, 1, 53-58, 1985.

[92] D. Kujawski, "A new (ΔK+ Kmax) 0.5 driving force parameter for crack growth in aluminum alloys", Int. J. Fatigue, 23, 8, 733-740, 2001.

[93] R. G. Forman, V. E. Kearney, and R. M. Engle, “Numerical Analysis of Crack Propagation in Cyclic-Loaded Structures,” J. Basic Eng., 89, 3, 459, 1967.

[94] R. Jones, L. Molent, and K. Walker, "Fatigue crack growth in a diverse range of materials", Int. J. Fatigue, 40, 43-50,2012.

[95] D. Tamboli, S. Barter, and R. Jones, "On the growth of cracks from etch pits and the scatter associated with them under a miniTWIST spectrum", Int. J. Fatigue, 109, 10-16, 2018.

[96] D. Lados and D. Apelian, "Fatigue crack growth characteristics in cast Al–Si–Mg alloys: Part I. Effect of processing conditions and microstructure", Mater. Sci. Eng. A, 385, 1-2, 200-211, 2004.

[97] A. Shyam, J. Allison, C. Szczepanski, T. M. Pollock, and J. W. Jones,"Small fatigue crack growth in metallic materials: a model and its application to engineering alloys", Acta Materialia, 55, 19, 6606-6616, 2007.

[98] S. Fintová, R. Konečná, and G. Nicoletto, "Statistical description of largest pore size in modified Al-Si alloys", Materials engineering, 16, 3, 24-28, 2009.

[99] D. Lados, D. Apelian, P. Paris, and J. K. Donald, "Closure mechanisms in Al–Si–Mg cast alloys and long-crack to small-crack corrections", Int. J. Fatigue, 27, 10-12, 1463-1472, 2005.

[100] K. J. Miller, and D. C. Chandler. "High strain torsion fatigue of solid and tubular specimens." Proc. Inst. Mech. Eng., 184, 1, 433-448, 1969.

[101] N. Shamsaei, and A. Fatemi, "Small fatigue crack growth under multiaxial stresses", Int. J. Fatigue, 58, 126-135, 2014.

[102] A. Fatemi and L. Yang, “Cumulative fatigue damage and life prediction theories: A survey of the state of the art for homogeneous materials,” Int. J. Fatigue, 20, 1, 9–34, 1998.

[103] ASTM-E1049-85, “Standard practices for cycle counting in fatigue analysis,” Annu. B. ASTM Stand., 03.01, 2017.

[104] N. R. Gates and A. Fatemi, “Multiaxial variable amplitude fatigue life analysis using the critical plane approach, Part II: Notched specimen experiments and life estimations,” Int. J. Fatigue, 106, 56–69, 2018.

[105] S. Sharifimehr and A. Fatemi, “Fatigue analysis of ductile and brittle behaving steels under variable amplitude multiaxial loading,” Fatigue Fract. Eng. Mater. Struct., 42, 8, 1722–1742, 2019.

[106] C. M. Sonsino, "Fatigue testing under variable amplitude loading", Int. J. Fatigue, 29, 6, 1080-1089, 2007.

[107] C. M. Sonsino, "Principles of variable amplitude fatigue design and testing", ASTM International, 2005.

[108] D. Lados and D. Apelian, "Fatigue crack growth characteristics in cast Al–Si–Mg alloys: Part II. Life predictions using fatigue crack growth data", Mater. Sci. Eng. A, 385, 1-2, 187-199, 2004.

[109] J. C. Newman, K. Kota, and T. E. Lacy, "Fatigue and crack-growth behavior in a titanium alloy under constant-amplitude and spectrum loading", Eng. Fract. Mech., 187, 211-224, 2018.